

**Probing Biological Performance Diversity and the  
Discovery of Autophagy-Specific Inhibitors**

BY

Ivan Pavlinov  
B.S., Wayne State University, 2015

DISSERTATION

Submitted in partial fulfillment of the requirements  
for the degree of Doctor of Philosophy in Chemistry  
in the Graduate College of the  
University of Illinois at Chicago, 2020

Chicago, Illinois

Defense Committee:

Leslie Aldrich, Chair and Advisor  
Stephanie Cologna, Chemistry  
Leslie Wo-Mei Fung, Chemistry  
Ying Hu, Chemistry  
Terry Moore, Pharmaceutical Sciences

## ACKNOWLEDGMENTS

I would like to thank my advisor, Leslie Aldrich, for all of her unwavering support and great advice throughout my research endeavors. I would also like to extend my gratitude to the other members of my committee, Leslie Fung, Stephanie Cologna, Ying Hu and Terry Moore, for their constructive comments that were critical to improving the overall quality of this dissertation. Additionally, I would like to thank all my lab members and specifically Erica Gerlach, Alara Korkmaz, Ryan Hippman and Maryna Salkovski for their tireless collaborative efforts on our shared projects. Thank you also to Ratia Kiira and Hyun Lee, who are members of the High Throughput Screening and Biophysics cores, respectively, and whose kind assistance with instrumentation was critical for the completion of this dissertation.

IP

## CONTRIBUTIONS OF AUTHORS

Chapter 1 is focused on the application of Cell Painting to the evaluation of the biological performance diversity of natural product libraries. For these projects two libraries of small molecules were synthesized by Erica Gerlach, Alara Korkmaz and Ryan Hippman. I undertook all other works involved in screening and evaluating the molecules. All figures included in the Results and Discussion section of this chapter are from two published manuscripts and represent data I personally generated. Chapter 2 is focused on the discovery of autophagy-specific inhibitors by targeting protein-protein interactions. All figures included in the Results and Discussion section of this chapter are from a published manuscript and represent data I generated, except for Figure 51E and Figure 53D, which were the work of Maryna Salkovski, and Figure 54, which represents unpublished data.

## TABLE OF CONTENTS

CHAPTER 1 .....	1
I. Introduction.....	1
A. History, background, design strategies and current limitations of small molecule libraries .....	1
B. The utility of natural products and natural product-inspired libraries in drug discovery .....	6
C. Assessing library diversity – structure vs. performance.....	8
D. Quantifying biological performance-diversity through phenotype .....	11
II. Methodology.....	13
A. Measuring phenotype through cellular morphology profiling using fluorescence microscopy .....	13
B. Compound treatment, staining, image acquisition and processing.....	16
C. Profile aggregation, normalization and feature selection .....	20
D. Dimensionality reduction and activity determination .....	22
E. Chemical feature measurement and correlation with compound activity.....	26
F. Assessing diversity through PCA and hierarchical clustering.....	27
III. Results and Discussion.....	29
A. Profiling flavone derivatives enriched in sp <sup>3</sup> character .....	29
B. Effects of appendages on performance diversity of the pyrone scaffold.....	32
C. Profiling a stereochemically and structurally diverse library of benzofurans and benzopyrans.....	34
D. Establishing correlations between chemical features and bioactivity .....	38
E. Determining the structure activity relationship driving similarity using hierarchical clustering analysis ..	41
F. The synergistic effects of scaffold, stereochemistry and appendage variation on biological performance diversity .....	48
IV. Conclusion .....	52
CHAPTER 2 .....	55
I. Introduction.....	55
A. The history and molecular biology of autophagy .....	55
B. Dual role of autophagy in cancer .....	59
C. The dual role of autophagy in other diseases .....	61
D. Autophagy modulators as cancer therapeutics .....	63
E. Targeting the VPS34 complex for the development of autophagy inhibitors .....	65
F. Targeting the ATG5-ATG12-ATG16L1 complex for the development of autophagy inhibitors .....	70
G. Feasibility of targeting PPIs for small molecule probe development.....	72
II. Methodology.....	75
A. Design and development of NanoBRET assays targeting the Beclin 1-ATG14L and the Beclin 1-UVRAG interactions.....	75
B. Validation of NanoBRET assay targeting the Beclin 1-ATG14L interaction.....	79
C. Optimization of NanoBRET for HTS .....	81

## TABLE OF CONTENTS (continued)

D.	Performance of NanoBRET screen using PPI inhibitor library .....	83
E.	Prioritization of hit molecules based on the inhibition of autophagy .....	83
F.	Confirmation of the potency and activity of prioritized hit.....	86
G.	Elucidation of compound mechanism using Complex I pull-down and cellular thermal shift assay .....	87
H.	Performance of NanoBRET assay targeting the Beclin 1-UVRAG interaction.....	90
I.	Experiments confirming specificity for autophagy inhibition over disruption of vesicle trafficking.....	91
J.	Design of ATG5-ATG16L1 FP assay .....	93
K.	Preparation of reagents for the ATG5-ATG16L1 FP assay .....	94
L.	Development and confirmation of specificity for the ATG5-ATG16L1 FP assay.....	97
III.	Results and Discussion .....	98
A.	Development and validation of NanoBRET assay targeting the Beclin 1-ATG14L interaction.....	98
B.	Optimization of NanoBRET assay targeting the Beclin 1-ATG14L interaction for HTS.....	99
C.	Pilot screen for small molecules targeting the Beclin1-ATG14L interaction .....	101
D.	Prioritization of hits based on autophagy inhibition.....	104
E.	Confirmation of the disruption of VPS34 Complex I formation by compound 19 .....	108
F.	Evaluation of autophagy inhibition caused by Complex I disruption .....	111
G.	Insights into the impact of selective Complex I disruption on vesicle trafficking .....	112
H.	Development and validation of FP assay targeting the ATG5-ATG16L1 interaction .....	116
IV.	Conclusion .....	119
	CITED LITERATURE.....	122
	VITA .....	147
	APPENDIX .....	148

## LIST OF TABLES

<b>Table 1.</b> Stains and filters used in Cell Painting assay.....	15
<b>Table 2.</b> Mean cell counts and activity scores for highly correlated and highly dissimilar compounds. ....	44
<b>Table 3.</b> Mahalanobis distances for each stereoisomer (left) and scaffold (right) pair at 100 $\mu$ M.....	51
<b>Table 4.</b> Vectors generated for NanoBRET experiments.....	78
<b>Table 5.</b> Primers and their sequences.....	78

## LIST OF FIGURES

<b>Figure 1</b> Sample structures of biologically active small molecules derived from each library.....	3
<b>Figure 2.</b> Impact of the method of selection on the activity of small molecule libraries. ....	5
<b>Figure 3.</b> Examples of strategies used to generate natural product-like analog libraries. ....	8
<b>Figure 4.</b> Different methods for assessing compound diversity.....	10
<b>Figure 5.</b> Cell Painting workflow. ....	17
<b>Figure 6.</b> Example of the plate layout used for Cell Painting experiments.....	19
<b>Figure 7.</b> The three parts of image processing. ....	21
<b>Figure 8.</b> Schematic of the feature selection procedure based on the maximal relevance and minimal redundancy algorithm.....	23
<b>Figure 9.</b> Schematic of PCA. ....	24
<b>Figure 10.</b> Activity determination through the calculation of treatment-specific Mahalanobis distances (activity scores) and mp-values. ....	26
<b>Figure 11.</b> Diagram of agglomerative hierarchical clustering.....	29
<b>Figure 12.</b> Structure of natural and reduced flavones. ....	31
<b>Figure 13.</b> Comparison of biological performance diversity using the Cell Painting assay. ....	33
<b>Figure 14.</b> Correlation between biological activity and clogP.....	34
<b>Figure 15.</b> Chemical features of the benzofuran and benzopyran library. ....	36
<b>Figure 16.</b> Overall activity of the benzofuran and benzopyran library. ....	37
<b>Figure 17.</b> Correlation plots for the mean activity score and mean cell count and (A) clogP and (B) tPSA. ....	39
<b>Figure 18.</b> Correlation plots for the average activity score and average cell count and (A) MW and (B) fsp3. ....	40
<b>Figure 19.</b> Heatmap of benzofuran and benzopyran library. ....	42
<b>Figure 20.</b> The feature profiles generated for each of the clustered compounds at 100 $\mu$ M.....	45
<b>Figure 21.</b> Representative images showcasing the different phenotypes induced by a representative compound in each highly correlated cluster in comparison to DMSO control wells. ....	46
<b>Figure 22.</b> Representative images showcasing the phenotypes induced by three molecules that were uncorrelated with the rest of the library.....	47
<b>Figure 23.</b> PCA plots of compound pairs and their structures. ....	49
<b>Figure 24.</b> PCA plots of compound pairs in dose. ....	50
<b>Figure 25.</b> The autophagy pathway and the proteins involved in autophagy activation. ....	58
<b>Figure 26.</b> The various molecules that activate or inhibit autophagy and the relative position of their targets within the pathway.....	64
<b>Figure 27.</b> Structural characterization of the VPS34 Complexes.....	67

## LIST OF FIGURES (continued)

<b>Figure 28.</b> Lack of specificity limits the utility of the current generation of autophagy probes. ....	69
<b>Figure 29.</b> The crystal structure of the ATG5-ATG12 conjugate associated with the N-terminal domain of ATG16L1. ....	71
<b>Figure 30.</b> Energetic contributions of residues on different faces of interfacial helices. ....	73
<b>Figure 31.</b> The NanoBRET method and its advantages. ....	76
<b>Figure 32.</b> Creation of the NanoBRET vectors. ....	77
<b>Figure 33.</b> The donor saturation assay (DSA). ....	80
<b>Figure 34.</b> Plot illustrating the Z'-factor. ....	82
<b>Figure 35.</b> Methods used to estimate autophagic flux through quantification of LC3. ....	85
<b>Figure 36.</b> Schematic of HaloTag pull-down of VPS34 Complex I. ....	88
<b>Figure 37.</b> Principle of the use of CETSA to determine ligand binding. ....	90
<b>Figure 38.</b> Principle of the use of DQ-BSA to monitor endocytic trafficking. ....	92
<b>Figure 39.</b> Targeting the ATG5-ATG16L1 interaction using and FP assay. ....	94
<b>Figure 40.</b> Plasmid map for the vector used for the expression of MBP-ATG5. ....	95
<b>Figure 41.</b> Development of NanoBRET assay targeting the PPI of Beclin 1 and Atg14L in Hek293T cells. ....	99
<b>Figure 42.</b> Optimization of NanoBRET assay. ....	101
<b>Figure 43.</b> Comparison of NanoBRET performance between the Spectramax i3x and the Victor 3V. ....	101
<b>Figure 44.</b> Assay metrics from the NanoBRET-based HTS targeting the Beclin 1-ATG14L interaction in Hek293T cells. ....	103
<b>Figure 45.</b> Exclusion of hits based on cytotoxicity. ....	104
<b>Figure 46.</b> Dose curves of the 19 hits from pilot NanoBRET HTS. ....	106
<b>Figure 47.</b> Prioritization of the 19 hits from pilot NanoBRET HTS through assesment of autophagy inhibition. ....	107
<b>Figure 48.</b> Limited SAR and potency of <b>19</b> . ....	108
<b>Figure 49.</b> Effect of VPS34 inhibitors on the protein-protein interactions of Beclin1 in Hek293T cells. ....	110
<b>Figure 50.</b> Compound <b>19</b> inhibits autophagy through disruption of VPS34 Complex I by potential binding to ATG14L. ....	110
<b>Figure 51.</b> Evaluation of compound treatment on autophagy in A549 and HeLa cells. ....	112
<b>Figure 52.</b> Development of NanoBRET assay targeting the PPI of Beclin 1 and UVRAG in Hek293T cells. ....	114
<b>Figure 53.</b> Determination of specificity of <b>19</b> for the autophagic pathway as compared to VPS34 inhibitors. ....	115
<b>Figure 54.</b> Development of the ATG5-ATG16L1 FP assay. ....	118

## LIST OF ABBREVIATIONS

DOS	Diversity Oriented Synthesis
tPSA	Topological Polar Surface Area
PPIs	Protein-Protein Interactions
FP	Fluorescence Polarization
HTS	High Throughput Screening
SAR	Structure Activity Relationship
BIOS	Biology Oriented Synthesis
CtD	Complexity-to-Diversity
PMI	Principal Moment of Inertia
MOA	Mechanism of Action
HCS	High-Content Screening
FBS	Fetal Bovine Serum
DMEM	Dulbecco's Modified Eagle Medium
BSA	Bovine Serum Albumin
HBSS	Hank's Buffer Salt Solution
MAD	Mean Absolute Deviation
t-SNE	t-Distributed Stochastic Neighbor Embedding
UMAP	Uniform Manifold Approximation and Projection
PCA	Principal Component Analysis
PC	Principal Component
MW	Molecular Weight
CMA	Chaperone-Mediated Autophagy
ER	Endoplasmic Reticulum
PI	Phosphatidylinositol
PI3P	Phosphatidylinositol-3-phosphate
PE	Phosphatidylethanolamine
LC3	MAP1LC3B
LAP	LC3-associated Phagocytosis
ROS	Reactive Oxygen Species

## LIST OF ABBREVIATIONS (continued)

CQ	Chloroquine
BafA1	Bafilomycin A1
CCD	Coiled-coil Domains
FRET	Forster Resonance Energy Transfer
BRET	Bioluminescence Resonance Energy Transfer
NanoLuc	Narrow-spectrum Luciferase
ATG16N	N-terminal domain of ATG16L1
DSA	Donor Saturation Assay
CETSA	Cellular Thermal Shift Assay
TSA	Thermal Shift Assay
T <sub>m</sub>	Melting temperature
Fsp3	Fraction of sp <sup>3</sup> hybridized carbons
AUC	Area under the curve

## SUMMARY

Chapter 1 is focused on the determination of the chemical features that are most relevant to producing small compound libraries with diverse biological activity. The current generation of compound libraries are assembled based on the maximization of a diverse set of chemical features. These libraries have overall low hit rates and a lot of synthesized chemical matter that may not have any biological activity. Utilizing diversity oriented synthesis (DOS) we created two libraries inspired by the flavonoid natural products and profiled these molecules using a target-agnostic technique called Cell Painting, which attempts to characterize the overall morphological change that occurs under compound treatment.

For the first library, which was based around the flavone and pyrone scaffolds, we found that maximizing the fraction of sp<sup>3</sup> carbons on the flavone scaffold did not produce a diverse set of molecules and instead lowered their activity relative to the flatter natural product flavone and novel pyrones. However, we found the second library, which was based around sp<sup>3</sup>-enriched benzofuran and benzopyran derivatives, to be highly active. Using this set of molecules, we were able to demonstrate that this activity was correlated with cLogP and topological polar surface area (tPSA). Additionally, we found that scaffold, stereochemistry and appendage variation had synergistic effects on the overall diversity of the observed biological profiles.

Chapter 2 is focused on the discovery of autophagy inhibitors by targeting protein-protein interactions (PPIs) found within the autophagy initiation pathway. Autophagy is a catabolic process responsible for the recycling of cellular cargo and it has been implicated in a variety of diseases, including cancer. We aimed to find new more autophagy-specific inhibitors to provide better probes and potential therapeutics. Two PPIs were chosen, the Beclin 1-ATG14L interaction and the ATG5-ATG16L1 interaction, because they occur in two autophagy-specific initiation complexes.

We designed a NanoBRET assay to target the Beclin 1-ATG14L interaction. After confirming the specificity of this assay, we screened 2,560 molecules, discovering 19 hits that were then evaluated for their ability to inhibit autophagy. One molecule was chosen as the priority hit based on potency in the NanoBRET assay and evidence of the disruption of autophagic flux due to the inhibition of LC3-II formation. This molecule was also confirmed to disrupt the overall formation of VPS34 Complex I and showed more specificity for the autophagy

## **SUMMARY (continued)**

pathway relative to the current generation of autophagy inhibitors which also inhibit vesicle trafficking. We used fluorescence polarization (FP) to target the ATG5-ATG16L1 interaction and successfully demonstrated that this method could be used to quantify this interaction in a robust, specific way compatible with high-throughput screening (HTS).

## CHAPTER 1

The Methodology, and Results and Discussion sections of this chapter were previously published in Gerlach, E. M.; Korkmaz, M. A.; Pavlinov, I.; Gao, Q.; Aldrich, L. N. Systematic Diversity-Oriented Synthesis of Reduced Flavones from  $\gamma$ -Pyrone to Probe Biological Performance Diversity. *ACS Chem. Biol.* **2019**, *14* (7), 1536–1545 with permission Copyright 2019 American Chemical Society and Hippman, R, S.; Pavlinov, I.; Gao, Q.; Mavlyanova, M. K.; Gerlach E. M.; Aldrich L. N. Multiple chemical features impact biological performance diversity of a highly active flavonoid natural product-inspired library. *ChemBioChem* **2020** with permission Copyright 2020 Wiley.

### **I. Introduction**

#### **A. History, background, design strategies and current limitations of small molecule libraries**

In the last four decades, HTS has emerged as a universal part of the infrastructure driving small molecule drug discovery efforts.<sup>1,2</sup> New technologies such DNA encoded libraries could allow for the routine screening of tens of millions of molecules,<sup>3</sup> but despite such advances evidence suggests that the rate of the discovery of novel therapeutics is stagnating.<sup>4,5</sup> This may be because even a library containing millions of compounds will only sample an infinitesimally small portion of the possible chemical space for molecules under 500 Da, which may be as large as  $10^{60}$  molecules.<sup>6</sup> Therefore, the success of future screening campaigns is likely to be more dependent on library composition, rather than library size, with an emerging emphasis on the inclusion of more structurally diverse compounds.

There exist three broad types of small molecule libraries: natural product and natural product-inspired libraries, combinatorial libraries and DOS libraries (Figure 1). Natural product libraries are created from isolated and resynthesized natural products and their derivatives, as well as natural product extracts that are composed of fractionated mixtures of many molecules.<sup>7</sup> Combinatorial libraries, on the other hand, are typically composed of molecules that are synthetically derived from high-throughput chemical techniques that involve the linear combination of a preset number of building blocks, with an early example of this being peptide chemistry.<sup>8</sup> Lastly, DOS derived libraries typically have more structural complexity than combinatorial libraries, attempting to create molecules with more sp<sup>3</sup> character in an effort to increase the coverage of novel chemical space.<sup>9</sup>

Historically, natural products and their derivatives have been the most often used class of compounds in small molecule screens.<sup>10</sup> Prior to the development of automated screening and modern synthetic techniques, natural products were assessed as mixed extracts with isolation and fractionation efforts driven by assay activity. To date, natural products, their derivatives, and the synthetic pharmacophores based on them are the single largest source of new small molecule drugs, making up around 65% of all anti-cancer drugs approved by the FDA between 1981 and 2019.<sup>11</sup> Today, advances in screening technology and synthetic methodology allow for the direct screening of thousands of pure natural products as well as hundreds of thousands of novel natural product extracts.<sup>12</sup> However, despite this past success, natural product libraries, especially those that contain extracts, suffer from severe drawbacks due to their incompatibility with many HTS assays and their high irreproducibility, along with the persistent problem that many “successful” screening campaigns result in the re-isolation of known natural products often with promiscuous activity.<sup>13,14</sup>

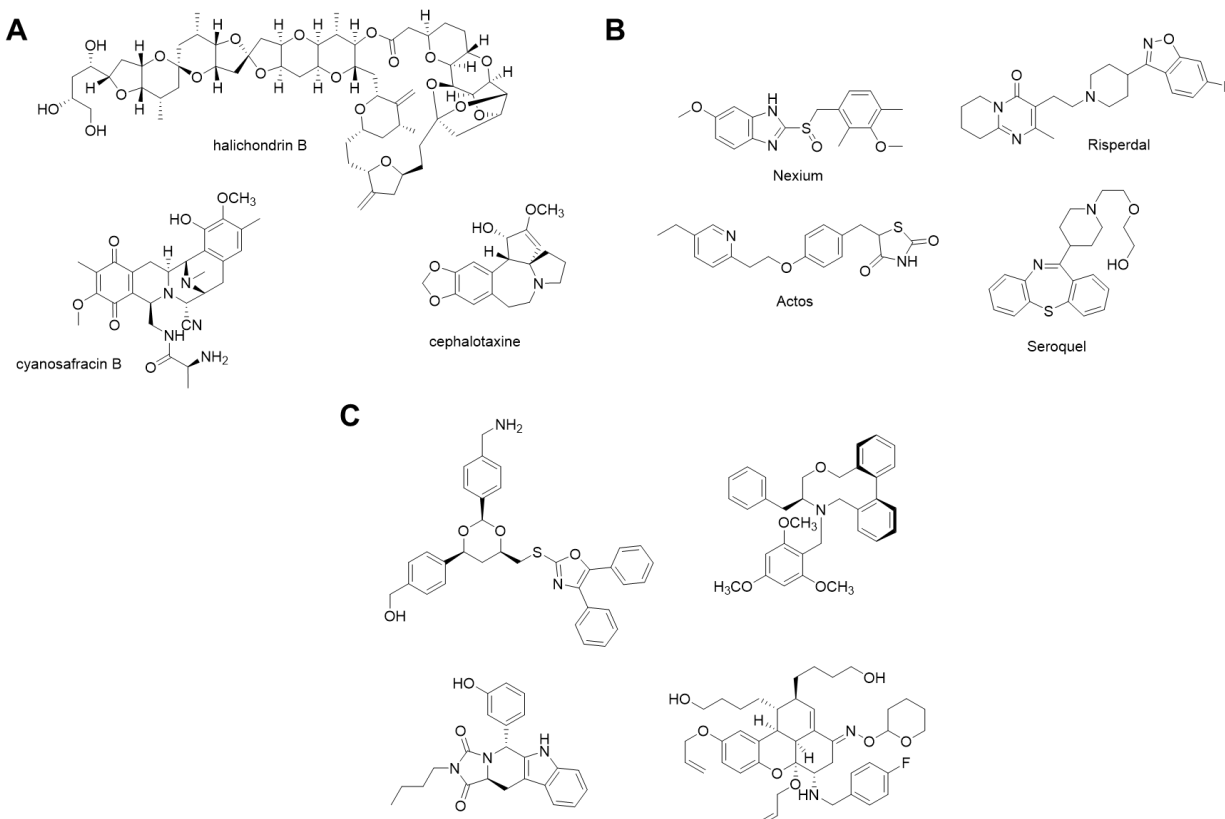


**Figure 1** Sample structures of biologically active small molecules derived from each library: (A) natural product, (B) combinatorial and (C) DOS.

Combinatorial libraries originally emerged out of developments in peptide chemistry that allowed for the rapid synthesis of peptides using standardized reaction conditions that were compatible with solid-phase bead supports, greatly simplifying both synthesis and purification.<sup>15,16</sup> This method has evolved to encompass compound libraries that are encoded genetically, allowing for the rapid selection of wide variety of peptides with specific affinities through the use of directed evolution.<sup>17,18</sup> While capable of creating highly specific ligands that are often useful as *in vitro* probes, peptide based combinatorial libraries struggle to generate true therapeutic lead molecules due their poor bioavailability and absorption properties.<sup>19</sup> Therefore, this synthetic strategy has also been widely applied to the creation of libraries of non-peptide small molecules.<sup>20</sup> Due to its ability to generate such a large quantity of molecules relatively rapidly this technique was extensively applied in industry to generate larger initial screening libraries in addition to seeing broad use in the lead optimization-step, where thousands of molecules

would be synthesized to establish a structure-activity relationship (SAR). In both cases this approach did not improve efficiency and instead lead to the generation of a large quantity of completely inactive chemical matter, though there was some success in producing new drugs based around heterocyclic scaffolds.<sup>21-23</sup> A detailed analysis of commercial combinatorial libraries found the absence of some 1,300 scaffolds commonly found in many natural products, potentially explaining why the success of these libraries was so limited.<sup>24</sup>

Diversity-oriented synthesis was a response to the realization that a major limitation of combinatorial libraries was that they often lacked the motifs and the structural complexity that was common in drug-like molecules and natural products. To address this, DOS methods increase the scaffold and stereochemical diversity of library molecules through several different approaches. Reagent-based methods utilize different reagents to transform or pair functional groups on the starting molecule in a branching manner to generate scaffold diversity (Figure 2). This can be done either through the presence of many such functional groups, each one capable of a specific transformation, or by using a more limited number of pluripotent functional groups that can transform into various products depending on the reagents used.<sup>25,26</sup> Meanwhile, scaffold-based methods use one standard set of conditions to transform a set of molecules into different scaffolds.<sup>27</sup> Typically, a simple precursor is derivatized in a linear fashion to generate a set of molecules that vary the positionality of the functional group that carries the relevant reactivity for the final scaffold-forming reaction, thus the final scaffold is “pre-encoded” by these initial steps. Lastly, “build/couple/pair” can feature combinations of both of the previously mentioned strategies and involves the generation of building blocks that are capable of undergoing intermolecular coupling reactions that result in all possible stereochemical combinations, followed by intramolecular pairing reactions that result in diverse skeletal arrangements.<sup>28</sup> While more complex and difficult to do than combinatorial synthesis, due to smaller set of compatible building blocks, DOS produces molecules with increased sp<sup>3</sup> character, a property that has been demonstrated to improve library performance.<sup>29</sup> Importantly, it has become apparent that DOS derived libraries are successful at modulating targets previously believed to be “undruggable” such as PPIs and transcription factors.<sup>27,30</sup> One limitation of DOS is that its larger, more complex molecules tend to be more specific, resulting in lower hit rates and potentially making hit-to-lead optimization more difficult.<sup>31</sup>

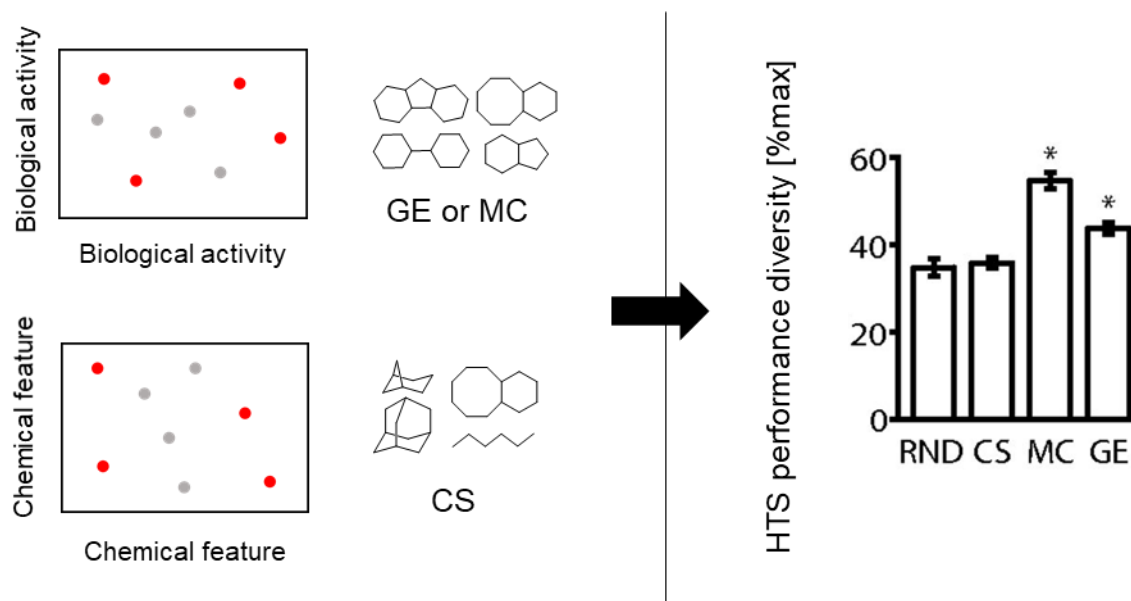


**Figure 2.** Impact of the method of selection on the activity of small molecule libraries. Composition of libraries based on diversity of biological activity or structural features with selected molecules shown in red within the two plots. Libraries selected for diversity of biological activity (gene expression, GE or multiplexed-cytological, MC) produce sets of compounds with higher performance-diversity than random selection (RND) or selection based on chemical features (CS). This figure is adapted from reference 32 with permission.

Another universal limitation of current small molecule libraries is their low hit rates. The average high-throughput screen has a hit rate around 1%.<sup>32,33</sup> This may be due to the fact that though the source of small molecules is different for each library the current paradigm in screening library composition is built on the assumption that a set of molecules with diverse structural and chemical properties will have diverse bioactivity. This assumption may be untrue as most of the molecules contained in current structurally diverse commercial libraries are not active when screened for biological activity.<sup>34</sup> Although it has emerged that this “dark chemical matter” can occasionally produce highly specific hits,<sup>35,36</sup> it is unnecessary to include these molecule in untargeted libraries just in order to maximize structural diversity. In fact, a library selected based on structural diversity does not perform better than one selected randomly (Figure 2).<sup>37</sup> Therefore, in order to compose better libraries, a paradigm shift is necessary from a selection strategy based on structural diversity alone to one based biological performance-

diversity. This type of strategy necessitates the characterization of the types of chemical features that are likely to produce sets of molecules that have a high quantity of targets with little redundancy.

## **B. The utility of natural products and natural product-inspired libraries in drug discovery**

The success of utilizing natural products and their derivatives in drug discovery is difficult to overstate. Along with currently being the largest source of drug-like molecules, natural products continue to be used in screening campaigns to discover molecules for intractable targets, such as PPIs and nucleic acid complexes.<sup>38</sup> Despite this, most commercial libraries are based around molecules, primarily synthesized through combinatorial chemistry, that often lack the larger range of chemical features accessed by natural products.<sup>39</sup> This constrains their ability to modulate novel biological targets and it is estimated that only 10-14% of the human genome can be accessed by them.<sup>40</sup> Thus, it is important to prioritize the creation of additional libraries that include natural products and their derivatives.

One way to create libraries that are broadly bioactive is to utilize natural products as a synthetic starting point. One such strategy, biologically oriented synthesis (BIOS), attempts to do this by basing libraries around minimal natural product pharmacophores from which derivatives are produced (Figure 3A).<sup>41</sup> Simplification of the original scaffold allows for broader derivatization while potentially maintaining the bioactivity of the original natural product. This approach has been successful in generating compounds that access novel targets such as autophagy and Hedgehog pathway inhibitors.<sup>42,43</sup> Recently, this strategy has also yielded a novel class of molecules called pseudo-natural products by fusing multiple natural product scaffolds together. Importantly, these pseudo-natural products have been shown to retain bioactivity while being distinct from their parent natural products, demonstrating that it is possible access new areas of bioactive chemical space utilizing this approach.<sup>44</sup>

Another strategy, complexity-to-diversity (CtD), uses readily available complex natural products and then derivatizes them through concise synthetic routes using methods like ring distortion to introduce more structural diversity (Figure 3B). The resulting sets of molecules have greatly increased sp<sup>3</sup> character and more stereogenic centers relative to both natural products and commercial libraries.<sup>45,46</sup> Recent work has demonstrated that a series of 180 diverse compounds synthesized in this way were used to establish physiochemical properties that contributed to compound penetration into gram-negative bacteria, allowing for the rapid and effective derivatization of deoxybomycin into an antibiotic that was effective against gram-negative bacteria.<sup>47</sup> This establishes the

possibility of using libraries that are diverse in structure and bioactivity to establish which chemical features are relevant for a particular target.

Lastly, a large variety of natural products have also been accessed by the previously mentioned DOS strategies. For example, the scaffold-based approach was used to solid-phase synthesis to rapidly transform *tert*-butylsulfonamide precursors into a series of enyne and diyne intermediates that were derivatized by a small set of final reactions into a library of 190 alkaloid/terpenoid-like small molecules, many of which had chemical properties that were similar to alkaloid/terpenoid natural products.<sup>48</sup> Build-couple-pair has been particularly successful in generating natural product-like macrocycles (Figure 3C). For example, Beckmann *et al.* developed an advanced approach that incorporates a branched coupling reaction with different linkers allowing for structural diversity to be further expanded beyond that of the original building blocks employed.<sup>49</sup> They applied this step-efficient approach to generate a library of 73 macrocyclic compounds of which 59 had unique scaffolds, a significant accomplishment. In addition, unlike traditional total synthesis, DOS generates unnatural product analogs in parallel with the original product, allowing for ready expansion of the unexplored chemical space around a particular target, as in the case of lycopodium alkaloids.<sup>50</sup> In fact, due to the step-efficient nature of most DOS methods, a large number of such derivatives can be generated very rapidly, as demonstrated by the creation of a library of 30,000 DOS-derived small molecules, of which 14,400 were macrolactam derivatives.<sup>51</sup>

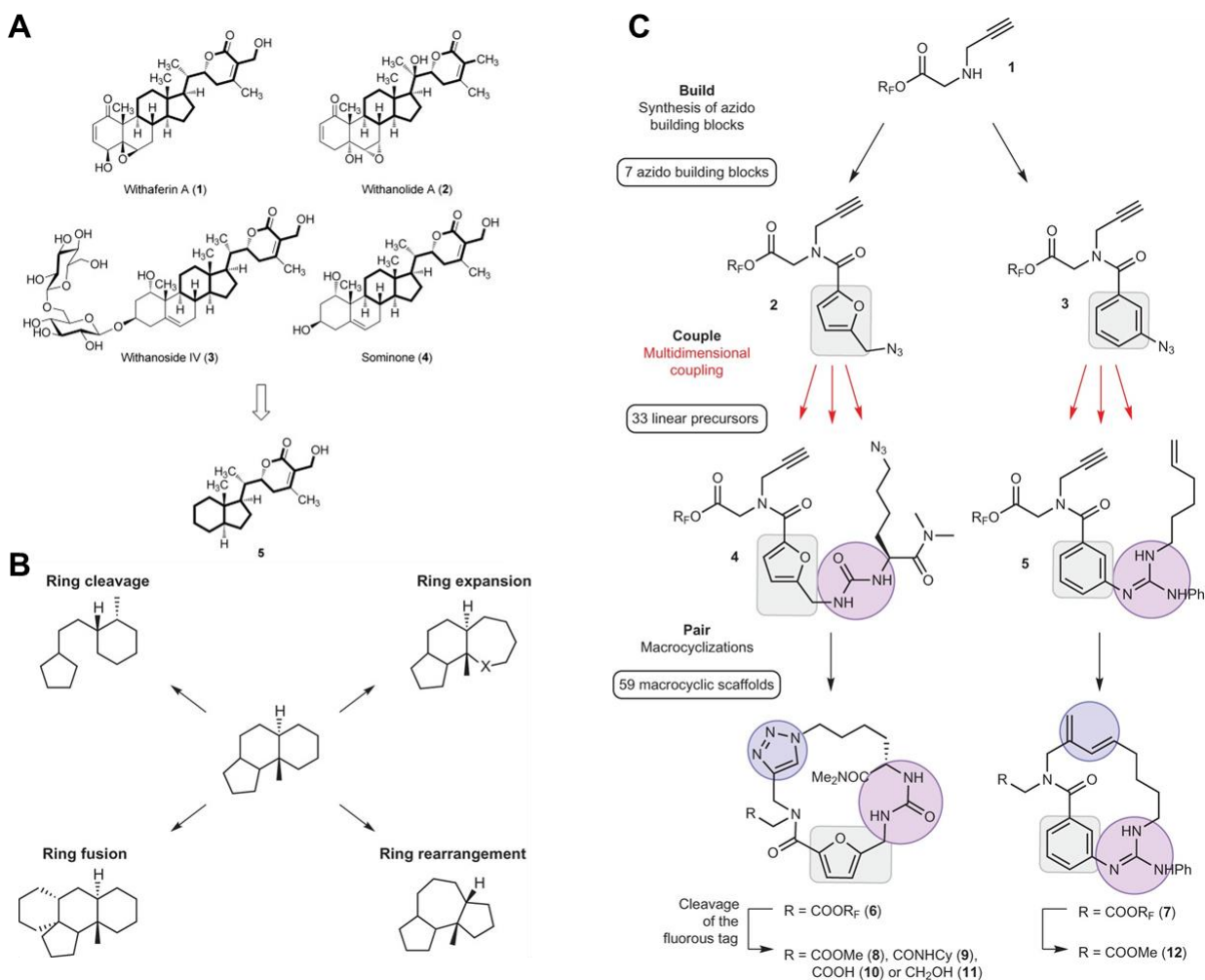


**Figure 3.** Examples of strategies used to generate natural product-like analog libraries. (A) BIOS reduces the complexity of the original Withanolide natural products to the core bioactive scaffold simplifying the synthesis and allowing for the generation of bioactive analogs.<sup>42</sup> (B) CtD uses complex natural product scaffolds as a starting point from which diverse derivatives can be generated, most often through ring distortion reactions.<sup>46</sup> (C) Build-couple-pair derivatizes a simple building blocks by coupling them together through linker molecules to generate linear intermediates for which the final scaffold is set during the pair phase, in this case cyclization reactions.<sup>49</sup> Adapted from references 42, 46, 49 with permission.

### C. Assessing library diversity – structure vs. performance.

Assessing the overall structural, or shape, dissimilarity of molecules remains the central source of metrics used to measure overall library diversity (Figure 4A). 2D structural similarity methods are typically the most efficient because they simply breakdown the overall molecular structure into a binary bit string, or fingerprint, that

describes what substructures are contained in the original molecule and how they are connected. This fingerprint can then be compared to the fingerprints of other molecules using a variety of similarity coefficients.<sup>52</sup> 3D shape similarity methods can also utilize fingerprinting,<sup>53</sup> but also include truly shape based methods such as principal moment of inertia (PMI),<sup>54</sup> and rapid overlay of chemical structures.<sup>55</sup> PMI is routinely used to assess natural product, combinatorial, and especially DOS libraries. All these methods, while effective in creating a set of molecules that are diverse in shape and structural features are not particularly effective at creating sets of that are bioactive, let alone diverse in their bioactivity. One study assessed how well several different types of structural diversity methods were able to assemble libraries that covered the 25 largest activity classes found in the ChEMBL.<sup>56</sup> It was determined that only a couple methods were able to outperform random selection and that the popularly used PMI performed the worst out of all methods. Potentially, most of these methods, while effectively characterizing the geometric shape of small molecules, are limited by their neglect of the critical importance of specific functional groups and general physiochemical properties for bioactivity.

Assessing compounds for the presence of specific chemical features and physiochemical properties is another way to create diverse libraries (Figure 4B). Examples of specific chemical features that can be measured are the fraction of sp<sup>3</sup> carbons or hydrogen-bond donors found in each molecule, both have been correlated with bioactivity.<sup>29,57</sup> Measures of hydrophobicity, such as clogP, or molecular rigidity are examples of the physiochemical properties and also influence the performance of small molecules.<sup>58,59</sup> One benefit of using these metrics over shape-based diversity measurements is because for many of these characteristics a desirable range of properties is already known, thus potentially avoiding the inclusion of completely inactive molecules. Additionally, data analysis strategies can combine several measurements into overall composites that can conveniently illustrate the diversity of a library. Recently, it has demonstrated that these composite methods can effectively evaluate libraries of DOS derived macrocyclic peptides and peptidomimetics and show that they have different biologically relevant chemical and physical features when compared to known macrocyclic natural products.<sup>60,61</sup>

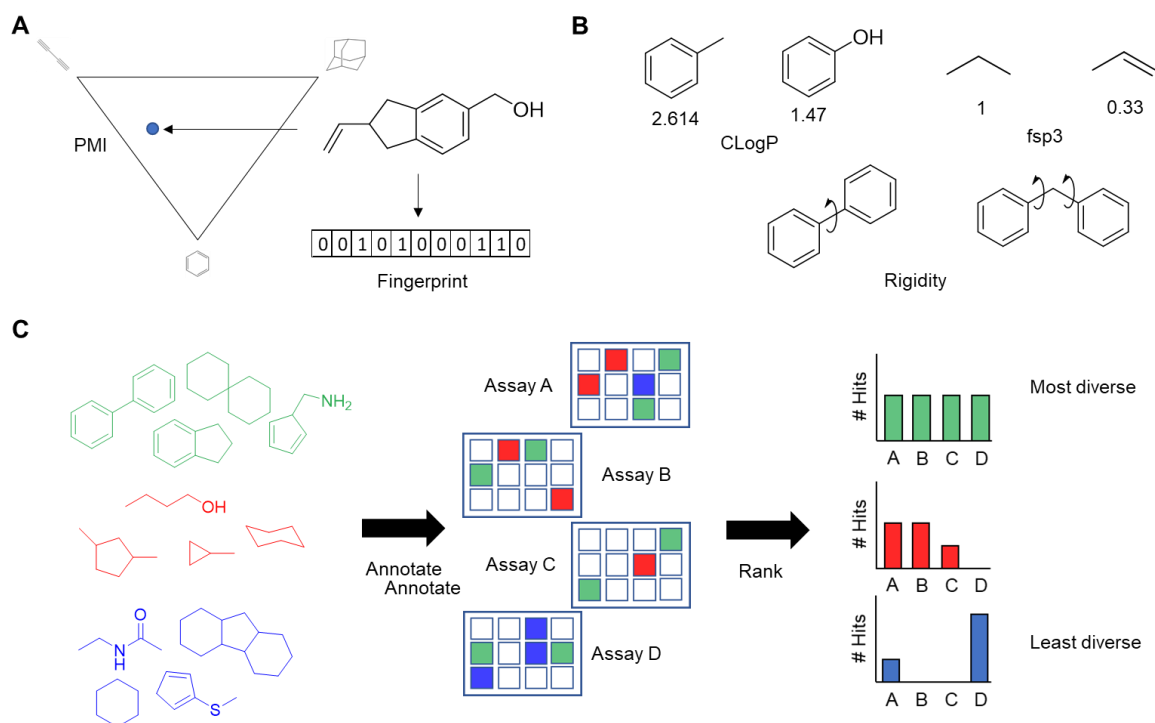


**Figure 4.** Different methods for assessing compound diversity. (A) Shape or structure-based assessment. PMI quantifies the overall shape of a given molecule with the plot illustrating how rod, disk or sphere-like a molecule is. Fingerprinting breaks a molecules structural features into a bit string, with a 0 or 1 denoting the presence or absence of a specific feature. (B) Physiochemical property-based assessment. clogP calculates the theoretical hydrophobicity of a molecule, with a higher clogP representing higher hydrophobicity. Fsp3 calculates the fraction of sp<sup>3</sup> carbons found in a molecule. Rigidity measures the number of rotatable bonds, the more rotatable bonds a molecule has, the less rigid it is. (C) Biological-performance diversity based-assessment. Assess library performance in different assays. Rank libraries based on how evenly distributed hits were among all assays. The first library (green) is the most performance diverse because it contains hits from each of the four assays, while the third library (blue) is the least performance diverse, even though it has the most hits in Assay D.

Because the use of chemical structure- and property-based methods alone has not been successful at creating libraries with diverse biological activity, it has become increasingly important to develop methods that can directly assess this property. Biologically performance-diverse libraries are those that maximize the possible number of targets perturbed while minimizing redundancy, thereby increasing the chance to produce hits across a panel of assays (Figure 4C). Several studies have now attempted to either assess biological performance-diversity or otherwise create libraries that are biologically performance-diverse. Performance-diversity has been assessed for compounds of different origins (commercial, natural product and DOS) using 100 parallel protein-binding assays in

addition to known results of functional assays found on ChemBank.<sup>62</sup> Clemons *et al.* found that commercial libraries tend to contain molecules that are promiscuous (active in a large quantity of assays) while DOS libraries exhibit much more specificity towards single targets. This adds another important consideration for measuring performance-diversity, as a set of molecules that is highly promiscuous would be performance diverse, but such molecules may not be particularly valuable as hits. Petrone *et al.* used a similar approach to generate HTS fingerprints based on the activity of compounds in 195 assays.<sup>63</sup> These were then used for target-based hit expansion, typically such hit expansion is based on chemical structure alone, but in this case, it was based on similarity of biological activity allowing for the inclusion of chemically unrelated but biologically similar compounds. This greatly reduces the number of compounds that needed to be screened to discover all possible hits, with a follow up study showing that 50-80% of all actives could be captured by screening only 19% of a library.<sup>64</sup> This result confirms the effectiveness of using biological similarity, rather than structural similarity, to evaluate the diversity of a compound library.

#### **D. Quantifying biological performance-diversity through phenotype**

Previously described approaches to the characterization of biological performance-diversity have mainly focused on creating composite profiles from the screening of molecules in many assays. This cannot be routinely applied to all synthesized compounds because it is labor and material intensive. Several strategies exist that can characterize the aggregate biological performance of small molecule libraries through a smaller number of more target-agnostic assays. Additionally, due to the large quantity of targets (protein, DNA, RNA etc.) found in a single cell, methods that are target-agnostic should be able to better capture the diversity in biological activity, especially for molecules with unknown targets. Most target-agnostic methods attempt to capture the phenotype produced by small molecule treatment and can be broadly segmented into three groups: cytotoxicity, genetic, and phenotypic.

The earliest significant use of cytotoxicity profiling of small molecules was the development of a panel of 60 diverse cell lines by the National Cancer Institute in the 1990s. Patterns of cell proliferation caused by treatment with known and unknown molecules were used to establish bioactivity for the unknown molecules.<sup>65,66</sup> Over 100,000 molecules have been screened since then, providing a dataset of annotated biologically active molecules and identifying novel protein targets and mechanisms.<sup>67,68</sup> These early efforts were further expanded in the Cancer Target Discovery and Development Initiative (CTD<sup>2</sup>), which attempts to repurpose molecules that are found to target particular types of cancer cells.<sup>69</sup> Out of all the annotation methods presented, it is the fastest and potentially

the most approachable due to the large quantity of available cytotoxicity measurements, though not all of them are compatible with HTS.<sup>70</sup> Additionally, this method necessitates the use of multiple, diverse cell lines to truly capture a diverse range of bioactivity for a single library and the selection of these cell lines may introduce bias. However, it is also possible to use a single cell line in multiple cytotoxicity assays that assess different cell death pathways or biomarkers. This approach has been used to generate an algorithm that can effectively predict cytotoxicity-based compound structure.<sup>71</sup> Lastly, the use of just two cell lines has been shown to capture differences in bioactivity driven by multiple chemical features such as fps3 character and lipophilicity.<sup>72,73</sup>

Genetic profiling aims to determine overall expression level of genes with the assumption that changes in expression, relative to a control, represent a unique molecular phenotype caused by the perturbation of a particular pathway. Initial methods utilized mixed cultures of genetically barcoded *S. cerevisiae* mutation and deletion strains to generate expression profiles based on the survivability of these reference strains after compound treatment. This allowed for the rapid screening of the sensitivity of thousands of genes and the full characterization of the diverse performance of molecules, including the identification of novel targets.<sup>74-78</sup> In mammalian cells, a reference set of molecules with known bioactivity was used to generate The Connectivity Map, which established the whole genome mRNA expression changes induced by each treatment.<sup>79</sup> This Connectivity Map allowed for the grouping of molecules by their specific mechanism of action (MOA) and thus could elucidate the molecular target for those molecules with unknown MOAs.<sup>80,81</sup> However, extracting whole genome expression levels using mRNA microarrays remains laborious and expensive, limiting its application in HTS. Recently, the L1000 platform has been developed to address this limitation by measuring the expression level of approximately 1000 “landmark” genes using fluorescent beads conjugated to the transcripts during amplification.<sup>82</sup> This original set of landmark genes can then be used to infer most of the remainder of the whole transcriptome (83%) through computational methods, making it relatively unbiased towards a specific molecular target and lower cost than traditional mRNA screens. It has even been used to identify the biological targets of “dark matter” molecules, which have shown no biological activity in hundreds of assays, but still make up the majority of molecules in commercial libraries.<sup>35</sup> While L1000 makes genetic profiling more cost effective, it hasn’t been broadly applied due to the necessity for specialized equipment.

While microscopy has a long been used to determine cellular morphology, early efforts in high-content screening (HCS) focused on extracting only a limited number of features from a small number of cells ( $< 10^3$ ) due to technical and computational limitations.<sup>83</sup> However, as the variety of organelle-specific dyes and fluorescent protein has grown, and image acquisition and processing has become more automated, this method has enabled the quantification of a much larger multitude of features.<sup>84</sup> One early example of multiparameter HCS used 11 different fluorescent probes to generate a per-treatment profile of 93 parameters relating to the size, intensity, and shape of their aggregate cellular distribution.<sup>85</sup> This assay successfully demonstrated that these per-treatment profiles could be distinct for each active compound treatment. A central limitation in this methods' ability to quantify biological performance-diversity is the bias introduced into the measured morphological phenotype by the selection of fluorescent probes, due to the limitation in the number of probes caused by spectral overlap. One method addressed this by using machine learning to select an isogenic reporter cell that most effectively sorted known molecules into their correct compound class and was then used to annotate the biological performance-diversity of a set of 22,000 molecules from commercial libraries.<sup>86</sup> The application of machine learning in image processing has also enabled the use of completely dye-free methods like bright field microscopy to characterize morphological changes.<sup>87,88</sup> Lastly, Cell Painting addresses this by quantifying almost 2,000 features derived from just six dyes that stain large organelles within cells, such as the nucleus, ER and cytoskeleton, to most effectively capture a complete unbiased phenotype.<sup>89,90</sup> This method has now been applied to the profiling of small molecule libraries,<sup>91</sup> and has also been used to elucidate the link between biological performance-diversity and the inclusion of scaffold and stereochemical diversity in compound libraries.<sup>73,92,93</sup>

## **II. Methodology**

### **A. Measuring phenotype through cellular morphology profiling using fluorescence microscopy**

It has been demonstrated that dynamic changes in cellular morphology are informative and often reflect the mechanism of action of a drug or genetic perturbation.<sup>94</sup> The creation of multiparametric profiles that capture the whole-cell morphology provides a wealth of data that can then be mined for specific information of interest or used as training datasets for machine learning techniques. Thus, the quantitative measurement of cellular morphology has been used extensively for the determination of the mechanism of action,<sup>94,95</sup> and the identification of novel targets

that alter whole-cell phenotype in particular ways at single-cell resolution.<sup>96,97</sup> As mentioned in the introduction, fluorescence microscopy has been extensively used for HCS. HCS typically combines one to three organelle or protein-specific fluorescent probes enabling the quantification of many features, typically selected for their relevance towards a particular biological target or pathway. The selection of fluorescent probes, as well as what features are quantified for each, introduces bias into most HCS assays preventing them from accurately capturing the whole cell morphology. Additionally, using traditional HCS necessitates the performance of a large number of such screens for the composition of the multiparametric profiles that represent whole-cell morphology which are necessary for the evaluation of biological performance-diversity of a library of molecules.

One way to overcome this limitation is to create an optimal reporter cell line that can accurately classify molecules in a known set.<sup>86</sup> In this method a large number of fluorescent reporter cell lines are generated using random whole-genome labeling of full length protein with YFP,<sup>98</sup> using a cell line expressing two other fluorescent proteins, mCherry and the fusion protein H2B-CFP, which are used for labeling the cytosol and nucleus, respectively. Under compound treatment, each cell line generates a unique profile of approximately 200 features that captures the overall distribution, shape, intensity and colocalization of the fluorescent protein. Though the original purpose of this paper was to accelerate drug discovery by providing a single cell line that can be used for large scale annotation of unknowns into known compound classes, its compound profiles may also be used to evaluate performance-diversity for a given library. This can be analyzed based on the number of compound classes the library is annotated for, with highly performance-diverse libraries being annotated for every compound class. One critical limitation for this method is that the reporter cell line may still be biased, since it was trained on a set of known molecules and evaluated using only compounds that were already known to be biologically active. Thus, novel compounds may exhibit phenotypes that this cell line does not accurately measure necessitating the creation of a new reporter cell line.

An alternative method involves the selection of several spectrum compatible dyes that can “paint” a broad range of cellular compartments and thus effectively capture the whole-cell phenotype. The Cell Painting method uses six dyes imaged across five channels to effectively stain eight cellular compartments (Table 1). In the original protocol, these images were segmented and analyzed using Cell Profiler 2.0 to generate a profile of about 800 features for use in mechanism of action prediction.<sup>99</sup> Improvements in software now allow the quantification of well

over 2,000 features per well using Cell Profiler 3.0.<sup>100</sup> Using these expanded profiles, Cell Painting ability to effectively characterize whole-cell morphology has also been validated under chemical and genetic perturbation.<sup>90,91</sup> Additionally, using this method carries several advantages. The dyes it utilizes are commercially available and do not require specialized filter sets, allowing for easy, cost-effective scaling into a high-throughput format using an automated microscope. Downstream analysis of images and data is also fairly well characterized and available publicly.<sup>100,101</sup> Data analysis and quality control strategies are also being widely adapted allowing for wide interpretability and transferability of generated profile data bases.<sup>102</sup> Importantly, this assay has also been used to profile novel chemical matter with unknown mechanisms of action in order to interpret if the inclusion of stereochemical diverse molecules in libraries results in biological performance diversity.<sup>92,93</sup>

<b>Dye</b>	<b>Excitation Filter(nm)</b>	<b>Emission Filter(nm)</b>	<b>Organelle</b>
<b>Hoechst 33342</b>	387/11 (DAPI)	417-477 (DAPI)	Nucleus
<b>Concanavalin A Alexa Fluor 488 conjugate</b>	472/30 (TRITC)	503-538 (TRITC)	Endoplasmic Reticulum
<b>SYTO 14 green fluorescent nuclear stain</b>	531/40 (FITC)	573-613 (FITC)	Nucleoli, cytoplasmic RNA
<b>Phalloidin Alexa Fluor 568 conjugate, WGA Alexa Fluor 555 conjugate</b>	562/40 (Texas Red)	622-662 (Texas Red)	F-actin cytoskeleton, Golgi, Plasma Membrane
<b>MitoTracker Deep Red</b>	628/40 (Cy5)	672-712 (Cy5)	Mitochondria

**Table 1.** Stains and filters used in Cell Painting assay.

Fluorescence involves the absorption of a photon by an indicator (dye) followed by the emission of a lower energy a few nanoseconds later. The emitted photon has less energy than the absorbed photon because some energy is lost in this process to other types of radiation.<sup>103</sup> This is called the Stokes shift and is especially important for the selection of indicator molecules for multi-dye experiments as excitation and emission spectra should not overlap as you cannot differentiate which fluorophore emitted light of the same emission wavelength. The separation of the excitation and emission light, as well as noise caused by autofluorescence at other wavelengths, can be achieved through the use of filter cubes and dichromatic mirrors. For widefield fluorescence microscopy a parallel beam of light passes through the entire sample (widefield of view) and then the emitted light can be readily captured either by eye or digitally using a camera. Though simple, scalable and fast, widefield microscopy does come with disadvantages. Widefield is diffraction-limited, thus it can't differentiate between two fluorescent points less than 200 nm apart, leading to loss of resolution, additionally the unavoidable projection of out-of-focus light onto the single image plane of the camera also results to further loss of image quality. Other methods exist that can overcome these limitations such as superresolution methods like PALM/STORM that overcome this limitation by multiple excitation of a photoswitchable fluorophore, allowing its localization through fitting emitted photons to a Gaussian distribution,<sup>104,105</sup> and confocal microscopy, which reduces out-of-focus light by excitation and detection point across the specimen and sequentially compiling the entire image.<sup>103</sup> However, PALM/STORM are too costly and slow to be adequately used for HTS and lower resolution is not required to adequately image the large organelles stained by its dyes and, while both widefield and confocal microscopy have been used successfully for Cell Painting, confocal microscopes often have more limited filter sets in addition to being more expensive.<sup>106</sup> Thus, for our experiment we decided to use a widefield fluorescence microscope, the IXM-XLS.<sup>107</sup> This is an automated microscope capable of rapidly imaging 384 well plates using a large field of view and laser-focusing to find well bottoms in addition to being able to fit the five filter cubes required to image all the dyes necessary for Cell Painting.

## **B. Compound treatment, staining, image acquisition and processing**

The general workflow for Cell Painting involves compound treatment, staining, image acquisition and processing (Figure 5). At the end of a single experiment each tested condition generates hundreds of single-cell profiles of at least 1,500 features which can then be aggregated and analyzed further. Each step in the protocol has potential pitfalls that can alter any number of features for these treatment conditions and cause misattribution of

morphological differences to compound treatment rather than to other variables. Cell type, growth conditions, growth time, and image quality can all contribute to the overall quality of the extracted data. Because the published Cell Painting protocol was written to adequately address all these factors, it was adapted with as few changes as possible.<sup>89</sup>

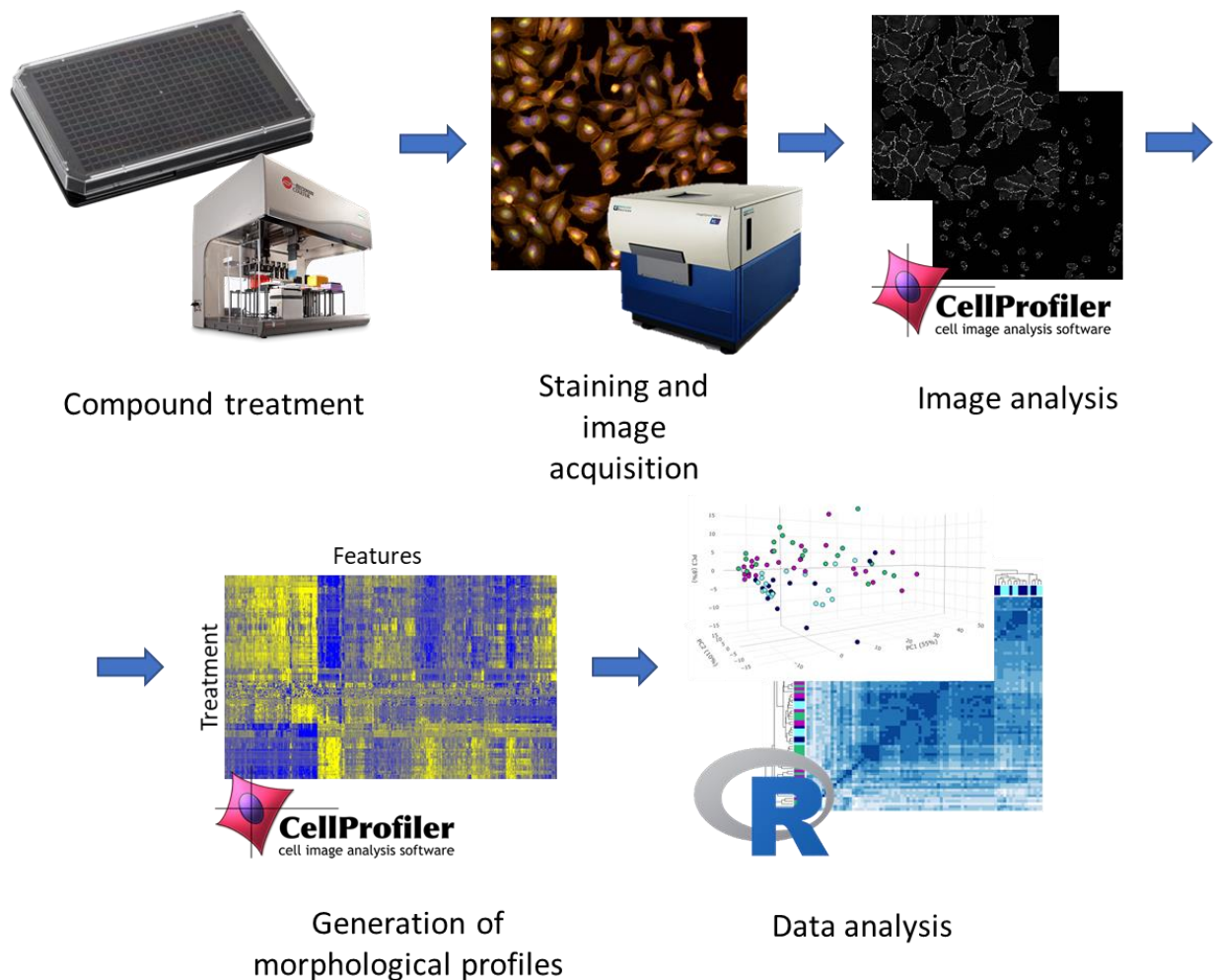


**Figure 5.** Cell Painting workflow. Cells are first treated with compounds in dose using an automated liquid handler. After 24 hours cells are fixed with formaldehyde and stained to visualize the nucleus, endoplasmic reticulum, nucleoli and cytoplasmic RNA, F-actin cytoskeleton, Golgi, and plasma membrane, and mitochondria. Next, CellProfiler is used to segment and analyze images and extract 1,700 features per each cell in every well. Per-cell profiles are then aggregated by calculating the median morphological profile in each well. These per-well morphological profiles are then used in downstream analysis.

Cell Painting has been demonstrated to work in over a dozen adherent cell types, with the most used cell lines being those that have homogenous and geometrically simple morphology, which simplifies image analysis and ensures replicability. That is why for this experiment we used HeLa cells, as they meet these criteria and their organelles have been successfully stained using the original staining protocol. The protocol describes that use of two common incubation times for compound treatment, 24 and 48 hours, stating that at a longer time point the authors typically observe more active molecules as those that might induce subtle phenotypes take longer to perturb aggregate morphology<sup>37,99</sup>. However, we chose to use the shorter time point because many of our molecules are cytotoxic and thus might not have quantifiable phenotypes at a longer time point. Lastly, the protocol recommended culturing the cells at a lower fetal bovine serum (FBS) concentration (4% instead of the typical 8-10%) in order to prevent cells from becoming overconfluent and causing cells to overlap, but we found that this slowed cell division too much for HeLa cells so we cultured them using standard conditions (1,500 cells, 50 uL per well, Dulbecco's Modified Eagle Medium (DMEM), 3.6 mM L-Glutamine, 1x Penicillin-Streptomycin, 8.8% FBS, 37°C, 5% CO<sub>2</sub>).

Plate effects describe the changes in cellular morphology that occur simply due to effects from temperature and humidity gradients present for a particular well position on a plate.<sup>108</sup> Mitigation of all these effects is required in order to accurately measure the morphological profiles caused by chemical perturbation and not by other variables. This is mostly addressed through the use of four biological replicates, which are spread between four different plates, each measured on a different day in addition to the inclusion of at least 30 vehicle-only (DMSO) control wells that can be used to normalize features between different plates. Ideally replicates would be spread randomly throughout each plate, with no compound present in the same well in two separate replicates. However, this extensively complicates the compound treatment of cells, so instead we took a more moderate approach, spreading the DMSO wells evenly throughout each plate in addition to inverting plates for each replicate (Figure 6). Lastly, we chose to plate our cells in CellCarrier Ultra 384-well plates as they are designed to prevent evaporation and have well bottoms made with cyclic olefin which has high optical clarity and low within-plate height variation allowing us to get more clear images in every increasing the amount of cells from which we can gather data.

	1	2	3	4	5	6	7	8	9	10	11	12	13	14	15	16	17	18	19	20	21	22	23	24
A																								
B			RH-01-12	RH-01-13	RH-01-14	RH-01-15	RH-01-16																	
C																								
D																								
E																								
F																								
G																								
H																								
I																								
J																								
K																								
L																								
M																								
N																								
O																								
P																								

**Figure 6.** Example of the plate layout used for Cell Painting experiments. Each plate contains at least 34 controls distributed in a chevron pattern in order to account for plate effects. Each compound is present in six doses with the highest doses located toward the top of the plate. Outer columns (gray) are left empty to minimize edge effects.

The staining protocol remained unchanged and was performed using a Biotek Multiflo FX in order to reduce variability caused by user error. Additionally, plates were protected from light as much as possible as all the dyes were sensitive to photobleaching and were spun down for 1 minute at 500 g between each step in order to prevent bubbles from forming at the bottom of the plate. After 24 hours of compound treatment 40  $\mu$ L of media was aspirated from each well and cells were treated with MitoTracker Deep Red (30  $\mu$ L/well, pre-warmed media, 500 nM final). Cells were incubated 30 min at 37  $^{\circ}$ C, aqueous paraformaldehyde was added to each well (10  $\mu$ L/well, 1x PBS, 0.8% final) to fix the cells. After incubating for 20 min, cells were washed once with 1x Hank's Buffer Salt Solution (HBSS) (70  $\mu$ L/well) and a solution of Triton X-100 was added to each well (30  $\mu$ L/well, 1x HBSS, 0.075% final) to permeabilize the cells. Cells were then incubated for 20 min at room temp, wells were washed twice and the staining solution was added to each well (30  $\mu$ L/well, 1x HBSS, 1% Bovine Serum Albumin (BSA), 1.5  $\mu$ g/mL Wheat Germ Agglutinin, 100  $\mu$ g/mL Concanavalin A, 5  $\mu$ L/mL Phalloidin, 5  $\mu$ g/mL Hoechst 33342, and 3  $\mu$ M SYTO 14). After 30 minutes of incubation at room temp, wells were washed three times with no final aspiration, and the plates were sealed with foil. Images were captured on an ImageXpress Micro XLS Widefield High-Content Analysis System using five filter cubes: DAPI, FITC, TRITC, Texas Red and Cy5 (Table 1). Photobleaching of low-intensity dyes was avoided by imaging in the order of Cy5, Texas Red, TRITC, FITC and DAPI. Nine sites were imaged per well in a 3  $\times$  3 array, with laser-based autofocus on the first site per well.

The image analysis pipeline from the original protocol also remained largely unchanged but was adapted to be compatible with the latest version of Cell Profiler (3.0). For each plate the image analysis involved three parts: illumination correction, quality control and feature extraction (Figure 7). Illumination correction corrects the uneven illumination in each image which can be introduced by the microscope optics. This was done because heterogenous illumination can bias intensity-based measurements as well as complicate cellular segmentation. Images were aggregated on a per-plate basis to produce an estimate of the overall 2D illumination distribution, one for each channel, per plate. The corresponding 2D matrix for each channel can then be applied to each individual image to adjust intensity values. It has been shown that illumination corrections increase the ability to detect borderline phenotypic differences between treatment conditions.<sup>109</sup> Next, quality control annotates those images that can be determined to be overexposed or blurry based on two previously identified aggregate metrics, percent maximal and power log-log slope respectively. This is done to further improve data quality as fluorescent artifacts could contain their own detectable phenotypes which would be meaningless and affect the measurements of per-well aggregates. Finally, for feature extraction, cells are first segmented, and the nucleus, cell body, and cytoplasm are identified based on their corresponding fluorescent markers. Next measurements of morphology, intensity, texture, and adjacency are quantified for each compartment. These measurements are then exported to a MySQL or SQLite database and used for further analysis.

### **C. Profile aggregation, normalization and feature selection**

The image analysis data are composed of several hundred thousand single-cell profiles made up of at least 1700 features per plate. While these data could be used directly for all further analysis steps it is better to create aggregate per-well profiles to decrease computational load and also to allow for data transferability, as the data file for each plate can range from 2 -6 GBs. The aggregation of single-cell profiles into per-well profiles is done through the calculation of the median cellular profile in each well and every feature, excluding cell counts which were calculated by taking the sum of identified nuclei in each well. The median is the aggregate statistic of choice, because it is better at estimating the aggregate profile for non-normal distribution and is less sensitive to outliers found within a population (i.e. well). Additionally, it has been shown to out-perform other commonly used methods in a mechanism of action study.<sup>110</sup>

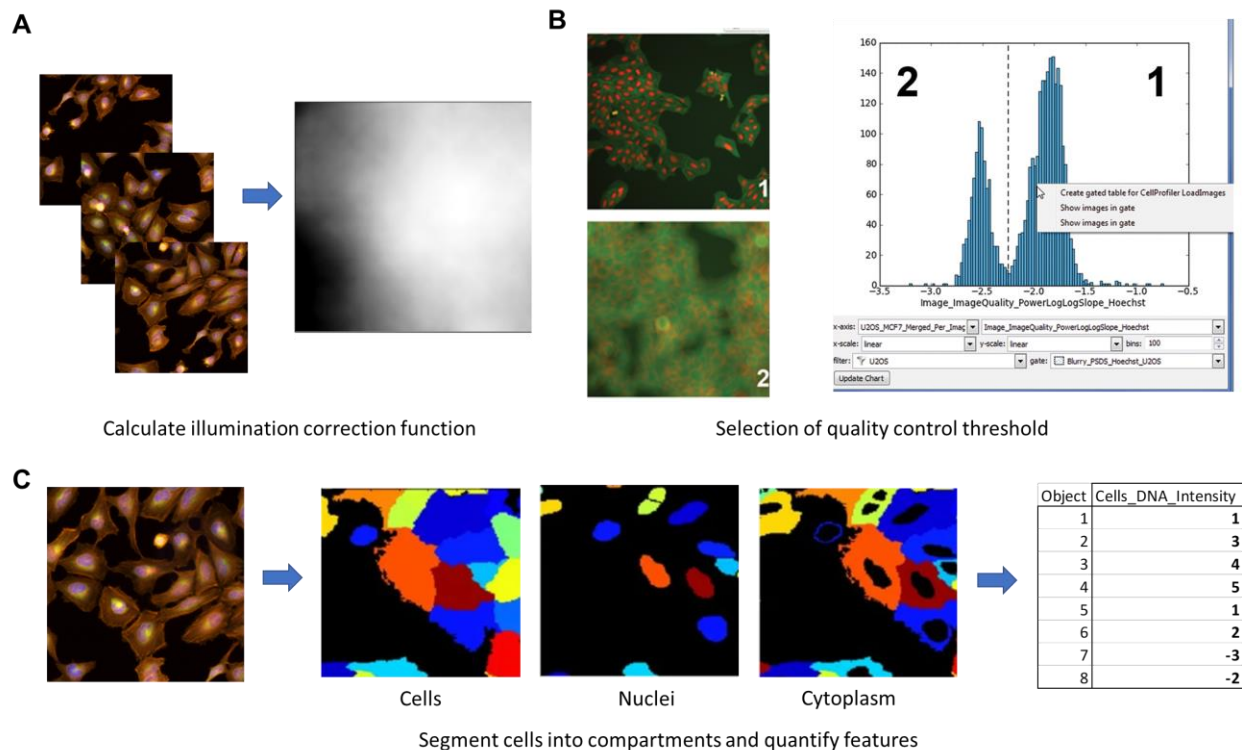


**Figure 7.** The three parts of image processing. (A) Illumination correction involves the calculation of the illumination correction function for each channel. This is done by averaging all the image for a specific channel to capture the overall heterogeneity of illumination in a matrix. During the later image analysis step each image for a specific channel can be normalized by dividing by this matrix.<sup>109</sup> (B) Quality control involves the selection of the threshold value for a specific whole-image metric that will annotate images that are out of focus or overexposed. This is done by plotting a histogram for a chosen metric and images are then sampled from different areas of the plot to determine if a specific value corresponds to good or bad image. As an example, the PowerLogLogSlope metric can be used to exclude out-of-focus images.<sup>111</sup> (C) Illumination corrected images are segmented into three compartments: cell, nuclei and cytoplasm, and then all features are calculated for each compartment to generate single-cell (Object) profiles.<sup>89</sup> Adapted from references 109 and 111 with permission.

Next, because the median profile for each plate will be affected by uncontrolled variables specific to the time the plate was processed (batch effects) and so they must be normalized. This is done by calculating robust z-scores for each well using the formula below:

$$\text{robust } z - \text{score} = \frac{x - \mu_{1/2}}{MAD * 1.4826}$$

$$MAD = \text{median}(|X_i - \text{median}(X_{1...n})|)$$

The median ( $\mu_{1/2}$ ) and median absolute deviation (MAD) is calculated using the entire set of single-cell vehicle-treated profiles. The MAD is then multiplied by 1.4826 to estimate the normal distribution of these values and allow z-score calculation.<sup>112</sup> Robust z-scores are chosen for the same reason that median was chosen for profile aggregation, they are less sensitive to population-specific outliers. In addition to improving the reproducibility of profiles across replicates, normalization also scales the relative intensity of each feature which is useful for downstream analysis as each feature exists with its own scale which impedes direct comparison. The aggregation and normalization steps can be achieved either through the use of the R package cytominer or the python script published with the original protocol with some adjustment relating to metadata values .<sup>89,101</sup>

Lastly, we performed feature selection in order to retain only the most informative set for downstream analysis (Figure 8). First, those features for which variance is near zero are removed as they have the same value for every sample and thus do not contain any sample specific information that could be useful. Next, features with poor reproducibility between plates are removed by calculating the Pearson correlations between all treatment conditions and then using the median value for each to retain only those that have median correlation of 0.5 or above. Many of the remaining features will be highly correlated with one another, potentially affecting downstream analysis, so features are pruned based on this correlation. Pearson correlations are calculated between every feature and then highly correlated features are grouped together and only one feature in each of these groups is retained. This grouping procedure is done iteratively until no feature has a correlation coefficient higher than 0.95 with any other feature.

#### **D. Dimensionality reduction and activity determination**

After feature selection, we are still left with compound profiles that contain several hundred to a thousand features making it challenging to analyze the activity of compounds by directly comparing any two features between compound treated cells and controls, as it is hard to establish the criteria that would make any two (or more) features good points of comparison. Dimensionality reduction techniques offer a solution to this problem by attempting to reduce the overall number of features significantly while retaining the spatial relationships that exist between data points. Several techniques are commonly used for biological data sets, such as t-Distributed Stochastic Neighbor Embedding (t-SNE),<sup>113</sup> uniform manifold approximation and projection (UMAP),<sup>114</sup> and principal component analysis (PCA).<sup>115</sup> Though nonlinear methods like t-SNE and UMAP are becoming more popular for modeling high

dimension data, PCA was chosen for our data set due to its linearity which allows for the preservation of the overall architecture of the data and easy interpretability of the new dimensions.

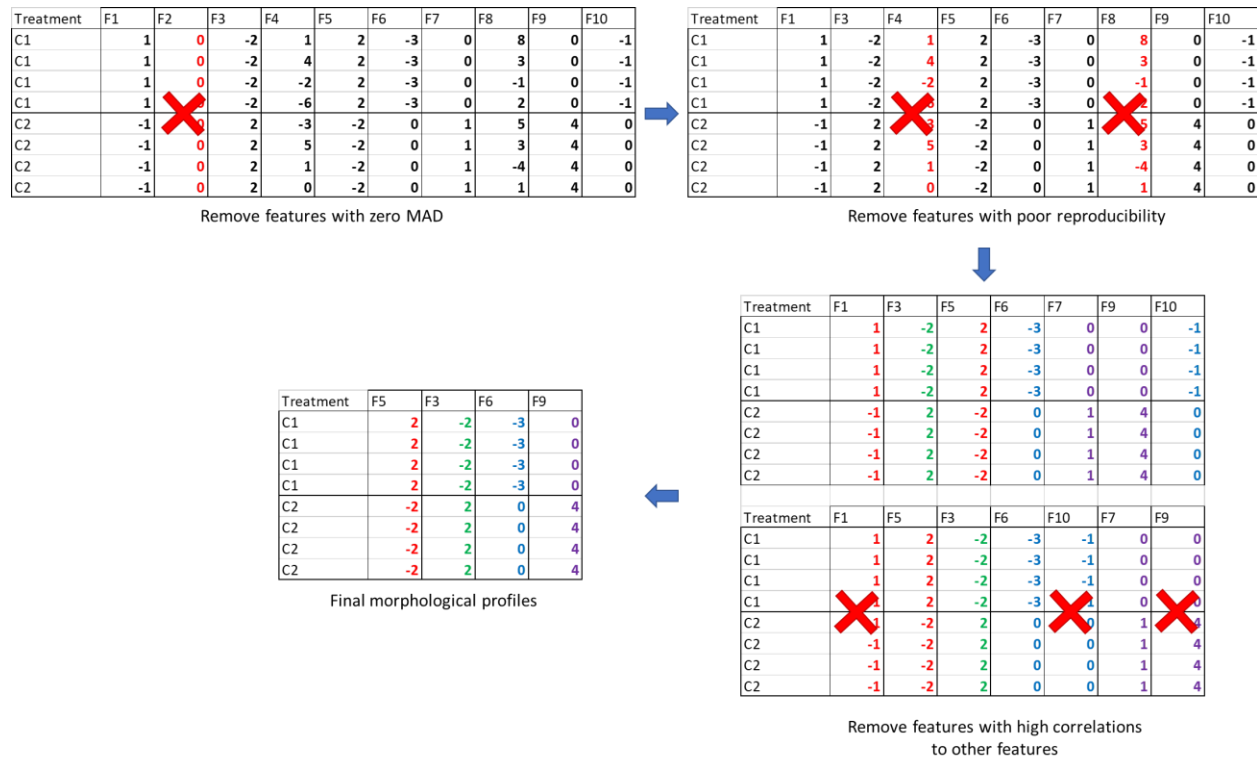


**Figure 8.** Schematic of the feature selection procedure based on the maximal relevance and minimal redundancy algorithm. First, features with a MAD of zero are removed as they do not contain any treatment specific information. Next, features with poor replicate reproducibility are removed to minimize noise. Lastly, correlation coefficients are calculated between every feature across all treatments and highly correlated features are paired together in groups. Only a single feature from each group is retained to minimize the inclusion of features that contain redundant information.

PCA is a technique that reduces the dimensionality of datasets by creating new uncorrelated dimensions. Finding such new dimensions, the principal components (PCs), is based around the calculation of eigenvalues and eigenvectors that generate linear combinations of the original dimensions that contain the majority of the original

variance (Figure 9). A huge advantage of PCA is that the new dimensions are defined by the data itself and thus it is adaptable to novel data for which a known metric of evaluation does not exist, such as the Cell Painting profiles induced by novel chemical matter. As mentioned previously, the linear nature of PCA allows for the preservation of the original relationship between all points, unlike with t-SNE and UMAP, which only preserve such a relationship for the nearest neighbors. This invalidates the interoperability of the Cell Painting profiles, as any new data generated by additional compounds graphed in dimensions derived from t-SNE and UMAP would have no relationship to the original data. Lastly, the PCs are combinations of the original dimensions and thus once they are calculated for a particular dataset they can be extracted, informing us of which features were most important in generating similar or dissimilar profiles. For our datasets, PCs for per-well aggregate profiles were calculated using the `prcomp` function found in the R package `stats` and used for further analysis.<sup>116</sup> All PCAs were done using the `prcomp` command in the `stats` package of R version 3.6.2.

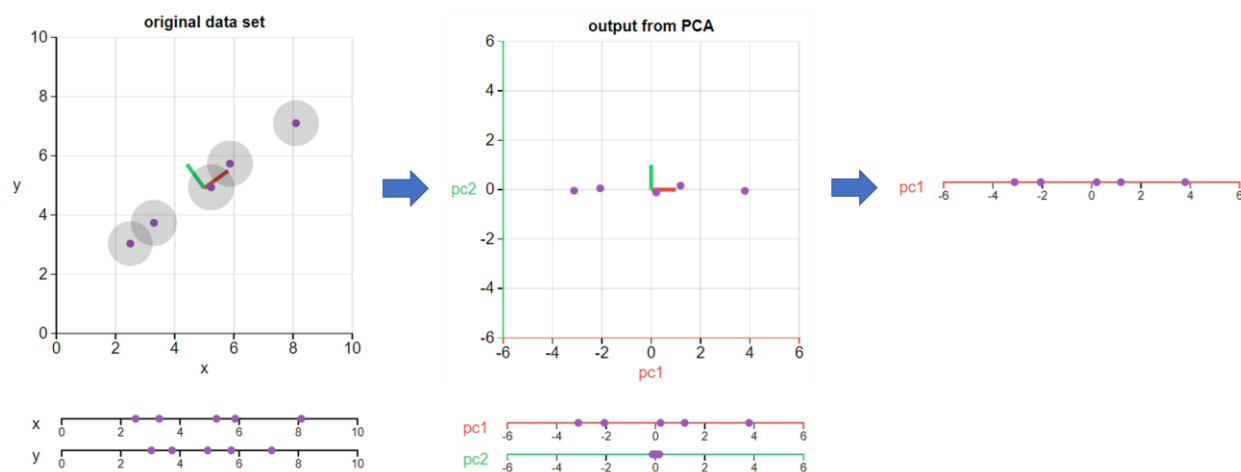


**Figure 9.** Schematic of PCA. In the original data set the explained variance is spread fairly evenly between the two original dimensions. PCA attempts to reduce the amount of dimensionality by finding new dimensions (principal components, PCs, highlighted red and green) that maximally capture the variance in the data set. The dimension that explains the highest percentage of the total variance is the first principal component with the rest ranked in descending order. We can see that PC2 in this example explains almost none of the variance for this data set and thus can be dropped. Data can then be replotted using the new lower number of dimensions while losing a minimal amount of information. Adapted from Explained Visually (<https://setosa.io/ev/>).

Although PCA effectively reduces the number of dimensions and is capable of identifying groupings of similar profiles, it does not directly provide objective metrics by which to determine which treatments induced phenotypes that were significantly different from DMSO-treated cells. In a typical screen two treatments could be determined to be significantly different from each other through statistical methods such as *t*-tests, but the calculation of such parameters is difficult for multidimensional data even after PCA because it would need to be done for each component individually. To address this problem, the multidimensional perturbation value (mp-value) was created.<sup>117</sup> Mp-values describe the statistical significance of the dissimilarity of two treatment conditions in a multidimensional space and are similar in interpretation to standard *p*-values. These mp-values are calculated as part of the last step in activity determination (Figure 10). First, per-well profiles of all replicates for a specific treatment condition are grouped together with the profiles of all DMSO-treated replicates in a single matrix and dimensionality is reduced through PCA, retaining only those PC which capture 90% of the original variance. Next, a Mahalanobis distance (activity score) is calculated between the two groups.<sup>118</sup> A Mahalanobis distance is the same as a Euclidian distance between two points, but for a multidimensional space, and is calculated based on the formula below:

$$\text{Mahalanobis distance} = \sqrt{(x - \mu)^T * S^{-1} * (x - \mu)}$$

Where **x** is a vector composed of the means of each PC for the treatment replicates, **μ** is a vector composed of the means of each PC for the control replicates and **S** is their covariance matrix. Next, the mp-value for this distance is generated by permutation of the replicate labels 1000 times. Each time the replicate labels are permuted, a new Mahalanobis distance is calculated between the new assignments. The mp-value represents the total fraction of the 1000 permutation-derived Mahalanobis distances that are greater than the original distance. A maximum cut-off mp-value of 0.05 was chosen for activity determination, as the significance of permutation derived *p*-values can be interpreted the same way as those that are generated by parametric methods.<sup>119</sup>

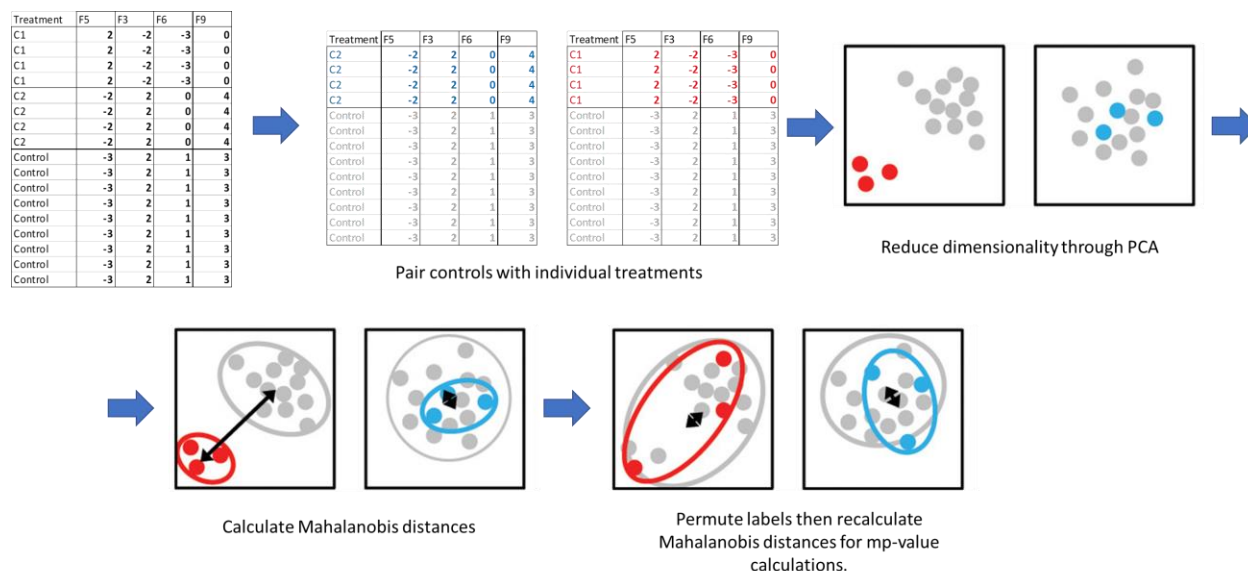


**Figure 10.** Activity determination through the calculation of treatment-specific Mahalanobis distances (activity scores) and mp-values.<sup>117</sup> Replicates of the same treatment are paired with controls and each paired set is then processed individually. Dimensionality is reduced by PCA which is followed by the calculation of Mahalanobis distances using the new principal components. Lastly, treatment and control labels are permuted and then Mahalanobis distances are recalculated again. Mp-values are calculated based on the fraction of times the permuted distance was greater than the original distance. Adapted from reference 117 with permission.

### E. Chemical feature measurement and correlation with compound activity

One of the goals of this project was to try and establish correlations between the activity of molecules in Cell Painting and chemical features in order to better inform what features are relevant to the creation of biologically diverse libraries. We selected features that were already commonly used to assess the structural and physiochemical diversity of a library and they were molecular weight (MW), topological polar surface area (tPSA), clogP, PMI and  $\text{fsp}^3$ . MW and tPSA were estimated using ChemDraw. MW being calculated based on the average molecular mass of the structure, with atomic masses weighted based on the natural abundance of all isotopes of the element. tPSA estimates the total surface of a molecule that belongs to polar atoms by summing the contribution of individual polar fragments,<sup>120</sup> and is biologically relevant because it has been shown to affect molecular absorbance in the body and is especially important for drugs that cross the blood-brain barrier.<sup>121</sup> clogP is the calculated logP, where P is the

partition coefficient of a molecule between octanol and water, thus it represents the lipophilicity of a molecule and estimates the ability of a molecule to cross cellular membranes. While traditionally determined experimentally, it is now commonly calculated. We used the SwissADME tool to estimate this feature, which calculates a consensus clogP based on five different models.<sup>122</sup> PMI describes the overall shape of a molecule based on the calculation of three principal moments of inertia ( $I_1$ ,  $I_2$ ,  $I_3$ ), ranked in ascending magnitude and then the two lower moments are normalized by the moment of the highest magnitude ( $I_3$ ).<sup>54</sup> The resulting coordinates ( $I_1/I_3$ ,  $I_2/I_3$ ) generate a plot in the shape of an isosceles triangle with each corner representing an archetype molecular shape, i.e. rod ( $0,0$ ), sphere ( $1,1$ ) and disc ( $0.5,0.5$ ). Thus, the specific coordinates estimate the overall rod, sphere or disc-ness of a given molecule. Lastly, fsp3 is just the fraction of carbons in a molecule that are sp<sup>3</sup> hybridized. Pearson correlations between the activity scores (Mahalanobis distances) or cell counts and each of these features were calculated using GraphPad Prims 8.0 and significant correlations were identified by a *p*-value less than 0.05.

#### **F. Assessing diversity through PCA and hierarchical clustering**

Previously applied methods used to determine compound activity relative the DMSO controls can also be used to measure the diversity of the entire compound set. Because PCA captures the variance of a data set, analyzing the entire library's morphological profiles at once using this method will visualize the overall dissimilarity between compounds as those that are dissimilar will be located away from each other in one or several PCs. Mahalanobis distances and mp-values can then be used to measure the magnitude and statistical significance of this dissimilarity. Using this information, we can then analyze if the alteration of specific chemical features, such as a specific appendage or the overall stereochemistry, causes a significant change in the observed cellular morphology. Additionally, the overall PCA plot will also visualize if the library is performance diverse, as a performance-diverse library will have an even distribution of all compounds in the first two PCs, with none clustering closely together.

Although the calculation of individual Mahalanobis distance and mp-values for every pair of compounds is computationally possible, it is not easily visualized even for libraries of moderate size. One possible way to visualize the similarity/dissimilarity of all library molecules is to calculate Pearson correlations between all molecules which can then be visualized as a heatmap. Additionally, these Pearson correlations can then be used as the distance measurements for an agglomerative hierarchical clustering algorithm which will attempt to create clusters of similar compounds.<sup>123</sup> Like PCA, the unsupervised nature of hierarchical clustering is advantageous for our data set as we

do not necessarily know which compounds are likely to cluster together, especially because established assumptions about structural similarity and biological performance may be untrue.<sup>63</sup> Agglomerative clustering starts from the division of the data set into single points, these points are then merged together into pairs based on proximity, pairs are then merged into groups step by step until all pairs have been merged together (Figure 11).<sup>124</sup> Various clustering methods share this general procedure but differ in the way in which the measure of inter-cluster dissimilarity is updated after each step. For our data set, we chose to use the between-group average linkage method, which calculates dissimilarity based on the formula below:

$$\text{Distance between clusters} = \frac{1}{|A||B|} \sum_{x \in A} \sum_{y \in B} d(x, y)$$

Where **A** and **B** are two clusters and the distance between them is taken to be the average of all distances between pairs of objects **x** in **A** and **y** in **B**. This method was chosen for its ability to form tight-knit clusters which can vary in size and shape. The final calculated distances between each point, pair and cluster can then be visualized as a dendrogram which can easily be paired with the original heatmap of the Pearson correlations in order to reorder the columns based on these new clusters. For our data set, hierarchical clustering analysis was accomplished by first calculating the correlation matrix using the `cor` function in the stats package of R version 3.6.2, followed by the calculation of pairwise distances using the `dist` function and finally clusters were determined using the `hclust` function using the average linkage setting.

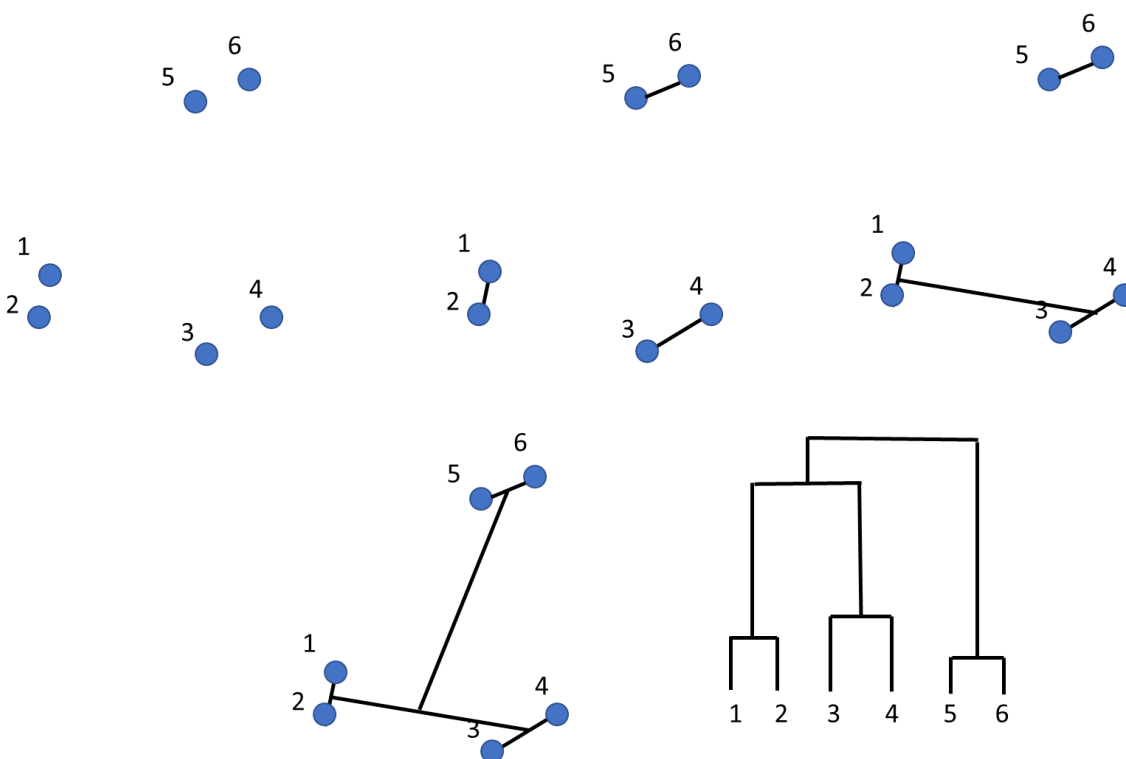


**Figure 11.** Diagram of agglomerative hierarchical clustering. Single points are first connected to their nearest neighbor until all points are connected as pairs. Pairs are then associated together into clusters based on proximity until all pairs have been associated together. The distance measurements of these linkages can then be visualized as a dendrogram, where the distance of each stem of a particular fork represents the total dissimilarity between the other points that join at that fork.

### **III. Results and Discussion**

#### **A. Profiling flavone derivatives enriched in sp<sup>3</sup> character**

The libraries we chose to profile using Cell Painting were all based around privileged natural product scaffolds to reduce the risk that our synthesized libraries would lack biological activity. The first library for which we systematically evaluated biological performance diversity using Cell Painting was based around the pyrone and flavone scaffolds.<sup>73</sup> Pyrones and flavones are commonly occurring biologically active natural products with a broad range of activity.<sup>125</sup> Because of the polypharmacology of the parent natural product, derivatives from  $\gamma$ -pyrones could pose unique and useful biological properties. The reduced flavone scaffold is of particular interest due to the

increase in the fraction of sp<sup>3</sup> hybridized atoms and stereochemical complexity of the flavone core, features that are lacking in naturally occurring flavones (Figure 12A). Additionally, previous research shows that small molecules with more fsp<sup>3</sup> character have increased selectivity for specific targets.<sup>29</sup> Thus, we assembled a library of flavones that display polypharmacology,  $\gamma$ -pyrones, and reduced flavones to determine if increasing the ratios of fsp<sup>3</sup> would generate a library with biological performance diversity. The reduced flavones were prepared using a DOS approach from  $\gamma$ -pyrones in an efficient manner to access a diverse array of scaffold, appendage, stereochemical, and physicochemical properties. Synthesis of these flavonoid analogues also enabled the direct comparison of the effect of increasing the fraction of sp<sup>3</sup> hybridized atoms in a particular scaffold to the biological performance diversity of a class of compounds (Figure 12A).

To determine the effects that the systemic variation of these features had on biological performance we used Cell Painting and cytotoxicity assays. Using two methods allowed us to compare the utility of each for the evaluation of performance diversity as well as providing additional data for this metric for our library. For this library, each compound was screened in six-point dose for the Cell Painting (2-fold dilution, 80 to 2.5  $\mu$ M) and for the cytotoxicity assay (2-fold dilution, 40 to 1.25  $\mu$ M). Additionally, the treatment time for the cytotoxicity assay was 72 hours and it utilized two cell lines, HeLa cells and OVCAR-8 cells, allowing for the evaluation of compound-specific differences in sensitivity. One of our major findings was that greater fsp<sup>3</sup> character does not always lead to greater performance diversity for this scaffold as the  $\gamma$ -pyrones had the highest activity and the greatest amount of variance in both assays (Figure 12B,C). Because the esters were inactive in the Cell Painting assay, as determined by their mp-values (mp-value > 0.05), it was not possible to measure their performance diversity using this assay, however, there were significant differences in the toxicity of many esters which we established to be due to the variation of both stereochemistry and appendages.

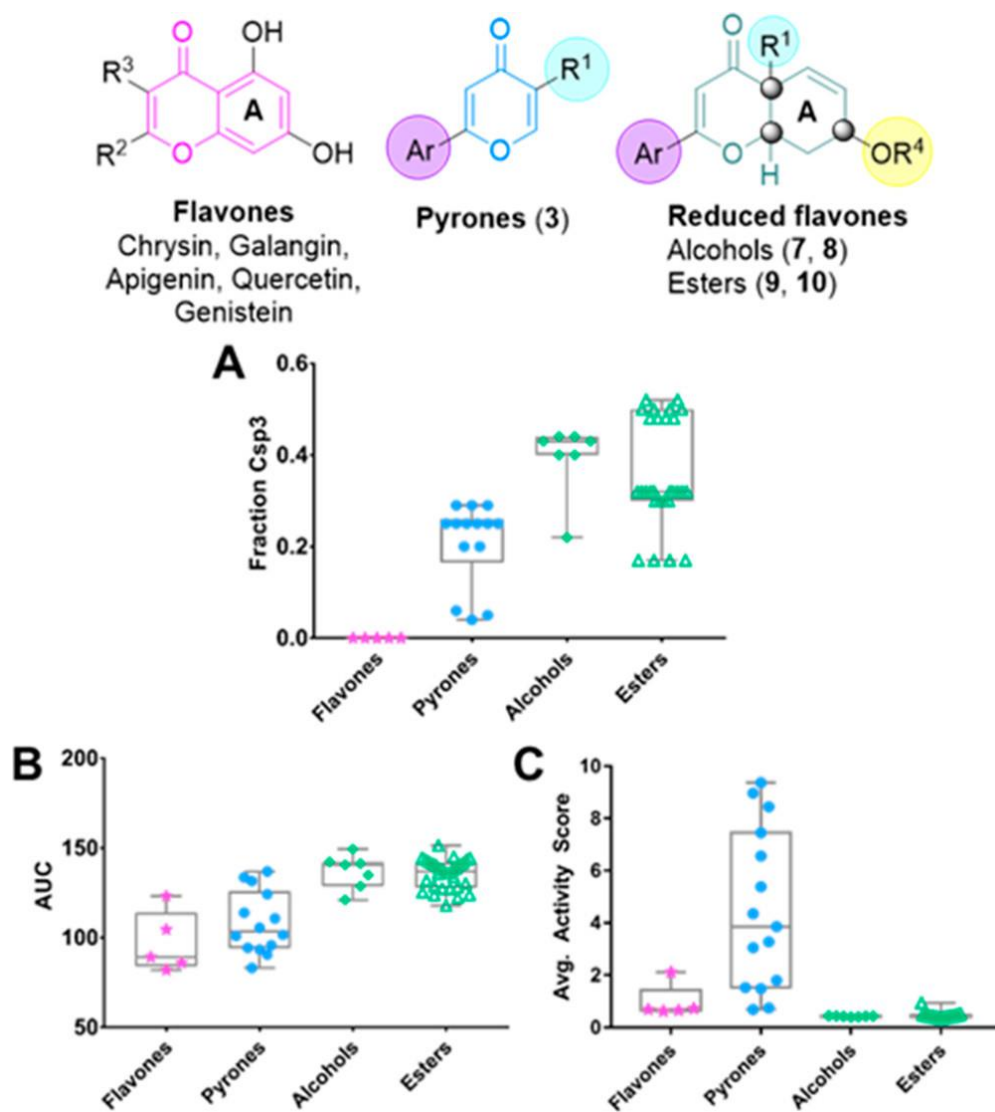


**Figure 12.** Structure of natural and reduced flavones. (A) The fsp3 was considerably increased in the alcohol and ester reduced flavones compared to the natural flavones. (B) Pyrones and flavones had a broad range of activity in the toxicity assay. (C) Pyrones displayed the largest amount of range in activity in the Cell Painting assay.

## **B. Effects of appendages on performance diversity of the pyrone scaffold**

In contrast, 11 out of 14 pyrones were active and one of the natural products, apigenin, was active in the Cell Painting assay and the pyrones displayed a variety of biological profiles as visualized by PCA (Figure 13A,B). For the active pyrones, it was clear that appendages greatly contributed to the observed diversity of activity as determined by the pairwise calculation of mp-values between every pyrone (Figure 13C). We found that two pyrones (**3d**, **3e**) induced a significantly different profile from every other pyrones in the library (mp-value < 0.05), while others were only significantly different from some pyrones and not others (**3m**). Additionally, a comparison of the lipophilicity of the pyrones using clogP reveals a correlation between calculated clogP and toxicity as measured by the area under the dose curve (AUC) (Figure 14A,B). Pearson correlation values were calculated for each library to compare activity score, AUC values, and clogP (Figure 14C). While the toxicity of the pyrones significantly correlated with clogP, the activity score of the pyrones did not, thus demonstrating the utility of using multiple assays to reveal features that drive biological performance diversity. For this library, further enhancement of biological performance diversity could be accomplished through the inclusion of compounds with diverse physicochemical properties, specifically lipophilicity.

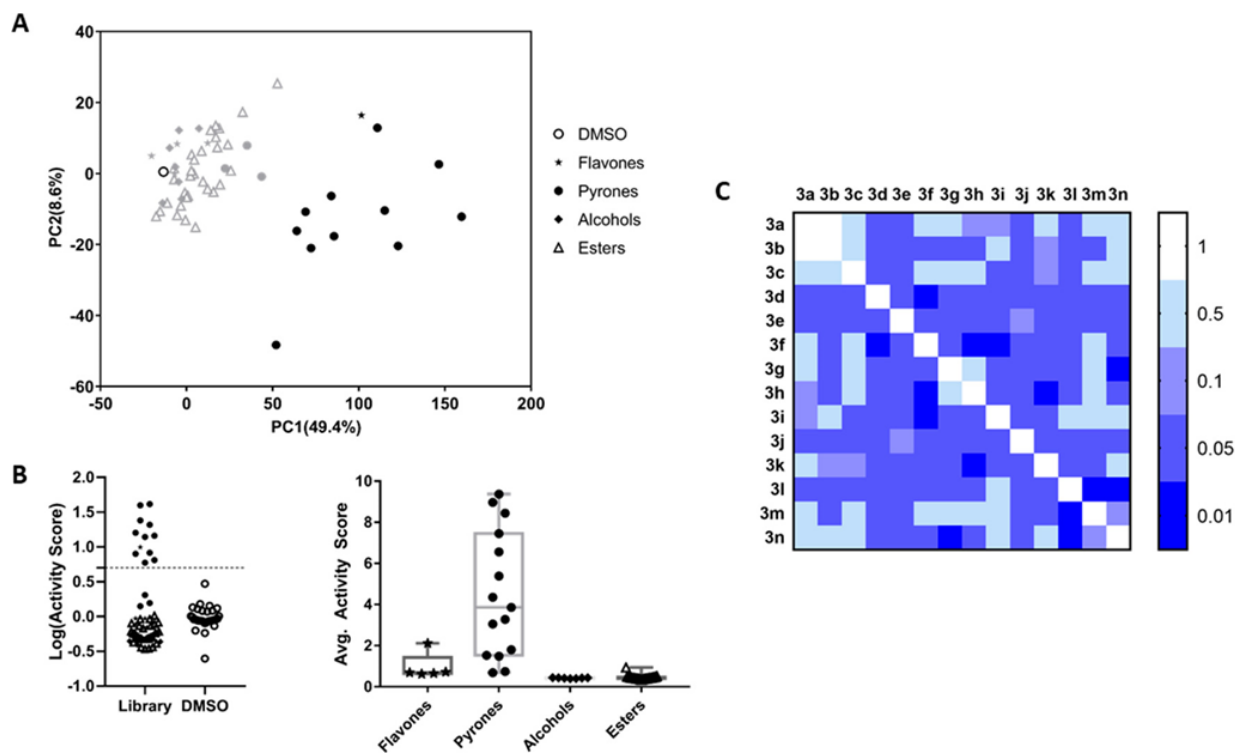


**Figure 13.** Comparison of biological performance diversity using the Cell Painting assay. (A) Scatter plot visualizing the variance of each compound class based on the first two principal components from the PCA. Each point represents the average of four replicates at 80  $\mu$ M, and points shown in gray are inactive as determined by their mp-values ( $>0.05$ ). (B) Dot plot on the left shows the overall variation in activity scores for the entire library in comparison to DMSO with the activity score at which a compound typically become active (mp-value  $< 0.05$ ) represented as a dotted line. The box and whisker plot on the right displays the distribution of the average activity scores for each compound class. Each point is the average of the activity scores for one compound across all doses. (C) Heat map represents the effect of appendages on driving performance diversity for the pyrones. Mp-values were calculated based on the Mahalanobis distance between a pair of pyrones.

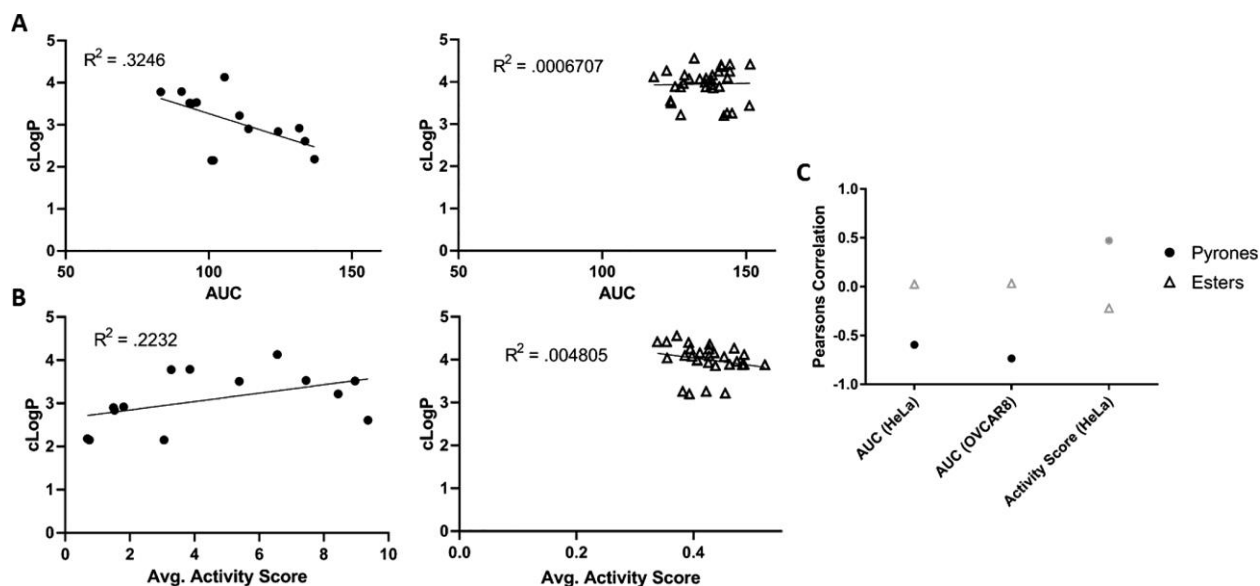


**Figure 14.** Correlation between biological activity and clogP. (A) Scatter plots reveal the correlation between AUC of pyrones (left) and reduced flavone esters (right) with clogP in HeLa cells. (B) Scatter plots reveal the correlation between average activity scores of pyrones (left) and esters (right) with clogP in HeLa cells. In panels A and B, clogP values were calculated using SwissADME.<sup>(13)</sup> (C) Dot plot of the Pearson's correlation between clogP and AUC or average activity scores for each class of compounds with grayed out points showing insignificant correlations ( $p$ -value  $> 0.05$ ). The pyrones show a significant correlation between biological activity and clogP in the cytotoxicity assays.

### C. Profiling a stereochemically and structurally diverse library of benzofurans and benzopyrans

For our next library we focused on the benzofuran and benzopyran flavonoid scaffolds to generate a structurally diverse library of molecules. Like the flavone and pyrone scaffolds these have also been found to have a variety of biological activities.<sup>126–128</sup> However, their current physicochemical properties limit their membrane permeability and thus their activity within the cell.<sup>129</sup> We addressed this through the inclusion of nitrogen-containing groups to the scaffold to increase the variance in chemical properties and potentially enhance the efficacy, as well as further improve the biological performance diversity, of these molecules.<sup>130,131</sup> Our previously published DOS oriented synthetic strategy allowed us to systematically generate a library that was diverse in scaffold, appendage, and stereochemistry (Figure 15A).<sup>72,132</sup> These molecules sampled a broad range of the 3D chemical space as measured by PMI (Figure 15B). In addition, they also exhibited a diverse array of physicochemical

properties such as MW, clogP and tPSA (Figure 15C). As with the previous library, we also wanted to generate molecules that were more enriched in sp<sup>3</sup> character to further drive biological performance diversity (Figure 15D). For this Cell Painting assay we again used HeLa cells which were treated in six-point dose (2-fold dilution, 100 to 3.125  $\mu$ M in DMSO). In contrast to our first profiling experiment, which used the entire feature set (around 1,700 features) for the calculation of activity scores, mp-values and other analysis, this time we decided to reduce the number of features by using the previously describe selection method which could potentially improve the predictive power of our PCA. This reduced set of 434 normalized, maximally informative and minimally redundant features which composed the profiles that were used in all downstream analysis.

Through the calculation of activity scores and mp-values for all doses and compounds we determined that, in contrast the previous pyrone and flavone library, our new library of sp<sup>3</sup>-enriched benzofurans and benzopyrans was highly bioactive, with 72 out of 82 molecules active at the highest dose (Figure 16A). Overall, the series based on the benzofuran scaffold (Series 1 and 2) contain the most active molecules and the largest range of activity at all doses (Figure 16A). Because the activity scores are highly negatively correlated with cell count (Figure 16B), and cytotoxicity induces large changes in cellular morphology regardless of the actual molecular target, compounds with moderate activity scores are also of interest as they could contribute meaningfully to the performance diversity of the library. However, the most active molecules contained in Series 1 and 2 tended to display more variable phenotypes as visualized by the PCA of their profiles at 100  $\mu$ M (Figure 16C).

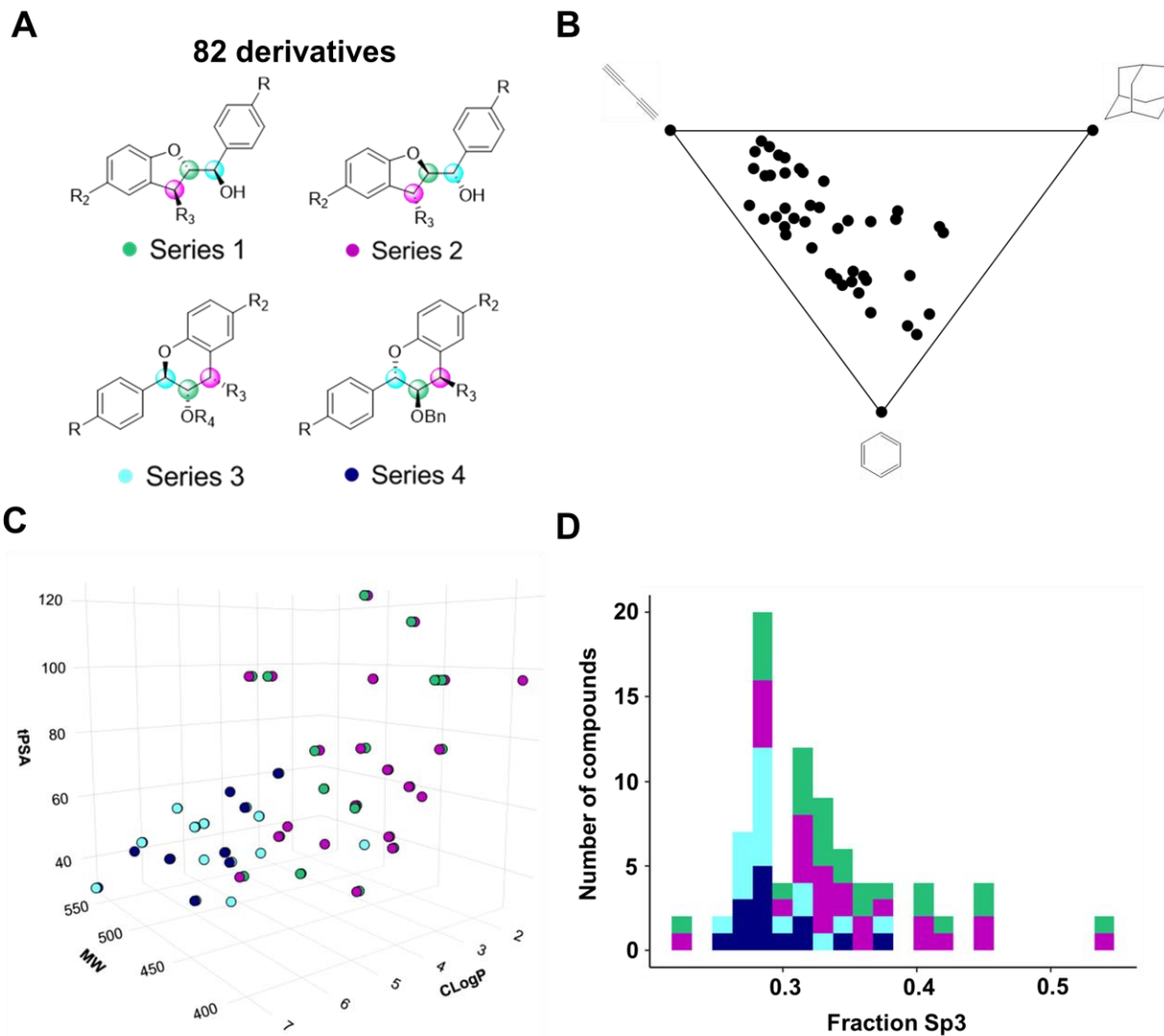


**Figure 15.** Chemical features of the benzofuran and benzopyran library (A) Composition of the library. (B) PMI plot of the lowest energy conformer for each enantiomeric pair of flavonoid derivatives. (C) 3D plot of the MW, tPSA and clogP of flavonoids. (D) Histogram of the fraction of sp<sup>3</sup> carbons.

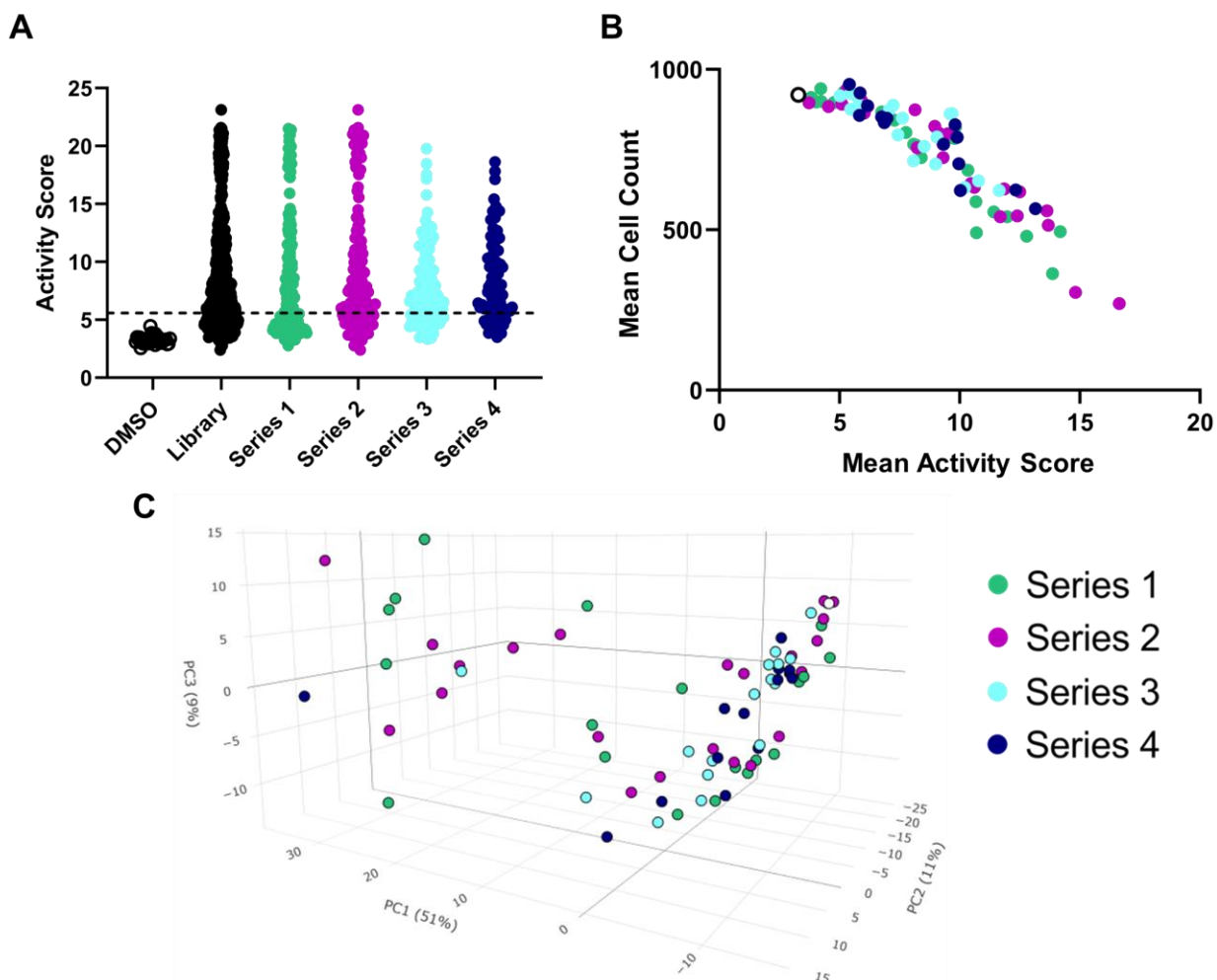


**Figure 16.** Overall activity of the benzofuran and benzopyran library. (A) Dot plot showing the activity score (Mahalanobis distance) for each dose for every compound and the DMSO controls. Dashed line represents the distance at which a treatment was typically observed to be statistically active ( $p$ -value  $< 0.05$ ). (B) Scatter plot of the mean activity score and cell count for each compound averaged across all doses. The mean of all DMSO wells used in normalization is represented as an open circle. (C) PCA plot of the profiles of all active compounds at  $100 \mu\text{M}$ . Each point represents the mean of 4 replicates. The mean of all DMSO wells used in normalization is represented as an open circle.

#### **D. Establishing correlations between chemical features and bioactivity**

Discovering the correlations that may exist between chemical features, that can be quantified *in silico*, and biological activity is important for informing the construction of performance-diverse libraries. Because we built our library from molecules that included moieties with variable polarity, we expected two physiochemical properties, clogP and tPSA, to be predominant in driving biological performance diversity. As discussed previously, these features also correlate remarkably well with the permeability of organic compounds, which may be the underlying mechanism in the variance of activity.<sup>130,131</sup> For our library, we found a strong correlation between activity score and cell count with clogP for molecules in Series 1 and 2, indicating that increasing clogP increases the bioactivity of this set of compounds (Figure 17A). Interestingly, the reverse was true for Series 3 and 4, where increasing clogP decreased cytotoxicity and where activity score does not seem to be significantly correlated with clogP (Figure 17A). This dependence was generally inverted for tPSA and this dependence was much weaker for Series 1 and Series 2 than for Series 3 and 4 (Figure 17B). We also found that the variation of MW and fsp3 had no impact on the given activity of for any of the scaffolds (Figure 18). Taken together, these observations illustrate the need to determine which chemical features are important for driving performance diversity for a particular scaffold and that having molecules with diverse set of these critical properties is likely to enhance the biological performance diversity of a library.

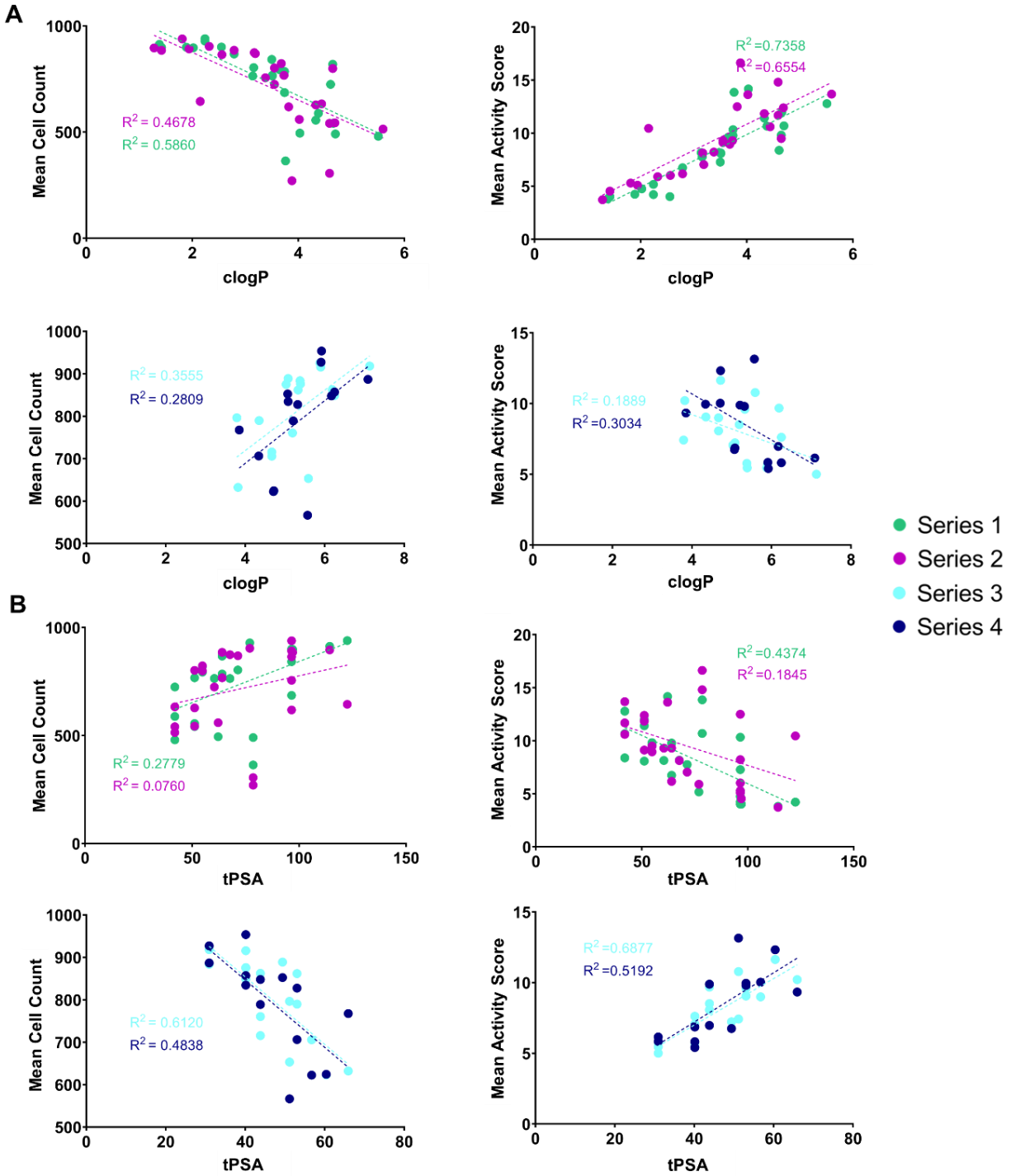


Figure 17. Correlation plots for the mean activity score and mean cell count and (A) clogP and (B) tPSA.

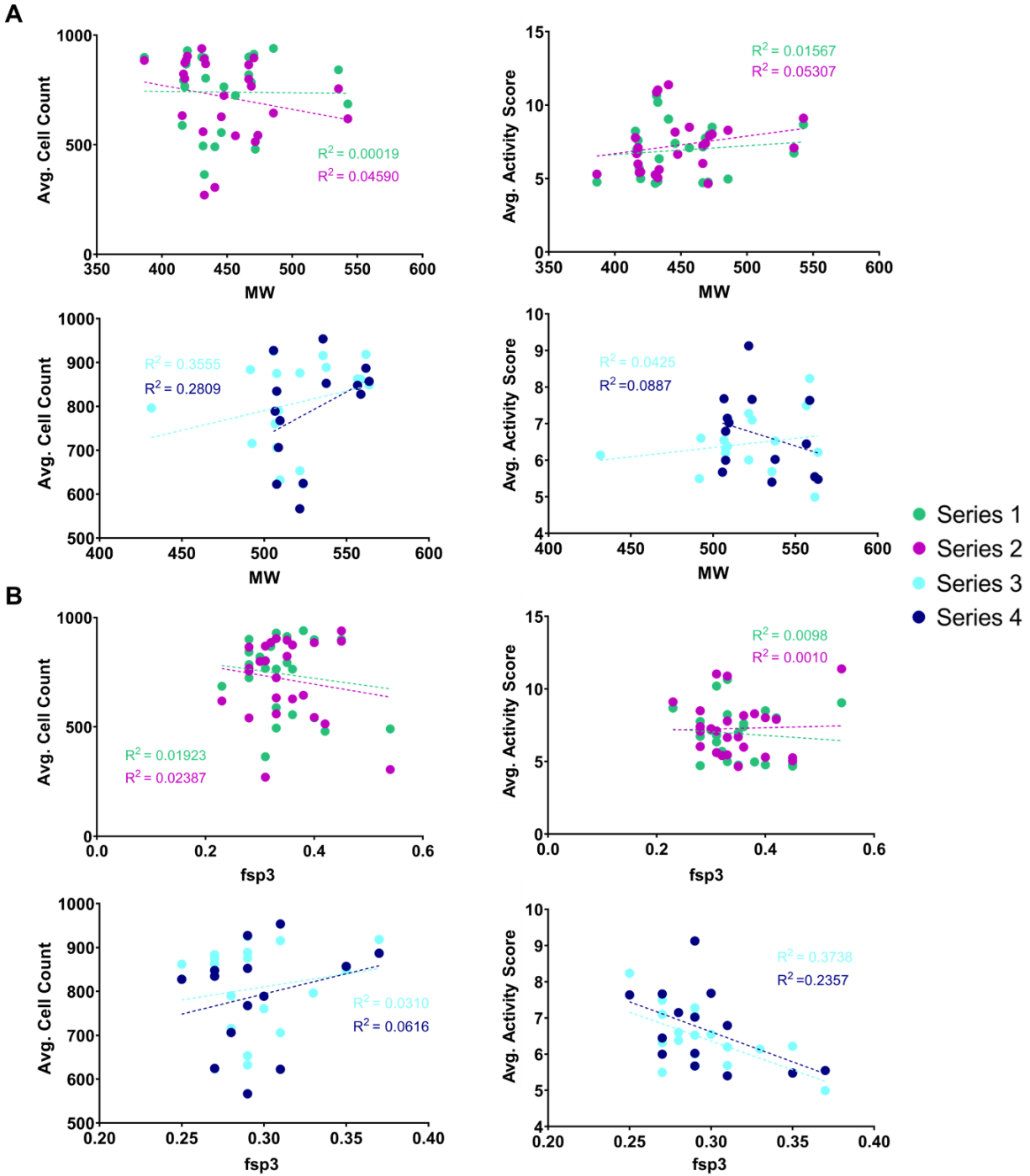
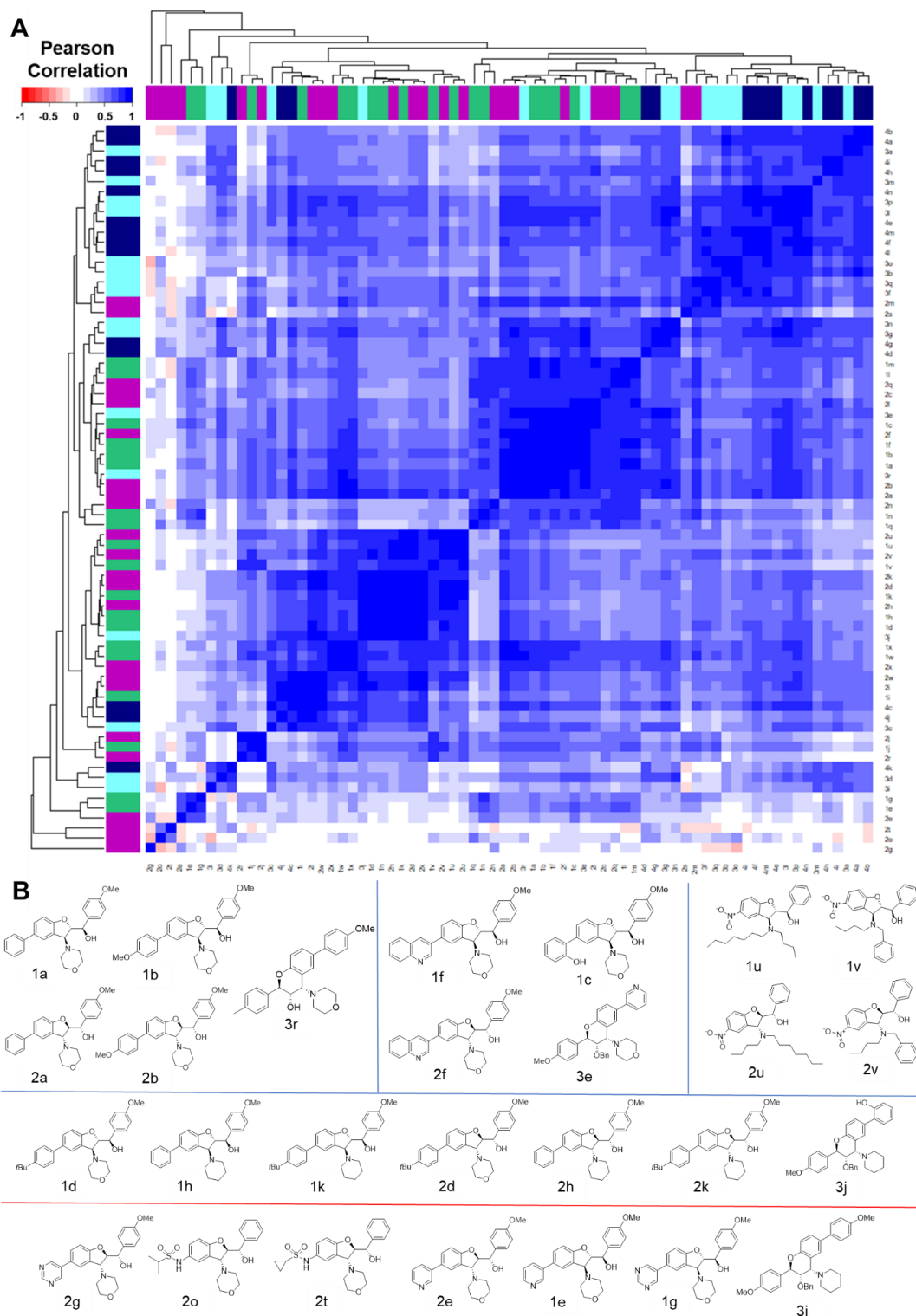


Figure 18. Correlation plots for the average activity score and average cell count and (A) MW and (B) fsp3.

#### **E. Determining the structure activity relationship driving similarity using hierarchical clustering analysis**

It is possible that a library of highly biologically active molecules is not performance diverse, as all molecules may still generate morphological profiles that are very similar. To determine if our library induced a range of unique morphological profiles and which molecules were most dissimilar, we decided to analyze how correlated the profiles of different molecules were to each other. We used the 100  $\mu$ M dose profile as the representative profile for each compound on the assumption that any induced differences are dose dependent and thus would be greatest at the highest dose. Using these profiles, we calculated the Pearson correlations between all compounds. These Pearson correlations were then used as the distance measurements for the hierarchical clustering of the entire library, which would allow us to determine the dissimilarity (Figure 19A). From this analysis, we observed that clustering was driven primarily by scaffold, with the most structurally similar molecules, including some stereoisomers, having the highest correlations. Critically, almost half of all the active molecules (35) induced profiles which were not highly correlated with any other molecule (Pearson  $R^2 < 0.9$ ), indicating that there is some dissimilarity induced through scaffold or stereochemical variation within each series.

Looking closely at the structures found within highly correlated clusters allowed us to establish the SAR responsible for morphological profile similarities (Figure 19B). The largest highly correlated cluster mostly contains molecules from Series 1 and 2, featuring three matched stereoisomeric pairs (**1d**, **2d**, **1h**, **2h**, **1k**, **2k**) each containing methoxy substituents and a non-polar tert-butyl group or phenyl ring. Interestingly, this cluster contains a molecule from Series 3 which also contains a methoxy group and a polar hydroxyl group (**3j**). This observation reveals that differences in substituent polarity may not guarantee diverse performance, but that molecules with the most similar substituents and scaffolds tend to produce redundant biological profiles, which highlights that it is still worthwhile to vary these features in order to create performance-diverse libraries. Other clusters (**1a**, **2a**, **1b**, **2b**, **3r**) and (**1f**, **2f**, **1c**, **3e**) also contain matched stereoisomer pairs from series 1 and 2, which indicates that diversity of stereochemistry may be less impactful for diverse performance, at least for this scaffold.



**Figure 19.** Heatmap of benzofuran and benzopyran library. (A) Heatmap showing Pearson correlation between compounds with a dendrogram showing the results of hierarchical clustering. Column and row colors indicate which series compounds belong to (Series 1 – Green, Series 2 – Magenta, Series 3 – Teal, Series 4 – Navy). (B) Structures of compounds found in the most tightly correlated clusters ( $R^2 > 0.9$ ), separated by blue lines, and structures of the most dissimilar molecules, separated by a red line.

The four molecules that contain alkyl-substituted tertiary amines form the highest correlated cluster (**1u**, **1v**, **2u**, **2v**). These molecules are also the most potent out of all the clustered molecules as well as the entire library (Table 2). The least potent of the active molecules are also the most dissimilar from the rest of the library (**2g**, **2o**, **2t**, **2e**, **1e**, **3i**). These compounds are mostly from Series 1 and 2 and tend to contain sulfonamides and nitrogen-containing aromatic heterocycles, except for **3i**, **3d**, **4k**. This result may suggest that the inclusion of further such substituents in future libraries could further expand the performance diversity exhibited by these scaffolds. Additionally, though they are less potent, they exhibit much more specific morphological profiles than the molecules found in highly correlated clusters, with only a couple key features changing relative to the DMSO control (Figure 20). Looking directly at representative images, the highly active molecules from each cluster induce unique phenotypes that are readily visible by eye (Figure 21), while the phenotypes of each dissimilar molecule are not readily distinguishable from DMSO (Figure 22). This highlights the utility of Cell Painting in detecting subtle phenotypes and the importance of avoiding the selection of too many highly cytotoxic molecules as they may have promiscuous activity as indicated by the shift of a large range of features.

Compound	Mean Activity Score	Mean Cell Count
2v	16.6	270.5
2u	14.8	305.6
1v	13.9	364.0
2k	13.7	514.2
1k	12.8	480.2
2d	12.4	543.6
1d	12.0	541.6
2i	11.8	628.0
3c	11.6	623.1
1i	11.4	555.9
3j	10.8	653.2
1u	10.7	491.1
1h	10.7	588.3
2h	10.6	633.0
1f	9.8	785.4
2f	9.3	767.3
2b	9.3	725.1
2a	9.1	802.2
3e	9.1	789.8
1b	8.1	764.5
1a	8.1	767.3
3r	7.4	796.5
1e	6.8	868.0
2e	6.2	885.7
2g	5.9	904.0
3i	5.7	915.6
2t	5.3	939.1
2o	5.1	891.9
DMSO	3.3	921.3

**Table 2.** Mean cell counts and activity scores for highly correlated and highly dissimilar compounds.

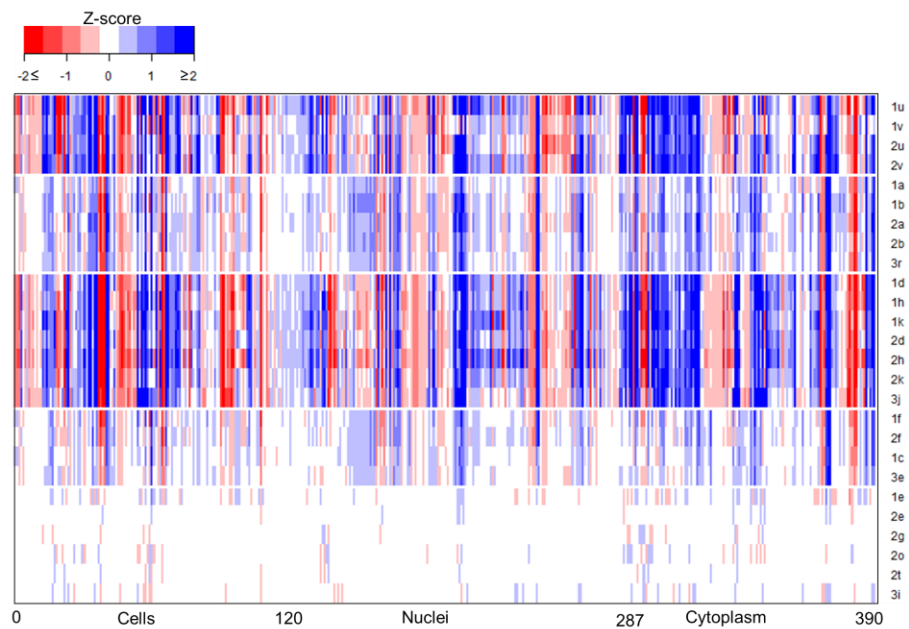


**Figure 20.** The feature profiles generated for each of the clustered compounds at 100  $\mu\text{M}$ . Red indicates an increase and blue a decrease in the relevant feature as compared to DMSO control. Compounds are grouped by cluster.

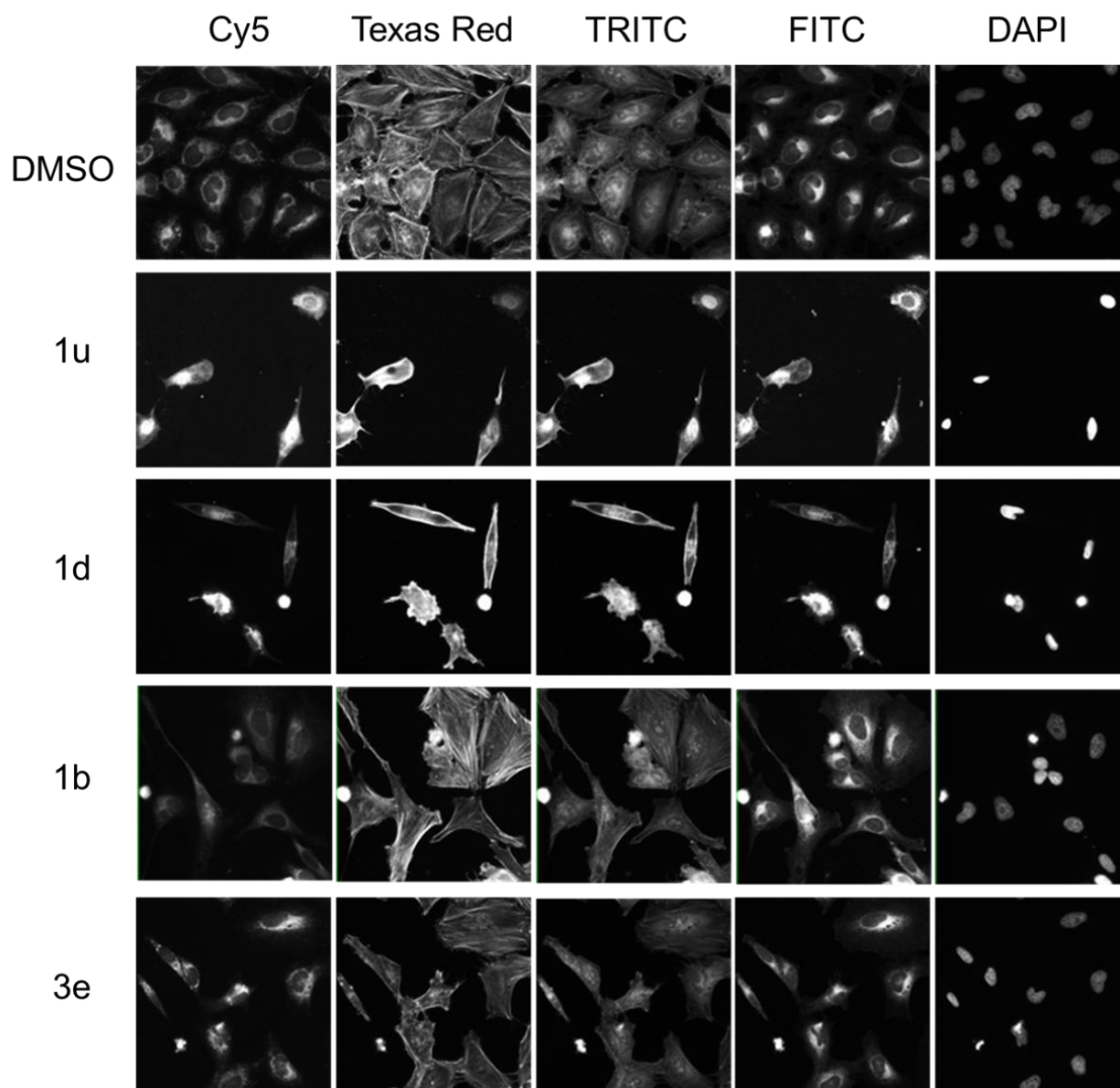


**Figure 21.** Representative images showcasing the different phenotypes induced by a representative compound in each highly correlated cluster in comparison to DMSO control wells.

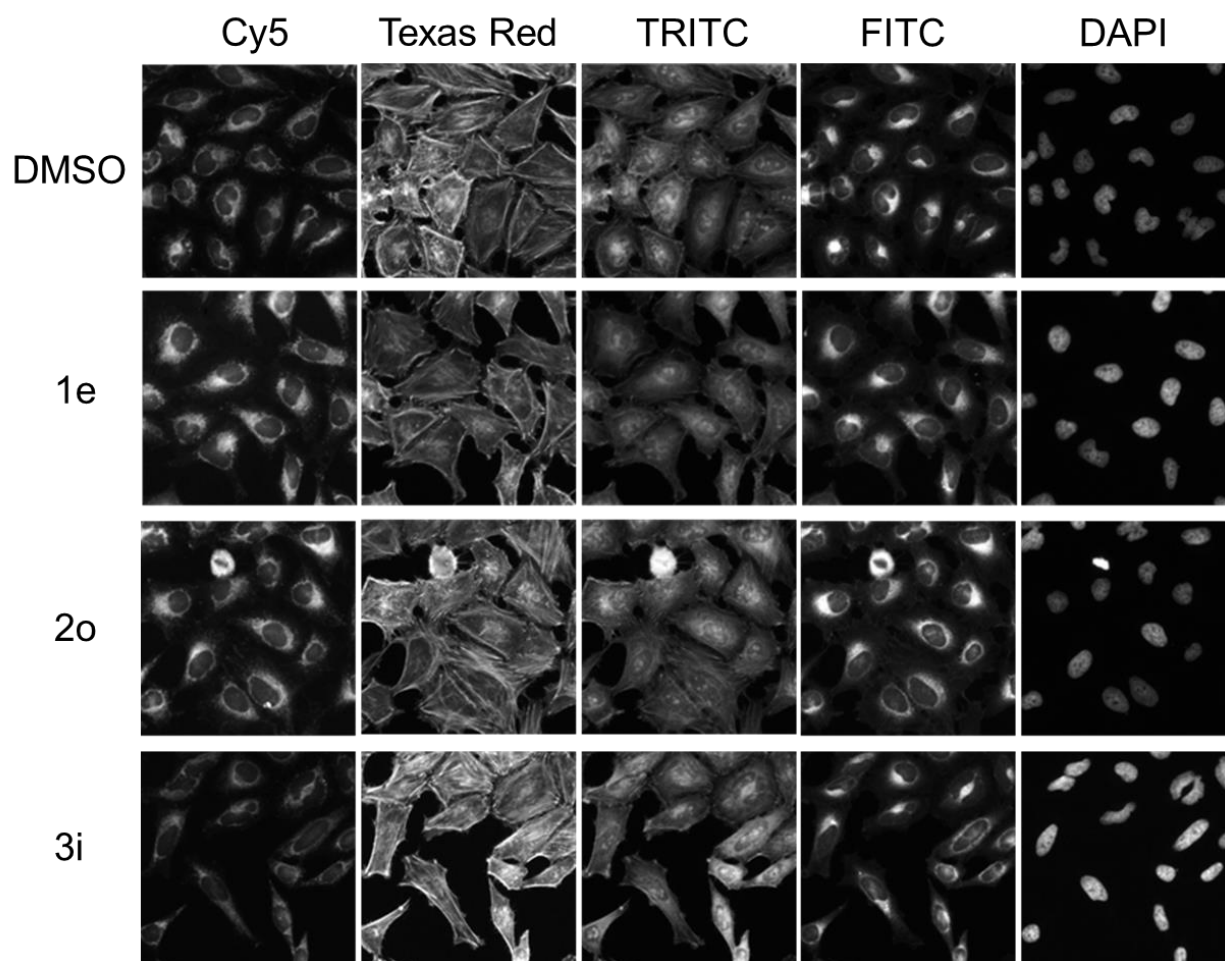


**Figure 22.** Representative images showcasing the phenotypes induced by three molecules that were uncorrelated with the rest of the library.

## **F. The synergistic effects of scaffold, stereochemistry and appendage variation on biological performance diversity**

Previously Cell Painting has been used to demonstrate that variation of just stereochemistry can produce sets of performance diverse molecules.<sup>93</sup> Our hierarchical clustering analysis already established that each scaffold tended to sample distinct areas of biological space as indicated by their tendency to not cluster together, while stereoisomers and structurally similar molecules tended to exhibit much more similarity in their biological profiles (Figure 19). To estimate this effect in a more quantitative way, we calculated pairwise activity scores for all the active molecules in our library using the profiles from the 100  $\mu$ M dose. This allowed us to determine which analogs were significantly different from each other when only the stereochemistry or scaffold were changed (mp-value < 0.05). In total we compared 26 scaffold pairs and 31 stereoisomeric pairs. Only one instance was observed in which pairs were dissimilar for both scaffolds and stereoisomers (Figure 23A). More frequently stereoisomeric pairs were dissimilar only for one scaffold and not the other (Figure 23B) or stereoisomeric pairs were not dissimilar for both (Figure 23C). We also confirmed that this dissimilarity was dose dependent with the greatest distance often observed at 100  $\mu$ M (Figure 24). Additionally, we showed that scaffold pairs were more distant, and thus dissimilar, from each other on average with a mean activity score of 29.7 (Table 3, right), while stereoisomeric pairs had a mean activity score of 16.4 (Table 3, left).

While all scaffold pairs were significantly dissimilar from one another and at least some of this dissimilarity was due to the protecting group on the alcohol of the benzopyran as **3q** and **3r** are significantly different from each other (Figure 23D). This is important, because all the molecules in Series 3 and 4 were benzyl protected, except for **3q**. In comparison, only 12 out of 31 stereoisomeric pairs were significantly dissimilar. From this analysis, we can conclude that variation in the scaffold is more important for driving biological performance diversity than the variation of the stereochemistry. Although it is hard to draw conclusions about which specific appendages are more likely to make stereoisomers dissimilar, the dissimilarity does seem to be scaffold- and appendage-dependent, as only one pair (**1m**, **2m**, **3m**, **4m**) is dissimilar in both scaffolds. Additionally, the only structural difference between the m analogues, that are all dissimilar, and the f analogues (**1f**, **2f**, **3f**, **4f**), for which stereochemistry has no impact on dissimilarity, is the substitution of a piperidine with a morpholine. These results support the conclusion that there is synergy in the joint variation of scaffold, appendage, and stereochemistry in

producing unique biological profiles as specific combinations of each are necessary for compound pairs to exhibit profiles that are significantly distinct from each other.

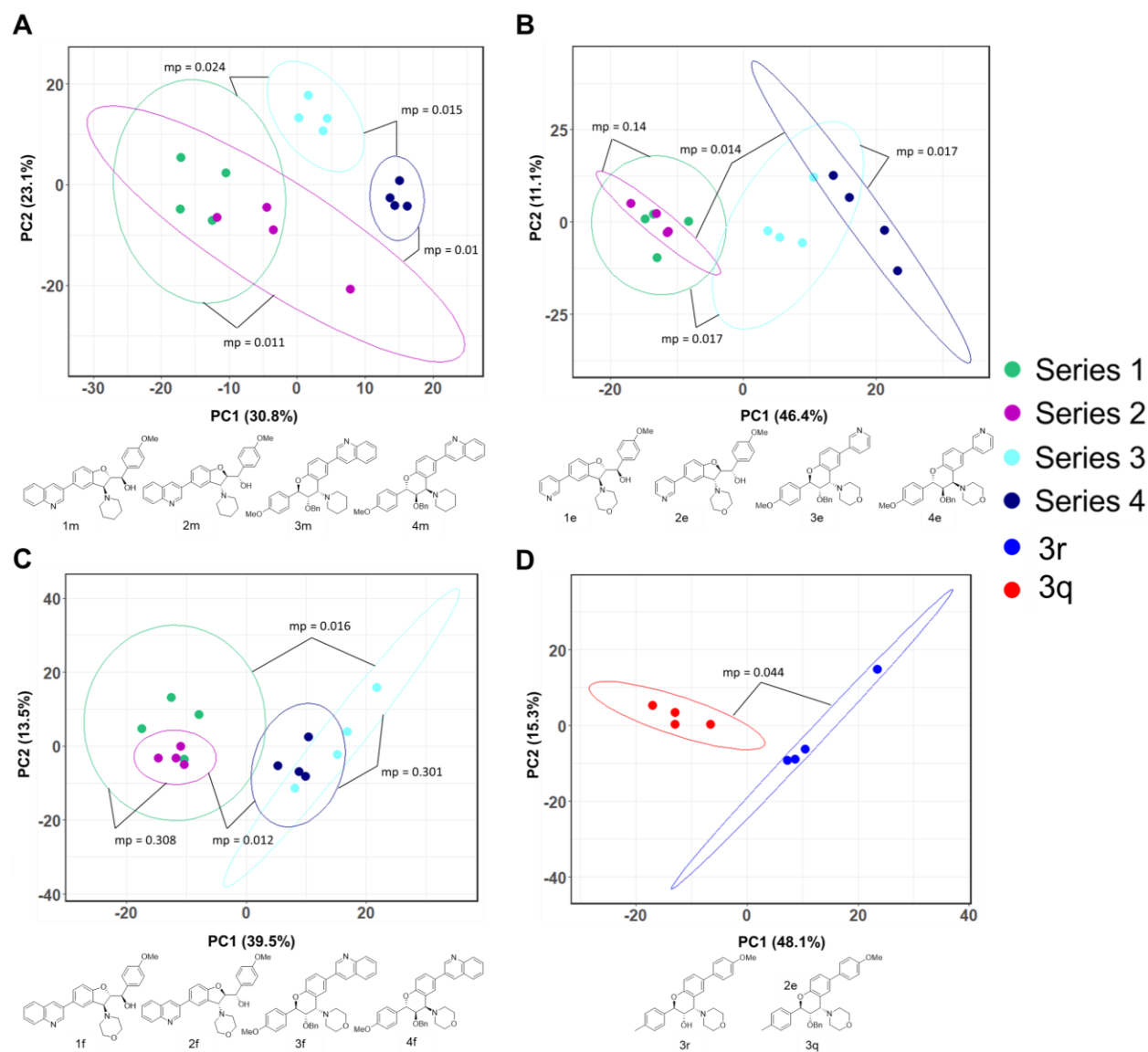


**Figure 23.** PCA plots of compound pairs and their structures. Points represent individual replicates of each compound at 100  $\mu$ M and encircled by ellipses representing the 95% confidence intervals. An mp-value < 0.05 signifies a statistically significant separation of clusters. (A) Compounds 1m, 2m, 3m, 4m. (B) Compounds 1e, 2e, 3e, 4e. (C) Compounds 1f, 2f, 3f, 4f. (D) Compounds 3q and 3r.

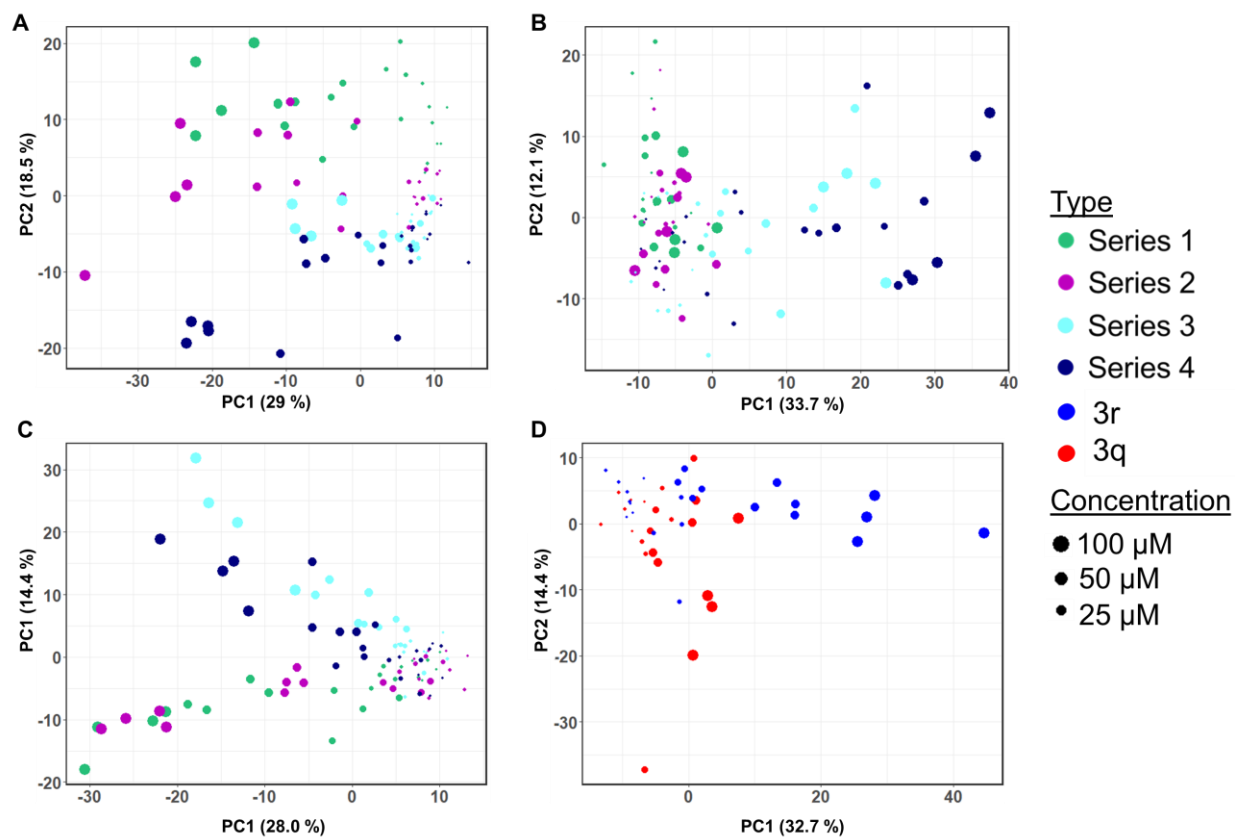


**Figure 24.** PCA plots of compound pairs in dose. Points represent individual replicates of each compound at 100  $\mu\text{M}$ . (A) Compounds 1m, 2m, 3m, 4m. (B) Compounds 1e, 2e, 3e, 4e. (C) Compounds 1f, 2f, 3f, 4f. (D) Compounds 3q and 3r.

<i>RSS</i>	<i>SRR</i>	Activity Score	mp-value	Benzopyran	Benzofuran	Activity Score	mp-value
1w	2w	19.8	0.01	3g	1g	13.4	0.005
1m	2m	22.9	0.011	3i	1i	32.7	0.008
1j	2j	136.9	0.014	4d	2d	21.3	0.008
1x	2x	32.3	0.014	3d	1d	28.1	0.009
3l	4l	61.1	0.014	4c	2c	32.1	0.01
3m	4m	18.6	0.015	4h	2h	8.9	0.01
1b	2b	13.5	0.016	4k	2k	28.0	0.01
1v	2v	10.0	0.016	4m	2m	10.4	0.01
3e	4e	25.5	0.017	4a	2a	36.9	0.011
3g	4g	13.9	0.036	4f	2f	29.0	0.012
3j	4j	6.4	0.041	3c	1c	28.7	0.013
1c	2c	6.4	0.048	3n	1n	25.8	0.013
3d	4d	19.5	0.059	4b	2b	30.1	0.013
1g	2g	11.4	0.06	4e	2e	28.7	0.014
1l	2l	13.7	0.072	3b	1b	23.6	0.015
1n	2n	14.3	0.075	3j	1j	12.9	0.015
3a	4a	11.0	0.084	4g	2g	111.6	0.015
1a	2a	6.8	0.107	3f	1f	22.2	0.016
3c	4c	7.8	0.125	4l	2l	23.0	0.016
1h	2h	6.6	0.137	3e	1e	55.4	0.017
1e	2e	6.7	0.14	3l	1l	35.3	0.019
1u	2u	4.9	0.144	4j	2j	39.9	0.019
1q	2q	6.1	0.18	4n	2n	16.6	0.019
3i	4i	5.2	0.202	4i	2i	19.4	0.021
2k	1k	5.5	0.249	3m	1m	22.6	0.024
3f	4f	2.5	0.301	3a	1a	35.1	0.025
1f	2f	4.3	0.308		Mean	29.7	
3b	4b	3.8	0.333				
1i	2i	2.4	0.334				
3n	4n	4.1	0.336				
1d	2d	3.2	0.4				
	Mean	16.4					

**Table 3.** Mahalanobis distances for each stereoisomer (left) and scaffold (right) pair at 100  $\mu$ M

#### **IV. Conclusion**

Traditional approaches to composing a library with diverse biological activity emphasized the inclusion of molecules with varied chemical structures and properties. However, a majority of molecules in such libraries have been found to be biologically inactive and are thus outperformed by libraries selected for biological performance diversity.<sup>37,64</sup> This necessitates the creation of a new paradigm focused on identifying the types of chemical features that are most predictive of diverse biological activity. To this end we utilized scaffolds found in broadly bioactive flavonoid natural products to assemble two libraries containing novel moieties, increased sp<sup>3</sup> character and diverse stereochemistry using DOS. Along with structural diversity these libraries also accessed a diverse range of physicochemical properties. Using a target-agnostic method called Cell Painting we profiled these libraries to determine which of these chemical features were most important for driving biological performance diversity.

For our first library, which was focused on the pyrone and flavone scaffolds, we found that increased fsp<sup>3</sup> of the reduced flavones does not significantly improve biological performance diversity of these scaffolds compared to the natural flavones and pyrones within the limits of the detectable phenotypes for this morphological profiling assay. We discovered that lipophilicity, through the incorporation of different appendages, predicted scaffold activity and resulted in performance diversity among the pyrone analogues in the cytotoxicity assay but not in Cell Painting. By comparison of the pyrones, natural flavones, and reduced flavone esters, it is clear that the scaffold makes a significant contribution to performance diversity. Cell Painting also allowed us to determine the effects that appendage variation had on the variance in bioactivity. Although the ester class was not active in the Cell Painting assay it was still possible to determine the effects that the variation of appendages and stereochemistry had using the cytotoxicity assay. This project revealed the importance of including various assays for the measurement of performance diversity to evaluate diversity early in the library construction phase to decrease performance-redundant scaffolds. It also revealed the significance of chemical properties such as lipophilicity for performance diversity and the observation that compounds with lower fsp<sup>3</sup> can also possess diverse biological activities. In conclusion, our first profiling experiment established that a diverse combination of several factors, including scaffold, appendages, stereochemistry, fsp<sup>3</sup>, and physicochemical properties, combined with early assessment of performance diversity of pilot libraries, will contribute to the development of performance-diverse, small-molecule libraries.

Our second profiled library, which was based around the benzofuran and benzopyran scaffolds, further confirmed and built on these previous results. We found that our library was active across both scaffolds and stereoisomers and this activity correlated with clogP or tPSA in a scaffold-dependent manner. This dependence illustrates the relevance of using such a metric for the selection of molecules with diverse activity, as previously shown for the pyrone scaffold. Lastly, using hierarchical clustering analysis and PCA, we managed to determine the relative contribution of each feature (scaffold, appendage, stereochemistry) to the generation of performance diversity for these flavonoid scaffolds. Our previous work showed that a library of sp<sup>3</sup>-enriched flavonoid derivatives had limited cytotoxicity and activity in Cell Painting. Other studies utilizing DOS also produced libraries where the majority of molecules were inactive.<sup>92,93</sup> This stresses the importance of discovering which chemical features can be accessed through a systematic DOS approach to library creation in order to generate a large number of molecules that are diversely bioactive, as structural similarity alone has been shown to be a poor predictor for this task.<sup>63,133</sup> We confirmed that scaffold variation had the biggest impact on how different the generated morphological profiles were for pairs of molecules with matching appendages, as was also the case for the previous library. Additionally, we saw that certain appendages and almost half of the stereoisomers exhibited significant differences in the profiles they generated. Importantly, this variance in biological activity was also synergistic with the type of scaffold since some stereoisomers and appendage pairs were only different from each other for one scaffold and not the other. A previous study from the Schreiber group also noted this effect,<sup>93</sup> further confirming the validity of including stereoisomers to improve the performance diversity of a library. Additionally, we found that even subtle differences in appendage structure could make stereochemistry impact the biological profile that is generated.

The evolution of target-agnostic, high-content screening technology has enabled the direct evaluation of the biological performance of novel chemical matter. It is becoming increasingly important that new compounds are tested for performance as they are synthesized, thus helping guide further synthetic efforts. Additionally, access to the morphological profiles generated by compounds will assist in building better libraries, as we can establish which chemical features are relevant for a target or assay. Ultimately, we demonstrate that a systematic, diversity-oriented approach based around a biologically active scaffold can be an effective synthetic strategy for accessing a focused library that is highly bioactive and performance diverse. Performance-diverse libraries can be used in the future in a multitude of target-based assays and potentially yield improved hit rates as compared to larger compound libraries, greatly improving the efficiency of probe discovery efforts. Additional scaffolds will need to be explored to

determine if the observed trends are general and to obtain a better understanding of the generality of the structural and physical properties of small molecules that are most predictive of biological performance diversity to create efficient, diverse compound libraries for probe and drug discovery programs. It will also be critical to follow this research with the screening of these two libraries, which have differing activities in Cell Painting, in other assays to demonstrate that library construction based on biological performance diversity could help improve hit rates against a diverse array of targets.

## CHAPTER 2

The Methodology, and Results and Discussion sections of this chapter were previously published in Pavlinov, I.; Salkovski, M.; Aldrich, L. N. Beclin1-ATG14L Protein-Protein Interaction Inhibitor Selectively Inhibits Autophagy through Disruption of VPS34 Complex I. *J. Am. Chem. Soc.* **2020**, *142* (18), 8174-8182 with permission from Copyright 2020 American Chemical Society.

### **I. Introduction**

#### **A. The history and molecular biology of autophagy**

Autophagy is a broad term used to describe the collection of evolutionarily conserved catabolic pathways found in all eukaryotes responsible for maintaining homeostasis. Though there are several distinct pathways for autophagy, they utilize the same cellular machinery, and all involve the sequestration, engulfment and degradation of cytosolic contents inside autophagosomes.<sup>134</sup> This process is characterized by the unique double-membrane structure of the autophagosomes, which were originally discovered over 50 years ago using electron microscopy. The characterization of the molecular mechanism of autophagy started in the 1990s using yeast mutational studies.<sup>135</sup> These early efforts elucidated the numerous genes involved in autophagy, as well as their relative importance and overall role in the proper functioning of this process and have thus been recently recognized with the 2016 Nobel Prize in Medicine.<sup>136</sup> Similar studies have been repeated in plants, worms, fruit flies, mice, and humans, and have shown that many autophagy genes are highly conserved between disparate species in their overall structure and function, thus demonstrating the vital role autophagy plays in the physiology of multicellular organisms.<sup>137</sup>

The autophagy process can be split into three pathways: chaperone-mediated autophagy (CMA), microautophagy, and macroautophagy. CMA is a target specific process that involves the targeting of proteins to the lysosome for degradation based on the presence of the sequence KFERQ which is recognized by specific chaperones. Microautophagy, is more nonspecific and involves the engulfment of cytosolic content by the lysosomal membrane. The exact molecular mechanism underlying this pathway remains largely unknown, but has now been observed degrading various types of cellular cargo in several different species including endosomes in mammals.<sup>138</sup> In contrast to CMA and microautophagy, macroautophagy (hereafter referred to as autophagy) entails the formation of brand new autophagosome. It is this form of autophagy that is most critical to the proper functioning of cellular

homeostasis as it is capable delivering a much larger quantity of cargo for recycling in the lysosome.<sup>139</sup> The trafficking of cellular cargo via autophagosomes involves several steps: induction, elongation, fusion and degradation. Under nutrient-rich conditions, autophagy occurs at a low basal level during which it plays a general “house-keeping” role, but nutrient deprivation, energy depletion, or cellular stress induce autophagy, leading to the biogenesis of a larger quantity of new autophagosomes.<sup>140</sup> Upon induction, new autophagosomes are generated to sequester cellular cargo (damaged organelles and proteins, engulfed pathogens, etc.) within a double membrane vesicle which are then trafficked to the lysosome (Figure 25).<sup>141</sup> At the lysosome the outer membrane fuses with the lysosomal membrane after which the inner membrane along with the cargo it contained is degraded.

In mammals, the early autophagy pathway involves several distinct complexes among which the majority of autophagy genes can be divided. These are the pre-initiation ULK complex, the initiation VPS34 Complex I, and the two ubiquitin-like conjugation systems (Figure 25). The ULK complex consists of ULK1/2, Atg13, FIP200 and Atg101 in mammals, and is required for the biogenesis of new autophagosomes.<sup>142-145</sup> Being the most upstream complex in the autophagy pathway, it is the main target of most autophagy regulating pathways, particularly the mTOR pathway.<sup>146</sup> The proteins, often other kinases, found in these pathways are responsible for the extensive network of post-translational modifications, specifically phosphorylation, that the ULK complex undergoes upon autophagy induction.<sup>143,144,147</sup> ULK1, for which the complex is named, is a serine kinase and its activity is critical for the regulation and recruitment of the other complexes to the endoplasmic reticulum (ER), where new autophagosomes form in mammals.<sup>147</sup> The autophagy-specific VPS34 Complex I is composed of four core members: VPS34, VPS15, Beclin 1 and ATG14L and its main role is the elongation of the autophagosomal membrane through the phosphorylation of phosphatidylinositol (PI) to produce phosphatidylinositol-3-phosphate (PI3P).<sup>148</sup> The protein involved in this complex are typically disbursed throughout the cytoplasm or localized at other organelles and are only recruited to the ER in an ULK1- dependent way during autophagy induction. Lastly, there are the two ubiquitin-like autophagy proteins, ATG5 and MAP1LC3B (hereafter referred to as LC3), and their respective overlapping conjugation systems. Under basal conditions, ATG5 is conjugated to ATG12 through the ubiquitin-like activity of ATG7 and ATG10.<sup>149</sup> This conjugate is then recruited to the autophagosome by ATG16L1 where it forms a multimeric complex critical to the formation of the autophagosome-specific biomarker LC3-II.<sup>150</sup> LC3-II is a form of LC3 that has undergone proteolytic cleavage by ATG4, forming LC3-I, followed by ATG7 and ATG3-mediated conjugation to phosphatidylethanolamine (PE). Recruitment and integration of LC3-II into the

growing phagophore is dependent on Atg5–Atg12,<sup>151,152</sup> where it plays a role in inducing membrane curvature, controlling hemifusion, and acting as a biomarker for the recruitment of specific cargo and other autophagy proteins.<sup>153</sup>

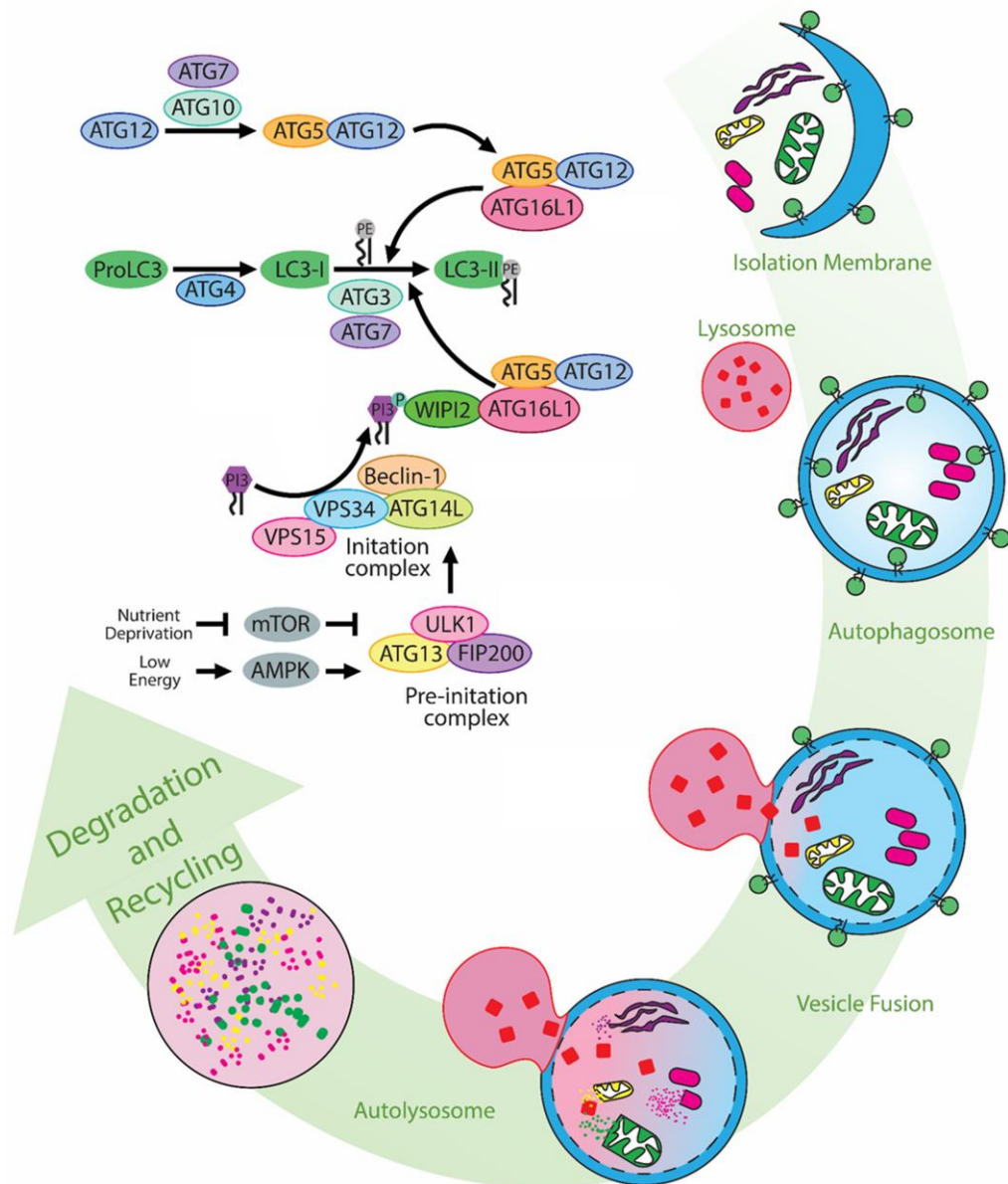


**Figure 25.** The autophagy pathway and the proteins involved in autophagy activation. Autophagy starts with the ULK1 mediated activation of the initiation complex (VPS34 Complex I), which begins to generate the PI3P necessary for the formation of the autophagosome. Concurrently the two ubiquitin-like conjugation systems (ATG4-ATG3-ATG7 and ATG5-ATG12-ATG16L1) cooperate to generate LC3-II, an autophagy-specific biomarker critical to the formation of the autophagosome and the recruitment of cargo for sequestration.

## **B. Dual role of autophagy in cancer**

Autophagy has long been suspected to play an important role in cancer biology, as the allelic deletion of essential autophagy genes like *BECN1* (Beclin 1) was found frequently in breast, ovarian and prostate cancer.<sup>154</sup> One potential mechanism behind this link could be accumulation of autophagy-specific substrate p62 in autophagy-deficient cells.<sup>155</sup> This protein has been shown to regulate Ras-driven NF- $\kappa$ B activation which is a family of transcription factors that act as master regulators for prosurvival and proinflammatory response genes.<sup>156,157</sup> Overactivation of NF- $\kappa$ B can lead to chronic inflammation through the accumulation of pro-inflammatory cytokines that support the tumor micro-environment by helping it escape immune surveillance and accelerating cell proliferation and oncogenic mutation.<sup>158,159</sup> p62 is also known to bind to and inhibit Keap1, which promotes the degradation of Nrf2, a transcription factor that regulates the expression of genes critical for the management of reactive oxygen species (ROS) and stress response.<sup>160,161</sup> Thus, the p62-dependent inhibition of Keap1 leads to the accumulation of Nrf2, which promotes tumorigenesis through the overexpression of cytoprotective ROS scavengers.<sup>162,163</sup> In addition to the accumulation of oncogenic and damaged protein,<sup>164</sup> autophagy-deficient cells also exhibit more chromosomal instability as indicated by upregulated DNA damage response, evidence of DNA double-strand breaks, and aneuploidy.<sup>165,166</sup> Thus, the impairment of survival due to deficiency in autophagy may be somewhat mitigated by the enhanced mutation rate thereby promoting tumorigenesis.<sup>167</sup> This is also important for the emergence of aggressive and resistant forms of cancer, especially after chemotherapy, as the increased mutation rate of autophagy-deficient cancer cells may allow for the selection of more favorable phenotypes. While the origin of the increased DNA damage in autophagy-defective cells is not yet known, its inhibition is linked to the accumulation of many toxic macromolecules and ROS which are known to induce genome damage.<sup>168</sup> In sum, autophagy inhibition limits the ability of individual cells and the immune system more generally to respond to the development of mutations critical to further tumorigenesis.

Paradoxically, autophagy induction has also been linked to cancer cell survival and tumorigenesis.<sup>166,169</sup> It has been established that the low basal level of autophagy in normal tissues serves an important homeostatic role, as the deletion of *ATG5* or *ATG7* in neurons leads to the accumulation of poly-ubiquitinated protein aggregates and has been linked to neuronal degeneration.<sup>164,170</sup> Autophagy induction in response to external stress signals and nutrient deprivation has a crucial role in cell survival through the recycling of existing macromolecules, providing cells

under metabolic stress with needed nutrients and energy.<sup>171,172</sup> Early tumors undergo rapid proliferation while lacking blood flow, and thus experience metabolic stress even more acutely, making them even more reliant on autophagy for survival. Long-term autophagy activation typically triggers apoptosis, but in many tumors this process is already blocked, due to oncogenic mutations that cause BCL-2/BCL-X<sub>L</sub> activation or BAX/BAK inhibition, leading to sustained autophagy activation, necrosis and tumor maturation.<sup>166,173</sup> Sustained autophagy activation has been shown to be essential to the continued survival of these apoptosis-defective necrotic tumors, and its inhibition during metabolic stress leads to rapid cell death.<sup>174,175</sup> In addition, because autophagy plays such a broad cryoprotective role its activation is often a factor in tumor resistance to chemotherapy. Many small-molecule chemotherapies, such as 5-fluorouracil or cisplatin, which attempt to inhibit tumor progression by targeting the cell division process are ineffective against tumors which overexpress essential autophagy protein like Beclin 1.<sup>176,177</sup> This process may be mediated by the ability of autophagy to degrade internalized chemotherapeutics or through providing tumors enough energy and nutrients to survive increased metabolic stress due to the inhibition of cell division. Taken together, autophagy induction protects rapidly dividing tumors from their increased stress load, helping them avoid metabolic catastrophe even under treatment with chemotherapeutics.

Autophagy also plays a role in tumor dormancy and metastasis because, as described in the previous paragraph, autophagy can support the nutrient and energy needs of the hypoxic, metabolically stressed tumor cells even as they disseminate throughout the body and are deprived of key growth factors.<sup>174,175</sup> The ability of tumor cells to become dormant is closely linked to their ability to maintain quiescence, or reversible growth-cycle arrest, during which they are particularly resistant to cellular stress and capable of evading immune detection.<sup>178,179</sup> Autophagy may facilitate this process as its impairment has been linked to senescence in adult stem cells,<sup>180</sup> and the induction of autophagy leads to G1 arrest and cell survival.<sup>181</sup> It has also been shown that inhibition of autophagy in dormant cancer cells through knockdown of essential autophagy genes or treatment with lysosomotropic agents caused rapid cell death.<sup>182</sup> Though the quantification of autophagy activation directly in primary cell cultures remains a challenge, increased staining for LC3 has been associated with lymph node and melanoma metastasis and reduced survival in human breast cancer.<sup>183,184</sup> In addition, LC3 expression has been correlated with metastasis in hepatocellular carcinoma and more aggressive and invasive forms of glioblastoma.<sup>185,186</sup> The strong correlation between autophagy activation and tumor metastasis has since been well characterized and autophagy has been shown to play some role in every step of the metastatic cascade.<sup>187</sup>

### C. The dual role of autophagy in other diseases

Autophagy's role as the "housekeeper" of the cell makes it an indispensable part of the many mechanisms underlying other human diseases including infectious, immune and neurodegenerative.<sup>188</sup> Autophagy plays a direct role in mediating infection through elimination of invading microbes. Upon invasion of the cytosol by bacteria, sequestosome 1/p62-like receptors recognize and bind to microbe-specific molecular tags and physically recruit autophagic machinery leading to the sequestration of these microbes and their eventual degradation in lysosomes.<sup>189</sup> The Toll-like receptor pathway is responsible for activating the innate immune response through recognition of classes of molecules shared by many different pathogens allowing for their engulfment and clearance by macrophages. This process is called phagocytosis and the activation of Toll-like receptors has been shown to induce autophagy, which assists the maturation of phagosomes into autolysosomes through LC3-associated phagocytosis (LAP).<sup>190</sup> However, because autophagy can promote the uptake of extracellular material, it also serves as a potential route of infection by both bacteria and viruses. This can occur when autophagic flux, the normal maturation process where autophagosomes becoming autolysosomes, is interrupted by the invading pathogens, allowing for their uptake through vesicles and escape into the cytosol.<sup>191</sup> There is also evidence that individual pieces of the autophagy machinery are co-opted by viruses and used for early RNA replication, concealment and nonlytic release of virus from cells.<sup>192,193</sup>

Genome-wide association studies have exposed a link between autophagy and several autoimmune and inflammation disorders, such as ATG16L1's role in Crohn's disease,<sup>194</sup> or ATG5's link to systemic lupus erythematosus.<sup>195</sup> Further investigation of this link has begun to illuminate the regulatory role autophagy has in managing innate immunity and regulating the inflammasome.<sup>196</sup> While autophagy is important for the elimination of invading pathogens in a single cell and it is also crucial to modulating the innate immune response through the reprocessing of viruses and bacteria into major histocompatibility complex class II molecules that can be trafficked to the cell surface for presentation to CD-4+ T cells as antigens. Inhibition of autophagy has been shown to suppress immune response to Epstein-Barr virus with notable buildup of the Epstein-Barr virus nuclear antigen 1 in autophagosomes.<sup>197</sup> A similar effect was noted for the presentation of immunodominant mycobacterial antigen Ag85B in cells infected with wild-type or attenuated mycobacterium tuberculosis H37Rv where autophagy activation after vaccination improved immune response during reinfection.<sup>198</sup> Though basal autophagy is generally

required for the survival of many cell types it seems to be especially important for the survival and proper function of naïve T cells,<sup>199</sup> and the survival and renewal of B1 cells, which cannot be replenished from adult bone marrow.<sup>200</sup> Inflammation is triggered when the recognition of an agonist (endogenous or pathogenic) triggers the secretion of mature IL-1 $\beta$  and other interleukin protein.<sup>201</sup> This process is upregulated in autophagy-deficient cells,<sup>194,202</sup> and basal autophagy has been shown to be important for overall control of inflammasome response through the clearance of damage organelles, specifically mitochondria.<sup>203</sup> Autophagy inhibition leads to the accumulation of depolarized mitochondria which release mitochondrial DNA and ROS into the cytosol triggering NALP3- and RIG-I-like receptors-dependent production of IL-1 $\beta$  and IL-18.<sup>203,204</sup> Additionally, Rubicon, an autophagy protein involved in VPS34 Complex I, has been shown to suppress RIG-I-like receptor-dependent inflammation through its interaction with CADR9, a crucial component of the CMB signaling complex that regulates cytokine production.<sup>205</sup> In sum autophagy contributes to the regulation of innate immunity and inflammation through involvement in secretory pathways of antigens and interleukins, and the general maintenance of homeostasis in immune cells.

The expression and function of autophagy proteins, like Beclin 1, has been linked to the prevention of neurodegeneration and lifetime extension.<sup>206</sup> It has also been observed that there is significant buildup of autophagosomes in patients suffering from Alzheimer's, Parkinson's, and Huntington's disease though it is not clear if this due to autophagy activation or the disruption of autophagic flux.<sup>207-209</sup> Neuronal soma exhibit a basal levels of autophagy as synapses require a large amount of energy in addition to extensive protein remodeling in order to function correctly, and it has been shown that autophagy disruption leads to the accumulation of toxic protein aggregates.<sup>170</sup> Alzheimer's disease is characterized by progressive loss of neurons caused by formation of extracellular plaques made of amyloid-precursor protein and intracellular filaments made of tau-protein.<sup>210</sup> The inhibition of autophagic flux through the disruption of autophagosome-lysosome fusion has been linked to the formation of these protein aggregates and would explain the accumulation of autophagosome in AD cells.<sup>211,212</sup> In contrast, constitutive autophagy activation through the inhibition of mTOR in AD mouse models leads to the turnover of amyloid aggregates and the restoration of cognitive decline.<sup>213</sup> Parkinson's disease presents itself through motor dysfunction and bradykinesia caused by progressive loss of dopaminergic neurons and accumulation of Lewy bodies.<sup>214</sup> Mutant  $\alpha$ -synuclein aggregates are found within these Lewy bodies and thus this protein is implicated in the pathogenesis of this disease.<sup>215</sup> Wild-type  $\alpha$ -synuclein is typically degraded through CMA, while

the mutant acts as a uptake inhibitor for itself and other cargo leading to the accumulation and aggregation of damaged protein and compensatory activation of bulk autophagy.<sup>207</sup> Similarly to Alzheimer's disease, autophagy activation has led to clearance of synuclein aggregates,<sup>216</sup> but has also been found to lead to cell death.<sup>217</sup> Huntington's disease is an inherited autosomal dominant disease characterized by the accumulation of aggregates formed from abnormally long huntingtin protein containing a repeating polyQ domain due to an insertion mutation within the gene.<sup>218</sup> Mouse models have demonstrated that autophagy seems to be activated in mice with accumulating huntingtin, potentially as a compensatory response to the inability of the proteasomal system to properly clear these aggregates.<sup>219,220</sup> Additionally, the disruption of autophagy due to continued accumulation of huntingtin plays a role in disease progression and its reactivation can lead to the reversal of cognitive decline.<sup>220</sup> Recently, it has been found that the polyQ of wild-type huntingtin plays a role in protecting Beclin 1 from proteasomal degradation and the longer polyQ region of mutant huntingtin inhibits this interaction and suppresses starvation-activated autophagy.<sup>221</sup> In conclusion, basal and induced autophagy play a role in preventing the accumulation of toxic protein aggregates common in many neurological diseases, but due to its role in activating cell death sustained autophagy induction may also contribute to neurodegeneration.

#### **D. Autophagy modulators as cancer therapeutics**

As previously discussed, autophagy plays a role in tumor development, progression, drug resistance and metastasis. It remains unclear whether autophagy activation or autophagy inhibition is the most viable therapeutic strategy for cancer treatment and so significant development has been directed towards the discovery of both autophagy inhibitors and autophagy activators for use as probes and treatments. There now exist dozens of molecules that are known to perturb the autophagy pathway at multiple points (Figure 26).<sup>222</sup> Autophagy activators include a broad range of molecules with many of them having targets outside of the actual autophagy pathway because many pathways interlink with autophagy and because it serves a broad role in responding to stress or energy deprivation. Specific autophagy activators include molecules that inhibit the mTOR kinase, which negatively regulates autophagy, such as Rapamycin and Torin 1/2,<sup>223,224</sup> or activate the kinase AMPK, which negatively regulates mTOR, such as A-769662.<sup>225</sup> Other target downstream protein, such as the Beclin 1 targeting peptide Tat-Beclin, activates Beclin 1 and induces autophagic flux.<sup>226</sup> Meanwhile, autophagy inhibitors can be grouped into three broad categories. These include kinase inhibitors, protease inhibitors and lysosomotropic compounds. The

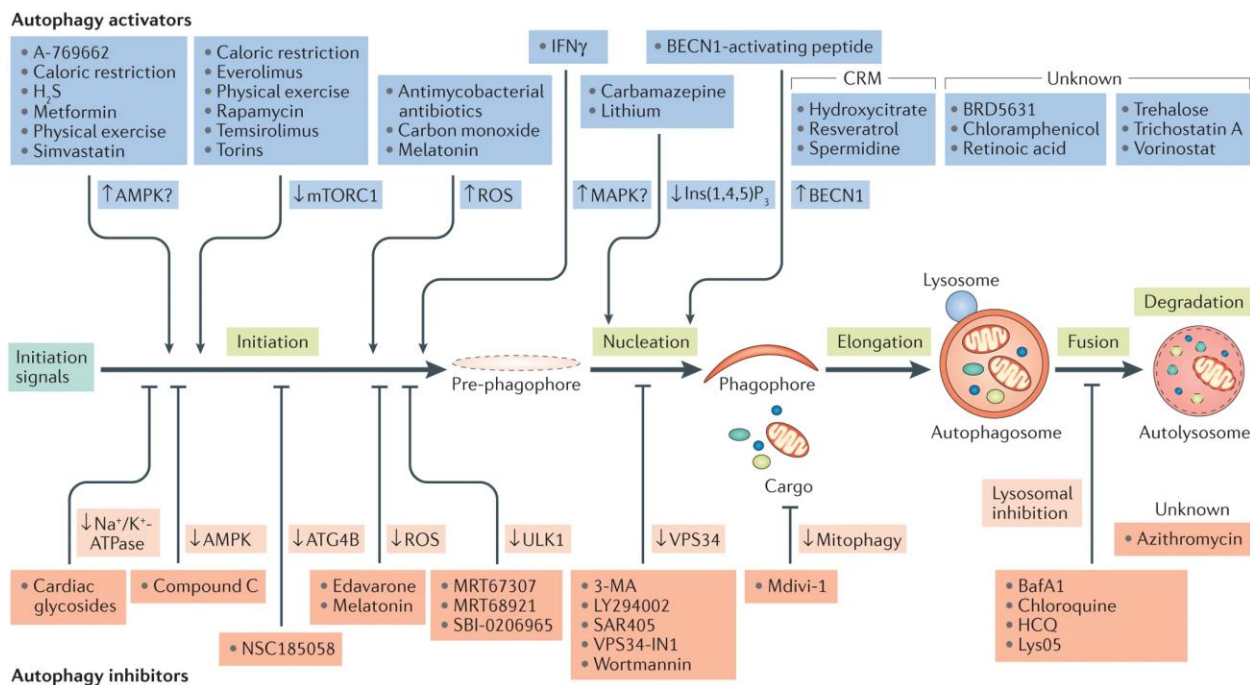


**Figure 26.** The various molecules that activate or inhibit autophagy and the relative position of their targets within the pathway.<sup>222</sup> Adapted from reference 222 with permission.

kinase inhibitors constitute possibly the largest class, as much of autophagy is regulated through the activity of various kinases. These include molecules that inhibit the kinase AMPK, such as compound C,<sup>227</sup> molecules that inhibit the kinase ULK1, such as SBI-0206965,<sup>228</sup> and molecules that target the various PI3 kinases, such as 3-methyladenine, wortmannin and PIK-III.<sup>229–231</sup> Autophagy also relies on proteases to process autophagy-specific protein into their mature form, such as LC3. Molecules in this class include the ATG4B inhibitor S130,<sup>232</sup> and lysosomal protease inhibitors Pepstatin A and E64d.<sup>233</sup> The last step in autophagy is the fusion of the autophagosome to the lysosome and the degradation of the autophagosomal cargo. This requires the proper functioning of the various protein involved in the fusion process along with maintenance of the acidic environment in the lysosome. Several molecules are known to perturb this step, including chloroquine (CQ), which localizes to

the lysosome and acts as a proton sponge,<sup>234</sup> Bafilomycin A1 (BafA1), which inhibits proton pump V-ATPase,<sup>235</sup> and EACC, which prevents the loading of Stx17,<sup>236</sup> a protein critical for fusion, onto the autophagosome.

Systemic inhibition of autophagy as a therapeutic strategy could have short-term and long-term side-effects that are detrimental to patients for several reasons. First, because autophagy is important for the survival, development and proper function of immune cells that are critical for tumor suppression, inhibition may lead to tumorigenesis and progression.<sup>237,238</sup> Second, inhibiting autophagy may hypothetically increase the risk of healthy tissues undergoing malignant transformation as well as increasing the rate of premature ageing.<sup>239</sup> Thus, autophagy activators have been viewed as the safer alternative for autophagy-based cancer therapies. However, clinical trials aimed at using autophagy inhibitors to treat cancer have been limited by their reliance on using molecules like CQ, which inhibits autophagy by increasing lysosomal pH and inhibiting late stage autophagy, and previous results have been mixed.<sup>240</sup> More recent studies have demonstrated that autophagy inhibition with CQ can improve the chemosensitivity of resistant cancers to MAPK pathway inhibitors, leading to a successful clinical outcome for this combination therapy and demonstrating that autophagy inhibition is viable if susceptible cancer types are identified.<sup>241,242</sup> However, any observed effect from CQ treatment may not be specific for autophagy and resultant cell death may be the outcome of off-target effects.<sup>243,244</sup> The lack of more specific autophagy inhibitors has made it difficult to discern which cell types are susceptible to autophagy inhibition and so it has remained a controversial target for therapy.<sup>245</sup> Therefore future progress in this area of research relies on the discovery of more specific autophagy inhibitors. These molecules will have fewer off-target effects and enable the selective evaluation of autophagy inhibition in human disease and establish the therapeutic potential of autophagy modulation in cancer.

#### **E. Targeting the VPS34 complex for the development of autophagy inhibitors**

As mentioned previously, the PI3 kinases have been an important target for the inhibition of autophagy as these kinases generate several lipids that serve as regulatory molecules within the pathway.<sup>246</sup> This class of enzymes all phosphorylate the 3-OH of inositol lipids and can be grouped into three classes based on their architecture and their substrates. While there are four class I and three class II PI3 kinases in mammalian cells, there is only one class III kinase, VPS34, which is evolutionarily conserved across all eukaryotes. VPS34 has one specific substrate, PI, which it phosphorylates to generate PI3P. The generation of PI3P is especially important during the biogenesis of new autophagosomes, as it has been observed to be necessary for the formation of the highly curved dual

membranes that characterize autophagosomes.<sup>247,248</sup> In addition, PI3P serves as an autophagy-specific biomarker and it is responsible for the recruitment of many protein critical to the formation of the phagophore that contain PI3P-binding domains.<sup>249</sup> Thus, VPS34 emerged as a particularly enticing target in inhibiting autophagy, due to its conserved role and because molecules like chloroquine or pan-PI3 kinase inhibitors lacked specificity. In the last five years several molecules that target this kinase with high potency and selectivity over other kinases have been identified such as SAR405, PIK-III, and VPS34-IN1.<sup>231,250,251</sup>

Mammalian VPS34 is characterized by three domains: a N-terminal C2 domain, a helical domain, and a C-terminal kinase domain which also fulfills a self-regulating role.<sup>252</sup> It forms two distinct hetero-tetrameric complexes: the autophagy initiation complex (Complex I) which is made up of VPS15, VPS34, ATG14L and Beclin 1, and the endosomal trafficking complex (Complex II) which is made up of VSP15, VPS34, UVRAG and Beclin 1. X-ray crystallography along with Cryo-EM of both the mammalian and the yeast complexes have established that they both adopt a similar Y-shaped architecture with the C-termini of each subunit being important for membrane binding (Figure 27A,B).<sup>253,254</sup> The difference in only one subunit between the two complexes controls the overall localization and thus the activity of the VPS34 kinase. Though the direct mechanism that controls the activity of the two complexes in different compartments has not been established in mammals research has demonstrated that yeast Complex I had preferential activity on highly curved membranes such as those present at the phagophore.<sup>253</sup> Under normal conditions free cytosolic VPS34 has been shown to be inactive and gains moderate activity upon forming a dimer with VPS15 through the association of their helical domains.<sup>255</sup> Beclin 1 serves as the critical regulatory component of both complexes as it can competitively associate with multiple targets including itself, Bcl-2, UVRAG or ATG14L.<sup>256,257</sup> It has been established that it has a stronger affinity for Bcl-2 and UVRAG over ATG14L, making Beclin 1-Bcl-2 and Complex II the dominant Beclin 1 complexes, which helps maintain the low levels of autophagy observed under basal conditions.<sup>257</sup> Knocking down either VPS34 or Beclin 1 in model organisms has been shown to abolish the formation of autophagosomes under starvation, demonstrating the viability of targeting this kinase for autophagy inhibition.<sup>258</sup> However, because VPS34 is present into both Complex I and Complex II, direct kinase inhibition results in undesirable side effects within the endolysosomal pathway.<sup>250,259</sup>

During autophagy activation, the recruitment of the VPS34-VPS15 dimer to the ER, where the phagophore is thought to form, is mediated by the C-terminal domain of ATG14L.<sup>260</sup> Deletion studies have also established that

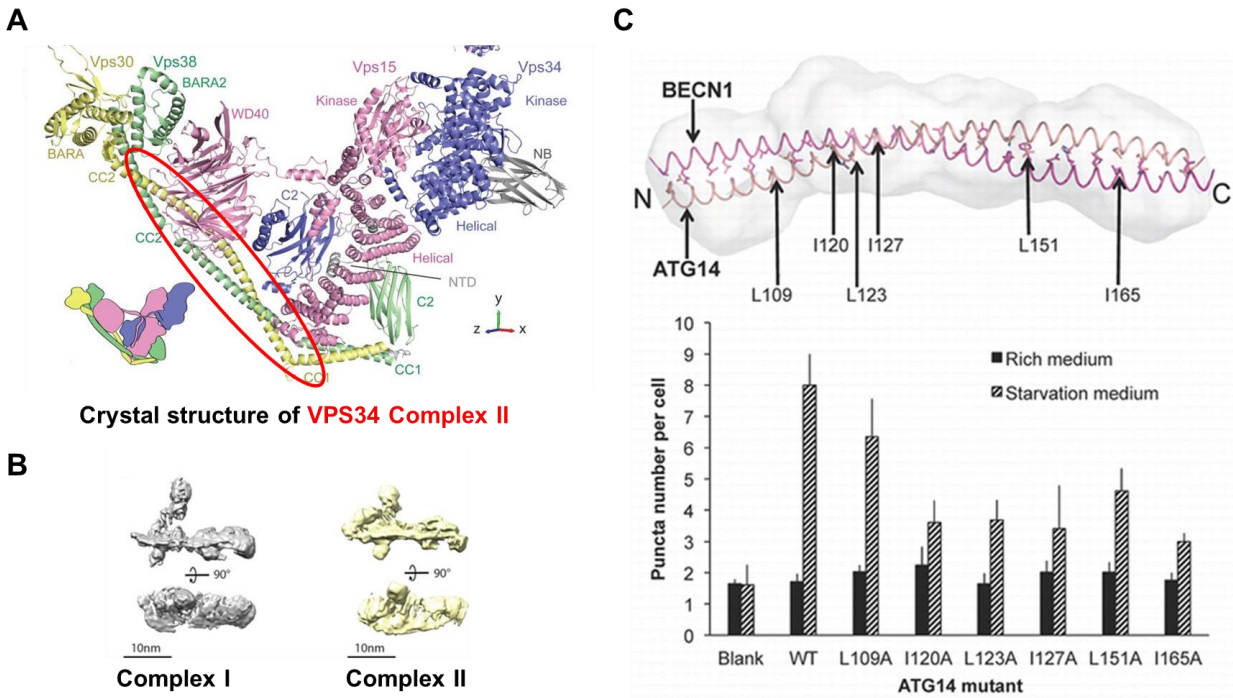


**Figure 27.** Structural characterization of the VPS34 complexes. (A) Crystal structure of VPS34 Complex II in yeast, establishes the association of Vps38 (UVRAG yeast ortholog) and Vps30 (Beclin 1 yeast ortholog) through a CCD.<sup>253</sup> (B) Cryo-EM of the mammalian VPS34 Complexes establishes that they have similar architecture allowing for inferences to be made about the structure of VPS34 Complex I from the crystal structure of Complex II.<sup>261</sup> (C) Crystal structure of the interacting CCD of Beclin 1 and ATG14L and the residues that were identified to be critical for starvation induced autophagy.<sup>262</sup> Adapted from references 253, 261 and 262 with permission.

this recruitment is dependent on the ability of ATG14L to bind associate with Beclin 1 through the parallel interaction of their a coiled-coil domains (CCD) (Figure 27C).<sup>260,263</sup> ATG14L has three distinct regions within its CCD that are responsible for the association and stabilization of Complex I as demonstrated through pull-down experiments.<sup>260</sup> Furthermore, research has shown that mutation of critical leucine and isoleucine residues within this region in either Beclin 1 or ATG14L inhibits starvation induced autophagy.<sup>262</sup> Beclin 1 associates with UVRAG in a similar way and direct comparison between the two dimers using X-ray crystallography and isothermal calorimetry has demonstrated that UVRAG has an almost ten-fold higher affinity for Beclin 1 over ATG14L.<sup>264,265</sup> Therefore, we hypothesized that small molecules that disrupt the PPI between Complex I members Beclin 1 and ATG14L, but not the interaction between Beclin 1 and UVRAG, will inhibit autophagy without impacting the vesicle trafficking

role of VPS34 (Figure 28). These molecules will be critical for understanding if autophagy inhibition is therapeutically valuable in the treatment of cancer. In addition, these molecules can be used as probes in the further elucidation of poorly understood mechanisms related to VPS34. For instance, they will allow for the spatiotemporal control of Complex I activity and serve as useful tools for the study of PI3P signaling.<sup>266</sup> Alternatively, because the disruption of this PPI will maintain both Beclin 1 and ATG14L in their endogenous state, it will also be possible to understand the activity of these proteins outside of autophagy as well as better understand how Beclin 1-independent autophagy occurs.<sup>267,268</sup>

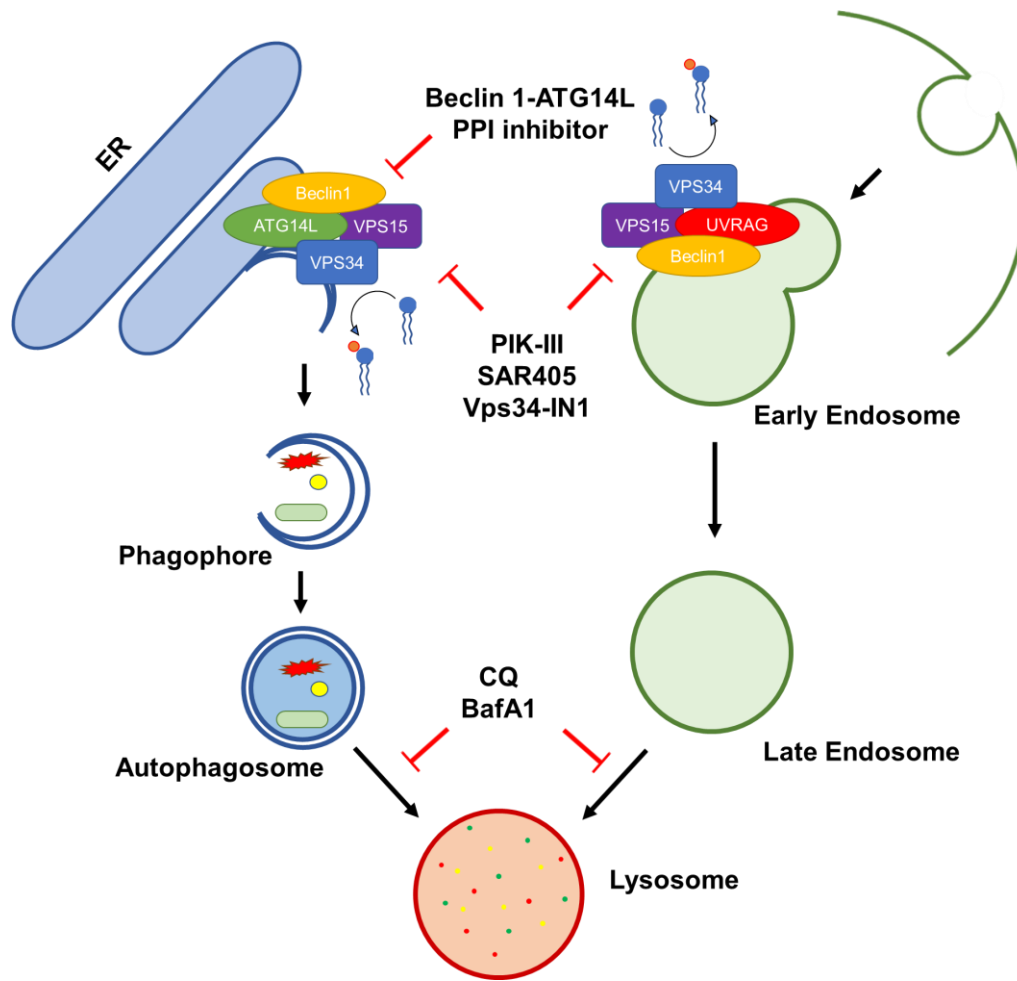


**Figure 28.** Lack of specificity limits the utility of the current generation of autophagy probes. VPS34 is involved in two distinct complexes, the autophagy initiation complex (VPS15-VPS34-ATG14L-Beclin 1) and the endosomal trafficking complex (VPS15-VPS34-UVRAG-Beclin 1). Both complexes direct the localization of VPS34, which is responsible for the phosphorylation of PI into PI3P. PI3P is required for the formation of the both the early autophagosome and the early endosome and so direct VPS34 inhibitors inhibit both autophagy and endocytotic trafficking.<sup>231,250,251</sup> Lysosomotropic agents, CQ, and BafA1, also inhibit both pathways as they disrupt vesicle fusion between the lysosome and other vesicles.<sup>234,235</sup>

## **F. Targeting the ATG5-ATG12-ATG16L1 complex for the development of autophagy inhibitors**

A key step in autophagy initiation is the lipidation of LC3-I with PE, transforming it into LC3-II and allowing it to localize to the growing phagophore where it can recruit cargo and promote the elongation of the isolation membrane.<sup>153</sup> The lipidation cascade relies on the activity of several autophagy proteins and culminates with the transfer of LC3-I from ATG3 to the PE found on the membrane of the autophagosome.<sup>149</sup> The ATG12-ATG5-ATG16L1 complex is thought to mediate the lipidation reaction by recruiting the ATG3-LC3-I conjugate to the phagophore and through the facilitation of the transfer reaction to PE.<sup>151</sup> Though the underlying mechanisms of the function of this complex in autophagy is unclear, this transfer reaction is thought to occur through a ubiquitin-like conjugation mechanism.<sup>269</sup> It has also been observed that the membrane association of ATG5-ATG16L1 induces the formation of giant vesicles and that the disruption of the formation of this complex inhibits the biogenesis of autophagosomes more than blocking the lipidation of LC3.<sup>270</sup> Through these two functions, the ATG5-ATG12-ATG16L1 complex regulates the location at which new autophagosomes are formed.<sup>151</sup> In addition, this complex also plays a role in autophagosome maturation, which is mediated by the binding of ATG5-ATG12 to the AIR domain of the lysosomal protein TECPR1,<sup>271</sup> freeing its PH domain and allowing it to bind PI3P and facilitate the fusion of the late autophagosome and lysosome. Lastly, the absence of ATG5 has been shown to be lethal in mice embryos undergoing starvation as well as leading to toxic protein aggregates in models of neural disease,<sup>272</sup> and the reduction of ATG5 protein level impairs the formation of autophagosomes,<sup>273</sup> indicating its overall importance for the proper functioning of autophagy.

While free ATG5 has been shown to have membrane binding properties, it is thought to undergo immediate conjugation to ATG12 in the cytosol, which inhibits its membrane binding activity.<sup>270</sup> Under autophagy activation, the N-terminal helical domain of ATG16L1 binds to ATG5 restoring its membrane binding ability which then allows the entire complex to translocate to the growing phagophore.<sup>270</sup> Though purifying the functional and endogenous hexameric complex has been challenging, the crystal structure of the trimeric ATG5-ATG12-ATG16L1 complex has been characterized by X-Ray crystallography.<sup>274</sup> These structures along with other studies have helped identify the critical minimal interface of ATG16L1 that is required for binding to ATG5, which is 33 amino acids in length (Figure 29).<sup>152,275</sup> Binding hotspots have also been identified within this region and at least one virtual screen has identified small molecules that disrupt this interaction and potentially inhibit autophagy, though with moderate

potency.<sup>276</sup> This established this interaction as a feasible target for the discovery of a PPI-based autophagy inhibitor. Molecules that can disrupt this interaction without altering the endogenous state of these protein will allow for the further characterization of the membrane protein during autophagy and other cellular processes and diseases. As mentioned previously, ATG5 particularly has been shown to have various other autophagy-dependent and independent activities within adaptive and innate immunity.<sup>277</sup> The specific disruption of the interaction between ATG5-ATG16L1 will allow for the more accurate annotation of these functions as truly autophagy-independent.

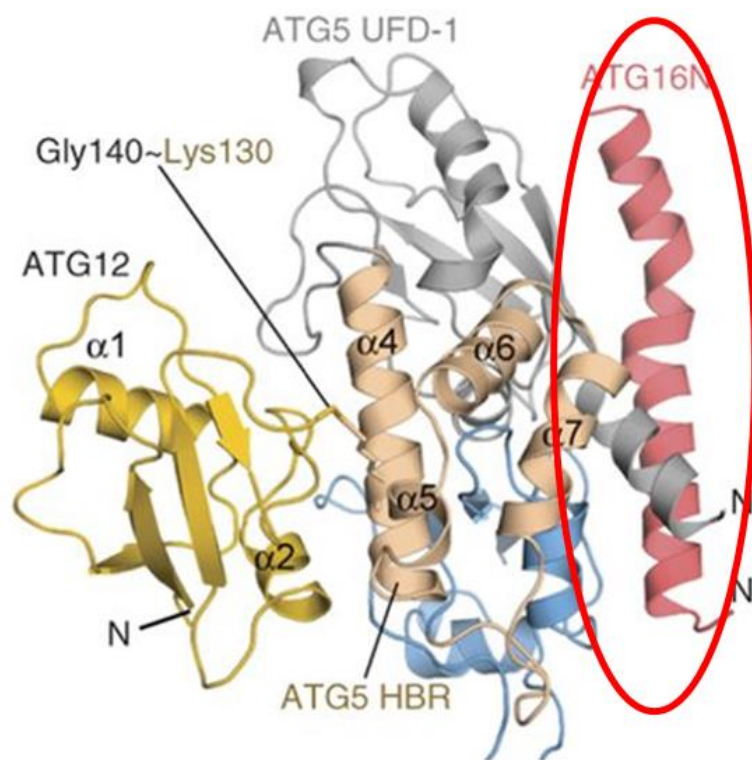


**Figure 29.** The crystal structure of the ATG5-ATG12 conjugate associated with the N-terminal domain of ATG16L1 (ATG16N).<sup>152</sup> Adapted from reference 152 with permission.

### **G. Feasibility of targeting PPIs for small molecule probe development**

PPIs represent a vast set of untapped therapeutic targets that have several advantages over traditional substrate-based enzyme inhibitors which suffer from the lack of selectivity.<sup>278</sup> As demonstrated in the previous sections, the development of autophagy-specific inhibitors has been limited by the over reliance on perturbing traditional targets, such as kinases. Traditionally, PPIs have been viewed as undruggable targets because high-resolution structures of PPI interfaces showed them to be flat and large, in contrast to the typically cave-like targets of most small molecules.<sup>278</sup> Additionally, stereochemically and structurally complex molecules that could effectively bind to these interfaces often possessed poor pharmacokinetic properties for development into lead molecules.<sup>278</sup> However, in recent years, more drug-like molecules have emerged that can effectively disrupt PPIs, allowing for the elucidation of the types of interfaces that are most susceptible to inhibition. In particular, structural studies have shown that targeting interfaces that involve key secondary structural features, such as an  $\alpha$ -helix or CCD, has been successful for the development of BCL-2 and MDM2 inhibitors.<sup>279,280</sup> Computational studies of these types of interfaces have also revealed that many may be particularly tractable for small molecules, as their “hot spot” residues, which are the residues most critical to their interaction, tend to be clustered together on a single helical face (Figure 30).<sup>281,282</sup> Therefore inhibiting autophagy by targeting PPIs is theoretically feasible as two critical interactions within the autophagy pathway, the Beclin 1-ATG14L interaction and the ATG5-ATG16L1 interaction, occur through a CCD and an  $\alpha$ -helical domain, respectively. In addition, it may be unnecessary to target PPI interfaces directly, as small molecules that bind to a protein at a cryptic allosteric site can significantly deform its overall structure, preventing it from associating with some or all of the protein in its interactome as is the case with the molecules developed to target p97.<sup>283,284</sup> Finally, previously successful molecules can serve as templates, allowing the design of small molecule libraries that contain the chemical features most likely to produce hits.<sup>285</sup>

Many methods have been utilized for the discovery of PPI modulators, including computational, fragment-based, and peptidomimetic.<sup>286</sup> Computational methods have seen extensive use in the prediction of “hot-spot” residues that can inform structure-based approaches such as those used in fragment-based screens or in the design of potent synthetic peptides that mimic the binding interface.<sup>287</sup> Fragment-based screening usually involves the use of NRM or X-ray crystallography in order to detect where small molecule fragments, which are less than 300 Å in size, bind to an isolated protein target.<sup>288</sup> Because fragments usually lack the structural complexity that may

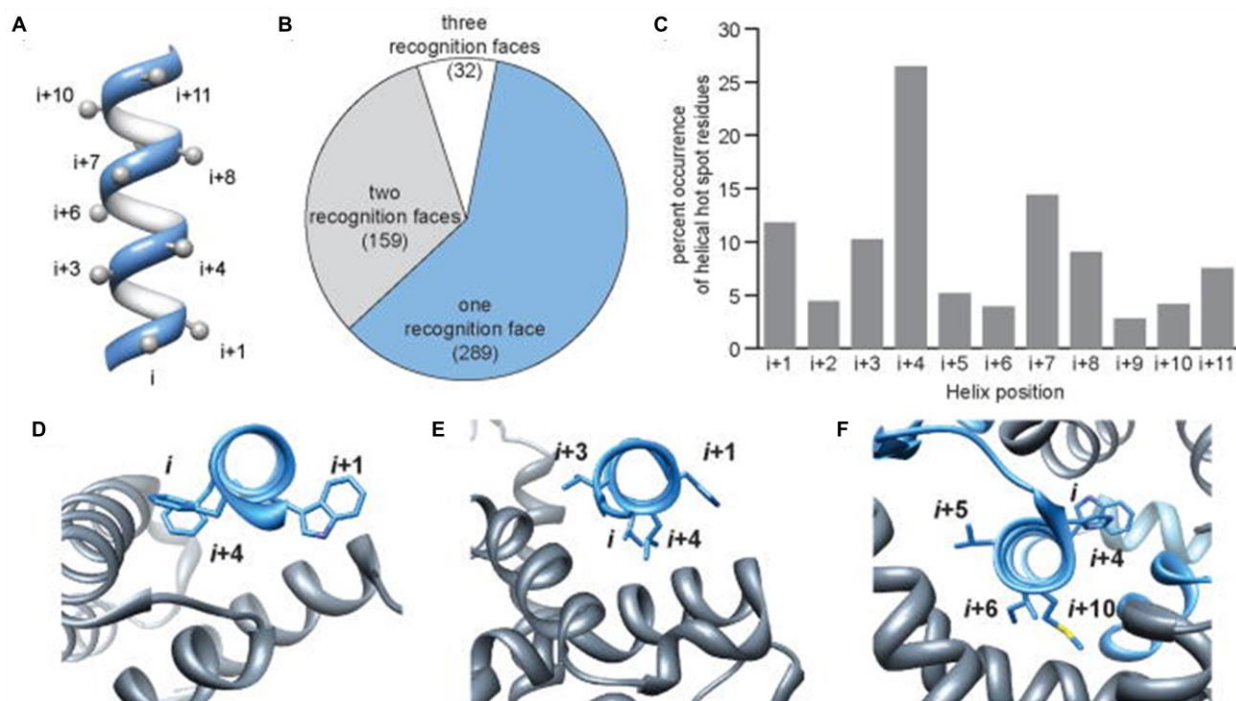


**Figure 30.** Energetic contributions of residues on different faces of interfacial helices. (A) Positioning of side chain residues on a canonical  $\alpha$ -helix, (B) percent occurrence of hot spot residues on one, two or three helical faces (total number helices in each category shown in parentheses), (C) percent occurrence of hot spot residues as a function of helix position, (D-F) examples of protein complexes with hot spot residues on one face, two faces and three faces (PDB codes: 1x13, 1xiu, and 1or7).<sup>281</sup> Reprinted with permission from Bullock, B. N.; Jochim, A. L.; Arora, P. S. Assessing Helical Protein Interfaces for Inhibitor Design. *J. Am. Chem. Soc.* **2011**, *133* (36), 14220–14223. Copyright 2011 American Chemical Society.

prohibit their interaction, they are useful in detecting electrostatic interactions that can drive binding. Multiple fragments that bind near each other can then be linked using synthetic methods to produce a complex potent binder that maximizes these electrostatic interactions while minimizing entropy and steric hindrance.<sup>289</sup> Several PPI modulators produced in this way have made it into the clinic, such as the previously mentioned Bcl-2 inhibitors.<sup>30</sup> Alternatively, structural data can be used to design synthetic peptides or peptidomimetics that effectively mimic the interface most critical to the PPI of interest.<sup>290</sup> Though such molecules are often plagued by stability issues, inability to penetrate cells and poor selectivity, recent developments using stapling have begun to produce high affinity probes that are stable and inherently cell penetrating.<sup>291,292</sup> However, all these approaches rely on access to high-

resolution structural information to guide screening efforts. In the absence of such information, identification of small-molecule hits can be achieved through a HTS based on the detection of PPI disruption.<sup>293</sup>

Multiple methods exist for the detection of PPIs in high throughput. Methods like ELISA, FP, Förster resonance energy transfer (FRET) and Alpha Screen work against isolated protein targets which can be purified directly from mammalian cell lysates or through large-scale protein expression using bacteria, yeast, or insect cells.<sup>294</sup> FP, which detects the change in the polarization of light that can occur when a small ligand binds to its larger substrate, works especially well against targets that interact through a relatively small and well characterized secondary structure, such as an  $\alpha$ -helix.<sup>295,296</sup> Thus, it is the ideal basis for the design of an HTS targeting the ATG5-ATG16L1 interaction, as this occurs through the association of the N-terminal domain of ATG16L1.<sup>152</sup> This interaction, which has been characterized to be about 33 amino acids in length,<sup>152</sup> is theoretically small enough that there will be a noticeable change in FP upon its binding to ATG5. Alternatively, molecules can be screened for activity against PPIs directly in cells, which can be especially useful when isolated targets are not stable. Methods that can effectively measure PPI dynamics in live cells rely on the energy transfer that can occur between molecules in close proximity, such as FRET or bioluminescence resonance energy transfer (BRET),<sup>297</sup> or on complementation assays that generate active fluorescent or bioluminescent proteins, such as GFP.<sup>298,299</sup> Both BRET and FRET allow for the effective measurement of molecular proximity within live cells, because energy transfer between an acceptor and donor fluorophore only occurs over a very short distance (<10 nm).<sup>300</sup> Meanwhile, complementation assays rely on the reconstitution of a split reporter protein, such as GFP, which will only become active when the two protein targets that are fused with its fragments interact. However, because the association of many reporter proteins is irreversible, this assay can increase the potency of the interaction of interest, greatly limiting its application in screens for inhibitors.<sup>299</sup> Lastly, in contrast to FRET, BRET utilizes a luminescent donor to excite the acceptor fluorophore. This bypasses one of the biggest limitations of FRET: high background noise due to autofluorescence from laser-based excitation, which limits its application in the characterization of PPIs within cellular systems and makes it the ideal assay for the perturbation of the Beclin 1-ATG14L interaction.<sup>301</sup>

## **II. Methodology**

### **A. Design and development of NanoBRET assays targeting the Beclin 1-ATG14L and the Beclin 1-UVRAG interactions**

Since its first development almost 20 years ago, the BRET technique has grown to encompass several methods, each with its own combination of bioluminescent donor and acceptor fluorophore. The original version is now called BRET1 and uses Renilla luciferase (Rluc), which has a maximal emission at 480 nm, as the donor and yellow fluorescent protein (YFP), which has a maximal emission at 530 nm, as the acceptor.<sup>302</sup> Further refinement of this original method has led to the development of BRET2 and BRET3, which attempt to overcome one of the major limitation of the original method, the small spectral separation, through the use of other bioluminescent protein or substrates.<sup>303,304</sup> However, these methods have their own limitation in the form of very low signal from the donor, necessitating its overexpression relative to the acceptor impairing the specificity of the observed signal as well as reducing the overall dynamic range of the assay. Thus, out of the available BRET methods, the NanoBRET assay is particularly robust because it utilizes an extremely bright narrow-spectrum luciferase (NanoLuc) as a donor for an efficient long-wavelength fluorophore (HaloTag 618 ligand), providing it a larger spectral separation (158 nm) than any other BRET assay while maintaining overall signal strength (Figure 31). This makes it an ideal choice for an HTS because it is sensitive enough to evaluate the modulation of PPIs by compound treatment.<sup>305</sup>

The efficiency of resonance energy transfer depends on the alignment of the dipoles of the donor and acceptor tags. Because the optimal orientation for both tags is not already known from previous research, it must be determined by altering the position and type of donor our two protein of interest, Beclin 1 and ATG14L, are fused to. To accomplish this, eight pairs of fusion proteins were evaluated by cloning each gene into four vectors that would produce either N- or C-terminally labeled fusion proteins (Figure 32). The creation of these eight vectors was accomplished using Promega's Flexi Vector system.<sup>306</sup> This system is able to rapidly transfer cloned and sequence-verified genes between different vectors. It is a ligation-dependent method that is facilitated by the replacement of a toxic insert, which expresses the barnase protein, in each acceptor vector with the gene of interest. This effectively eliminates the background of colonies produced from undigested acceptor vectors, as those that remain intact, but do not contain the gene of interest, will kill the *E. coli* cells they are transformed into. In addition, the AsiSI and PmeI restriction sites used for cloning were selected due to the rarity with which their sequence was observed within the

human genome and their combination in the Flexi Vector system allows cloning of 98.9% of all human genes, including Beclin 1 and ATG14L.

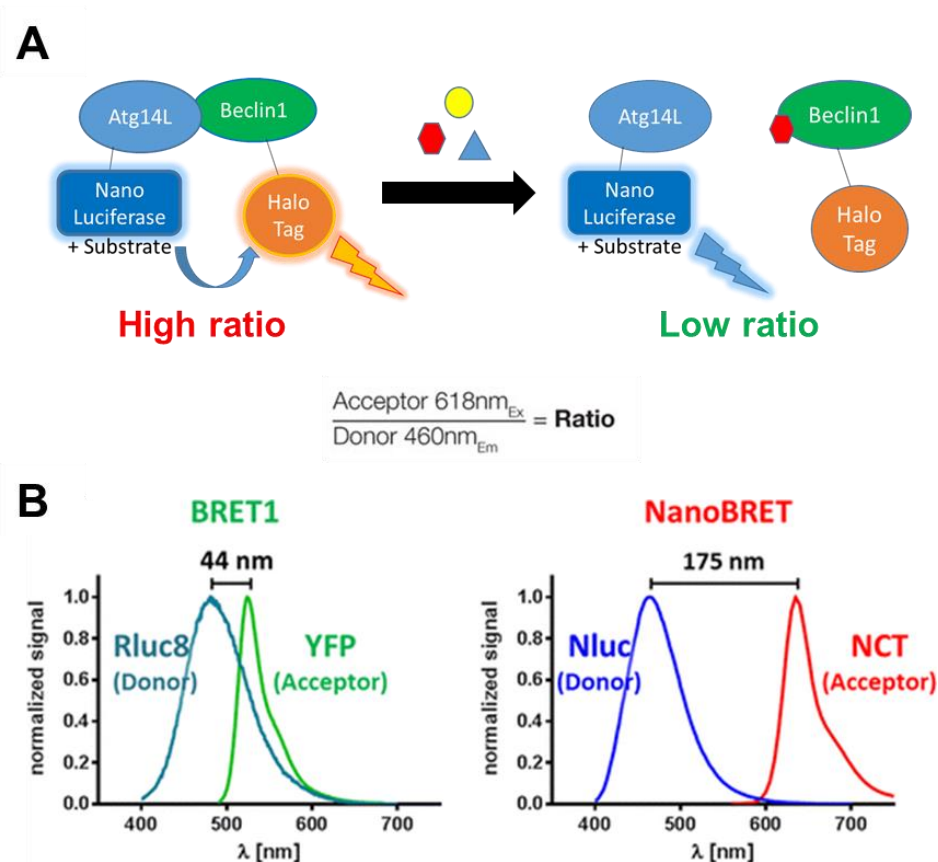


**Figure 31.** The NanoBRET method and its advantages. (A) NanoBRET relies on the energy transfer that occurs between the bioluminescent NanoLuc donor and the acceptor ligand bound the HaloTag, for instance when two proteins interact, this leads to a high BRET ratio, which is the ratio of the observed acceptor to donor signal. (B) NanoBRET has a larger spectra separation than other alternatives such as BRET1, leading to enhanced dynamic range and higher signal-to-noise due to the reduced amount of bleed-through signal from the donor.<sup>305</sup> (B) was reprinted with permission from Machleidt, T.; Woodrooffe, C. C.; Schwinn, M. K.; Méndez, J.; Robers, M. B.; Zimmerman, K.; Otto, P.; Daniels, D. L.; Kirkland, T. A.; Wood, K. V. NanoBRET—A Novel BRET Platform for the Analysis of Protein–Protein Interactions. *ACS Chem. Biol.* **2015**, *10* (8), 1797–1804. Copyright 2015 American Chemical Society.

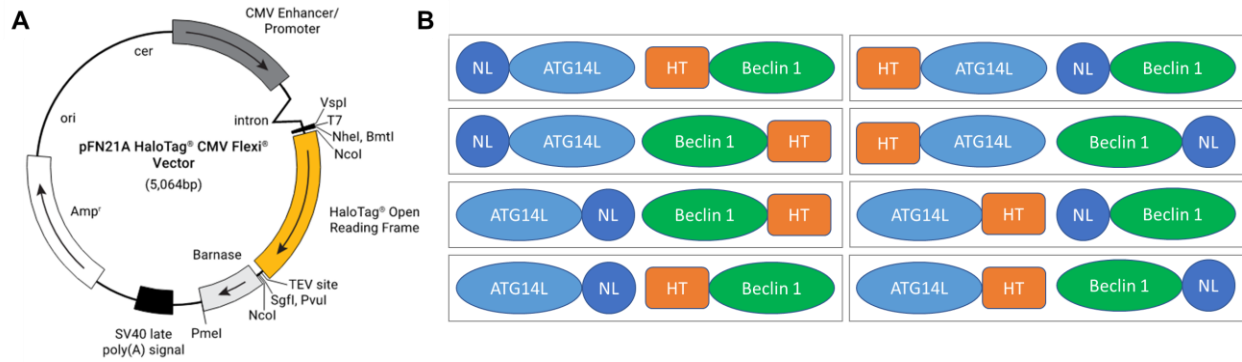


**Figure 32.** Creation of the NanoBRET vectors. (A) Plasmid map for the N-terminal HaloTag vector used as the vector for initial cloning. (B) The eight pairs generated to optimize tag placement.

All genes (ATG14L, Beclin 1 and UVRAG) were first cloned into the N-terminal HaloTag vector (pFN21A) using standard cloning techniques. Table 4 and Table 5 contain the information related to the Flexi vectors used, their names, and the sequence of the primers used for each gene. In brief, each gene was first amplified by polymerase chain reaction (PCR) to add restriction digestion sites for AsiSI and PmeI, gel purified and then restriction digested alongside the acceptor vector. For each gene the PCR reaction was performed using Phusion polymerase and the following general protocol: 98°C for 30 sec, (98°C for 10 sec, 67-72°C for 30 sec, 72°C for 1 min) x 35, 72°C for 5 minutes using the Biorad T100 thermal cycler, and gel purified. Inserts and vector were then annealed and ligated using T4 DNA ligase. *E. coli* (DH5 $\alpha$ ) were then transformed with ligated vector and plated on plates containing 100  $\mu$ g/mL ampicillin and grown overnight at 37 °C. Single colonies were picked, grown overnight and plasmids were isolated using a PureLink Quick Plasmid Miniprep Kit (Thermo, #K210011). Cloning was confirmed by sequencing using the HT7F and Flexi R primers. Generation of the remaining vectors was achieved by transferring the inserted gene from the pFN21A plasmid using restriction digestion. In brief, the donor vector (pFN21A) containing each gene was digested with PmeI and AsiSI alongside an acceptor vector. PmeI and AsiSI were used for N-terminally tagged acceptor vectors and AsiSI and Eco53kI were used for C-terminally tagged acceptor vectors. The digestion reactions were then heat inactivated, mixed, and ligated with DNA ligase. *E. coli* (DH5 $\alpha$ ) cells were then transformed with ligated vector and plated on plates containing 25  $\mu$ g/mL of kanamycin. Single colonies were picked, grown overnight and plasmids were isolated using a DNA purification kit.

Vector Name	Acceptor Vector	Expressed Protein
ANL	pFN31K	NanoLuc-ATG14L
ACL	pFC32K	ATG14L-NanoLuc
ANH	pFN21A	HaloTag-ATG14L
ACH	pFC14K	ATG14L-HaloTag
BNL	pFN31K	NanoLuc-Beclin1
BCL	pFC32K	Beclin1-NanoLuc
BNH	pFN21A	HaloTag-Beclin1
BCH	pFC14K	Beclin1-HaloTag
UNL	pFN31K	NanoLuc-UVRAG
UCL	pFC32K	UVRAG-NanoLuc
UNH	pFN21A	HaloTag-UVRAG
UCH	pFC14K	UVRAG-HaloTag
ACLΔCC	ACL	ATG14L-NanoLuc w/ no CCD
BCHΔCC	BCH	Beclin1-HaloTag w/ no CCD

**Table 4.** Vectors generated for NanoBRET experiments.

Primer Name	Sequence
ATG14L F	5'-TTACGCGATCGCCATGGCGTCTCCCAGTGGGAAG-3'
ATG14L R	5'-CGAGGTTTAAACACGGTGTCCAGTGTAAGCTTTAAACCA-3'
Beclin1 F	5'-TCAGGCGATCGCCATGGAAGGGTCTAAGACGTCCAACAACAG-3'
Beclin1 R	5'-CGCGGTTTAAACTTTGTTATAAAATTGTGAGGACACCCAAGCA-3'
UVRAG F	5'-ATTGGCGATCGCCATGAGCGCCTCCGCGTCGGT-3'
UVRAG R	5'-GATTGTTTAAACCTTATCGGAACTCCTGCGCGGC-3'
ATG14LΔCC F	5'-GACTTAAGAAGTCATTATGAGCGTCTG-3'
ATG14LΔCC R	5'-GCGGCCGTGCGAAGTAGAC-3'
Beclin1ΔCC F	5'-AATGCAACCTTCCACATC-3'
Beclin2ΔCC R	5'-TGTGCATTCCACAGAG-3'
HT7 F	5'-ACATCGGCCCGGGTCTGAATC-3'
Flexi R	5'-CTTCCTTTCGGGCTTTGTTAG-3'
Chime F	5'-CTTACTGACATCCACTTTGCCTTTCTCT-3'

**Table 5.** Primers and their sequences.

Beclin 1 and ATG14L pairs were then evaluated based on the BRET ratio they were able to produce. The BRET ratio is calculated based on the formula below:

$$BRET\ Ratio = \frac{PC\ Acceptor\ Signal}{PC\ Donor\ Signal} - \frac{NC\ Acceptor\ Signal}{NC\ Donor\ Signal}$$

For the evaluation, Hek293T cells were plated at a density of  $1.2 \times 10^6$  cells/well in 6 well plates in DMEM, incubated for 4 h and then transfected with 1:10 ratio of NanoLuc donor and HaloTag acceptor vectors (2.2  $\mu$ g total) using a 1:2.5 ratio of Lipofectamine 2000. Cells were grown for an additional 20 h and then replated into 96 well white plates at a density of  $2.2 \times 10^4$  cells/well in Opti-MEM with addition of HaloTag 618 ligand to all wells (PC) except for negative controls (NC). Hek293T cells were grown for an additional 24 h after which NanoLuc substrate was added and plates were incubated for 5 minutes at room temperature. Plates were then measured with a Spectramax i3x plate reader (Molecular Devices) using the monochromator set to measure at 450 nm (acceptor signal) and 625 nm (donor signal) for 1000 ms. BRET ratios were then calculated based on raw data using Microsoft Excel.

#### **B. Validation of NanoBRET assay targeting the Beclin 1-ATG14L interaction**

The first experiment we used to validate the specificity of the observed BRET ratio is called a donor saturation assay (DSA) and is typically used to validate BRET assays.<sup>307</sup> In this assay a fixed amount of donor vector (ACL) is transfected with increasing amounts of acceptor vector (BCH). It is possible that BRET may occur nonspecifically due to the random proximity of donor and acceptor which might occur at high concentrations. Such nonspecific BRET would increase linearly with increasing amounts of acceptor molecule. In contrast, a specific interaction would reach a signal plateau beyond which increasing amounts of acceptor protein would not increase the signal because all binding sites on the donor were saturated (Figure 33).<sup>308</sup> For the DSA, Hek293T cells were plated at a density of  $1.2 \times 10^6$  cells/well in 6 well plates in DMEM, incubated for 4 h and then each well was transfected with a fixed amount of NanoLuc donor vector (1  $\mu$ g, ACL) and increasing amounts of HaloTag acceptor vector (0.01, 0.02, 0.1, 0.3, 1  $\mu$ g, BCH) using a 1:2.5 ratio of Lipofectamine 2000. Cells were grown for an additional 20 h and then replated into 96 well white plates at a density of 22,000 cells/well in Opti-MEM with addition of HaloTag ligand to all wells except for negative controls. Hek293T cells were grown for 24 h after which NanoLuc substrate was added and plates were incubated for 5 minutes at room temperature. Plates were then

measured with a Spectramax i3x plate reader using the monochromator set to measure at 450 nm and 625 nm for 1000 ms.

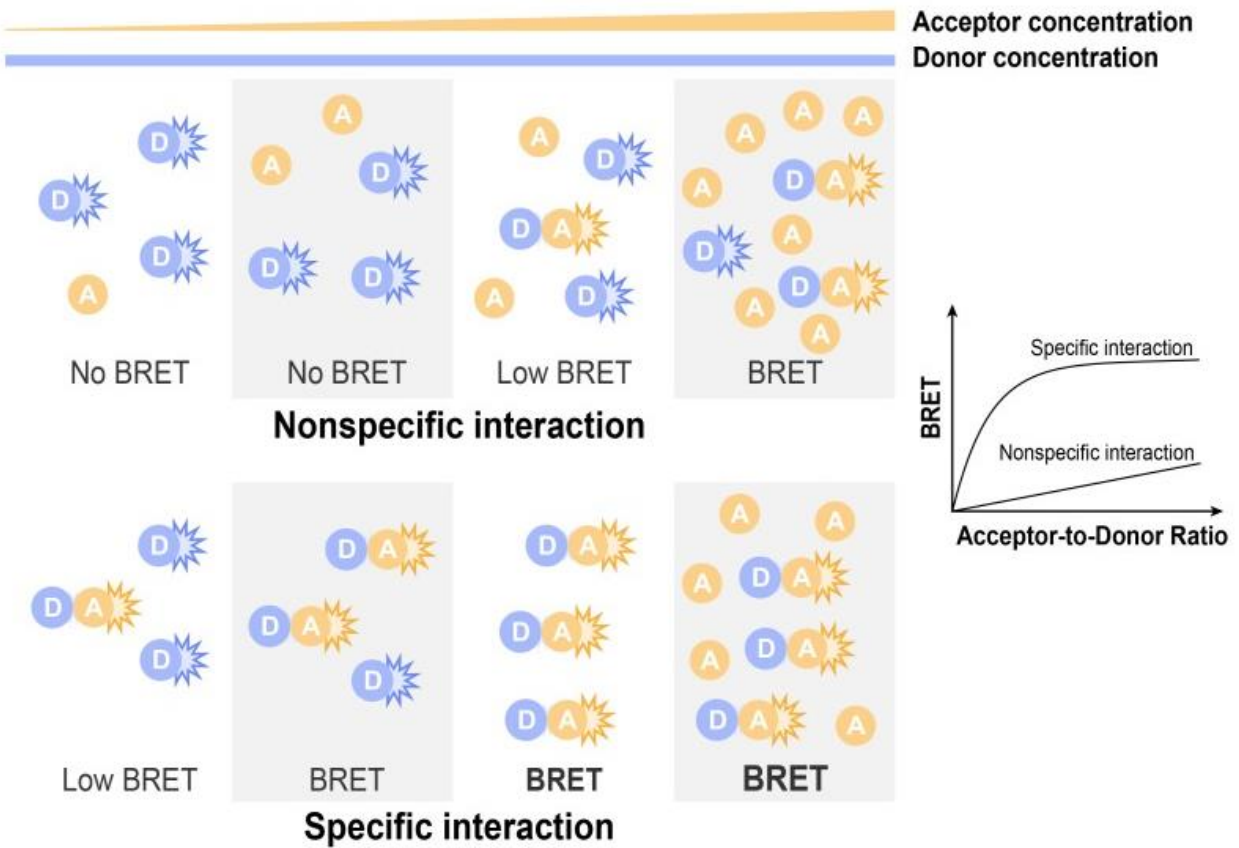


**Figure 33.** The donor saturation assay (DSA). This assay is used to confirm the specificity of the BRET signal. At high concentration of acceptor fluorophore nonspecific BRET signal is possible and would increase linearly with the acceptor concentration. If the BRET signal is specific, then the donor would quickly become saturated with the acceptor fluorophore and thus the signal would plateau, exhibiting a hyperbolic dependence. Reprinted with permission from E. Lilly, Assay Guidance Manual. 1338.

Previous studies have shown that ATG14L associates with Beclin 1 through the binding of their CCDs and that deletion of this domain abolished this interaction;<sup>262</sup> therefore, for our second validation experiment, we produced coiled-coil deletion mutant ( $\Delta$ CC) versions of both proteins in our original pair.  $\Delta$ CC mutants were generated using PCR-mediated deletion.<sup>309</sup> This method reproduces the entire plasmid of interest with PCR using a set of two primers that flank the region that is to be deleted. After the reaction is finished the template plasmid is digested using DpnI. DpnI is a restriction digestion enzyme that cleaves the sequence GA|TC, but only if the adenosine has been methylated.<sup>310</sup> This methylation only occurs to a plasmid directly isolated from *E. coli*, thus selectively digesting only the template plasmid and not the PCR product. The ACL and BCH vectors (Table 4) were PCR amplified using primers (Table 5) that would remove the CCD of ATG14L (residues 71-180) and Beclin 1 (residues 142- 270). Reactions were then digested with DpnI overnight, treated with T4 DNA kinase, ligated with DNA ligase and transformed into *E. coli* (D5H $\alpha$ ) cells. Single colonies were picked, grown overnight and plasmids were isolated using a DNA purification kit. Deletions were confirmed by sequencing with Chime F.

To test the effect of CCD deletion, Hek293T cells were plated at a density of  $1.2 \times 10^6$  cells/well in 6 well plates in DMEM, incubated for 4 h and then each well was transfected with a 1:1 ratio of NanoLuc donor (ACL $\Delta$ CC) and HaloTag acceptor (BCH $\Delta$ CC) vectors (2  $\mu$ g total) using a 1:2.5 ratio of Lipofectamine 2000. Cells were grown for an additional 20 h and then replated into 96 well white plates at a density of 22,000 cells/well in Opti-MEM with addition of HaloTag ligand to all wells with the exception of negative controls. Hek293T cells were grown for 24 h after which NanoLuc substrate was added and plates were incubated for 5 minutes at room temperature. Plates were then measured with a Spectramax i3x plate reader using the monochromator set to measure at 450 nm and 625 nm for 1000 ms.

### C. Optimization of NanoBRET for HTS

Once the specificity of the NanoBRET assay was confirmed, we proceeded to optimize parameters in order to increase the overall robustness of the assay and make it applicable in high throughput. To do this in a quantitative manner we used a statistical metric called the  $Z'$ -factor. This metric is based on the formula below:

$$Z' = 1 - \frac{(3 * SD \text{ of } PC \text{ BRET ratio} + 3 * SD \text{ of } NC \text{ BRET ratio})}{(\text{mean of } PC \text{ BRET ratio} - \text{mean of } NC \text{ BRET ratio})}$$

This is based off the in-plate positive controls (PC), which contain the HaloTag ligand and the in-plate negative controls (NC), which do not have the HaloTag ligand. The  $Z'$ -factor attempts to quantify the separation band between the mean of the positive and negative controls as an estimation of the overall quality of the assay (Figure 34).<sup>311</sup> For any given assay, the  $Z'$  can range from negative infinity to 1, with any value above zero indicating the existence of some separation between the distribution of negative and positive control values. Though any assay with a  $Z'$  over zero is technically usable, a value above 0.5 is ideal because it indicates that there is at least 12 SDs of separation between the negative and positive controls.<sup>312</sup> Using this metric we optimized the donor/acceptor ratio, the cell line (Hek239T vs HeLa), and the instrument used in the screen using the protocol based on the protocol described in the previous section and used for the pair selection.

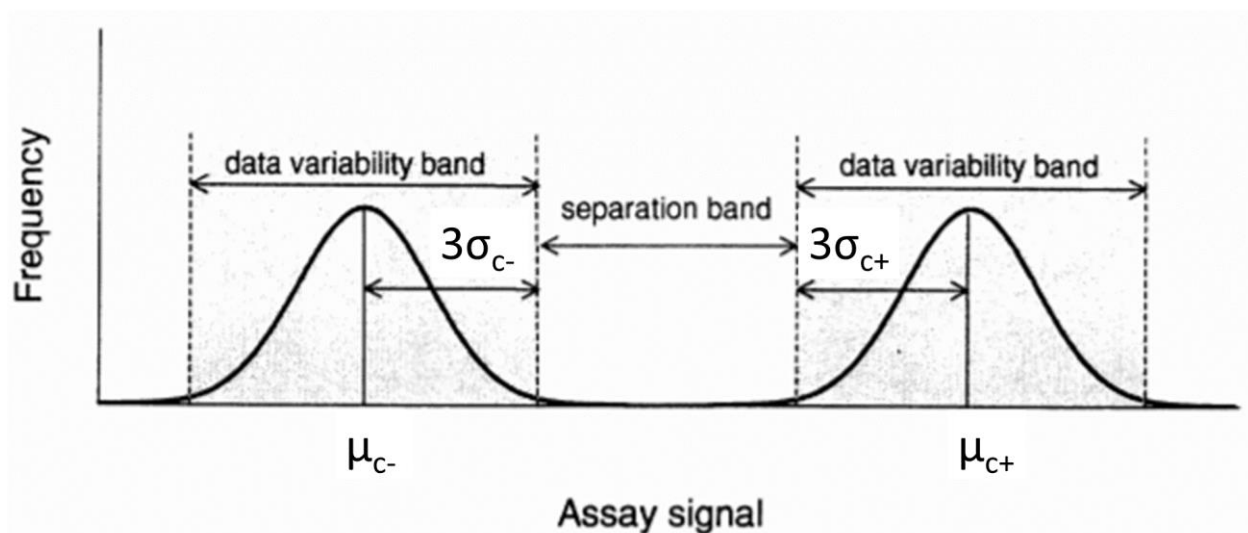


**Figure 34.** Plot illustrating the  $Z'$ -factor.<sup>311</sup> For the NanoBRET assay, the mean BRET ratio and SD of the no-ligand negative controls is represented by  $\mu_{c-}$  and  $\sigma_{c-}$  and the mean BRET ratio and SD of the ligand positive controls is represented by  $\mu_{c+}$  and  $\sigma_{c+}$ . Reprinted with permission from Zhang, J. H.; Chung, T. D.; Oldenburg, K. R. A Simple Statistical Parameter for Use in Evaluation and Validation of High Throughput Screening Assays. *J. Biomol. Screen.* **1999**, *4* (2), 67–73. Copyright 1991 The Society for Biomolecular Screening.

#### **D. Performance of NanoBRET screen using PPI inhibitor library**

After the optimizing the NanoBRET assay targeting the Beclin 1-ATG14L interaction we proceeded to screen 2,560 molecules in an HTS using this assay. These molecules were selected for properties that were common in other PPI modulators. Considerations for inclusion in the curated library included number of hydrogen bond acceptors > 3, molecular weight > 350, LogP = 3-7, and fraction of sp<sup>3</sup> centers > 0.3.<sup>285</sup> For the HTS and dose experiments, cells were plated in 10 cm dishes at a density of 8.0 x 10<sup>6</sup> cells and then transfected with a 1:1 ratio of NanoLuc donor (ACL) and HaloTag acceptor (BCH) vectors (12 µg of plasmid total) using a 1:2.5 ratio of Lipofectamine 2000. After 20 h cells were replated into 384 well white plates at a density of 1.1 x 10<sup>4</sup> cells/well, HaloTag ligand was added to all wells except for negative controls, and plates were incubated for 1 h at room temperature. 320 compounds were pin transferred using 96-well pin tool and a liquid handler, Biomek NXP Lab Automation Workstation. Cells were incubated for 24 h after which NanoLuc substrate was added and plates were incubated for 5 minutes. Plates were measured with a Victor 3V plate reader using the F460 and the 632/45 nm filter for 1 s. Hits were identified as compounds that significantly reduced the BRET ratio (< -2.5 z-score from positive control) in duplicate. Z-score was calculated based on the formula below:

$$z - score = \frac{x - \mu}{SD}$$

Where  $x$  is the uncorrected BRET ratio of the sample,  $\mu$  is the uncorrected mean BRET ratio of each plate excluding the negative controls and  $SD$  is the standard deviation of the uncorrected BRET ratio of each plate.

#### **E. Prioritization of hit molecules based on the inhibition of autophagy**

Hits were first excluded based on observed cytotoxicity from a previously conducted HTS, as highly cytotoxic molecules were likely to produce false positives. For this experiment, HeLa cells stably expressing eGFP-LC3 were plated at a density of 2,500 cells/well in 384 well black plates in DMEM and then grown for 24 h. Cells were treated with molecules from the PPI library (20 µM) for 4 h. Cells were fixed with 4% paraformaldehyde, nuclei were stained using Hoescht33342, and plates were sealed and imaged using the ImageXpress Micro (IXM) XLS automated fluorescence microscope. MetaXpress software was used to quantify cell count. Compounds that decreased the nuclei count more than a z-score of -2.0 in duplicate were excluded from further testing. The formula used for the calculation of the nuclei z-score was as follows:

$$z - score = \frac{x - \mu}{SD}$$

Where  $x$  is the nuclear count of the sample,  $\mu$  is the nuclear count in the DMSO-treated wells of each plate and  $SD$  is the standard deviation of the nuclear count for these wells. The remaining molecules were then evaluated for the dose-dependence of their activity in the NanoBRET assay in six-point dose mode in duplicate of duplicates, following the protocol used for the HTS, and only retained if this dependence was observed.

Concurrently with the dose experiments, the noncytotoxic molecules were tested for their inhibition of autophagy using assays that measure the autophagy-specific biomarker LC3. During autophagy, LC3-I is conjugated to PE to generate LC3-II, which then translocates from the cytosol to the membrane of autophagosomes.<sup>141</sup> As the autophagosome and its cargo are degraded in the lysosome the overall level of LC3-I and LC3-II can be used as a measure of autophagic flux.<sup>313</sup> One common experiment relies on the labeling of LC3 using eGFP, which allows the direct quantification of mature autophagosomes, which can be visualized as green puncta using fluorescence microscopy (Figure 35A).<sup>313</sup> Another experiment quantifies the overall levels of soluble LC3-I and LC3-II present in the cell using western blot. Late-stage autophagy inhibition caused by treatment with molecules like CQ will lead to an accumulation of LC3-II, which can be detected by both of these experiments (Figure 35B).<sup>313,314</sup> Co-treatment with molecules, like PIK-III or SAR405, that inhibit autophagy further upstream will lead to a decrease in this lipidation, and have been observed to lower the quantity of LC3-II and lead to a buildup of LC3-I.<sup>231,250</sup> Any molecule that disrupts the Beclin1-ATG14L interaction should produce a similar phenotype and thus were prioritized based on activity in both of these assays.

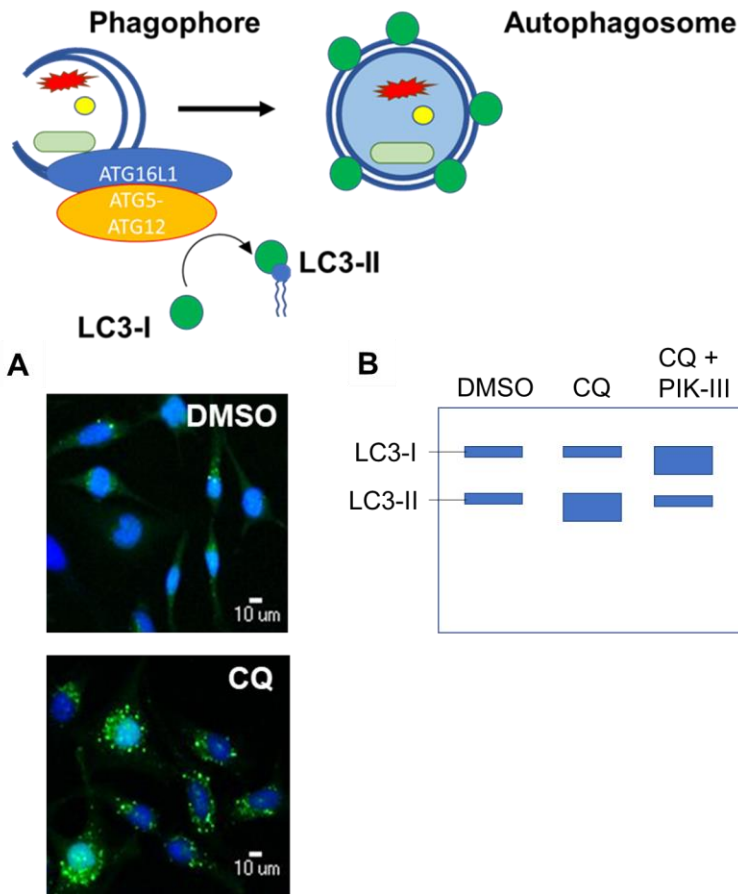


**Figure 35.** Methods used to estimate autophagic flux through quantification of LC3. During autophagy initiation the autophagy-specific biomarker LC3 undergoes lipidation which is mediated by the ATG5-ATG12-ATG16L1 complex, thus the normal functioning of autophagic flux can be determined by analyzing this protein. (A) Using eGFP-LC3 it is possible to visualize eGFP-LC3-labeled autophagosomes using fluorescence microscopy, under treatment with late-stage inhibitors, like CQ, a buildup of puncta can be detected. (B) The lipidation of LC3 can also be analyzed by western blot as the lipidated LC3-II travels faster through an SDS-PAGE gel than the unlipidated LC3-I. Under treatment with the late-stage inhibitor CQ, a buildup of LC3-II should be observed. Under co-treatment with a late-stage inhibitor (CQ) and an early stage inhibitor (PIK-III), LC3-I should accumulate instead.

For the eGFP assay, HeLa cells stably expressing eGFP-LC3 were plated at a density of 1,250 cells/well in 384 well black plates in DMEM and then grown for 24 h. Cells were treated with hits (25  $\mu$ M), PIK-III (Selleck Chemical, #S76835MG, 25  $\mu$ M) or DMSO for 20 h and then CQ (Sigma Aldrich, #C6628, 20  $\mu$ M) was added for 4 h. Cells were fixed with 4% paraformaldehyde, nuclei were stained using Hoechst 33342, plates were sealed and imaged using an IXM XLS. MetaXpress software was used to quantify cell and puncta count. This experiment was

performed in duplicate of duplicates. For the Western blot measurement of LC3, HeLa cells were plated at a density of  $5.0 \times 10^4$  cells/well in a 24 well plate in DMEM and then grown for 24 h. Cells were treated with compound hits, PIK-III (10  $\mu$ M) or DMSO for 20 h and then CQ (10  $\mu$ M) for 4 h. Cells were then lysed using Pierce IP Lysis supplemented with a Pierce protease and phosphatase inhibitor tablet. Lysate was centrifuged at 18,000 g for 30 minutes at 4 °C to remove debris, supernatant was separated by SDS-PAGE and protein was transferred onto PVDF membrane. The membrane was blocked with 5% Blotting-grade Blocker in TBS-T (Tris Buffer, 0.1% Tween-20) for 1 h at room temperature and then incubated overnight with primary antibody (LC3 and  $\beta$ -actin) in 5% Blotting-grade Blocker in TBS-T. The blots were washed with TBS-T and incubated with HRP-conjugated secondary antibody in 5% blotting-grade blocker in TBS-T for 1 h at room temperature. Membranes were washed with TBS-T and visualized with SuperSignal West Pico Chemiluminescent Substrate. Images were then analyzed using ImageJ to quantify the amount of LC3 (1:1000) and  $\beta$ -actin (1:2000). Levels of LC3-I and LC3-II were normalized to  $\beta$ -actin for each sample and all samples were then normalized the CQ control. This experiment was performed in singlicate. Data from both experiments was then analyzed for statistical significance using ANOVA with post-hoc Dunnett's multiple comparison test using GraphPad Prism 8.2.0.

#### **F. Confirmation of the potency and activity of prioritized hit**

The final prioritized molecule was reordered (ChemDiv, #L309-1226) and was reevaluated for overall potency. Another dose experiment in the NanoBRET assay was conducted in triplicate of duplicates based on the protocol described in the previous section. This allowed for the robust estimation of the  $IC_{50}$  for this molecule using log(inhibitor) vs response–variable slope (four parameters) analysis in GraphPad Prism 8.2.0. In addition, we also confirmed the activity of this molecule for autophagy inhibition in A549 and HeLa cells at an earlier time point under late-stage inhibition (CQ co-treatment) and autophagy induction (Torin 1 co-treatment). Torin 1 was selected because it is a very selective mTORC1 inhibitor,<sup>224</sup> which is a protein that negatively regulates autophagy, and this allowed us to test whether the prioritized molecule was more potent under conditions that induce autophagy. We used the two assays described in a previous section to confirm autophagy inhibition, with the A549 cells used for the immunoblotting experiments. The only change in either protocol was the compound treatment conditions. A549 cells were treated with the prioritized molecule (100  $\mu$ M), PIK-III (12.5  $\mu$ M), SAR405 (Selleck Chemical, #S76825MG,

12.5  $\mu\text{M}$ ) or DMSO for 4 h or 7 h and then either CQ (10  $\mu\text{M}$ ) or Torin 1 (LC Laboratories, #T-7887, 250 nM) was added for 4 h or 1 h, respectively.

#### **G. Elucidation of compound mechanism using Complex I pull-down and cellular thermal shift assay**

To confirm that the observed inhibition of autophagy by the prioritized molecule was due to the disruption of Complex I, the next assay we designed was a pull-down assay targeting this complex. For this assay, we used the previously generated HaloTag fusions of ATG14L as the bait protein and magnetic beads that were labeled with the HaloTag ligand (Figure 36). Because the HaloTag does not bind its ligand reversibly, and instead forms a covalent bond, it can be used to pull out any protein that is fused to it, along with any proteins that are able to interact with the fused protein.<sup>315</sup> After washing away protein that are non-specifically bound to the bead, the bound complex members can be eluted using SDS and then quantified by Western blot. Under treatment with a hit from the NanoBRET assay we would expect to see less of each complex member in the final western blot as the disruption of the Beclin 1-ATG14L interaction should also disrupt the formation of Complex I. Because the formed bond is covalent, the pull-down is more rapid than co-immunoprecipitation, and the use of a fusion protein instead of an antibody ensures that more of the complex members can bind.

Initial optimization involved determining the concentration of plasmid necessary for robust pull-down of the complex. The final protocol is as follows. First, Hek293T cells were plated at a density of  $8.0 \times 10^6$  cells in a 10 cm dish in DMEM, incubated for 4 h and then transfected an ATG14L-HaloTag fusion vector (ACH, 6  $\mu\text{g}$ ) using a 1:2.5 ratio of Lipofectamine 2000. After 20 h cells were replated at a density of  $3.0 \times 10^6$  cells in 6 cm dishes in DMEM and grown for 24 h. Cells were treated with the prioritized hit (100  $\mu\text{M}$ ), PIK-III (12.5  $\mu\text{M}$ ), SAR405 (12.5  $\mu\text{M}$ ) or DMSO for 8 h. Cells were then lysed using lysis buffer supplemented with protease inhibitor and centrifuged at 18,000 g for 30 min at 4 °C to remove debris. Protein concentration was checked by Bradford, supernatant was diluted in Tris buffer and then incubated with 25  $\mu\text{L}$  of Magne HaloTag Beads for 4 h on a rotator at room temperature. Supernatant was removed and beads were washed with washing buffer (Tris Buffer, 0.05% IGEPAL CA-630). Bound protein was eluted with elution buffer (Tris Buffer, 1% SDS) for 30 min with vigorous shaking at room temperature. Supernatant and eluent were then probed by immunoblot as described above for presence of VPS34 (1:1000), VPS15 (1:1000), Beclin 1 (1:1000) and  $\beta$ -actin (1:2000).

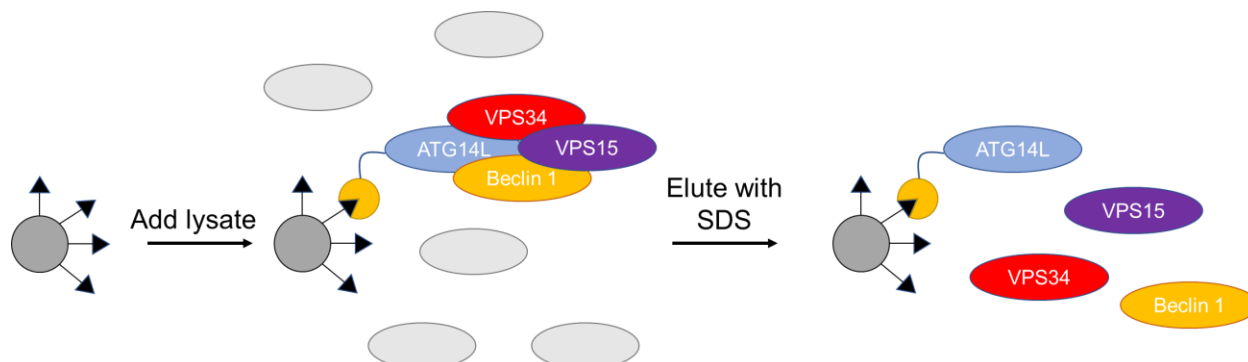


**Figure 36.** Schematic of HaloTag pull-down of VPS34 Complex I. VPS34 Complex I (VPS34-VPS15-ATG14L-Beclin 1) can be pulled out of a cell lysate using magnetic beads labeled with the HaloTag ligand, here represented as a black triangle. The ATG14L-HaloTag fusion protein will form a covalent bond with this ligand and pull out the rest of the complex from solution. The complex members can then be eluted off the bead with SDS and analyzed by immunoblot.

Next, we wanted to determine if our hit molecules disrupted the Beclin 1-ATG14L interaction through direct binding to either protein. For this we used cellular thermal shift assay (CETSA), which is an evolution of the original thermal shift assay (TSA) that relies on the thermodynamic stabilization of a protein upon the binding of a ligand.<sup>316</sup> Traditional TSA screens involve an isolate target protein which undergoes denaturation in real-time upon the application of a temperature gradient. This denaturation can be monitored using dyes that fluoresce upon binding to the exposed nonpolar surfaces of the denatured protein, such as SYPRO Orange.<sup>317</sup> In this way a melting curve for the target is generated and the initial melting temperature ( $T_m$ ), which represents the temperature at which half of all protein are denatured, is determined. This process can then be repeated in the presence of a ligand that binds to the protein, because ligand binding stabilizes the protein, a shift in the  $T_m$  is observed.<sup>317</sup> CETSA grew out of the observation that cell membranes remain intact when heat is applied for a brief period of time, allowing the application of the TSA protocol to live cells (Figure 37). In a typical experiment, cells are treated with the ligand of interest, heat-shocked for brief period of time and then lysed.<sup>318</sup> Aggregated protein and cell debris are removed, and the protein of interest is quantified with a variety of detection methods such as western blot or AlphaScreen.<sup>319</sup> As with TSA the melting curve for the protein of interest must be determined in the absence of the ligand before a shift in the melting

temperature can be quantified. Encouragingly, this method has been successfully used to measure target engagement for a diversity of proteins and ligands, including PPI inhibitors and membrane proteins.<sup>320–322</sup>

Three cell lines (A549, HeLa, Hek293T) were first screened by western blot to identify which had the highest expression of ATG14L. The A549 cell line was identified as having the highest ATG14L expression levels and was used in all following experiments. First, the temperatures necessary to generate the initial melting curve for both ATG14L and Beclin 1 were identified and were then used in subsequent experiments using the prioritized molecule. Because the melting curves for both proteins were determined to be similar, the following protocol was used. A548 cells were plated at a density of  $2.5 \times 10^6$  cells in a 10 cm dish in DMEM and grown overnight. Cells were then treated with the prioritized hit (50  $\mu$ M) or DMSO and incubated for 24 h, this time to mirror the NanoBRET experiment. Media was removed and cells were suspended by trypsinization, pelleted and washed with PBS and then resuspended to a density of  $1.0 \times 10^7$  cells/mL in PBS supplemented with Pierce protease inhibitor tablet. 50  $\mu$ L of each cell suspension was then dispensed into PCR tubes and heated at 48 – 56 °C using a Biorad T100 thermal cycler for 3 minutes and immediately lysed by freeze-thaw. Debris was then removed by centrifugation at 18,000 g for 30 minutes at 4 °C and then supernatant was probed by immunoblot as described in a previous section for the presence of ATG14L (1:1000) and  $\beta$ -actin (1:2000). Blots were quantified using ImageJ, the quantity of ATG14L was normalized to the DMSO treated room temperature controls, and melting curves were fitted using sigmoidal least squares fit using GraphPad Prism 8.2.0.

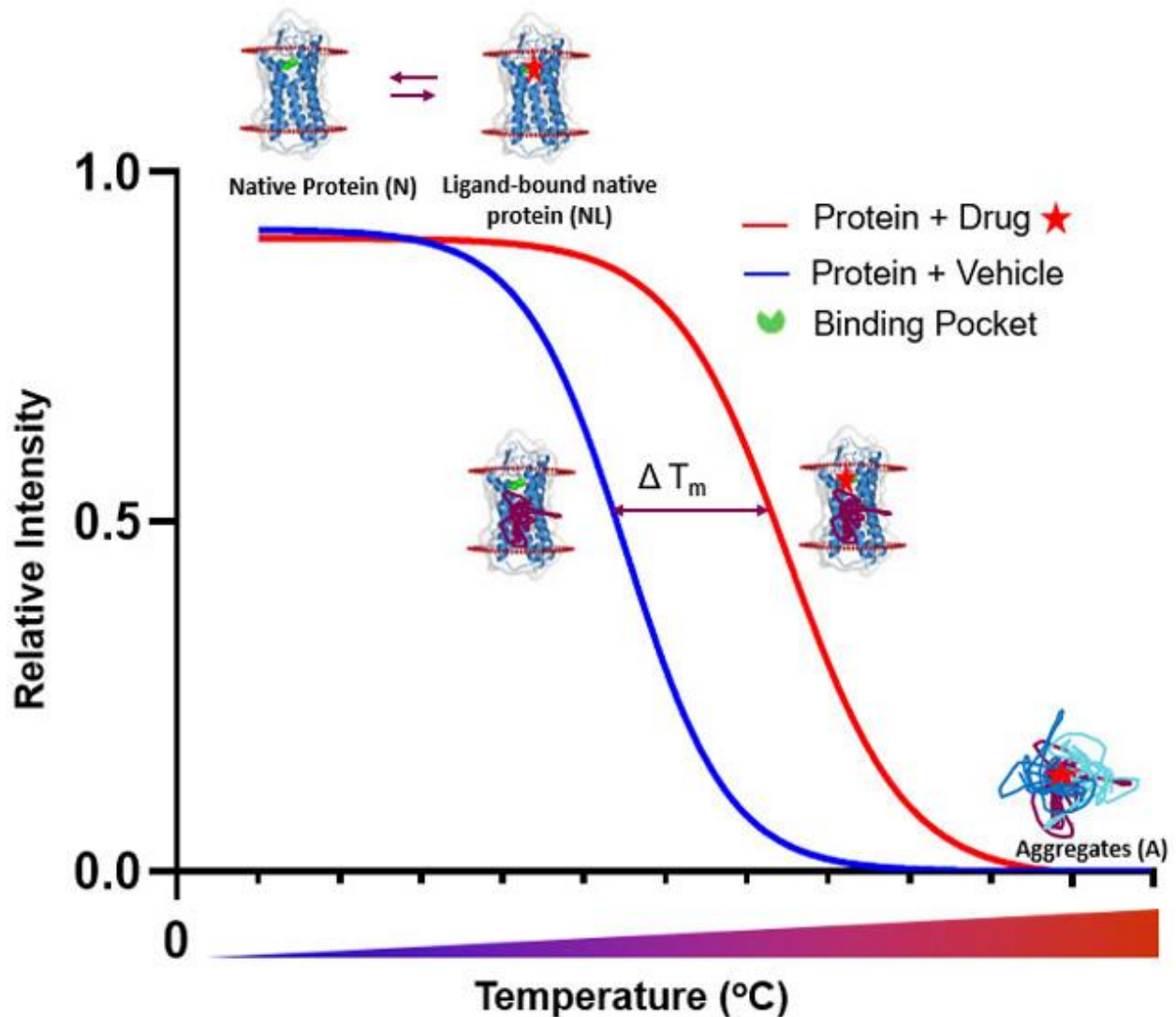


**Figure 37.** Principle of the use of CETSA to determine ligand binding. In this figure native protein (N) aggregates at a lower temperature than the native protein bound to a ligand or drug (NL). As the temperature rises more and more of the protein of interest is denatured and forms aggregates, thus it is no longer present in solution, so the relative intensity of the band corresponding to this protein is decreased.<sup>322</sup> Adapted from reference 322 with permission.

#### H. Performance of NanoBRET assay targeting the Beclin 1-UVRAG interaction

For any inhibitor of the Beclin 1-ATG14L interaction to be autophagy specific it must not disrupt the interaction that occurs between Beclin 1 and UVRAG. The Beclin 1-UVRAG PPI is critical to the formation of VPS34

Complex II, the endocytic complex (Figure 27, Figure 28) and so its disruption may impact vesicle trafficking.<sup>259</sup> For the development of this assay, four new vectors were generated to express the UVRAG gene fused with either NanoLuc and HaloTag at either the N or C-terminus as described above using PCR and restriction digestion cloning. The eight Beclin 1-UVRAG pairs were then tested for BRET signal following the protocol established for the selection of the Beclin 1-ATG14L pairs. The best pair was determined to be the BNH-UNL pair (Table 4) and was used for the dose experiments with the prioritized molecule from the original NanoBRET HTS. Hek293T cells were plated at a density of  $1.2 \times 10^6$  cells/well in 6 well plates in DMEM, incubated for 4 h and then transfected a 1:1 ratio of NanoLuc donor (UNL) to HaloTag acceptor (BNH) vectors (2  $\mu$ g total) using a 1:2.5 ratio of Lipofectamine 2000. After 20 h cells were replated into 384 well white plates at a density of  $1.1 \times 10^4$  cells/well, HaloTag ligand was added to all wells except for negative controls, and plates were incubated for 1 h at room temperature. Compounds were pin transferred using 96-well pin tool and liquid handler. Cells were incubated for 24 h after which NanoLuc substrate was added and plates were incubated for 5 minutes. Plates were measured with a Victor 3V plate reader using the F460 and the 632/45 nm filter for 1 s.

#### **I. Experiments confirming specificity for autophagy inhibition over disruption of vesicle trafficking**

The selective disruption of Complex I should inhibit autophagy without disrupting vesicle trafficking, in contrast to direct VPS34 kinase inhibitors such as PIK-III and SAR405, which inhibit both. To confirm this phenotype, we used several experiments, each time directly comparing the activity of the prioritized hit to the direct VPS34 inhibitors. The first experiment involved the maturation of the lysosomal aspartyl protease Cathepsin D. This protease is originally synthesized as an inactive preprocathepsin D in the ER that undergoes further processing to form procathepsin D in the trans-Golgi network and is then cleaved in the lysosome to produce the active subunits.<sup>323</sup> Thus, if vesicle trafficking is disrupted we will observe the buildup of the preprocathepsin D and procathepsin D isoforms. For this experiment, A549 cells were treated with the prioritized molecule (100  $\mu$ M), PIK-III (12.5  $\mu$ M), SAR405 (12.5  $\mu$ M) or DMSO for 8 h and then evaluated by western blot for the presence of Cathepsin D (1:500) and  $\beta$ -actin (1:2000) as described in a previous section.

Because direct VPS34 inhibitors have been shown to not only disrupt intracellular vesicle trafficking but also the up-take of external cargo, we further analyzed our prioritized hit using the DQ-BSA assay. DQ-BSA is a fluorescent probe that is bovine serum albumin (BSA) extensively labeled with BOPIDY dyes. Under excitation of

the fully constituted probe, the BODIPY dyes self-quench due to proximity allowing for this probe to be used to track the endocytic process because as the DQ-BSA is internalized and degraded in the lysosome individual pieces become fluorescent (Figure 38).<sup>324</sup> Thus, any molecule that inhibits either the acidification of the lysosome or the formation and fusion of endosomes will lead to a reduction in DQ-BSA degradation and fluorescence. A549 cells were plated at a density of 2,500 cells/well in 384 well black plates in DMEM and then grown for 24h. DQ-Red BSA (Thermo, #D12051) was added to a final concentration of 10  $\mu\text{g}/\text{mL}$  and plates were incubated for 1 h. Media was then removed, cells were washed with 1x PBS and fresh media was added. Cells were then treated with prioritized hit (100  $\mu\text{M}$ ), PIK-III (12.5  $\mu\text{M}$ ), SAR405 (12.5  $\mu\text{M}$ ), Bafilomycin A1 (LC Laboratories, #B-1080, 100 nM), or DMSO for 8 h. Nuclei were stained using Hoechst 33342, plates were sealed and imaged using IXM XLS. MetaXpress software was used to quantify cell and puncta count. Data was then analyzed for statistical significance using ANOVA with post-hoc Dunnett's multiple comparison test using GraphPad Prism 8.2.0.

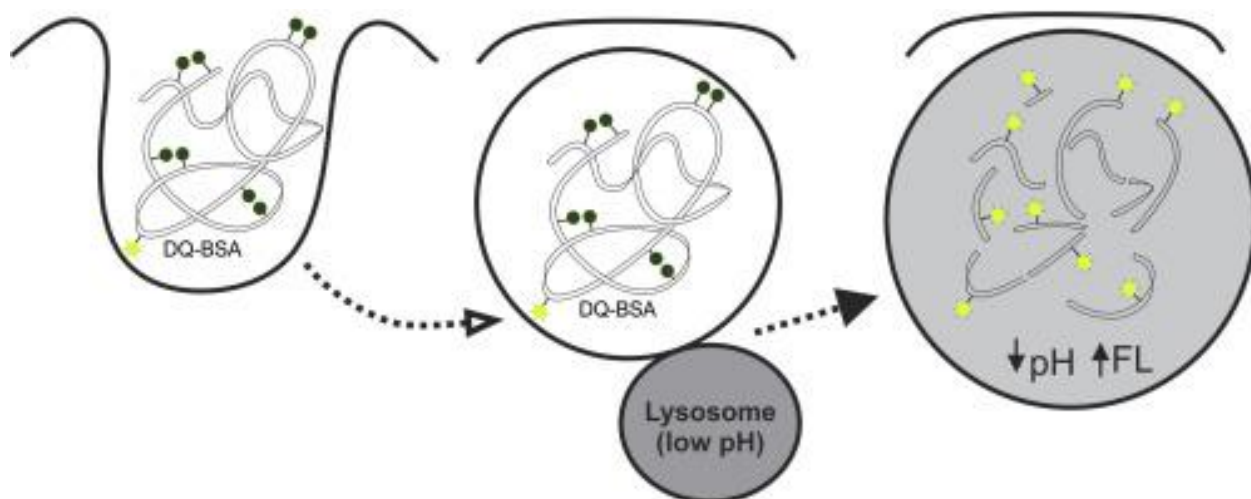


**Figure 38.** Principle of the use of DQ-BSA to monitor endocytic trafficking. DQ-BSA is heavily labeled with BODIPY dyes, which self-quench and thus do not fluoresce. When DQ-BSA is successfully internalized and trafficked to the lysosome it is degraded, and the individual pieces are too distant to self-quench and can be visualized using fluorescence microscopy.<sup>324</sup> Adapted from reference 324 with permission.

Lastly, we used phase contrast microscopy to directly visualize the formation of large vacuole-like vesicles that have been observed to form under treatment with compounds that inhibit vesicle trafficking. This is believed to occur due to the depletion of lipids necessary for proper vesicle formation and fusion and has been previously observed in cells treated with SAR 405 and in cells where the PIKfyve kinase, which generates PI3,5P<sub>2</sub> and PI5P, has been knocked out.<sup>250,325</sup> A549 cells were plated at a density of 2,500 cells/well in 384 well black plates in DMEM and then grown for 24h. Cells were then treated with prioritized hit (100 μM), PIK-III (12.5 μM), SAR405 (12.5 μM) or DMSO for 8 h. Nuclei were stained using Hoechst 33342 and plates were imaged using IXM XLS phase-contrast addition.

#### **J. Design of ATG5-ATG16L1 FP assay**

As described in the introduction the ATG5-ATG16L1 interaction is ideal for the development of an FP assay, due to it being mediated by a relatively small region of the ATG16L1 N-terminal α-helical domain. FP is based on the principle that the polarization of light emitted by a fluorophore is inversely proportional to the rate of molecular rotation. Because larger molecules rotate slower, it is possible to quantify the interaction of a small fluorescent ligand, such as a peptide or an enzyme substrate, with a larger substrate, such as a protein<sup>295,326,327</sup> Though theoretically any binding event can be evaluated in this way, there needs to be around a ten-fold difference in the size of the ligand and substrate. In our case the peptide of ATG16L1 that corresponds to the binding interface is around 4.3 kDa in size, while the size of ATG5 is around 35 kDa, which should make it tractable for this approach. In our case the N-terminal domain of ATG16L1 can be resynthesized as a peptide labelled with a fluorescent molecule, rhodamine, which would rotate rapidly in solution due to its smaller size. In the presence of ATG5, ATG16L1 should bind, and the rate of its rotation should slow down due to its association with ATG5 and increase the polarization of the emitted light (Figure 39). Quantitatively, FP is derived from the difference of the emission light intensity parallel and perpendicular to the excitation light plane normalized by the total fluorescence emission intensity.<sup>328</sup> Because fluorescence from small molecules can lead to false positives in an FP assay, we chose rhodamine as the fluorophore as fewer library compounds are fluorescent within the red region of the light spectrum.

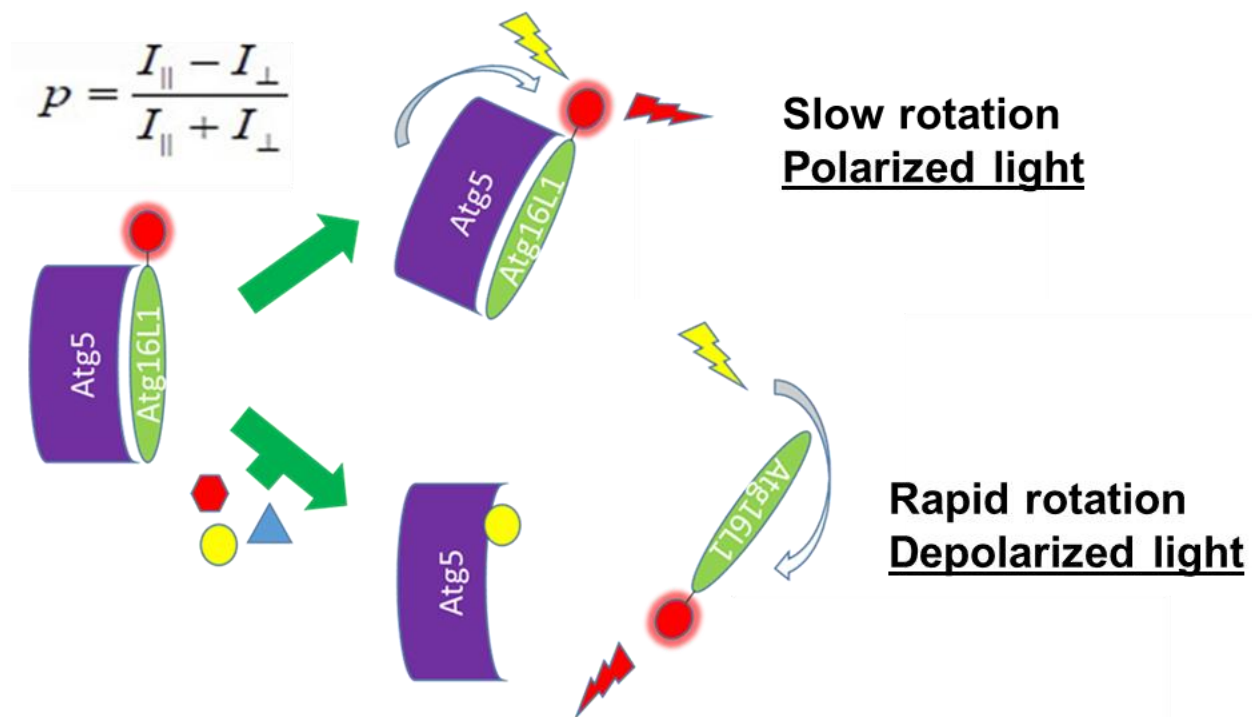


**Figure 39.** Targeting the ATG5-ATG16L1 interaction using an FP assay. The rhodamine-labeled N-terminal  $\alpha$ -helix of ATG16L1 (ATG16N) would rotate slowly when bound to ATG5 and if excited with polarized light will emit light that remains polarized. When treated with a compound that disrupts the interaction of ATG5 with rhodamine-labeled ATG16N, the peptide would tumble more rapidly in solution and thus the light emitted would be depolarized. The overall polarization of the light can be quantified through the formula displayed, where  $I_{\parallel}$  is the intensity of the polarized light (light emitted parallel to the plane of excitation) that is emitted and  $I_{\perp}$  is the intensity of the depolarized light (light emitted that is perpendicular to the plane of excitation).

### **K. Preparation of reagents for the ATG5-ATG16L1 FP assay**

Initial attempts to isolate ATG5 were made using Hek293T cells, but overall yield of pure ATG5 was too low to make it viable for use in an HTS, therefore we proceeded to create a vector that would express ATG5 in *E. coli*. First, the ATG5 gene was cloned from the pCMV-myc-Atg5 plasmid into the pET His6 MBP TEV LIC cloning vector (1M), using ligation-independent cloning (Figure 40). This vector was chosen because the His6 and MBP tag would allow for a two-step purification as both the His6 and MBP have ligands, Nickel for the His6 and maltose for MBP, that can be used for affinity-based purification. In addition, the MBP tag is a commonly used solubility tag,

which would allow for the ATG5 to remain soluble during expression. The ATG5 gene was amplified by PCR using forward (5'-TACTTCCAATCCAATGCAATGACAGATGACAAAGAT-GTGCTT-3') and reverse (5'-TTATCCACTTCCAATGTTATTATCAATCTGTTGGCTGTGGG-3') primers using the following protocol: 98°C for 30 sec, (98°C for 10 sec, 67-72°C for 30 sec, 72°C for 1 min) x 35, 72°C for 5 minutes using the Biorad T100 thermal cycler, and gel purified. The vector was linearized by digestion with SspI-HF, and gel purified. Next, the digested vector and the PCR product were treated with T4 DNA Polymerase in the presence of dGTP for the vector and dCTP for the PCR product for two hours at room temperature. The treated vector and PCR products were then mixed and incubated at room temperature for 30 minutes, transformed into competent DH5α *E. coli* cells which were plated on agar plates containing kanamycin at 50 µg/mL and grown overnight at 37 °C. Single colonies were picked and sequenced to confirm cloning.

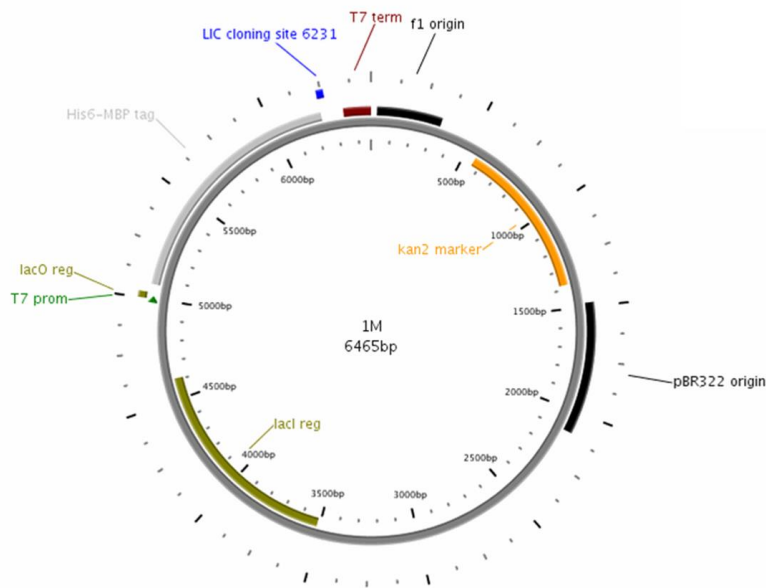


**Figure 40.** Plasmid map for the vector used for the expression of MBP-ATG5.

The plasmid was then transformed into BL21(DE3)pLysS *E. coli* cells for expression. Though previous protocols were available for the purification of ATG5, the parameters for optimal expression including incubation time, temperature, and amount of IPTG were optimized using small scale cultures. The final protocol is as follows. Cells were expanded at 37°C with 50 µg/mL Kanamycin and 25 µg/mL Chloramphenicol antibiotics at 250 RPM until OD600 of 0.6, and expression induced using 1mM IPTG at 16°C overnight for ~15 hours. The cultures were then centrifuged for 10 minutes at 4,000 g, and the supernatant was removed. The cell pellet was suspended in lysis buffer (20 mM Na<sub>2</sub>PO<sub>4</sub>, 500 mM NaCl, 5 mM Imidazole, 5 mM 2-Mercaptoethanol, 1 mM PMSF, 0.5% Triton X-100, ~pH 7.4). BME & PMSF were added last right before lysis in order to ensure their stability. The cells were then lysed using a Branson 150 sonicator (6 cycles: 10 seconds on, 50 seconds off). This lysate was clarified by centrifugation at 26,000 g at 4 °C for 30 minutes and MBP-ATG5 was purified using ÄKTA start in a cold room, where the clear lysate was loaded onto the HisTrap HP column and washed with wash buffer (20 mM Na<sub>2</sub>PO<sub>4</sub>, 20 mM Imidazole, 500 mM NaCl, ~pH 7.4). MBP-ATG5 was then eluted with elution Buffer (20 mM Na<sub>2</sub>PO<sub>4</sub>, 500 mM Imidazole, 500 mM NaCl, ~pH 7.4). The eluate was desalted using a HiTrap Desalting column.

We attempted further purification of the MBP-ATG5 using the MBPTrap HP column, but our fusion protein bound very weakly to this column either due to the overall age of the column or occlusion of the binding epitope. Additionally, because we wanted to isolate pure ATG5, we also tried to optimize the cleavage of the MBP tag from the ATG5 using TEV protease, as this fusion is produced with a TEV-cleavable linker between the two protein. However, this was also unsuccessful as upon cleavage of the MBP tag, the ATG5 protein would precipitate at high concentration, an effect also noted in previous research that may be caused by the absence of its endogenous conjugate ATG12.<sup>275</sup> Therefore, the MBP tag was left on the protein and the eluate was stored in storage buffer (20 mM Na<sub>2</sub>PO<sub>4</sub>, 250 mM NaCl, 0.05% Tween 20, pH 7.4). The protein concentration was then determined using Bradford Assay, after which DTT (2 mM) was added, and then the protein was flash frozen using methanol and dry ice. Protein production and overall purity was confirmed via SDS-PAGE. Lastly, the labeled and unlabeled alpha helical segment of ATG16L1 (PRWKRHISEQLRRRDRLQRQAFEEIILQYNKLL), which corresponds to the minimal binding interface between ATG5 and ATG16L1,<sup>152</sup> was purchased through the UIC Research Resources Center, where the ATG16L1 was tagged with 5,6 carboxytetramethylrhodamine on the N-terminus of the  $\alpha$ -helix.

#### **L. Development and confirmation of specificity for the ATG5-ATG16L1 FP assay**

As with the NanoBRET assay the next step was to demonstrate that a robust signal could be produced from the association of the MBP-ATG5 protein with the rhodamine-tagged N-terminal domain of ATG16L1 (Rho-ATG16N). Purified MBP-ATG5 was diluted in assay buffer (1x PBS, 0.05% Tween-20) to generate a 12-point dose (7.3 nM to 15  $\mu$ M). Then Rho-ATG16N (10 nM) was added to each well, and the plate was covered with foil and incubated in the dark at room temperature for two hours. A Spectramax i3x with the FP-Rhodamine module at 500 ms integration time and 9 mm read height was then used to determine the mP, which is based on the following equation:

$$mP = \frac{I_{\parallel} - I_{\perp}}{I_{\parallel} + I_{\perp}} * 1000$$

where  $I_{\parallel}$  is the fluorescence intensity parallel to excitation plane, and  $I_{\perp}$  is the fluorescence intensity perpendicular to excitation plane. This assay was performed in duplicate.

Specificity of this interaction was then confirmed using two follow up assays. First, we conducted a competition assay using an unlabeled ATG16L1 N-terminal  $\alpha$ -helical peptide (ATG16N). Because their amino acid sequence is the same, they should compete for the same binding interface, thus increasing quantity of ATG16N should displace the Rho-ATG16N, causing a decrease in the observed polarization. ATG16N was diluted in assay buffer to generate a 12-point dose curve (2.4 nM to 5  $\mu$ M). Next, MBP-ATG5 (6  $\mu$ M) and Rho-ATG16N (10 nM) were added, and wells with no ATG5 added served as a control to account for the possible interaction of the two peptides with each other. Then the plate was covered in foil, placed in the dark, and incubated for two hours. Lastly, because the MBP tag was still fused to the ATG5 protein, it was possible that any increase in polarization observed could be caused by the binding of Rho-ATG16N to the MBP tag. Thus, we purified the MBP tag following the expression and purification protocol described above with adjustments to the temperature (from 16°C to 37°C), incubation time (from 15 hours to 3 hours) and IPTG (from 1 mM to 250  $\mu$ M). This isolate MBP was then used as the titrant of Rho-ATG16N. The MBP was diluted in assay buffer in 12-point dose (7.8 nM to 16  $\mu$ M) and Rho-ATG16N (10 nM) was added to each well, and then the plate was covered with foil and incubated in the dark at room temperature for two hours. Wells that contained no ATG5 served as the negative control and wells that contained ATG5 (6  $\mu$ M) served as the positive control. Both experiments were performed in duplicate and mP was

quantified as described above. Dose curves were fitted using log(agonist) vs response–variable slope (four parameters) analysis in GraphPad Prism 8.2.0.

### **III. Results and Discussion**

#### **A. Development and validation of NanoBRET assay targeting the Beclin 1-ATG14L interaction**

The first step in our assay development was the determination of the optimal placement of the HaloTag and NanoLuc tags for our protein pair of interest, Beclin 1 and ATG14L. As described in the methodology section, eight pairs of fusion proteins were created by cloning each gene into four vectors that would produce either N- or C-terminally labeled fusion proteins (Table 4). These vector pairs were then transiently transfected in Hek293T cells and evaluated based on the BRET ratio they produced (Figure 41A). Pairs in which both tags were on matching terminal ends produced higher signal, which matches previous research that established that Beclin 1 and ATG14L interact as a parallel dimer. We selected the Beclin 1 C-terminal HaloTag (BCH) and ATG14L C-terminal NanoLuc (ACL) as the best pair out of the set and proceeded to further validate the specificity of this signal. Although the Beclin 1 C-terminal Luciferase (BCL) and ATG14L C-terminal HaloTag (ACH) also produced a robust signal, it is more optimal to use the protein that is endogenously expressed at lower amounts for the bioluminescent donor as it potentially maximizes the amount of interactions that would occur between the donor and acceptor fusions.

To confirm that this signal occurred due to the specific interaction of the two proteins and not from non-specific binding or random proximity, we conducted two experiments as described in the methodology section. The first was DSA,<sup>307</sup> in which we transfected a fixed amount of donor vector (ACL) with increasing amounts of acceptor vector (BCH). For our chosen pair, we observed the plateau in signal that is characteristic for a specific interaction (Figure 41B). Previous research had established that the CCD of ATG14L with Beclin 1 are critical for their interaction;<sup>262</sup> therefore, for our second validation experiment, we produced coiled-coil deletion mutant ( $\Delta$ CC) versions of both proteins in our original pair. As expected, deletion of the CCD from one protein of the pair or both proteins produced a BRET signal comparable to that of the background (Figure 41C), confirming the requirement of the CCD for this interaction. Though both of these experiments did establish that our assay measures the specific interaction of Beclin 1 and ATG14L, one possible limitation is that it does not measure this interaction in an endogenous state. These proteins were both tagged at the C-terminus and it has been shown that the deletion of C-

terminal end of ATG14L abolishes its localization to the ER.<sup>260,329</sup> However, many of the functions of the ATG14L and Beclin 1 protein have been determined using C-terminal protein fusions. For example, C-terminal fusions have been used to show the co-localization of Beclin1 and ATG14L in puncta by fluorescence microscopy and double-membrane vesicles by electron microscopy, in addition to being used to pull-down the two VPS34 complexes.<sup>247,330</sup> A further study confirmed that the placement of the GFP at either the N- or C-terminus of ATG14L did not affect its distribution in the cell.<sup>331</sup> Thus, the modification of the C-termini of both Beclin 1 and ATG14L with the HaloTag and NanoLuc should not adversely affect their function or localization.

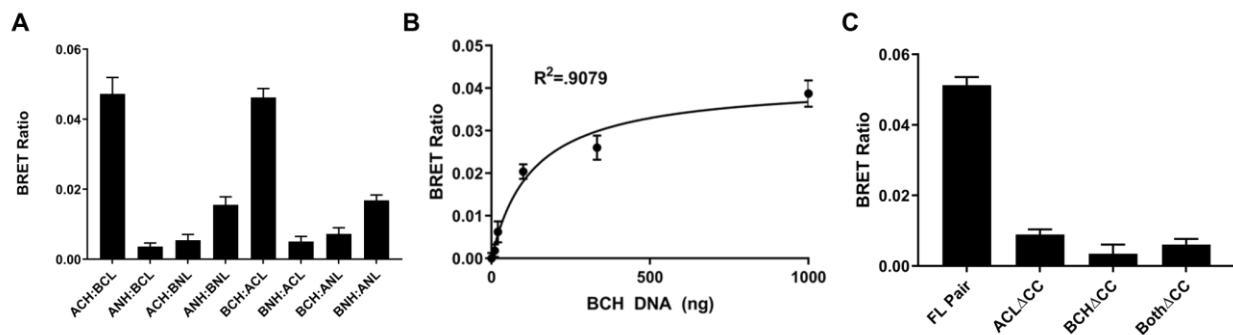


**Figure 41.** Development of NanoBRET assay targeting the PPI of Beclin 1 and Atg14L in Hek293T cells. All data are presented as mean  $\pm$  SEM. (A) Cells were transfected with a 1:10 ratio of each donor and acceptor vector pair. Matched C-terminally tagged pairs generated the highest BRET ratio, with the ACL (Atg14L-NanoLuciferase): BCH (Beclin 1-HaloTag) pair being chosen for further validation. (B) Cells were transfected with 1  $\mu$ g of the ACL vector and titrated with increasing amounts of the BCH vector, the non-linear increase in the BRET ratio indicates saturation of the ACL donor. (C) Hek293T cells were transfected with a 1:1 ratio of the original full length (FL) pair or pairs where the coiled coil (CC) domains of either protein were deleted. Deletion of either CC domain reduced signal to background levels.

## **B. Optimization of NanoBRET assay targeting the Beclin 1-ATG14L interaction for HTS**

After confirming the specificity of the NanoBRET signal generated by our chosen fusion protein, we next attempted to optimize some parameters to maximize the dynamic range of this assay and make it more viable for use

in an HTS. Towards this goal, our first experiment involved the selection of the ratio of donor and acceptor. Theoretically, a lower amount of the donor plasmid should lead to a larger BRET ratio as it would reduce the amount of donor signal that bleeds through into the acceptor channel; however, this may also increase the variability in the observed ratios as the signal for both donor and acceptor approach the limit of detection for the plate reader. As with pair selection, we transfected Hek293T cells with four ratios (1:1, 1:10, 1:100, 1:1000) of the ACL:BCH plasmid. Cells were then incubated for 20 h, replated in 96 well plates and the HaloTag ligand was added to the PC wells and cells were incubated for a further 24 h. We observed that while the BRET signal did increase with lower amounts of donor plasmid there was also a corresponding increase in variability, thus the 1:1 ratio was chosen to be the best for having the highest  $Z'$ -factor ( $Z' = 0.52$ , Figure 42A).

Because our aim was to discover an autophagy-specific PPI inhibitor for the inhibition of autophagy in cancer we decided to see if we could get a robust BRET signal and  $Z'$ -factor by using HeLa cells, which are a typical cell line used for the study of cancer biology. For this experiment, we transfected HeLa cells with a 1:1 ratio of the ACL:BCH plasmid pair using the exact protocol used of Hek293T cells. Although we observed BRET signal in HeLa cells, it was too low and too variable for us to use this cell type in an HTS (Figure 42B,  $Z' = 0.29$ ). We also transitioned our assay into 384 well format from a 96 well format to increase the throughput of our HTS, though this did lead to a reduction in assay robustness as measured by  $Z'$ -factor ( $Z' = 0.42$ ). We proceeded to screen compounds using Hek293T cells in 384 well plates; however, hit selection was somewhat unreliable and assay did not have good reproducibility (Figure 43A). This was largely due to the low quantity of signal detected in the acceptor channel by the Spectramax i3x (Figure 43B). Therefore, we switched to another instrument, the Victor 3V, which had a much more sensitive photon counter and detected much higher signals in both the acceptor and donor channels, (Figure 43C) and thus also had a better  $Z'$ -factor ( $Z' = 0.68$ ).

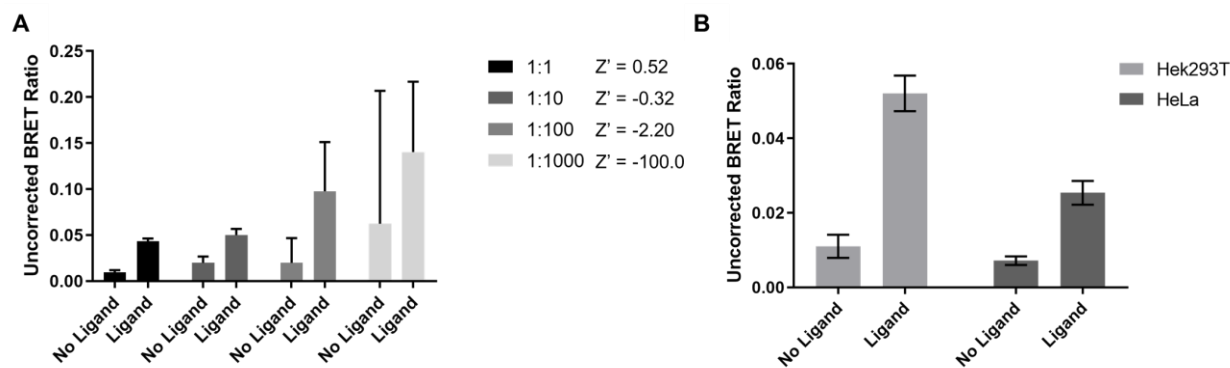


**Figure 42.** Optimization of NanoBRET assay. (A) Hek293T cells were transfected with different ratios of ACL:BCH plasmid (2  $\mu$ g of plasmid total) and evaluated for their BRET ratio and Z'-factor. Data is presented as mean  $\pm$  SD for 4 technical replicates. (B) Comparison of the acceptor signal recorded by the Spectramax i3x (light gray) and Victor 3V (dark gray), no ligand represents those wells where no HaloTag ligand was added and are used to establish background signal for both instruments and for the calculation of the Z'-factors. All data are presented as mean  $\pm$  SD generated from 16 technical replicates.

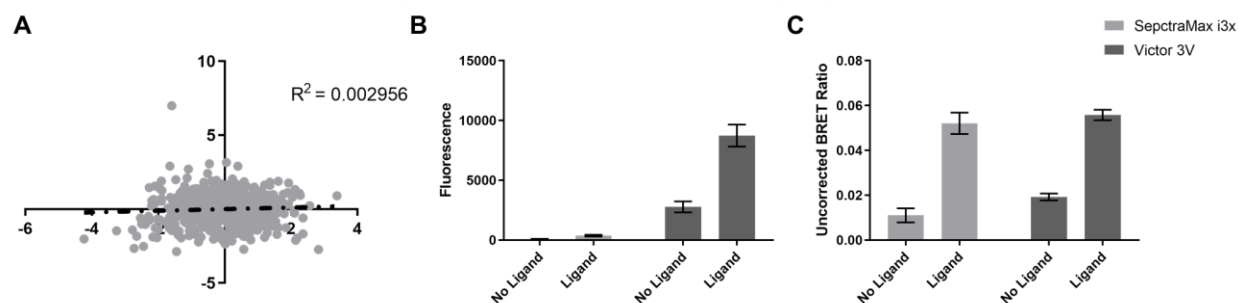


**Figure 43.** Comparison of NanoBRET performance between the Spectramax i3x and the Victor 3V. (A) Z-scores for 640 compounds screened in duplicate using the Spectramax i3x. (B) Comparison of the acceptor signal recorded by the Spectramax i3x (light gray) and Victor 3V (dark gray), no ligand represents those wells where no HaloTag ligand was added and are used to establish background signal. (C) Comparison of the uncorrected BRET ratio generated by the Spectramax i3x and Victor 3V. All data are presented as mean  $\pm$  SD generated from 16 technical replicates.

### C. Pilot screen for small molecules targeting the Beclin1-ATG14L interaction

Once the we had validated and optimized the NanoBRET assay for HTS we wanted to establish the feasibility of employing this assay to identify potential inhibitors of the Beclin 1-ATG14L PPI. Towards this goal we screened 2,560 molecules from our curated library enriched for molecules with properties favorable for PPI

inhibition.<sup>285</sup> To ensure accurate hit selection and allow for the determination of reproducibility for the assay, all molecules were screened in duplicate. As described in a previous section, Hek293T cells were transiently transfected with a 1:1 ratio of BCH:ACL vectors and then grown for 20 h, after which they were re-plated into 384-well white plates with the addition of HaloTag ligand across the plate excluding no-ligand background controls. Compounds were transferred by pin tool, and cells were treated for 24 h, after which NanoLuc substrate was added and donor and acceptor signal was measured by plate reader. The assay proved to be robust with an average  $Z' = 0.64$ , little variability between plates and days, and high reproducibility between replicates ( $R^2 = 0.55$ ) (Figure 44).<sup>311</sup> Hits were identified as compounds that significantly reduced the BRET signal ( $< -2.5$  z-score from positive control) in duplicate.<sup>332</sup> In total, 29 molecules met these criteria, giving an overall hit rate of 1.1%, of which 10 molecules were excluded because of cytotoxicity at 4 h in HeLa cells (Figure 45).

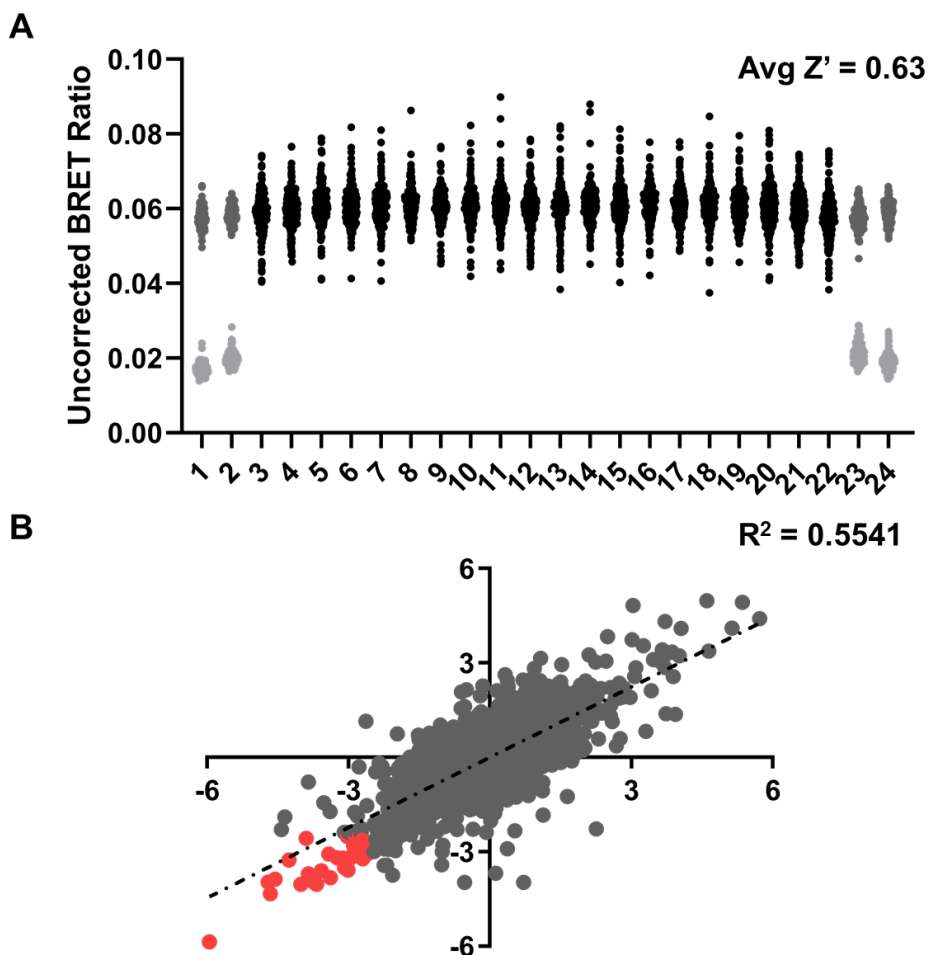


**Figure 44.** Assay metrics from the NanoBRET-based HTS targeting the Beclin 1-ATG14L interaction in Hek293T cells. (A) Dot plot showing the BRET ratios for each column in each 384 well plate. Values are presented as uncorrected NanoBRET so negative controls (light gray) could be visualized on the graph. These controls (represented in dark and light gray) showed little plate-to-plate and day-to-day variability. And the assay had a good separation between the negative (no HaloTag ligand, light gray) and positive (HaloTag ligand, dark gray) controls as represented by a  $Z'$  above 0.5.<sup>312</sup> (B) The correlation of the z-scores from each duplicate compound treatment establish assay reproducibility. Hits are highlighted in red. Each z-score was generated based on the average and standard deviation of each 384 well plate's positive and negative controls.

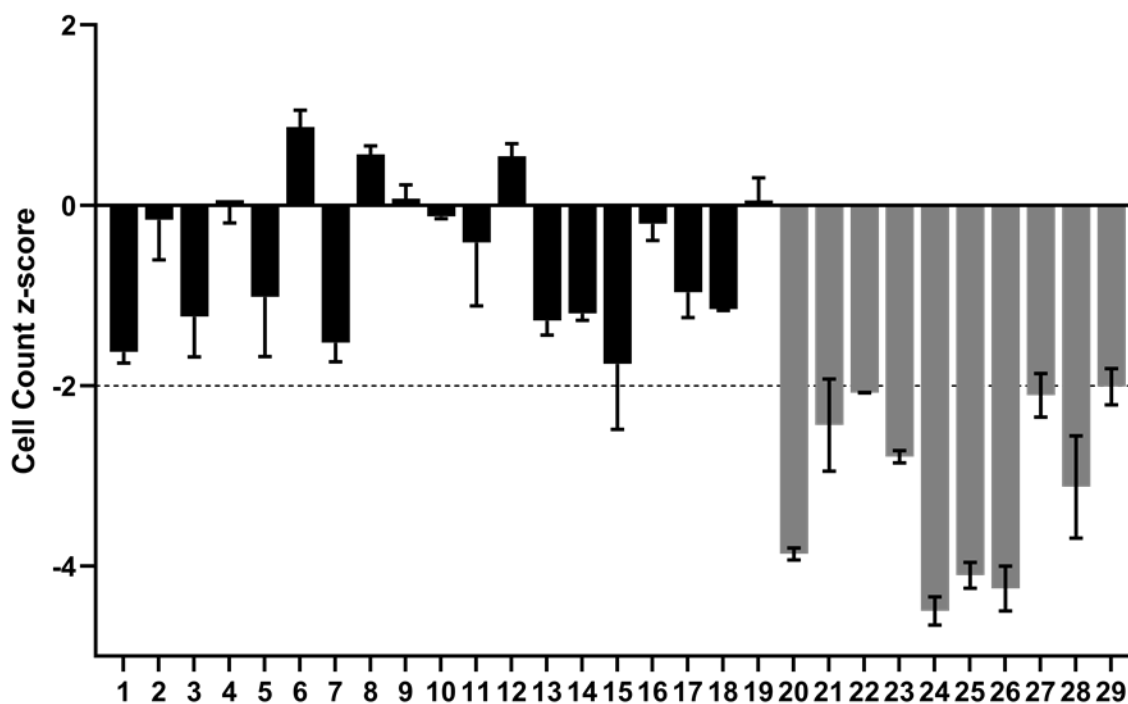


**Figure 45.** Exclusion of hits based on cytotoxicity. eGFP-LC3 expressing HeLa cells were treated with hits (20  $\mu$ M) for 4 h. Compounds that decreased the cell count (z-score < -2.0) are shown in dark gray and were deemed cytotoxic and excluded from further experiments. Data are presented as the mean z-score  $\pm$  SEM from two independent experiments.

#### **D. Prioritization of hits based on autophagy inhibition**

The 19 hits that were not cytotoxic were cherry-picked and re-screened in the NanoBRET assay using six doses. A known VPS34 inhibitor, PIK-III, was chosen as a negative control, due to its known binding to VPS34, but no known inhibition of the Beclin 1-ATG14L interaction.<sup>231</sup> Sixteen of the 19 molecules showed a dose dependent reduction in NanoBRET signal, while the negative control, PIK-III, did not (Figure 46). In addition to quantifying the false positive rate for our assay (15%) this result also further demonstrated the specificity of the signal produced by our fusion pair, as PIK-III induced cytotoxicity without decreasing the BRET signal. Next, we tested if any hits exhibited autophagy inhibition in HeLa cells. We did this by tracking the quantity and lipidation state of the autophagy-specific biomarker LC3 using fluorescence microscopy and immunoblotting.<sup>313</sup> Under treatment with

late-state inhibitors like CQ, which will lead to accumulation of LC3-II, molecules, like PIK-III or SAR405 or an inhibitor of the Beclin 1-ATG14L interaction, which inhibit autophagy further upstream should lead to a decrease in LC3-II.<sup>231,231,250</sup> Fifteen hits showed a reduction in eGFP-LC3 puncta relative to the CQ control (Figure 47A), though none as strongly as PIK-III, after 24 h of treatment at 25  $\mu$ M in duplicate. Additionally, though we did not see a decrease of LC3-II by western blot for the PIK-III treated sample, we did see an increase in LC3-I, which indicates early autophagy inhibition (Figure 47B,C). Three hits showed a similar increase in LC3-I after 24 h at 20  $\mu$ M and two led to a decrease in both LC3-I and LC3-II. Compound **19** was selected as a high priority hit due to the combination of its potency in all three assays. In addition, several analogs of **19** were included in the HTS and we were able to determine the presence of preliminary SAR (Figure 48A,B). **19** was repurchased from ChemDiv and re-screened in dose in the NanoBRET assay to confirm potency ( $IC_{50} = 33.9 \mu$ M) (Figure 48C).

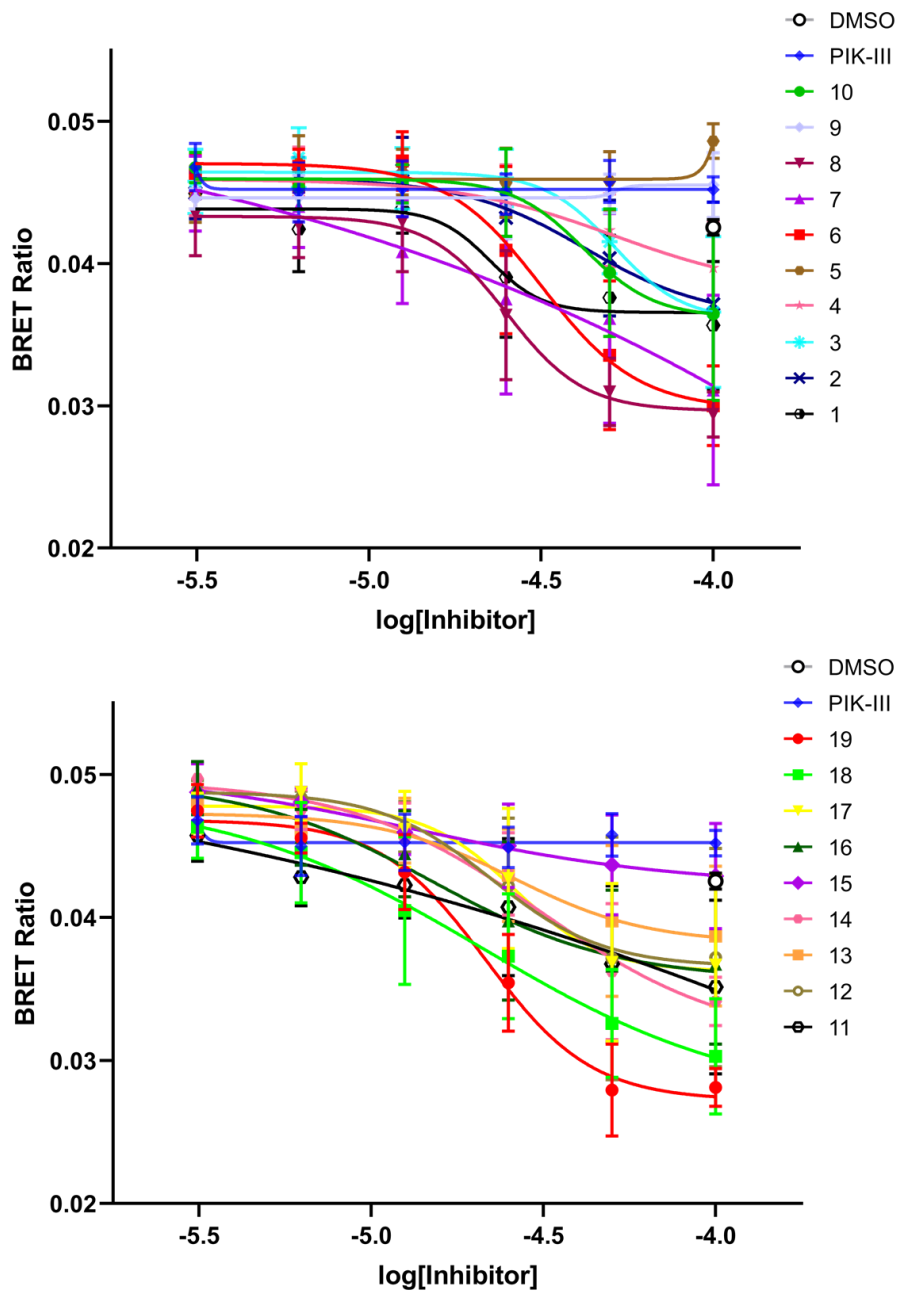


**Figure 46.** Dose curves of the 19 hits from pilot NanoBRET HTS. Hek293T cells were treated with 19 hit molecules in 6-point dose-response mode (100  $\mu$ M to 3.125  $\mu$ M) for 24 h. 16 out of the 19 hit molecules show a dose dependent reduction in NanoBRET ratio. **19** is shown in red and the negative control PIK-III is shown in blue and other hits are shown in multiple colors. DMSO is represented as an empty circle. Data are presented as the mean  $\pm$  SEM from two independent experiments in duplicate.

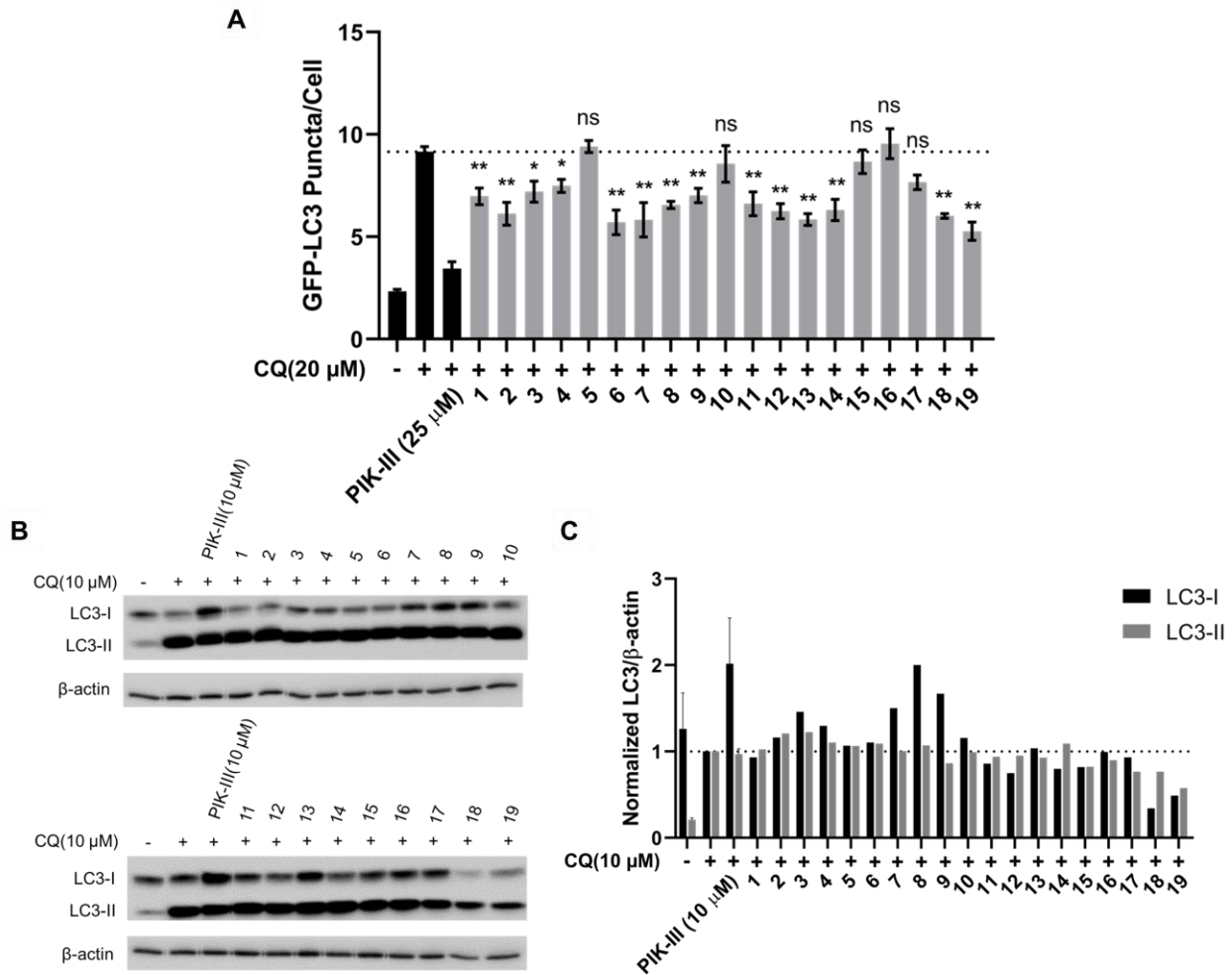


**Figure 47.** Prioritization of the 19 hits from pilot NanoBRET HTS through assessment of autophagy inhibition. (A) eGFP-LC3-expressing HeLa cells were treated with hits (25  $\mu$ M) or PIK-III for 20 h followed with 4 h of CQ treatment. Several compounds showed a decrease in eGFP-LC3 puncta relative to CQ control, indicating an inhibition of autophagy. Data are presented as mean  $\pm$  SEM from two independent experiments in duplicate. (B) LC3-I and LC3-II levels were determined by immunoblot following treatment of HeLa cells with either PIK-III or hits (20  $\mu$ M) for 20 h followed by 4 h of CQ treatment.  $\beta$ -actin is shown as a loading control. (C) Quantification of LC3-I and LC3-II normalized to  $\beta$ -actin. PIK-III caused an accumulation of LC3-I, indicating that LC3 lipidation was blocked, with several hits showing a similar increase (7,8,9). Others (18, 19) showed a decrease in both LC3-I and LC3-II levels, also indicating autophagy inhibition. Data were generated from one independent experiment with cherry-picked compounds. (\* $p$ <0.05, \*\* $p$ <0.01).

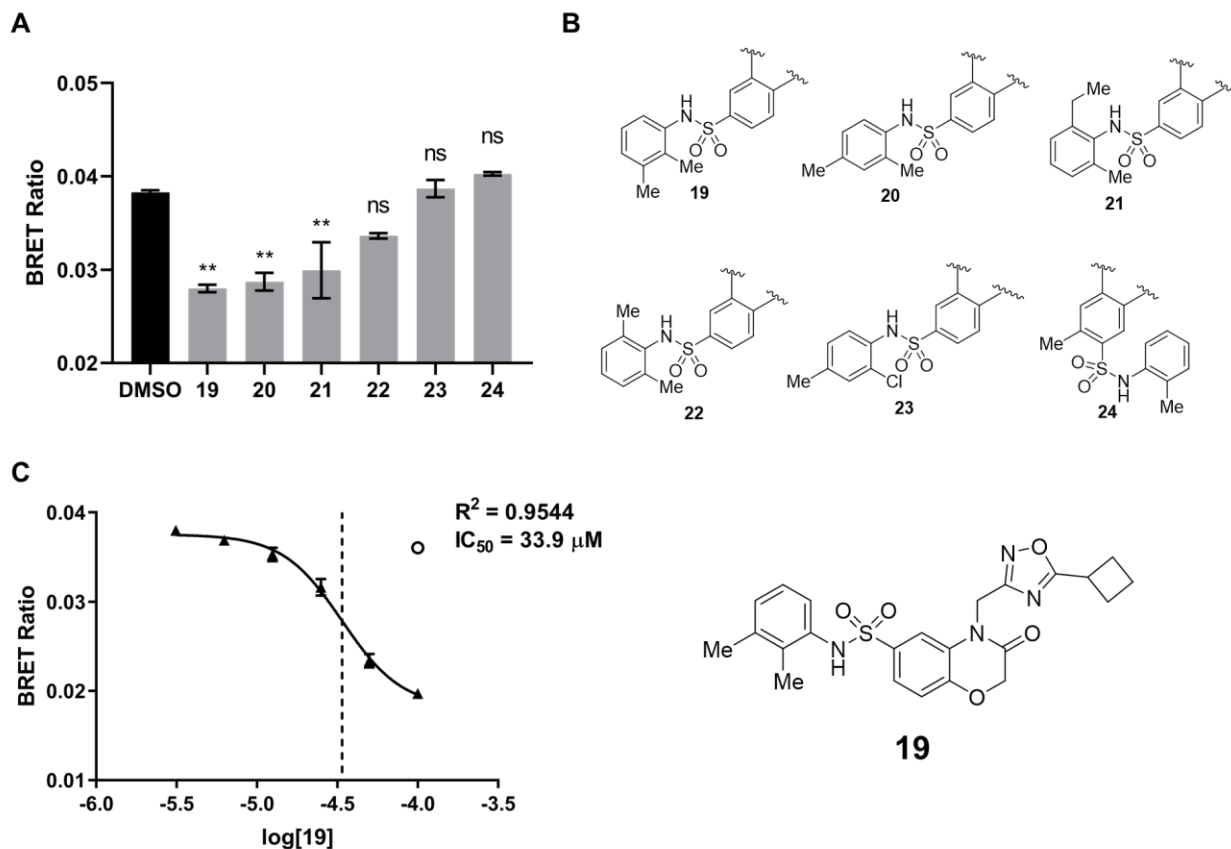


**Figure 48.** Limited SAR and potency of **19**. (A) The BRET ratios generated by derivatives of **19** that were present in the screened library. (B) Highlighted structural differences of the derivatives. Varying the position of sulfonamide appendage and position of aromatic ring substituents abolished the decrease in NanoBRET ratio. Data are presented as the mean  $\pm$  SEM of two independent experiments. (C) 6-point dose-response curve (100  $\mu M$  to 3.125  $\mu M$ ) of and chemical structure of **19**. This curve shows a dose-dependent reduction of the NanoBRET ratio, indicating disruption of the Beclin 1-ATG14L PPI. DMSO is represented as an empty circle. Data are presented as mean  $\pm$  SEM of three independent experiments carried out in duplicate. (\* $p < 0.05$ , \*\* $p < 0.01$ ).

#### E. Confirmation of the disruption of VPS34 Complex I formation by compound 19

Previous studies have shown that disruption of the Beclin 1-ATG14L interaction leads to the inhibition of VPS34 Complex I formation.<sup>260,263,331</sup> These studies, however, utilized genetic knockdown of ATG14L or the deletion of entire domains, not inhibition with small molecules, so we wanted to confirm that treatment with **19** would also disrupt the formation of Complex I. Additionally, using the NanoBRET assay we established that direct

VPS34 binders (SAR405, PIK-III) do not disrupt the Beclin 1-ATG14L interaction (Figure 49A); however, it was possible that upon binding these molecules disrupt the VPS34 Complex I through other conformational changes, and so we also wanted to check if this was true as well. To test this hypothesis, we used a previously generated NanoBRET vector which expressed ATG14L C-terminal HaloTag (ACH). As described in the methodology section, this fusion protein can react to form a covalent bond with the HaloTag ligand, thus allowing us to perform a pull-down for Complex I utilizing magnetic beads labeled with this ligand.<sup>315</sup> Hek293T cells were transfected with ACH vector in bulk and then treated with either **19**, PIK-III, or SAR405. After 8 h, cells were lysed and then incubated with the HaloTag magnetic beads for 4 hours, washed, and bound protein was eluted with buffer containing SDS. The lysate supernatant (S) and the SDS eluent (E) were then probed by western blot for the presence of each Complex I member (VPS34, VPS15, Beclin 1) and  $\beta$ -actin, but not ATG14L itself, because it would remain bound to the beads. Our results for this experiment demonstrated that treatment with **19** did effectively lead to Complex I disruption, as indicated by the lower quantities of each Complex I member protein relative to the DMSO control, while treatment with direct VPS34 inhibitors did not (Figure 50A).

These promising results led us to further investigate the specific mechanism of action behind the disruption of the Beclin 1-ATG14L interaction and whether it happened due to the direct binding of **19** to ATG14L. Because **19** proved to be insoluble in aqueous conditions above 100  $\mu$ M, we were limited in our ability to utilize direct biophysical methods such as isothermal calorimetry or surface plasmon resonance. To overcome these barriers, we performed a CETSA which involves determining the quantity of a target protein that remains soluble after the heating of intact cells, which allows for the generation of a melting curve and the determination of a  $T_m$  for ATG14L. Ligands that interact through direct binding should stabilize ATG14L and cause a rightward shift in the binding curve and  $T_m$ . For this assay, we utilized A549 cells due to their higher observed expression levels of ATG14L. Cells were treated with **19** for 24 h, to mirror the treatment time for the NanoBRET experiment, heat shocked for 3 min over a temperature range between 48 – 56 °C, and then lysed by freeze thaw. Debris and aggregated protein were removed by centrifugation, and the supernatant was probed by western blot for the quantity of ATG14L. We saw an increase in ATG14L quantity at elevated temperatures as compared to the DMSO-treated control, which may indicate that **19** potentially stabilized ATG14L by directly binding to it (Figure 50B,C). However, the produced  $T_m$  shift of 0.34°C was not great enough to confirm that this stabilization was significant, so further experiments with more potent and soluble derivatives will be necessary to confirm binding.

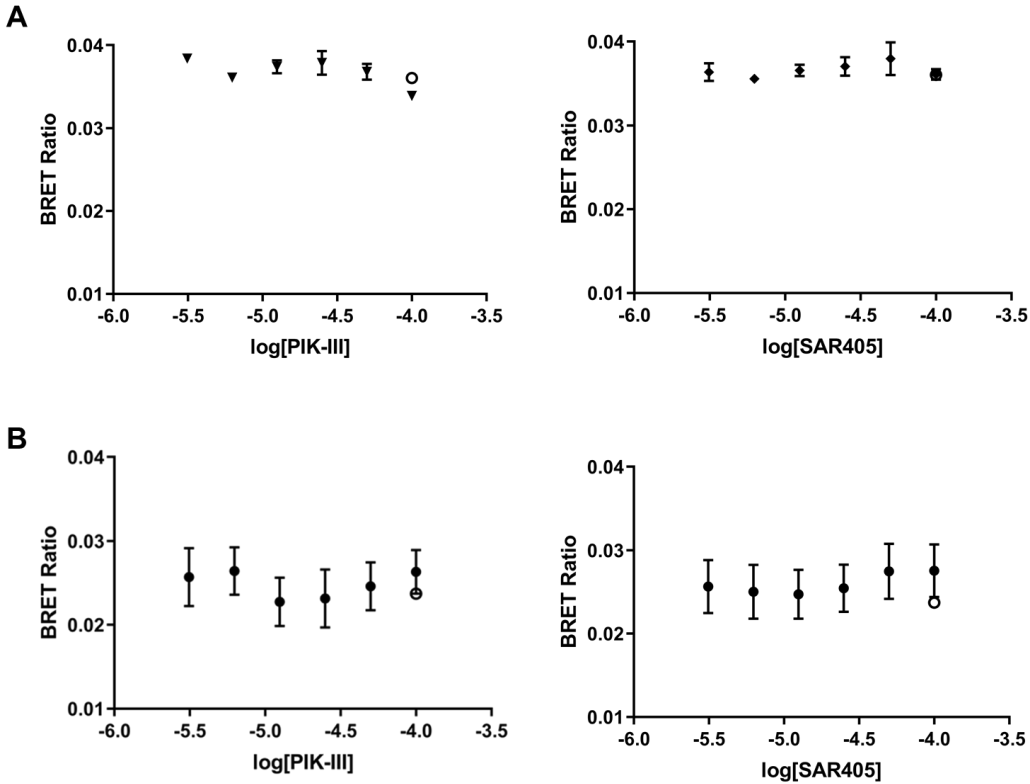


**Figure 49.** Effect of VPS34 inhibitors on the protein-protein interactions of Beclin1 in Hek293T cells. (A) & (B) 6-point dose curves (100  $\mu$ M to 3.125  $\mu$ M) of PIK-III and SAR405 do not show a disruption of either the Beclin1 and ATG14L interaction (A) or the Beclin1 and UVRAG interaction (B). DMSO is represented as an open circle. Data are presented as the mean  $\pm$  SEM of three independent experiments.

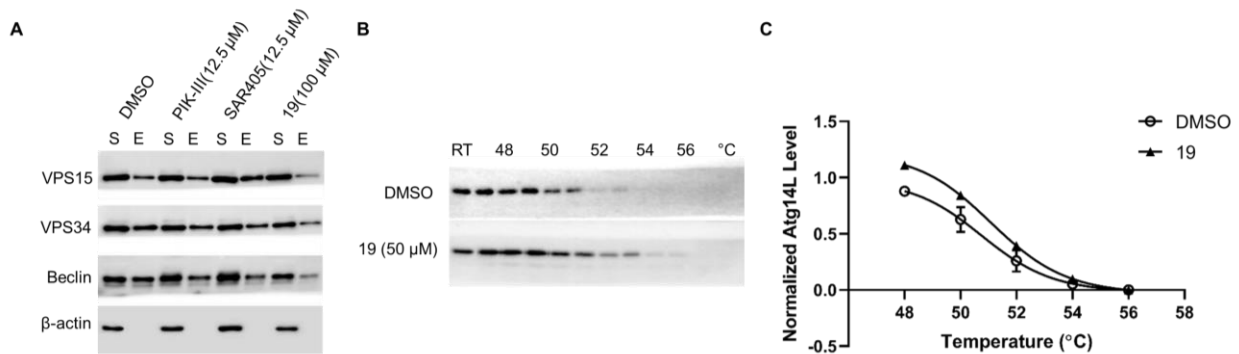


**Figure 50.** Compound **19** inhibits autophagy through disruption of VPS34 Complex I by potential binding to ATG14L. (A) Representative blot from three independent pull-down experiments in Hek293T cells treated with **19**, PIK-III, SAR405 for 8 h. Supernatant (S) and eluent (E) for each treatment were analyzed by immunoblot for the presence of each protein found in Complex I. VPS34 inhibitors, PIK-III and SAR405, did not lower the amount of each protein found in the eluent while **19** did, indicating Complex I disruption. (B) Representative blots from three independent CETSA experiments targeting ATG14L in A549 cells treated with **19** (50  $\mu$ M) for 24 h. (C) ATG14L levels were normalized to room temperature DMSO controls for each replicate and the mean  $\pm$ SEM of three independent experiments is reported.

## **F. Evaluation of autophagy inhibition caused by Complex I disruption**

During hit selection and prioritization, we were not able to extensively replicate the experiments used in selection due to the limited quantity of each compound available. Therefore, we wanted to replicate and further characterize the ability of **19** to disrupt autophagy at a shorter time point. To do this, we used LC3 immunoblotting, where cells were first treated with **19**, PIK-III, or SAR405, and then LC3-II accumulation was induced by treatment with CQ (late-stage autophagy inhibition) for 4 h or Torin 1 (autophagy activation) for 1 h.<sup>224</sup> For both conditions, **19** showed a significant decrease in LC3-II formation, though it had a lower potency than PIK-III or SAR405 (Figure 51A-D). Interestingly, unlike PIK-III and SAR405, which led to an accumulation of LC3-I, **19** led to a decrease in LC3-I. A similar effect has been noted in cells treated with Spautin-1, a small molecule that induces the degradation of Beclin 1 by blocking its deubiquitination by USP10 and USP13.<sup>333</sup> Lastly, we confirmed that treatment with **19** decreased CQ-induced eGFP-LC3 puncta accumulation even at this shorter time point (Figure 51E). Overall, these results paired with the data from the initial hit selection indicate that **19** can inhibit autophagy at two time points and in two different cell lines, although to a lesser extent as compared to direct VPS34 inhibitors.

Although the lack of relative potency could be due to the unoptimized nature of **19**, these results also highlight the importance of developing small molecule inhibitors of PPIs in order to better understand the effect of their disruption on cellular phenotypes. Previous studies have shown that ATG14L knockdown or mutation inhibited LC3-II build-up under both basal and induced conditions, and in some cases inhibited LC3-II formation completely.<sup>263,331,334</sup> But, this phenotype is not without controversy, as it has also been demonstrated that knockdown of ATG14L or its partner Beclin 1 led instead to no change in LC3-II levels or, in some cases, accumulation, even though autophagy was dysregulated.<sup>247,335,336</sup> Other research has also demonstrated that autophagy-deficient cells can still accumulate LC3-labeled puncta, even when LC3-II formation is abrogated, calling into question the reliability of this biomarker for the quantification of autophagic flux for early autophagy inhibition.<sup>337</sup> Finally, because most autophagy proteins exhibit a multitude of roles even within autophagy, small-molecule targeting of specific autophagy-related PPIs, instead of whole protein deletion, will likely clarify the true importance of each interaction in autophagy function. In the future, it will be important to confirm that more potent derivatives of **19** show other signs of autophagy inhibition, such as the generation of malformed and non-functional autophagosomes.<sup>335</sup>

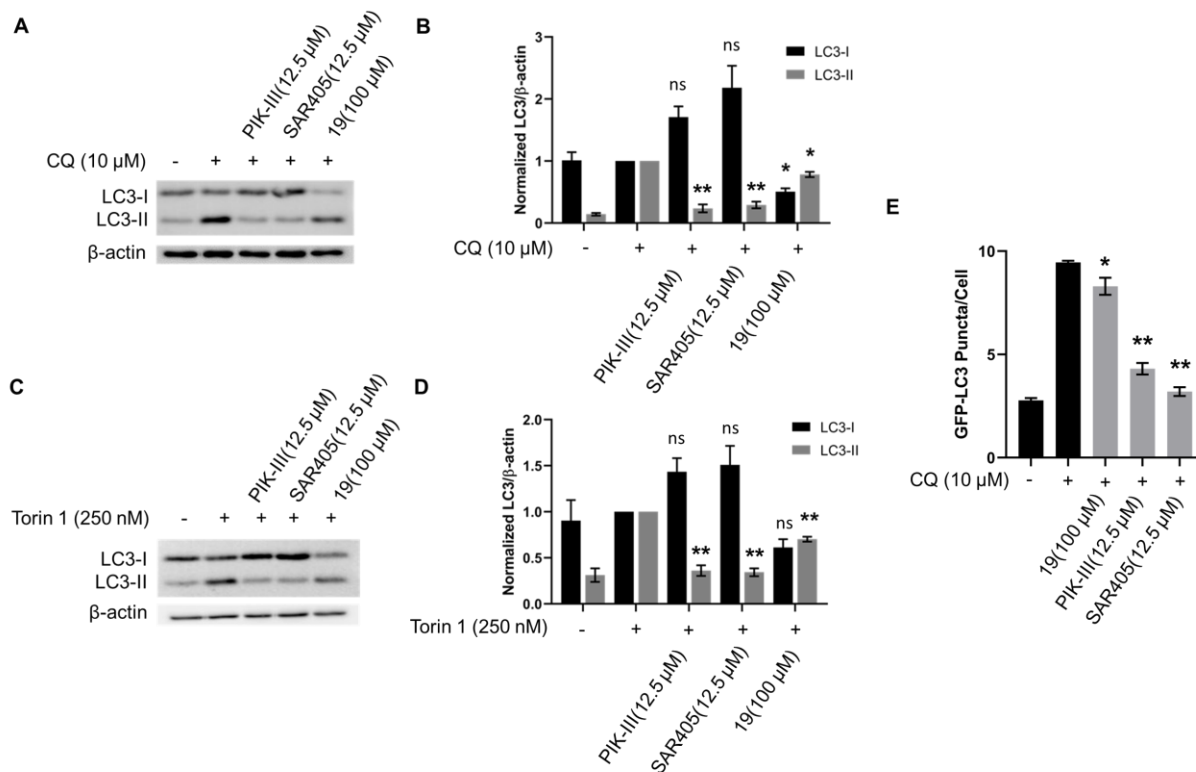


**Figure 51.** Evaluation of compound treatment on autophagy in A549 and HeLa cells. A549 cells were treated with **19**, PIK-III, SAR405 for 4 h or 7 h and then either CQ or Torin 1 was added and cells were incubated for an additional 4 h or 1 h, respectively, and the amount of LC3 and  $\beta$ -actin was quantified by immunoblot. (A) & (C) Representative blots showing the effect on LC3 levels of compounds co-treated with either CQ or Torin-1 (B) & (D) LC3-I and LC3-II levels were normalized to the CQ or Torin 1 control. While all compounds show a decrease in LC3-II, which is consistent with the inhibition of autophagy earlier in the pathway, **19** is the only one that also shows a corresponding decrease in LC3-I levels. Data are presented as mean  $\pm$ SEM of three independent experiments (\* $p$ <0.05, \*\* $p$ <0.01). (E) eGFP-LC3 expressing HeLa cells were treated with **19**, PIK-III, or SAR405 for 4 h and then CQ was added for 4 h. CQ inhibits the turnover of autophagosomes, causing an accumulation of eGFP-LC3 puncta. Data are presented as mean  $\pm$ SEM with three independent experiments in duplicate. (\* $p$ <0.05, \*\* $p$ <0.01).

### G. Insights into the impact of selective Complex I disruption on vesicle trafficking

Our previous experiments established that **19** was able to inhibit autophagy through the disruption of the Beclin 1-ATG14L interaction, but this inhibition may not be specific if **19** also disrupts the interaction of Beclin 1 with its other protein partners, such as UVRAG, that is critical for the formation of VPS34 Complex II. A specific PPI inhibitor should only inhibit the formation of the autophagy initiation complex (Complex I), leaving the

endosomal trafficking complex (Complex II) intact. Within Complex II, ATG14L is replaced with UVRAG, which interacts with Beclin 1 through a CCD with greater affinity than ATG14L.<sup>264</sup> In order to confirm the selectivity of **19** for the Beclin 1-ATG14L interaction, we used the NanoBRET assay. We followed the same developmental procedure as for our HTS, generating pairs of vectors coding for fusions of UVRAG and Beclin 1 (Table 4) and testing them to see which produced the most robust BRET signal (Figure 52). The chosen vector pair expressed UVRAG N-terminal NanoLuciferase (UNL) and Beclin 1 N-terminal HaloTag (BNH) and was then used to test the dose-dependent disruption of this interaction under treatment with **19**, PIK-III, or SAR405. As with our HTS, Hek293T cells were transfected first with the UNL:BNH pair at a 1:1 ratio and then treated with compounds for 24 h. Importantly, **19** did not show a dose-dependent change in BRET signal, indicating that it did not disrupt this interaction (Figure 53A). As with the Beclin 1-ATG14L, PIK-III and SAR405 also did not induce disruption of this interaction (Figure 49B).

Next, we wanted to demonstrate that this selectivity also meant that **19** would not inhibit vesicle trafficking in the same way as PIK-III and SAR405. We conducted three experiments to characterize its overall effects on vesicle trafficking. To analyze its impact on intracellular transport we evaluated the maturation of Cathepsin D by immunoblot. A549 cells were treated with **19**, PIK-III, SAR405, or CQ for 8 h and then lysed. The quantities of Cathepsin D and  $\beta$ -actin were determined by western blot. As expected, treatment with CQ, PIK-III, or SAR405 caused an accumulation of procathepsin D due to their inhibition of either lysosome function or vesicle trafficking, but **19** did not cause accumulation (Figure 53B). Additional characterization of the effects of compound **19** on intracellular vesicle trafficking was accomplished by monitoring A549 cells treated with **19**, PIK-III and SAR405 for 8 h using phase contrast microscopy. We observed the formation of large vacuole-like vesicles by phase-contrast microscopy in cells treated with PIK-III and SAR405. In contrast, cells treated with the Beclin 1-ATG14L PPI inhibitor, **19**, did not exhibit this phenotype (Figure 53C). The formation of such large vesicles was previously shown to be caused by direct VPS34 inhibition.<sup>250</sup>

Lastly, using an assay based on the uptake and degradation of DQ-BSA, we tested the effect of **19** on endosomal uptake and processing. DQ-BSA is heavily labeled with BODIPY dyes that self-quench. Following endosomal uptake and lysosomal fusion, the protein is degraded and produces a robust fluorescent signal that can be measured by fluorescence microscopy. A549 cells were pulsed with DQ-BSA for 1 h and treated with **19**, PIK-III,

SAR405 or BafA1 for 8 h, after which cells were imaged. Whereas treatment with PIK-III, SAR405 and BafA1 caused a significant decrease in lysosomal processing of DQ-BSA, as indicated by the reduced puncta count, compound **19** caused an increase in DQ-BSA puncta (Figure 53D). Beclin 1 is known to exist in equilibrium between three binding complexes: a Beclin 1 homodimer and two heterodimers (Beclin 1-ATG14L and Beclin 1-UVRAG).<sup>264</sup> Recent work has demonstrated that the inhibition of homodimer formation through treatment with a peptide that mimics this binding interface activated both autophagy and endocytic trafficking. This may be due to the increase in free Beclin 1 that can readily associate with both ATG14L and UVRAG.<sup>265</sup> This study also demonstrated that the Beclin 1-UVRAG interaction was more potent than the Beclin 1-ATG14L interaction; therefore, it is possible that a small molecule could selectively inhibit the association of Beclin 1-ATG14L and cause Beclin 1 to redistribute into Beclin 1-UVRAG complex upregulating DQ-BSA uptake and degradation. Taken together, these results show that specific disruption of Beclin 1-ATG14L over the Beclin 1-UVRAG interaction conferred selectivity towards autophagy inhibition over vesicle trafficking.

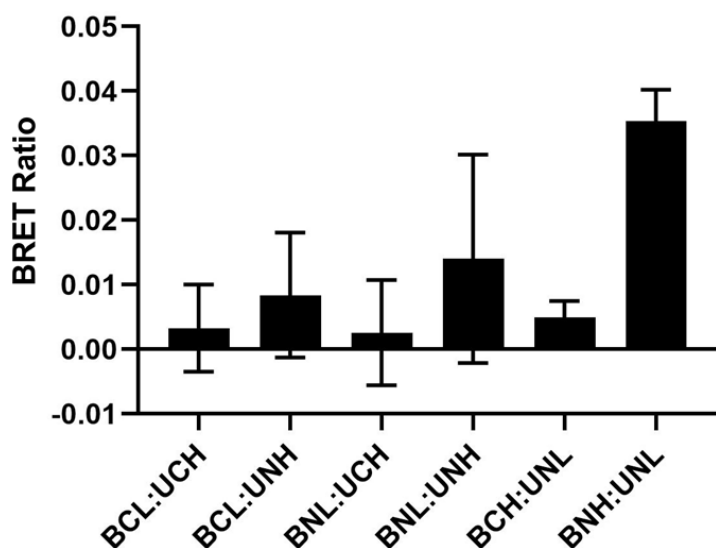


**Figure 52.** Development of NanoBRET assay targeting the PPI of Beclin 1 and UVRAG in Hek293T cells. All data are presented as mean  $\pm$  SEM generated from eight technical replicates. Cells were transfected with a 1:1 ratio of each donor and acceptor vector pair. UVRAG-NanoLuc pairs were excluded for lack of donor signal and **BNH:UNL** was chosen as the best pair.

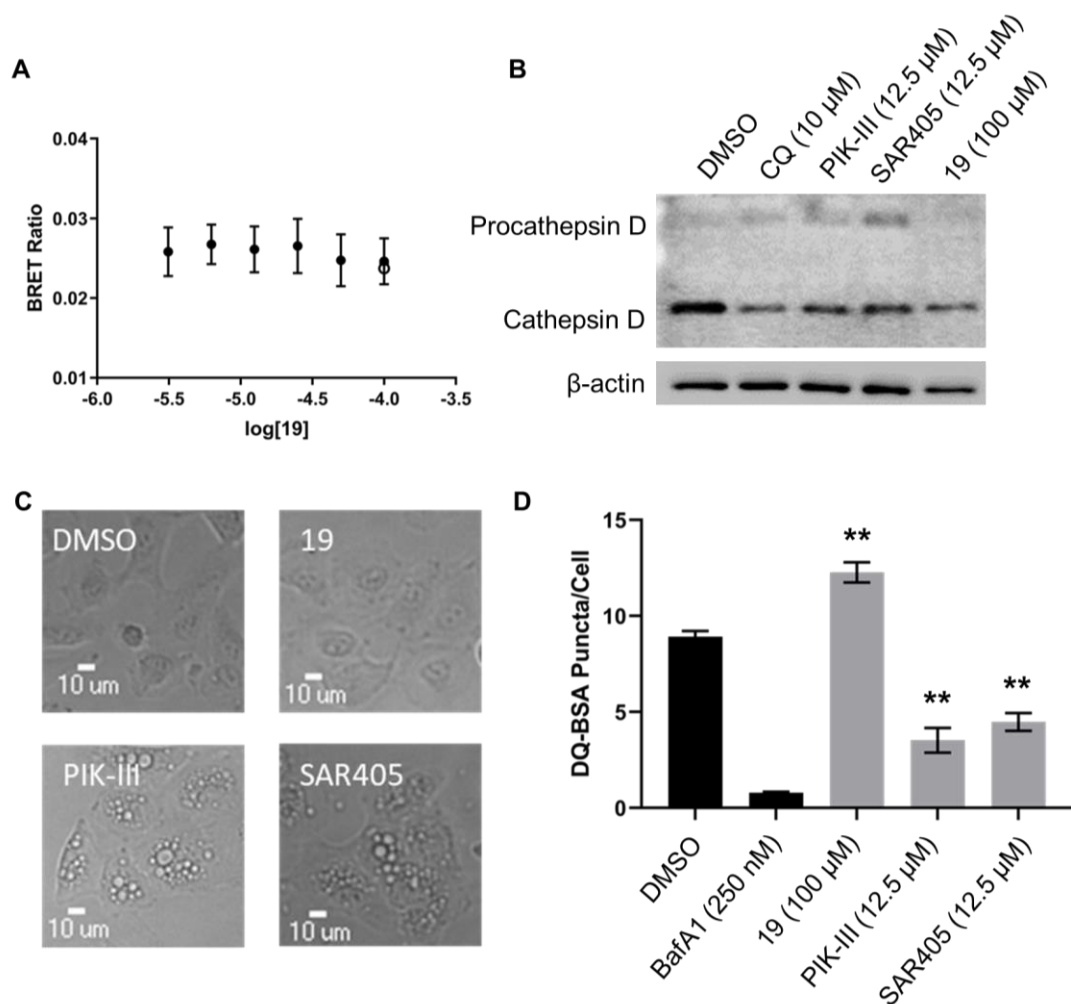


**Figure 53.** Determination of specificity of **19** for the autophagic pathway as compared to VPS34 inhibitors. (A) 6-point dose-response curve (100  $\mu$ M to 3.125  $\mu$ M) of compound **19** did not show a dose-dependent decrease in the NanoBRET ratio, indicating that the Beclin 1 and UVRAG interaction was not disrupted in Hek293T cells. DMSO is represented as an open circle. (B) A549 cells were treated with **19**, PIK-III, SAR405, or CQ for 8 h, and the quantities of Cathepsin D and  $\beta$ -actin were determined by immunoblot. Under normal conditions, pro-Cathepsin D is rapidly transported to the lysosome in order to be processed into Cathepsin D. Blot is representative of three independent experiments. (C) A549 cells were treated with **19** (100  $\mu$ M), PIK-III (12.5  $\mu$ M) or SAR405 (12.5  $\mu$ M) for 8 h. Images shown are representative of three independent experiments. (D) A549 cells were treated with DQ-BSA for 1 h and then treated with **19**, PIK-III, SAR405, or BafA1 for 8 h. BafA1 (lysosomotropic V-ATPase inhibitor). Data are presented as mean  $\pm$ SEM of three independent experiments (\*\* $p$ <0.01).

## **H. Development and validation of FP assay targeting the ATG5-ATG16L1 interaction**

The other autophagy-specific PPI of interest was the ATG5-ATG16L1 interaction that is critical for the formation and proper localization of the ATG5-ATG12-ATG16L1 complex, that mediates the lipidation of LC3. As described in the methodology section the first step in the development of the assay targeting this interaction was the preparation of reagents. This included the peptide synthesis of rhodamine labeled (Rho-ATG16N) and unlabeled (ATG16N) peptides that correspond to N-terminal  $\alpha$ -helix of ATG16L1 along with the purification of ATG5 as described in a previous section. Using these reagents, we conducted several experiments that would confirm that FP was a viable method to use to quantify the interaction between ATG5 and ATG16L1 and to enable small-molecule screening in order to find autophagy-specific PPI inhibitors. The first experiment was conducted by titrating Rho-ATG16N with increasing amounts of MBP-ATG5. Upon excitation with a plane of polarized light free Rho-ATG16N should emit depolarized light due to its rapid rotation in solution, while bound Rho-ATG16N would continue to emit polarized light as it would rotate more slowly. We saw a dose-dependent increase in the polarization (mP) of the emitted light (Figure 54A). Because we had to retain the MBP tag due to the insolubility of ATG5 at high concentrations, the next experiment we conducted tested whether the isolated MBP tag could also potentially bind Rho-ATG16N as indicated by an increase in the polarization of the light. Thus, Rho-ATG16N was titrated with MBP in the same manner as with the MBP-ATG5 and it was established that there is no significant binding occurring, although there is a slight increase in the observed mP at the highest doses of MBP (Figure 54B). Lastly, to confirm the overall specificity of the interaction between the Rho-ATG16N and the MBP-ATG5 we conducted a final experiment involving the unlabeled peptide ATG16N. Because their sequence is exactly the same, they should compete for the same binding interface on ATG5. We titrated a solution of Rho-ATG16N and ATG5 with an increasing amount of ATG16N and observed a dose-dependent reduction in the mP (Figure 54C). This demonstrates that the interaction of Rho-ATG16N is specific because it is being displaced by the ATG16N causing an increase of free Rho-ATG16N in solution which emits depolarized light. Additionally, we demonstrated that there is no significant self-association happening between the peptides themselves by titrating Rho-ATG16N with ATG16N. In conclusion, these results demonstrate that FP can quantify this interaction and that this assay can be used as the basis for an HTS campaign to find autophagy inhibitors targeting ATG5-ATG16L1. Recent work has focused on using this assay to screen small molecules. Promising hits are being optimized in order to increase their

potency to further investigate the effects that the selective disruption of the ATG5-ATG16L1 interaction will have on autophagy.

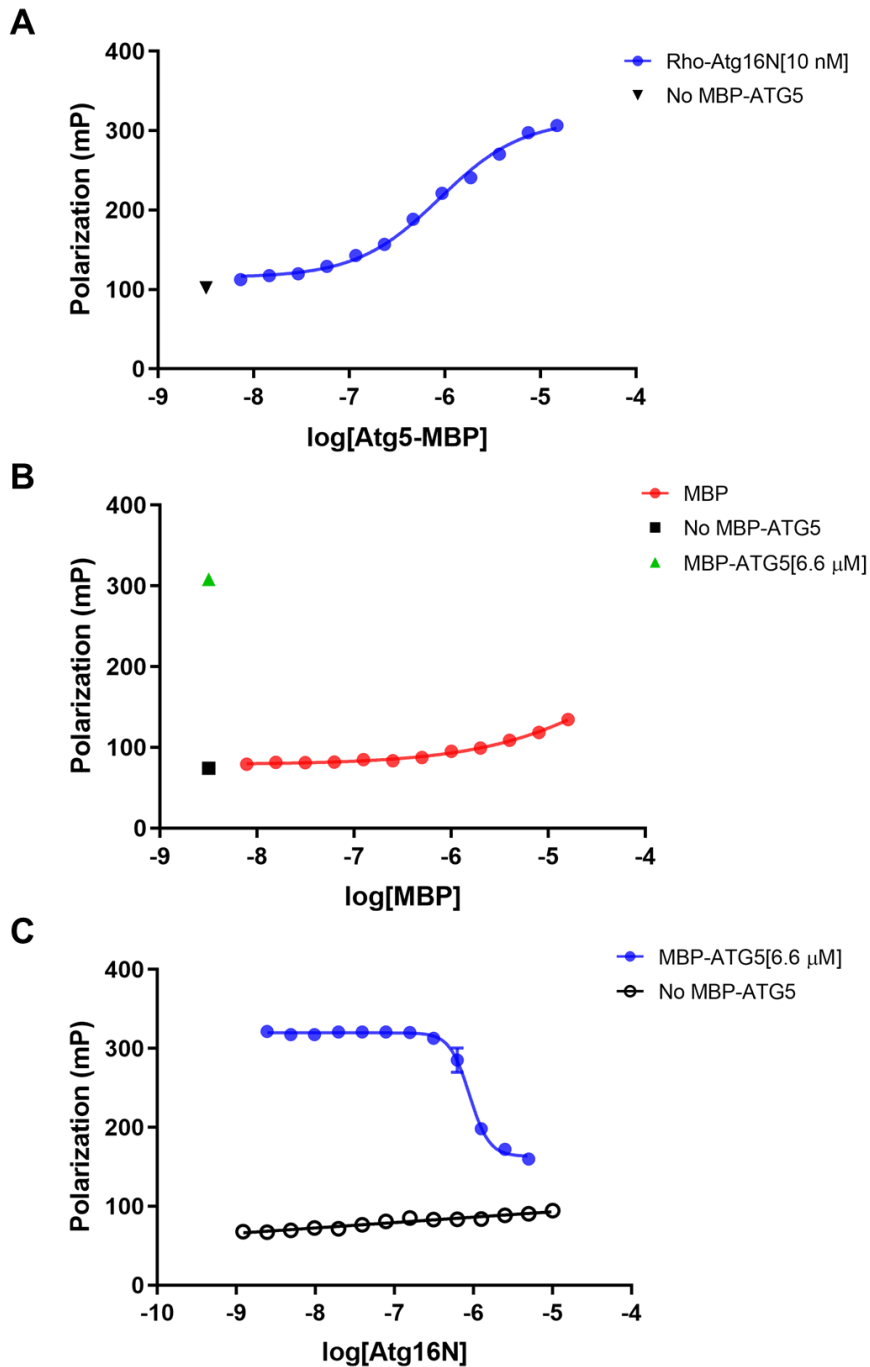


**Figure 54.** Development of the ATG5-ATG16L1 FP assay. (A) A 12-point dose curve of MBP-ATG5 (15 μM to 7.3 nM) and Rho-ATG16N (10 nM) shows an increase in mP. (B) A 12-point dose curve of MBP (16 μM to 7.8 nM) and Rho-ATG16N (10 nM) shows little increase in mP. (C) A competition assay between labeled and unlabeled ATG16N peptides. A 12-point dose curve of ATG16N (5 μM to 2.4 nM), MBP-ATG5 (6.6 μM) and Rho-ATG16N (10 nM) shows a decrease in mP.

#### IV. Conclusion

This chapter aimed to establish the importance of developing more useful and autophagy-specific probes in order to provide tools to understand the role of autophagy in human disease. Due to its broad homeostatic role, autophagy is implicated in a diverse array of malignancies from cancer to immune diseases and even aging. The current generation of autophagy probes lack specificity for the autophagy pathways and are thus insufficient for a more thorough understanding of autophagic processes underlying these diseases.<sup>222</sup> Because autophagy is interlinked with a multitude of cellular processes and because the essential autophagy proteins also play roles in different pathways, it has been difficult to find specific and potent modulators. We aimed to remedy this by targeting autophagy-specific PPIs with small molecules. Although PPIs were notorious for being “undruggable targets” for many decades, in the last ten years several dozen molecules have emerged as PPI modulators with many even making it into the clinic. This development has all allowed for the characterization of the types of chemical structures that are likely to inhibit protein binding along with the generation of novel methods that can effectively measure protein interactions both within cells and *in vitro*. However, despite these advancements, no significant efforts have yet emerged showing autophagy-specific PPI modulators outside of well-known probes such as rapamycin. We aimed to remedy this by targeting two PPIs found within the autophagy initiation pathway, the interaction between Beclin 1-ATG14L, which is critical to the formation of VPS34 Complex I,<sup>259</sup> and the interaction between ATG5-ATG16L1, which is critical to the formation of ATG5-ATG12-ATG16L1 complex.<sup>150</sup>

Herein, we described the development of a NanoBRET-based HTS targeting the Beclin 1-ATG14L interaction, which was then successfully used to identify inhibitors of this interaction by screening a curated set of 2,560 molecules enriched for properties found in PPI binders. This interaction has been established as critical for the formation of the autophagy initiation complex, VPS34 Complex I, which is responsible for the generation of the PI3P that forms the highly curved double membrane of the autophagosome. After confirmation that disruption was dose-dependent, hits were prioritized by their ability to inhibit LC3 lipidation, which was measured by quantifying eGFP-LC3 puncta with fluorescence microscopy and immunoblotting targeted towards LC3. One molecule, **19**, was capable of inhibiting LC3-II accumulation both under late-stage inhibition (CQ treatment) and autophagy induction (Torin 1 treatment). We also showed that treatment with **19** disrupted the formation of the autophagy initiation complex, VPS34 Complex I, and used CETSA to evaluate its potential direct binding to ATG14L. Lastly, we

obtained evidence for our original hypothesis, by demonstrating that **19** did not disrupt the Beclin 1-UVRAG interaction, using the NanoBRET assay, and therefore should have a limited impact on vesicle trafficking. We confirmed this impact through a combination of experiments that measured cathepsin D maturation, DQ-BSA uptake and degradation, and large vesicle formation. In each case, **19** showed no change in phenotype or caused upregulation relative to the DMSO control, in contrast to the inhibitory effects of direct VPS34 inhibitors, PIK-III and SAR405. Future work for this project will be directed towards the synthesis of more potent analogues of **19** in order to characterize its molecular target in detail and further confirm the phenotype generated by the selective disruption of VPS34 Complex I *in vitro* and *in vivo* with endogenous proteins. Critically, we effectively demonstrate the viability of targeting PPIs found within the autophagy pathway as a strategy for developing more specific molecules that can potentially become therapeutic leads. We have also highlighted the importance of the development of small-molecule probes that can more thoroughly characterize each key PPI within this important cellular pathway.

Outside of the Beclin 1 interactome there are several other PPIs in the autophagy pathway that occur through the association of defined secondary structures. One such interaction is between ATG5 and the N-terminal  $\alpha$ -helical domain of ATG16L1. This interaction has been demonstrated to be critical for the activation and localization of the endogenous ATG5-ATG12 conjugate to the early phagophore. We chose to target this interaction because the ATG5-ATG12-ATG16L1 complex is part of the ubiquitin-like conjugation system that is responsible for the lipidation of LC3-I into LC3-II.<sup>150</sup> Autophagy is dysfunctional in cells in which the generation of LC3-II is inhibited, due to its role in mediating the formation of the autophagosome and directing cargo for internalization. We hypothesize that a small molecule that disrupts formation of the ATG5-ATG16L1 complex will inhibit autophagic flux in cells. Towards this goal, we designed another HTS compatible assay based around the FP method, in which the polarization of light emitted by a fluorescent peptide representing ATG16L1 could be used to monitor its binding to MBP-ATG5. We effectively demonstrated that our assay specifically measured this interaction through a series of three experiments. These were the titration of free Rho-ATG16N with MBP-ATG5, the titration of Rho-ATG16N with MBP, and a competition assay in which Rho-ATG16N and MBP-ATG5 were titrated with increasing amounts of the unlabeled peptide ATG16N. Small molecules discovered by this assay will serve as the starting point for the generation of potent and specific PPI inhibitors that target the autophagy initiation pathway. Such molecules that selectively inhibit autophagy will allow for the evaluation of autophagy inhibition in

various disease states. Additionally, the proteins of this complex also have roles outside of canonical autophagy, and the specific, spatiotemporal disruption of this complex would aid in elucidating the purpose of these protein in other cellular functions. For example, ATG16L1 and ATG5 are involved in LAP,<sup>338</sup> and ATG5 is also involved in lymphocyte development and proliferation, MHC II antigen presentation, and apoptosis, among other roles.<sup>268</sup>

In conclusion, we developed two effective assays that target PPIs found in the autophagy pathway and demonstrated the viability of using small molecules to perturb these interactions. Molecules that are discovered by these assays will be the basis for novel therapeutics, especially for the inhibition of autophagy in cancer. Additionally, in contrast to genetic perturbation, a PPI inhibitor retains the endogenous state of its target protein allowing for the confirmation of the phenotype generated when only that specific PPI is disrupted. Therefore, the discovery of selective and potent PPI inhibitors could potentially limit off-target effects, providing a promising strategy to enable clarification of the role of autophagy in cancer and other diseases that rely on homeostasis as well elucidate the other roles of autophagic genes within the cell. The autophagy pathway is heavily regulated by protein-protein interactions, but reliable structural and biochemical data for many of them remains unavailable and is a limiting factor for the design of further assays. Other targets outside of protein-protein interactions, for instance protein-lipid interactions and the post-translational modifications on autophagy protein are also promising. As an example, it has recently been demonstrated that ATG14L localizes to the autophagosome by recognizing PI3,5P<sub>2</sub> and that the knockdown of PIPKIγ5, which binds to ATG14L and is responsible for generating this lipid, leads to autophagy inhibition and ATG14L and Beclin 1 instability.<sup>334</sup> Therefore, exciting opportunities for further autophagy-specific probe development remain and must be explored not only to develop new drugs, but to further our understanding of the one of the most important and primordial parts of cell biology.

## CITED LITERATURE

- (1) Pereira, D. A.; Williams, J. A. Origin and Evolution of High Throughput Screening. *Br. J. Pharmacol.* **2007**, *152* (1), 53–61. <https://doi.org/10.1038/sj.bjp.0707373>.
- (2) Macarron, R.; Banks, M. N.; Bojanic, D.; Burns, D. J.; Cirovic, D. A.; Garyantes, T.; Green, D. V. S.; Hertzberg, R. P.; Janzen, W. P.; Paslay, J. W.; Schopfer, U.; Sittampalam, G. S. Impact of High-Throughput Screening in Biomedical Research. *Nat. Rev. Drug Discov.* **2011**, *10* (3), 188–195. <https://doi.org/10.1038/nrd3368>.
- (3) Favalli, N.; Bassi, G.; Scheuermann, J.; Neri, D. DNA-Encoded Chemical Libraries: Achievements and Remaining Challenges. *FEBS Lett.* **2018**, *592* (12), 2168–2180. <https://doi.org/10.1002/1873-3468.13068>.
- (4) Munos, B. Lessons from 60 Years of Pharmaceutical Innovation. *Nat. Rev. Drug Discov.* **2009**, *8* (12), 959–968. <https://doi.org/10.1038/nrd2961>.
- (5) Mullard, A. 2019 FDA Drug Approvals. *Nat. Rev. Drug Discov.* **2020**, *19* (2), 79–84. <https://doi.org/10.1038/d41573-020-00001-7>.
- (6) Bohacek, R. S.; McMartin, C.; Guida, W. C. The Art and Practice of Structure-Based Drug Design: A Molecular Modeling Perspective. *Med. Res. Rev.* **1996**, *16* (1), 3–50. [https://doi.org/10.1002/\(SICI\)1098-1128\(199601\)16:1<3::AID-MED1>3.0.CO;2-6](https://doi.org/10.1002/(SICI)1098-1128(199601)16:1<3::AID-MED1>3.0.CO;2-6).
- (7) Butler, M. S.; Fontaine, F.; Cooper, M. A. Natural Product Libraries: Assembly, Maintenance, and Screening. *Planta Med.* **2014**, *80* (14), 1161–1170. <https://doi.org/10.1055/s-0033-1360109>.
- (8) Liu, R.; Li, X.; Lam, K. S. Combinatorial Chemistry in Drug Discovery. *Curr. Opin. Chem. Biol.* **2017**, *38*, 117–126. <https://doi.org/10.1016/j.cbpa.2017.03.017>.
- (9) Galloway, W. R. J. D.; Isidro-Llobet, A.; Spring, D. R. Diversity-Oriented Synthesis as a Tool for the Discovery of Novel Biologically Active Small Molecules. *Nat. Commun.* **2010**, *1* (1), 1–13. <https://doi.org/10.1038/ncomms1081>.
- (10) Butler, M. S. The Role of Natural Product Chemistry in Drug Discovery. *J. Nat. Prod.* **2004**, *67* (12), 2141–2153. <https://doi.org/10.1021/np040106y>.
- (11) Newman, D. J.; Cragg, G. M. Natural Products as Sources of New Drugs over the Nearly Four Decades from 01/1981 to 09/2019. *J. Nat. Prod.* **2020**. <https://doi.org/10.1021/acs.jnatprod.9b01285>.
- (12) Natural Product Libraries <https://nccih.nih.gov/grants/naturalproducts/libraries> (accessed Mar 25, 2020).
- (13) Atanasov, A. G.; Waltenberger, B.; Pferschy-Wenzig, E.-M.; Linder, T.; Wawrosch, C.; Uhrin, P.; Temml, V.; Wang, L.; Schwaiger, S.; Heiss, E. H.; Rollinger, J. M.; Schuster, D.; Breuss, J. M.; Bochkov, V.; Mihovilovic, M. D.; Kopp, B.; Bauer, R.; Dirsch, V. M.; Stuppner, H. Discovery and Resupply of Pharmacologically Active Plant-Derived Natural Products: A Review. *Biotechnol. Adv.* **2015**, *33* (8), 1582–1614. <https://doi.org/10.1016/j.biotechadv.2015.08.001>.
- (14) Henrich, C. J.; Beutler, J. A. Matching the Power of High Throughput Screening to the Chemical Diversity of Natural Products. *Nat. Prod. Rep.* **2013**, *30* (10), 1284–1298. <https://doi.org/10.1039/c3np70052f>.
- (15) Houghten, R. A. General Method for the Rapid Solid-Phase Synthesis of Large Numbers of Peptides: Specificity of Antigen-Antibody Interaction at the Level of Individual Amino Acids. *Proc. Natl. Acad. Sci. U. S. A.* **1985**, *82* (15), 5131–5135. <https://doi.org/10.1073/pnas.82.15.5131>.
- (16) Houghten, R. A.; Pinilla, C.; Blondelle, S. E.; Appel, J. R.; Dooley, C. T.; Cuervo, J. H. Generation and Use of Synthetic Peptide Combinatorial Libraries for Basic Research and Drug Discovery. *Nature* **1991**, *354* (6348), 84–86. <https://doi.org/10.1038/354084a0>.

- (17) Frankel, A.; Millward, S. W.; Roberts, R. W. Encodamers: Unnatural Peptide Oligomers Encoded in RNA. *Chem. Biol.* **2003**, *10* (11), 1043–1050. <https://doi.org/10.1016/j.chembiol.2003.11.004>.
- (18) Heinis, C.; Rutherford, T.; Freund, S.; Winter, G. Phage-Encoded Combinatorial Chemical Libraries Based on Bicyclic Peptides. *Nat. Chem. Biol.* **2009**, *5* (7), 502–507. <https://doi.org/10.1038/nchembio.184>.
- (19) Tibbitts, J.; Canter, D.; Graff, R.; Smith, A.; Khawli, L. A. Key Factors Influencing ADME Properties of Therapeutic Proteins: A Need for ADME Characterization in Drug Discovery and Development. *mAbs* **2016**, *8* (2), 229–245. <https://doi.org/10.1080/19420862.2015.1115937>.
- (20) Bunin, B. A.; Ellman, J. A. A General and Expedient Method for the Solid-Phase Synthesis of 1,4-Benzodiazepine Derivatives. *J. Am. Chem. Soc.* **1992**, *114* (27), 10997–10998. <https://doi.org/10.1021/ja00053a067>.
- (21) Kennedy, J. P.; Williams, L.; Bridges, T. M.; Daniels, R. N.; Weaver, D.; Lindsley, C. W. Application of Combinatorial Chemistry Science on Modern Drug Discovery. *J. Comb. Chem.* **2008**, *10* (3), 345–354. <https://doi.org/10.1021/cc700187t>.
- (22) Kodadek, T. The Rise, Fall and Reinvention of Combinatorial Chemistry. *Chem. Commun.* **2011**, *47* (35), 9757–9763. <https://doi.org/10.1039/C1CC12102B>.
- (23) Soral, M.; Bouillon, I.; Krchňák, V. Combinatorial Libraries of Bis-Heterocyclic Compounds with Skeletal Diversity. *J. Comb. Chem.* **2008**, *10* (6), 923–933. <https://doi.org/10.1021/cc8001074>.
- (24) Hert, J.; Irwin, J. J.; Laggner, C.; Keiser, M. J.; Shoichet, B. K. Quantifying Biogenic Bias in Screening Libraries. *Nat. Chem. Biol.* **2009**, *5* (7), 479–483. <https://doi.org/10.1038/nchembio.180>.
- (25) Barjau, J.; Schnakenburg, G.; Waldvogel, S. R. Diversity-Oriented Synthesis of Polycyclic Scaffolds by Modification of an Anodic Product Derived from 2,4-Dimethylphenol. *Angew. Chem. Int. Ed.* **2011**, *50* (6), 1415–1419. <https://doi.org/10.1002/anie.201006637>.
- (26) Thomas, G. L.; Spandl, R. J.; Glansdorp, F. G.; Welch, M.; Bender, A.; Cockfield, J.; Lindsay, J. A.; Bryant, C.; Brown, D. F. J.; Loiseleur, O.; Rudyk, H.; Ladlow, M.; Spring, D. R. Anti-MRSA Agent Discovery Using Diversity-Oriented Synthesis. *Angew. Chem. Int. Ed.* **2008**, *47* (15), 2808–2812. <https://doi.org/10.1002/anie.200705415>.
- (27) Ng, P. Y.; Tang, Y.; Knosp, W. M.; Stadler, H. S.; Shaw, J. T. Synthesis of Diverse Lactam Carboxamides Leading to the Discovery of a New Transcription-Factor Inhibitor. *Angew. Chem. Int. Ed.* **2007**, *46* (28), 5352–5355. <https://doi.org/10.1002/anie.200700762>.
- (28) Luo, T.; Schreiber, S. L. Gold(I)-Catalyzed Coupling Reactions for the Synthesis of Diverse Small Molecules Using the Build/Couple/Pair Strategy. *J. Am. Chem. Soc.* **2009**, *131* (15), 5667–5674. <https://doi.org/10.1021/ja900414s>.
- (29) Clemons, P. A.; Bodycombe, N. E.; Carrinski, H. A.; Wilson, J. A.; Shamji, A. F.; Wagner, B. K.; Koehler, A. N.; Schreiber, S. L. Small Molecules of Different Origins Have Distinct Distributions of Structural Complexity That Correlate with Protein-Binding Profiles. *Proc. Natl. Acad. Sci.* **2010**, *107* (44), 18787–18792. <https://doi.org/10.1073/pnas.1012741107>.
- (30) Di Micco, S.; Vitale, R.; Pellicchia, M.; Rega, M. F.; Riva, R.; Basso, A.; Bifulco, G. Identification of Lead Compounds As Antagonists of Protein Bcl-XL with a Diversity-Oriented Multidisciplinary Approach. *J. Med. Chem.* **2009**, *52* (23), 7856–7867. <https://doi.org/10.1021/jm9010687>.
- (31) Rishton, G. M. Nonleadlikeness and Leadlikeness in Biochemical Screening. *Drug Discov. Today* **2003**, *8* (2), 86–96. <https://doi.org/10.1016/S1359644602025722>.

- (32) Zhu, T.; Cao, S.; Su, P.-C.; Patel, R.; Shah, D.; Chokshi, H. B.; Szukala, R.; Johnson, M. E.; Hevener, K. E. Hit Identification and Optimization in Virtual Screening: Practical Recommendations Based Upon a Critical Literature Analysis. *J. Med. Chem.* **2013**, *56* (17), 6560–6572. <https://doi.org/10.1021/jm301916b>.
- (33) Evelyn, C. R.; Biesiada, J.; Duan, X.; Tang, H.; Shang, X.; Papoian, R.; Seibel, W. L.; Nelson, S.; Meller, J.; Zheng, Y. Combined Rational Design and a High Throughput Screening Platform for Identifying Chemical Inhibitors of a Ras-Activating Enzyme. *J. Biol. Chem.* **2015**, *290* (20), 12879–12898. <https://doi.org/10.1074/jbc.M114.634493>.
- (34) Muegge, I.; Mukherjee, P. Performance of Dark Chemical Matter in High Throughput Screening. *J. Med. Chem.* **2016**, *59* (21), 9806–9813. <https://doi.org/10.1021/acs.jmedchem.6b01038>.
- (35) Wassermann, A. M.; Tudor, M.; Glick, M. Deorphanization Strategies for Dark Chemical Matter. *Drug Discov. Today Technol.* **2017**, *23*, 69–74. <https://doi.org/10.1016/j.ddtec.2016.11.004>.
- (36) Wassermann, A. M.; Lounkine, E.; Hoepfner, D.; Le Goff, G.; King, F. J.; Studer, C.; Peltier, J. M.; Grippo, M. L.; Prindle, V.; Tao, J.; Schuffenhauer, A.; Wallace, I. M.; Chen, S.; Krastel, P.; Cobos-Correa, A.; Parker, C. N.; Davies, J. W.; Glick, M. Dark Chemical Matter as a Promising Starting Point for Drug Lead Discovery. *Nat. Chem. Biol.* **2015**, *11* (12), 958–966. <https://doi.org/10.1038/nchembio.1936>.
- (37) Wawer, M. J.; Li, K.; Gustafsdottir, S. M.; Ljosa, V.; Bodycombe, N. E.; Marton, M. A.; Sokolnicki, K. L.; Bray, M.-A.; Kemp, M. M.; Winchester, E.; Taylor, B.; Grant, G. B.; Hon, C. S.-Y.; Duvall, J. R.; Wilson, J. A.; Bittker, J. A.; Danik, V.; Narayan, R.; Subramanian, A.; Winckler, W.; Golub, T. R.; Carpenter, A. E.; Shamji, A. F.; Schreiber, S. L.; Clemons, P. A. Toward Performance-Diverse Small-Molecule Libraries for Cell-Based Phenotypic Screening Using Multiplexed High-Dimensional Profiling. *Proc. Natl. Acad. Sci.* **2014**, *111* (30), 10911–10916. <https://doi.org/10.1073/pnas.1410933111>.
- (38) Bauer, R. A.; Wurst, J. M.; Tan, D. S. Expanding the Range of ‘Druggable’ Targets with Natural Product-Based Libraries: An Academic Perspective. *Curr. Opin. Chem. Biol.* **2010**, *14* (3), 308–314. <https://doi.org/10.1016/j.cbpa.2010.02.001>.
- (39) Feher, M.; Schmidt, J. M. Property Distributions: Differences between Drugs, Natural Products, and Molecules from Combinatorial Chemistry. *J. Chem. Inf. Comput. Sci.* **2003**, *43* (1), 218–227. <https://doi.org/10.1021/ci0200467>.
- (40) Hopkins, A. L.; Groom, C. R. The Druggable Genome. *Nat. Rev. Drug Discov.* **2002**, *1* (9), 727–730. <https://doi.org/10.1038/nrd892>.
- (41) Koch, M. A.; Schuffenhauer, A.; Scheck, M.; Wetzel, S.; Casaulta, M.; Odermatt, A.; Ertl, P.; Waldmann, H. Charting Biologically Relevant Chemical Space: A Structural Classification of Natural Products (SCONP). *Proc. Natl. Acad. Sci.* **2005**, *102* (48), 17272–17277. <https://doi.org/10.1073/pnas.0503647102>.
- (42) Švenda, J.; Sheremet, M.; Kremer, L.; Maier, L.; Bauer, J. O.; Strohmann, C.; Ziegler, S.; Kumar, K.; Waldmann, H. Biology-Oriented Synthesis of a Withanolide-Inspired Compound Collection Reveals Novel Modulators of Hedgehog Signaling. *Angew. Chem. Int. Ed.* **2015**, *54* (19), 5596–5602. <https://doi.org/10.1002/anie.201500112>.
- (43) Laraia, L.; Ohsawa, K.; Konstantinidis, G.; Robke, L.; Wu, Y.-W.; Kumar, K.; Waldmann, H. Discovery of Novel Cinchona-Alkaloid-Inspired Oxazastwistane Autophagy Inhibitors. *Angew. Chem.* **2017**, *129* (8), 2177–2182. <https://doi.org/10.1002/ange.201611670>.
- (44) Christoforow, A.; Wilke, J.; Binici, A.; Pahl, A.; Ostermann, C.; Sievers, S.; Waldmann, H. Design, Synthesis, and Phenotypic Profiling of Pyrano-Furo-Pyridone Pseudo Natural Products. *Angew. Chem.* **2019**, *131* (41), 14857–14865. <https://doi.org/10.1002/ange.201907853>.

- (45) Rafferty, R. J.; Hicklin, R. W.; Maloof, K. A.; Hergenrother, P. J. Synthesis of Complex and Diverse Compounds through Ring Distortion of Abietic Acid. *Angew. Chem. Int. Ed.* **2014**, *53* (1), 220–224. <https://doi.org/10.1002/anie.201308743>.
- (46) Huigens, R. W.; Morrison, K. C.; Hicklin, R. W.; Flood, T. A.; Richter, M. F.; Hergenrother, P. J. A Ring Distortion Strategy to Construct Stereochemically Complex and Structurally Diverse Compounds from Natural Products. *Nat. Chem.* **2013**, *5* (3), 195–202. <https://doi.org/10.1038/nchem.1549>.
- (47) Richter, M. F.; Drown, B. S.; Riley, A. P.; Garcia, A.; Shirai, T.; Svec, R. L.; Hergenrother, P. J. Predictive Rules for Compound Accumulation Yield a Broad-Spectrum Antibiotic. *Nature* **2017**, *545* (7654), 299–304. <https://doi.org/10.1038/nature22308>.
- (48) Moura-Letts, G.; DiBlasi, C. M.; Bauer, R. A.; Tan, D. S. Solid-Phase Synthesis and Chemical Space Analysis of a 190-Membered Alkaloid/Terpenoid-like Library. *Proc. Natl. Acad. Sci.* **2011**, *108* (17), 6745–6750. <https://doi.org/10.1073/pnas.1015268108>.
- (49) Beckmann, H. S. G.; Nie, F.; Hagerman, C. E.; Johansson, H.; Tan, Y. S.; Wilcke, D.; Spring, D. R. A Strategy for the Diversity-Oriented Synthesis of Macrocyclic Scaffolds Using Multidimensional Coupling. *Nat. Chem.* **2013**, *5* (10), 861–867. <https://doi.org/10.1038/nchem.1729>.
- (50) Zhang, J.; Wu, J.; Hong, B.; Ai, W.; Wang, X.; Li, H.; Lei, X. Diversity-Oriented Synthesis of Lycopodium Alkaloids Inspired by the Hidden Functional Group Pairing Pattern. *Nat. Commun.* **2014**, *5* (1), 1–9. <https://doi.org/10.1038/ncomms5614>.
- (51) Marcaurelle, L. A.; Comer, E.; Dandapani, S.; Duvall, J. R.; Gerard, B.; Kesavan, S.; Lee, M. D.; Liu, H.; Lowe, J. T.; Marie, J.-C.; Mulrooney, C. A.; Pandya, B. A.; Rowley, A.; Ryba, T. D.; Suh, B.-C.; Wei, J.; Young, D. W.; Akella, L. B.; Ross, N. T.; Zhang, Y.-L.; Fass, D. M.; Reis, S. A.; Zhao, W.-N.; Haggarty, S. J.; Palmer, M.; Foley, M. A. An Aldol-Based Build/Couple/Pair Strategy for the Synthesis of Medium- and Large-Sized Rings: Discovery of Macrocyclic Histone Deacetylase Inhibitors. *J. Am. Chem. Soc.* **2010**, *132* (47), 16962–16976. <https://doi.org/10.1021/ja105119r>.
- (52) Willett, P. Similarity Searching Using 2D Structural Fingerprints. In *Cheminformatics and Computational Chemical Biology*; Bajorath, J., Ed.; Methods in Molecular Biology; Humana Press: Totowa, NJ, 2011; pp 133–158. [https://doi.org/10.1007/978-1-60761-839-3\\_5](https://doi.org/10.1007/978-1-60761-839-3_5).
- (53) Axen, S. D.; Huang, X.-P.; Cáceres, E. L.; Gendele, L.; Roth, B. L.; Keiser, M. J. A Simple Representation of Three-Dimensional Molecular Structure. *J. Med. Chem.* **2017**, *60* (17), 7393–7409. <https://doi.org/10.1021/acs.jmedchem.7b00696>.
- (54) Sauer, W. H. B.; Schwarz, M. K. Molecular Shape Diversity of Combinatorial Libraries: A Prerequisite for Broad Bioactivity. *J. Chem. Inf. Comput. Sci.* **2003**, *43* (3), 987–1003. <https://doi.org/10.1021/ci025599w>.
- (55) Rush, T. S.; Grant, J. A.; Mosyak, L.; Nicholls, A. A Shape-Based 3-D Scaffold Hopping Method and Its Application to a Bacterial Protein–Protein Interaction. *J. Med. Chem.* **2005**, *48* (5), 1489–1495. <https://doi.org/10.1021/jm040163o>.
- (56) Koutsoukas, A.; Paricharak, S.; Galloway, W. R. J. D.; Spring, D. R.; IJzerman, A. P.; Glen, R. C.; Marcus, D.; Bender, A. How Diverse Are Diversity Assessment Methods? A Comparative Analysis and Benchmarking of Molecular Descriptor Space. *J. Chem. Inf. Model.* **2014**, *54* (1), 230–242. <https://doi.org/10.1021/ci400469u>.
- (57) Chen, D.; Oezguen, N.; Urvil, P.; Ferguson, C.; Dann, S. M.; Savidge, T. C. Regulation of Protein-Ligand Binding Affinity by Hydrogen Bond Pairing. *Sci. Adv.* **2016**, *2* (3). <https://doi.org/10.1126/sciadv.1501240>.
- (58) Sarkar, A.; Kellogg, G. E. Hydrophobicity – Shake Flasks, Protein Folding and Drug Discovery. *Curr. Top. Med. Chem.* **2010**, *10* (1), 67–83.

- (59) Lawson, A. D. G.; MacCoss, M.; Heer, J. P. Importance of Rigidity in Designing Small Molecule Drugs To Tackle Protein–Protein Interactions (PPIs) through Stabilization of Desired Conformers. *J. Med. Chem.* **2018**, *61* (10), 4283–4289. <https://doi.org/10.1021/acs.jmedchem.7b01120>.
- (60) Isidro-Llobet, A.; Hadje Georgiou, K.; Galloway, W. R. J. D.; Giacomini, E.; Hansen, M. R.; Méndez-Abt, G.; Tan, Y. S.; Carro, L.; Sore, H. F.; Spring, D. R. A Diversity-Oriented Synthesis Strategy Enabling the Combinatorial-Type Variation of Macrocyclic Peptidomimetic Scaffolds †Electronic Supplementary Information (ESI) Available: Experimental Procedures, Characterization Data and Details of the Computational Analyses. See DOI: 10.1039/C5ob00371g Click Here for Additional Data File. *Org. Biomol. Chem.* **2015**, *13* (15), 4570–4580. <https://doi.org/10.1039/c5ob00371g>.
- (61) Lenci, E.; Innocenti, R.; Menchi, G.; Trabocchi, A. Diversity-Oriented Synthesis and Chemoinformatic Analysis of the Molecular Diversity of Sp<sup>3</sup>-Rich Morpholine Peptidomimetics. *Front. Chem.* **2018**, *6*. <https://doi.org/10.3389/fchem.2018.00522>.
- (62) Clemons, P. A.; Wilson, J. A.; Dančák, V.; Muller, S.; Carrinski, H. A.; Wagner, B. K.; Koehler, A. N.; Schreiber, S. L. Quantifying Structure and Performance Diversity for Sets of Small Molecules Comprising Small-Molecule Screening Collections. *Proc. Natl. Acad. Sci.* **2011**, *108* (17), 6817–6822. <https://doi.org/10.1073/pnas.1015024108>.
- (63) Petrone, P. M.; Simms, B.; Nigsch, F.; Lounkine, E.; Kutchukian, P.; Cornett, A.; Deng, Z.; Davies, J. W.; Jenkins, J. L.; Glick, M. Rethinking Molecular Similarity: Comparing Compounds on the Basis of Biological Activity. *ACS Chem. Biol.* **2012**, *7* (8), 1399–1409. <https://doi.org/10.1021/cb3001028>.
- (64) Petrone, P. M.; Wassermann, A. M.; Lounkine, E.; Kutchukian, P.; Simms, B.; Jenkins, J.; Selzer, P.; Glick, M. Biodiversity of Small Molecules – a New Perspective in Screening Set Selection. *Drug Discov. Today* **2013**, *18* (13–14), 674–680. <https://doi.org/10.1016/j.drudis.2013.02.005>.
- (65) Bates, S. E.; Fojo, A. T.; Weinstein, J. N.; Myers, T. G.; Alvarez, M.; Pauli, K. D.; Chabner, B. A. Molecular Targets in the National Cancer Institute Drug Screen. *J. Cancer Res. Clin. Oncol.* **1995**, *121* (9–10), 495–500. <https://doi.org/10.1007/BF01197759>.
- (66) Bai, R. L.; Paull, K. D.; Herald, C. L.; Malspeis, L.; Pettit, G. R.; Hamel, E. Halichondrin B and Homohalichondrin B, Marine Natural Products Binding in the Vinca Domain of Tubulin. Discovery of Tubulin-Based Mechanism of Action by Analysis of Differential Cytotoxicity Data. *J. Biol. Chem.* **1991**, *266* (24), 15882–15889.
- (67) Alvarez, M.; Paull, K.; Monks, A.; Hose, C.; Lee, J. S.; Weinstein, J.; Grever, M.; Bates, S.; Fojo, T. Generation of a Drug Resistance Profile by Quantitation of Mdr-1/P-Glycoprotein in the Cell Lines of the National Cancer Institute Anticancer Drug Screen. *J. Clin. Invest.* **1995**, *95* (5), 2205–2214.
- (68) Reinhold, W. C.; Sunshine, M.; Varma, S.; Doroshow, J. H.; Pommier, Y. Using CellMiner 1.6 for Systems Pharmacology and Genomic Analysis of the NCI-60. *Clin. Cancer Res. Off. J. Am. Assoc. Cancer Res.* **2015**, *21* (17), 3841–3852. <https://doi.org/10.1158/1078-0432.CCR-15-0335>.
- (69) The Cancer Target Discovery and Development Network; Schreiber, S. L.; Shamji, A. F.; Clemons, P. A.; Hon, C.; Koehler, A. N.; Munoz, B.; Palmer, M.; Stern, A. M.; Wagner, B. K.; Powers, S.; Lowe, S. W.; Guo, X.; Krasnitz, A.; Sawey, E. T.; Sordella, R.; Stein, L.; Trotman, L. C.; Califano, A.; Dalla-Favera, R.; Ferrando, A.; Iavarone, A.; Pasqualucci, L.; Silva, J.; Stockwell, B. R.; Hahn, W. C.; Chin, L.; DePinho, R. A.; Boehm, J. S.; Gopal, S.; Huang, A.; Root, D. E.; Weir, B. A.; Gerhard, D. S.; Zenklusen, J. C.; Roth, M. G.; White, M. A.; Minna, J. D.; MacMillan, J. B.; Posner, B. A. Towards Patient-Based Cancer Therapeutics. *Nat. Biotechnol.* **2010**, *28* (9), 904–906. <https://doi.org/10.1038/nbt0910-904>.
- (70) Kepp, O.; Galluzzi, L.; Lipinski, M.; Yuan, J.; Kroemer, G. Cell Death Assays for Drug Discovery. *Nat. Rev. Drug Discov.* **2011**, *10* (3), 221–237. <https://doi.org/10.1038/nrd3373>.

- (71) Mervin, L. H.; Cao, Q.; Barrett, I. P.; Firth, M. A.; Murray, D.; McWilliams, L.; Haddrick, M.; Wigglesworth, M.; Engkvist, O.; Bender, A. Understanding Cytotoxicity and Cytostaticity in a High-Throughput Screening Collection. *ACS Chem. Biol.* **2016**, *11* (11), 3007–3023. <https://doi.org/10.1021/acscchembio.6b00538>.
- (72) Helgren, T. R.; Xu, L. L.; Sotelo, D.; Mehta, Y. R.; Korkmaz, M. A.; Pavlinov, I.; Aldrich, L. N. Microwave-Assisted, Asymmetric Synthesis of 3-Amino-2,3-Dihydrobenzofuran Flavonoid Derivatives from Chalcones. *Chem. - Eur. J.* **2018**, *24* (18), 4509–4514. <https://doi.org/10.1002/chem.201705984>.
- (73) Gerlach, E. M.; Korkmaz, M. A.; Pavlinov, I.; Gao, Q.; Aldrich, L. N. Systematic Diversity-Oriented Synthesis of Reduced Flavones from  $\gamma$ -Pyrone to Probe Biological Performance Diversity. *ACS Chem. Biol.* **2019**, *14* (7), 1536–1545. <https://doi.org/10.1021/acscchembio.9b00294>.
- (74) Hughes, T. R.; Marton, M. J.; Jones, A. R.; Roberts, C. J.; Stoughton, R.; Armour, C. D.; Bennett, H. A.; Coffey, E.; Dai, H.; He, Y. D.; Kidd, M. J.; King, A. M.; Meyer, M. R.; Slade, D.; Lum, P. Y.; Stepaniants, S. B.; Shoemaker, D. D.; Gachotte, D.; Chakraburtt, K.; Simon, J.; Bard, M.; Friend, S. H. Functional Discovery via a Compendium of Expression Profiles. *Cell* **2000**, *102* (1), 109–126. [https://doi.org/10.1016/S0092-8674\(00\)00015-5](https://doi.org/10.1016/S0092-8674(00)00015-5).
- (75) Lee, A. Y.; St. Onge, R. P.; Proctor, M. J.; Wallace, I. M.; Nile, A. H.; Spagnuolo, P. A.; Jitkova, Y.; Gronda, M.; Wu, Y.; Kim, M. K.; Cheung-Ong, K.; Torres, N. P.; Spear, E. D.; Han, M. K. L.; Schlecht, U.; Suresh, S.; Duby, G.; Heisler, L. E.; Surendra, A.; Fung, E.; Urbanus, M. L.; Gebbia, M.; Lissina, E.; Miranda, M.; Chiang, J. H.; Aparicio, A. M.; Zeghouf, M.; Davis, R. W.; Cherfils, J.; Boutry, M.; Kaiser, C. A.; Cummins, C. L.; Trimble, W. S.; Brown, G. W.; Schimmer, A. D.; Bankaitis, V. A.; Nislow, C.; Bader, G. D.; Giaever, G. Mapping the Cellular Response to Small Molecules Using Chemogenomic Fitness Signatures. *Science* **2014**, *344* (6180), 208–211. <https://doi.org/10.1126/science.1250217>.
- (76) Lum, P. Y.; Armour, C. D.; Stepaniants, S. B.; Cavet, G.; Wolf, M. K.; Butler, J. S.; Hinshaw, J. C.; Garnier, P.; Prestwich, G. D.; Leonardson, A.; Garrett-Engle, P.; Rush, C. M.; Bard, M.; Schimmack, G.; Phillips, J. W.; Roberts, C. J.; Shoemaker, D. D. Discovering Modes of Action for Therapeutic Compounds Using a Genome-Wide Screen of Yeast Heterozygotes. *Cell* **2004**, *116* (1), 121–137. [https://doi.org/10.1016/S0092-8674\(03\)01035-3](https://doi.org/10.1016/S0092-8674(03)01035-3).
- (77) Parsons, A. B.; Brost, R. L.; Ding, H.; Li, Z.; Zhang, C.; Sheikh, B.; Brown, G. W.; Kane, P. M.; Hughes, T. R.; Boone, C. Integration of Chemical-Genetic and Genetic Interaction Data Links Bioactive Compounds to Cellular Target Pathways. *Nat. Biotechnol.* **2004**, *22* (1), 62–69. <https://doi.org/10.1038/nbt919>.
- (78) Parsons, A. B.; Lopez, A.; Givoni, I. E.; Williams, D. E.; Gray, C. A.; Porter, J.; Chua, G.; Sopko, R.; Brost, R. L.; Ho, C.-H.; Wang, J.; Ketela, T.; Brenner, C.; Brill, J. A.; Fernandez, G. E.; Lorenz, T. C.; Payne, G. S.; Ishihara, S.; Ohya, Y.; Andrews, B.; Hughes, T. R.; Frey, B. J.; Graham, T. R.; Andersen, R. J.; Boone, C. Exploring the Mode-of-Action of Bioactive Compounds by Chemical-Genetic Profiling in Yeast. *Cell* **2006**, *126* (3), 611–625. <https://doi.org/10.1016/j.cell.2006.06.040>.
- (79) Lamb, J.; Crawford, E. D.; Peck, D.; Modell, J. W.; Blat, I. C.; Wrobel, M. J.; Lerner, J.; Brunet, J.-P.; Subramanian, A.; Ross, K. N.; Reich, M.; Hieronymus, H.; Wei, G.; Armstrong, S. A.; Haggarty, S. J.; Clemons, P. A.; Wei, R.; Carr, S. A.; Lander, E. S.; Golub, T. R. The Connectivity Map: Using Gene-Expression Signatures to Connect Small Molecules, Genes, and Disease. **2006**, *313*, 8.
- (80) Hieronymus, H.; Lamb, J.; Ross, K. N.; Peng, X. P.; Clement, C.; Rodina, A.; Nieto, M.; Du, J.; Stegmaier, K.; Raj, S. M.; Maloney, K. N.; Clardy, J.; Hahn, W. C.; Chiosis, G.; Golub, T. R. Gene Expression Signature-Based Chemical Genomic Prediction Identifies a Novel Class of HSP90 Pathway Modulators. *Cancer Cell* **2006**, *10* (4), 321–330. <https://doi.org/10.1016/j.ccr.2006.09.005>.
- (81) Johnstone, A.; Reiersen, G.; Smith, R.; Goldberg, J.; Lemmon, V.; Bixby, J. A Chemical Genetic Approach Identifies Piperazine Antipsychotics as Promoters of CNS Neurite Growth on Inhibitory Substrates. *Mol. Cell Neurosci.* **2012**, *50* (2), 125–135. <https://doi.org/10.1016/j.mcn.2012.04.008>.
- (82) Subramanian, A.; Narayan, R.; Corsello, S. M.; Peck, D. D.; Natoli, T. E.; Lu, X.; Gould, J.; Davis, J. F.; Tubelli, A. A.; Asiedu, J. K.; Lahr, D. L.; Hirschman, J. E.; Liu, Z.; Donahue, M.; Julian, B.; Khan, M.; Wadden, D.;

Smith, I. C.; Lam, D.; Liberzon, A.; Toder, C.; Bagul, M.; Orzechowski, M.; Enache, O. M.; Piccioni, F.; Johnson, S. A.; Lyons, N. J.; Berger, A. H.; Shamji, A. F.; Brooks, A. N.; Vrcic, A.; Flynn, C.; Rosains, J.; Takeda, D. Y.; Hu, R.; Davison, D.; Lamb, J.; Ardlie, K.; Hogstrom, L.; Greenside, P.; Gray, N. S.; Clemons, P. A.; Silver, S.; Wu, X.; Zhao, W.-N.; Read-Button, W.; Wu, X.; Haggarty, S. J.; Ronco, L. V.; Boehm, J. S.; Schreiber, S. L.; Doench, J. G.; Bittker, J. A.; Root, D. E.; Wong, B.; Golub, T. R. A Next Generation Connectivity Map: L1000 Platform and the First 1,000,000 Profiles. *Cell* **2017**, *171* (6), 1437-1452.e17. <https://doi.org/10.1016/j.cell.2017.10.049>.

(83) Abraham, V. C.; Taylor, D. L.; Haskins, J. R. High Content Screening Applied to Large-Scale Cell Biology. *Trends Biotechnol.* **2004**, *22* (1), 15–22. <https://doi.org/10.1016/j.tibtech.2003.10.012>.

(84) Zanella, F.; Lorens, J. B.; Link, W. High Content Screening: Seeing Is Believing. *Trends Biotechnol.* **2010**, *28* (5), 237–245. <https://doi.org/10.1016/j.tibtech.2010.02.005>.

(85) Perlman, Z. E. Multidimensional Drug Profiling By Automated Microscopy. *Science* **2004**, *306* (5699), 1194–1198. <https://doi.org/10.1126/science.1100709>.

(86) Kang, J.; Hsu, C.-H.; Wu, Q.; Liu, S.; Coster, A. D.; Posner, B. A.; Altschuler, S. J.; Wu, L. F. Improving Drug Discovery with High-Content Phenotypic Screens by Systematic Selection of Reporter Cell Lines. *Nat. Biotechnol.* **2016**, *34* (1), 70–77. <https://doi.org/10.1038/nbt.3419>.

(87) Buggenthin, F.; Marr, C.; Schwarzfischer, M.; Hoppe, P. S.; Hilsenbeck, O.; Schroeder, T.; Theis, F. J. An Automatic Method for Robust and Fast Cell Detection in Bright Field Images from High-Throughput Microscopy. *BMC Bioinformatics* **2013**, *14* (1), 297. <https://doi.org/10.1186/1471-2105-14-297>.

(88) Kobayashi, H.; Lei, C.; Wu, Y.; Mao, A.; Jiang, Y.; Guo, B.; Ozeki, Y.; Goda, K. Label-Free Detection of Cellular Drug Responses by High-Throughput Bright-Field Imaging and Machine Learning. *Sci. Rep.* **2017**, *7* (1), 1–9. <https://doi.org/10.1038/s41598-017-12378-4>.

(89) Bray, M.-A.; Singh, S.; Han, H.; Davis, C. T.; Borgeson, B.; Hartland, C.; Kost-Alimova, M.; Gustafsdottir, S. M.; Gibson, C. C.; Carpenter, A. E. Cell Painting, a High-Content Image-Based Assay for Morphological Profiling Using Multiplexed Fluorescent Dyes. *Nat. Protoc.* **2016**, *11* (9), 1757–1774. <https://doi.org/10.1038/nprot.2016.105>.

(90) Rohban, M. H.; Singh, S.; Wu, X.; Berthet, J. B.; Bray, M.-A.; Shrestha, Y.; Varelas, X.; Boehm, J. S.; Carpenter, A. E. Systematic Morphological Profiling of Human Gene and Allele Function via Cell Painting. *eLife* **2017**, *6*. <https://doi.org/10.7554/eLife.24060>.

(91) Bray, M.-A.; Gustafsdottir, S. M.; Rohban, M. H.; Singh, S.; Ljosa, V.; Sokolnicki, K. L.; Bittker, J. A.; Bodycombe, N. E.; Dancik, V.; Hasaka, T. P.; Hon, C. S.; Kemp, M. M.; Li, K.; Walpita, D.; Wawer, M. J.; Golub, T. R.; Schreiber, S. L.; Clemons, P. A.; Shamji, A. F.; Carpenter, A. E. A Dataset of Images and Morphological Profiles of 30 000 Small-Molecule Treatments Using the Cell Painting Assay. *GigaScience* **2017**, *6* (12), 1–5. <https://doi.org/10.1093/gigascience/giw014>.

(92) Gerry, C. J.; Hua, B. K.; Wawer, M. J.; Knowles, J. P.; Nelson Jr., S. D.; Verho, O.; Dandapani, S.; Wagner, B. K.; Clemons, P. A.; Booker-Milburn, K. I.; Boskovic, Z. V.; Schreiber, S. L. Real-Time Biological Annotation of Synthetic Compounds. *J. Am. Chem. Soc.* **2016**, *138* (28), 8920–8927. <https://doi.org/10.1021/jacs.6b04614>.

(93) Melillo, B.; Zoller, J.; Hua, B. K.; Verho, O.; Borghs, J.; Nelson, S. D.; Maetani, M.; Wawer, M. J.; Clemons, P. A.; Schreiber, S. L. Synergistic Effects of Stereochemistry and Appendages on the Performance Diversity of a Collection of Synthetic Compounds. *J. Am. Chem. Soc.* **2018**. <https://doi.org/10.1021/jacs.8b07319>.

(94) Futamura, Y.; Kawatani, M.; Kazami, S.; Tanaka, K.; Muroi, M.; Shimizu, T.; Tomita, K.; Watanabe, N.; Osada, H. Morphobase, an Encyclopedic Cell Morphology Database, and Its Use for Drug Target Identification. *Chem. Biol.* **2012**, *19* (12), 1620–1630. <https://doi.org/10.1016/j.chembiol.2012.10.014>.

- (95) Bryce, N. S.; Failes, T. W.; Stehn, J. R.; Baker, K.; Zahler, S.; Arzhaeva, Y.; Bischof, L.; Lyons, C.; Dedova, I.; Arndt, G. M.; Gaus, K.; Goult, B. T.; Hardeman, E. C.; Gunning, P. W.; Lock, J. G. High-Content Imaging of Unbiased Chemical Perturbations Reveals That the Phenotypic Plasticity of the Actin Cytoskeleton Is Constrained. *Cell Syst.* **2019**, *9* (5), 496-507.e5. <https://doi.org/10.1016/j.cels.2019.09.002>.
- (96) Castoreno, A. B.; Smurnyy, Y.; Torres, A. D.; Vokes, M. S.; Jones, T. R.; Carpenter, A. E.; Eggert, U. S. Small Molecules Discovered in a Pathway Screen Target the Rho Pathway in Cytokinesis. *Nat. Chem. Biol.* **2010**, *6* (6), 457–463. <https://doi.org/10.1038/nchembio.363>.
- (97) Garvey, C. M.; Spiller, E.; Lindsay, D.; Chiang, C.-T.; Choi, N. C.; Agus, D. B.; Mallick, P.; Foo, J.; Mumenthaler, S. M. A High-Content Image-Based Method for Quantitatively Studying Context-Dependent Cell Population Dynamics. *Sci. Rep.* **2016**, *6* (1), 1–12. <https://doi.org/10.1038/srep29752>.
- (98) Cohen, A. A.; Geva-Zatorsky, N.; Eden, E.; Frenkel-Morgenstern, M.; Issaeva, I.; Sigal, A.; Milo, R.; Cohen-Saidon, C.; Liron, Y.; Kam, Z.; Cohen, L.; Danon, T.; Perzov, N.; Alon, U. Dynamic Proteomics of Individual Cancer Cells in Response to a Drug. *Science* **2008**, *322* (5907), 1511–1516. <https://doi.org/10.1126/science.1160165>.
- (99) Gustafsdottir, S. M.; Ljosa, V.; Sokolnicki, K. L.; Wilson, J. A.; Walpita, D.; Kemp, M. M.; Seiler, K. P.; Carrel, H. A.; Golub, T. R.; Schreiber, S. L.; Clemons, P. A.; Carpenter, A. E.; Shamji, A. F. Multiplex Cytological Profiling Assay to Measure Diverse Cellular States. *PLOS ONE* **2013**, *8* (12), e80999. <https://doi.org/10.1371/journal.pone.0080999>.
- (100) McQuin, C.; Goodman, A.; Chernyshev, V.; Kametsky, L.; Cimini, B. A.; Karhohs, K. W.; Doan, M.; Ding, L.; Rafelski, S. M.; Thirstrup, D.; Wiegraebe, W.; Singh, S.; Becker, T.; Caicedo, J. C.; Carpenter, A. E. CellProfiler 3.0: Next-Generation Image Processing for Biology. *PLOS Biol.* **2018**, *16* (7), e2005970. <https://doi.org/10.1371/journal.pbio.2005970>.
- (101) Becker, T.; Goodman, A.; McQuin, C.; Rohban, M.; Singh, S. *Cytominer: Methods for Image-Based Cell Profiling*; 2020.
- (102) Caicedo, J. C.; Cooper, S.; Heigwer, F.; Warchal, S.; Qiu, P.; Molnar, C.; Vasilevich, A. S.; Barry, J. D.; Bansal, H. S.; Kraus, O.; Wawer, M.; Paavolainen, L.; Herrmann, M. D.; Rohban, M.; Hung, J.; Hennig, H.; Concannon, J.; Smith, I.; Clemons, P. A.; Singh, S.; Rees, P.; Horvath, P.; Lington, R. G.; Carpenter, A. E. Data-Analysis Strategies for Image-Based Cell Profiling. *Nat. Methods* **2017**, *14* (9), 849–863. <https://doi.org/10.1038/nmeth.4397>.
- (103) Sanderson, M. J.; Smith, I.; Parker, I.; Bootman, M. D. Fluorescence Microscopy. *Cold Spring Harb. Protoc.* **2014**, *2014* (10), pdb.top071795. <https://doi.org/10.1101/pdb.top071795>.
- (104) Betzig, E.; Patterson, G. H.; Sougrat, R.; Lindwasser, O. W.; Olenych, S.; Bonifacino, J. S.; Davidson, M. W.; Lippincott-Schwartz, J.; Hess, H. F. Imaging Intracellular Fluorescent Proteins at Nanometer Resolution. *Science* **2006**, *313* (5793), 1642–1645. <https://doi.org/10.1126/science.1127344>.
- (105) Rust, M. J.; Bates, M.; Zhuang, X. Sub-Diffraction-Limit Imaging by Stochastic Optical Reconstruction Microscopy (STORM). *Nat. Methods* **2006**, *3* (10), 793–795. <https://doi.org/10.1038/nmeth929>.
- (106) Combs, C. A. Fluorescence Microscopy: A Concise Guide to Current Imaging Methods. *Curr. Protoc. Neurosci. Editor. Board Jacqueline N Crawley AI* **2010**, *0* 2, Unit2.1. <https://doi.org/10.1002/0471142301.ns0201s50>.
- (107) ImageXpress Micro XLS Widefield High-Content Analysis System <https://www.moleculardevices.com/products/additional-products/imagexpress-micro-xls-widefield-high-content-analysis-system> (accessed May 1, 2020).

- (108) Caraus, I.; Alsuwailem, A. A.; Nadon, R.; Makarenkov, V. Detecting and Overcoming Systematic Bias in High-Throughput Screening Technologies: A Comprehensive Review of Practical Issues and Methodological Solutions. *Brief. Bioinform.* **2015**, *16* (6), 974–986. <https://doi.org/10.1093/bib/bbv004>.
- (109) Singh, S.; Bray, M.-A.; Jones, T. R.; Carpenter, A. E. Pipeline for Illumination Correction of Images for High-Throughput Microscopy. *J. Microsc.* **2014**, *256* (3), 231–236. <https://doi.org/10.1111/jmi.12178>.
- (110) Ljosa, V.; Caie, P. D.; ter Horst, R.; Sokolnicki, K. L.; Jenkins, E. L.; Daya, S.; Roberts, M. E.; Jones, T. R.; Singh, S.; Genovesio, A.; Clemons, P. A.; Carragher, N. O.; Carpenter, A. E. Comparison of Methods for Image-Based Profiling of Cellular Morphological Responses to Small-Molecule Treatment. *J. Biomol. Screen.* **2013**, *18* (10), 1321–1329. <https://doi.org/10.1177/1087057113503553>.
- (111) Bray, M.-A.; Fraser, A. N.; Hasaka, T. P.; Carpenter, A. E. Workflow and Metrics for Image Quality Control in Large-Scale High-Content Screens. *J. Biomol. Screen.* **2012**, *17* (2), 266–274. <https://doi.org/10.1177/1087057111420292>.
- (112) Huber, P. J. *Robust Statistics*; Wiley series in probability and mathematical statistics; Wiley: New York, 1981.
- (113) Maaten, L. van der; Hinton, G. Visualizing Data Using T-SNE. *J. Mach. Learn. Res.* **2008**, *9* (Nov), 2579–2605.
- (114) Becht, E.; McInnes, L.; Healy, J.; Dutertre, C.-A.; Kwok, I. W. H.; Ng, L. G.; Ginhoux, F.; Newell, E. W. Dimensionality Reduction for Visualizing Single-Cell Data Using UMAP. *Nat. Biotechnol.* **2019**, *37* (1), 38–44. <https://doi.org/10.1038/nbt.4314>.
- (115) Jolliffe, I. T.; Cadima, J. Principal Component Analysis: A Review and Recent Developments. *Philos. Transact. A Math. Phys. Eng. Sci.* **2016**, *374* (2065). <https://doi.org/10.1098/rsta.2015.0202>.
- (116) R: Principal Components Analysis <https://stat.ethz.ch/R-manual/R-patched/library/stats/html/prcomp.html> (accessed Apr 28, 2020).
- (117) Hutz, J. E.; Nelson, T.; Wu, H.; McAllister, G.; Moutsatsos, I.; Jaeger, S. A.; Bandyopadhyay, S.; Nigsch, F.; Cornett, B.; Jenkins, J. L.; Selinger, D. W. The Multidimensional Perturbation Value: A Single Metric to Measure Similarity and Activity of Treatments in High-Throughput Multidimensional Screens. *J. Biomol. Screen.* **2013**, *18* (4), 367–377. <https://doi.org/10.1177/1087057112469257>.
- (118) De Maesschalck, R.; Jouan-Rimbaud, D.; Massart, D. L. The Mahalanobis Distance. *Chemom. Intell. Lab. Syst.* **2000**, *50* (1), 1–18. [https://doi.org/10.1016/S0169-7439\(99\)00047-7](https://doi.org/10.1016/S0169-7439(99)00047-7).
- (119) Rosenblad, A. B. F. J. Manly: Randomization, Bootstrap and Monte Carlo Methods in Biology, Third Edition. *Comput. Stat.* **2009**, *24* (2), 371–372. <https://doi.org/10.1007/s00180-009-0150-3>.
- (120) Ertl, P.; Rohde, B.; Selzer, P. Fast Calculation of Molecular Polar Surface Area as a Sum of Fragment-Based Contributions and Its Application to the Prediction of Drug Transport Properties. *J. Med. Chem.* **2000**, *43* (20), 3714–3717. <https://doi.org/10.1021/jm000942e>.
- (121) Pajouhesh, H.; Lenz, G. R. Medicinal Chemical Properties of Successful Central Nervous System Drugs. *NeuroRX* **2005**, *2* (4), 541–553. <https://doi.org/10.1602/neurorx.2.4.541>.
- (122) Daina, A.; Michielin, O.; Zoete, V. SwissADME: A Free Web Tool to Evaluate Pharmacokinetics, Drug-Likeness and Medicinal Chemistry Friendliness of Small Molecules. *Sci. Rep.* **2017**, *7*. <https://doi.org/10.1038/srep42717>.
- (123) Jaskowiak, P. A.; Campello, R. J.; Costa, I. G. On the Selection of Appropriate Distances for Gene Expression Data Clustering. *BMC Bioinformatics* **2014**, *15* (2), S2. <https://doi.org/10.1186/1471-2105-15-S2-S2>.

- (124) Müllner, D. Modern Hierarchical, Agglomerative Clustering Algorithms. *ArXiv11092378 Cs Stat* **2011**.
- (125) Wang, T.; Li, Q.; Bi, K. Bioactive Flavonoids in Medicinal Plants: Structure, Activity and Biological Fate. *Asian J. Pharm. Sci.* **2018**, *13* (1), 12–23. <https://doi.org/10.1016/j.ajps.2017.08.004>.
- (126) Abd-Elazem, I. S.; Chen, H. S.; Bates, R. B.; Huang, R. C. C. Isolation of Two Highly Potent and Non-Toxic Inhibitors of Human Immunodeficiency Virus Type 1 (HIV-1) Integrase from *Salvia Miltiorrhiza*. *Antiviral Res.* **2002**, *55* (1), 91–106. [https://doi.org/10.1016/S0166-3542\(02\)00011-6](https://doi.org/10.1016/S0166-3542(02)00011-6).
- (127) Panche, A. N.; Diwan, A. D.; Chandra, S. R. Flavonoids: An Overview. *J. Nutr. Sci.* **2016**, *5*. <https://doi.org/10.1017/jns.2016.41>.
- (128) Nevagi, R. J.; Dighe, S. N.; Dighe, S. N. Biological and Medicinal Significance of Benzofuran. *Eur. J. Med. Chem.* **2015**, *97*, 561–581. <https://doi.org/10.1016/j.ejmech.2014.10.085>.
- (129) Hemmersbach, S.; Brauer, S. S.; Hüwel, S.; Galla, H.-J.; Humpf, H.-U. Transepithelial Permeability Studies of Flavan-3-Ol-C-Glucosides and Procyanidin Dimers and Trimers across the Caco-2 Cell Monolayer. *J. Agric. Food Chem.* **2013**, *61* (33), 7932–7940. <https://doi.org/10.1021/jf402019f>.
- (130) Andrew, C. L.; Klemm, A. R.; Lloyd, J. B. Lysosome Membrane Permeability to Amines. *Biochim. Biophys. Acta BBA - Biomembr.* **1997**, *1330* (1), 71–82. [https://doi.org/10.1016/S0005-2736\(97\)00145-4](https://doi.org/10.1016/S0005-2736(97)00145-4).
- (131) Palm, K.; Stenberg, P.; Luthman, K.; Artursson, P. Polar Molecular Surface Properties Predict the Intestinal Absorption of Drugs in Humans. *Pharm. Res.* **1997**, *14* (5), 568–571. <https://doi.org/10.1023/a:1012188625088>.
- (132) Gao, Q.; Xu, L. L.; Parise, V. P.; Mehta, Y. R.; Aldrich, L. N. Enantioselective Synthesis of 4-Amino-3-hydroxybenzopyran Flavanol Derivatives from Chalcones. *Synthesis* **2018**, *50* (24), 4796–4808. <https://doi.org/10.1055/s-0037-161114>.
- (133) Martin, Y. C.; Kofron, J. L.; Traphagen, L. M. Do Structurally Similar Molecules Have Similar Biological Activity? *J. Med. Chem.* **2002**, *45* (19), 4350–4358. <https://doi.org/10.1021/jm020155c>.
- (134) Reggiori, F.; Komatsu, M.; Finley, K.; Simonsen, A. Autophagy: More Than a Nonselective Pathway. *Int. J. Cell Biol.* **2012**, *2012*. <https://doi.org/10.1155/2012/219625>.
- (135) Eskelinen, E.-L.; Reggiori, F.; Baba, M.; Kovács, A. L.; Seglen, P. O. Seeing Is Believing: The Impact of Electron Microscopy on Autophagy Research. *Autophagy* **2011**, *7* (9), 935–956. <https://doi.org/10.4161/auto.7.9.15760>.
- (136) Nakatogawa, H.; Suzuki, K.; Kamada, Y.; Ohsumi, Y. Dynamics and Diversity in Autophagy Mechanisms: Lessons from Yeast. *Nat. Rev. Mol. Cell Biol.* **2009**, *10* (7), 458–467. <https://doi.org/10.1038/nrm2708>.
- (137) Yang, Z.; Klionsky, D. J. Eaten Alive: A History of Macroautophagy. *Nat. Cell Biol.* **2010**, *12* (9), 814–822. <https://doi.org/10.1038/ncb0910-814>.
- (138) Oku, M.; Sakai, Y. Three Distinct Types of Microautophagy Based on Membrane Dynamics and Molecular Machineries. *BioEssays* **2018**, *40* (6), 1800008. <https://doi.org/10.1002/bies.201800008>.
- (139) Stipanuk, M. H. Macroautophagy and Its Role in Nutrient Homeostasis. *Nutr. Rev.* **2009**, *67* (12), 677–689. <https://doi.org/10.1111/j.1753-4887.2009.00252.x>.
- (140) Dikic, I.; Elazar, Z. Mechanism and Medical Implications of Mammalian Autophagy. *Nat. Rev. Mol. Cell Biol.* **2018**, *19* (6), 349–364. <https://doi.org/10.1038/s41580-018-0003-4>.
- (141) Glick, D.; Barth, S.; Macleod, K. F. Autophagy: Cellular and Molecular Mechanisms. *J. Pathol.* **2010**, *221* (1), 3–12. <https://doi.org/10.1002/path.2697>.

- (142) Ganley, I. G.; Lam, D. H.; Wang, J.; Ding, X.; Chen, S.; Jiang, X. ULK1·ATG13·FIP200 Complex Mediates MTOR Signaling and Is Essential for Autophagy. *J. Biol. Chem.* **2009**, *284* (18), 12297–12305. <https://doi.org/10.1074/jbc.M900573200>.
- (143) Hosokawa, N.; Hara, T.; Kaizuka, T.; Kishi, C.; Takamura, A.; Miura, Y.; Iemura, S.; Natsume, T.; Takehana, K.; Yamada, N.; Guan, J.-L.; Oshiro, N.; Mizushima, N. Nutrient-Dependent MTORC1 Association with the ULK1–Atg13–FIP200 Complex Required for Autophagy. *Mol. Biol. Cell* **2009**, *20* (7), 1981–1991. <https://doi.org/10.1091/mbc.E08-12-1248>.
- (144) Jung, C. H.; Jun, C. B.; Ro, S.-H.; Kim, Y.-M.; Otto, N. M.; Cao, J.; Kundu, M.; Kim, D.-H. ULK-Atg13-FIP200 Complexes Mediate MTOR Signaling to the Autophagy Machinery. *Mol. Biol. Cell* **2009**, *20* (7), 1992–2003. <https://doi.org/10.1091/mbc.E08-12-1249>.
- (145) Mercer, C. A.; Kaliappan, A.; Dennis, P. B. A Novel, Human Atg13 Binding Protein, Atg101, Interacts with ULK1 and Is Essential for Macroautophagy. *Autophagy* **2009**, *5* (5), 649–662. <https://doi.org/10.4161/auto.5.5.8249>.
- (146) He, C.; Klionsky, D. J. Regulation Mechanisms and Signaling Pathways of Autophagy. *Annu. Rev. Genet.* **2009**, *43*, 67–93. <https://doi.org/10.1146/annurev-genet-102808-114910>.
- (147) Zachari, M.; Ganley, I. G. The Mammalian ULK1 Complex and Autophagy Initiation. *Essays Biochem.* **2017**, *61* (6), 585–596. <https://doi.org/10.1042/EBC20170021>.
- (148) Funderburk, S. F.; Wang, Q. J.; Yue, Z. The Beclin 1-VPS34 Complex—at the Crossroads of Autophagy and Beyond. *Trends Cell Biol.* **2010**, *20* (6), 355–362. <https://doi.org/10.1016/j.tcb.2010.03.002>.
- (149) Mizushima, N.; Noda, T.; Yoshimori, T.; Tanaka, Y.; Ishii, T.; George, M. D.; Klionsky, D. J.; Ohsumi, M.; Ohsumi, Y. A Protein Conjugation System Essential for Autophagy. *Nature* **1998**, *395* (6700), 395–398. <https://doi.org/10.1038/26506>.
- (150) Walczak, M.; Martens, S. Dissecting the Role of the Atg12–Atg5–Atg16 Complex during Autophagosome Formation. *Autophagy* **2013**, *9* (3), 424–425. <https://doi.org/10.4161/auto.22931>.
- (151) Fujita, N.; Itoh, T.; Omori, H.; Fukuda, M.; Noda, T.; Yoshimori, T. The Atg16L Complex Specifies the Site of LC3 Lipidation for Membrane Biogenesis in Autophagy. *Mol. Biol. Cell* **2008**, *19* (5), 2092–2100. <https://doi.org/10.1091/mbc.E07-12-1257>.
- (152) Otomo, C.; Metlagel, Z.; Takaesu, G.; Otomo, T. Structure of the Human ATG12~ATG5 Conjugate Required for LC3 Lipidation in Autophagy. *Nat. Struct. Mol. Biol.* **2013**, *20* (1), 59–66. <https://doi.org/10.1038/nsmb.2431>.
- (153) Lee, Y.-K.; Lee, J.-A. Role of the Mammalian ATG8/LC3 Family in Autophagy: Differential and Compensatory Roles in the Spatiotemporal Regulation of Autophagy. *BMB Rep.* **2016**, *49* (8), 424–430. <https://doi.org/10.5483/BMBRep.2016.49.8.081>.
- (154) Aita, V. M.; Liang, X. H.; Murty, V. V. S.; Pincus, D. L.; Yu, W.; Cayanis, E.; Kalachikov, S.; Gilliam, T. C.; Levine, B. Cloning and Genomic Organization of Beclin 1, a Candidate Tumor Suppressor Gene on Chromosome 17q21. *Genomics* **1999**, *59* (1), 59–65. <https://doi.org/10.1006/geno.1999.5851>.
- (155) Bjørkøy, G.; Lamark, T.; Brech, A.; Outzen, H.; Perander, M.; Overvatn, A.; Stenmark, H.; Johansen, T. P62/SQSTM1 Forms Protein Aggregates Degraded by Autophagy and Has a Protective Effect on Huntingtin-Induced Cell Death. *J. Cell Biol.* **2005**, *171* (4), 603–614. <https://doi.org/10.1083/jcb.200507002>.
- (156) Duran, A.; Linares, J. F.; Galvez, A. S.; Wikenheiser, K.; Flores, J. M.; Diaz-Meco, M. T.; Moscat, J. The Signaling Adaptor P62 Is an Important NF-KappaB Mediator in Tumorigenesis. *Cancer Cell* **2008**, *13* (4), 343–354. <https://doi.org/10.1016/j.ccr.2008.02.001>.

- (157) Mathew, R.; Karp, C. M.; Beaudoin, B.; Vuong, N.; Chen, G.; Chen, H.-Y.; Bray, K.; Reddy, A.; Bhanot, G.; Gelinas, C.; Dipaola, R. S.; Karantza-Wadsworth, V.; White, E. Autophagy Suppresses Tumorigenesis through Elimination of P62. *Cell* **2009**, *137* (6), 1062–1075. <https://doi.org/10.1016/j.cell.2009.03.048>.
- (158) Karin, M.; Greten, F. R. NF-KappaB: Linking Inflammation and Immunity to Cancer Development and Progression. *Nat. Rev. Immunol.* **2005**, *5* (10), 749–759. <https://doi.org/10.1038/nri1703>.
- (159) Taniguchi, K.; Karin, M. NF-KB, Inflammation, Immunity and Cancer: Coming of Age. *Nat. Rev. Immunol.* **2018**, *18* (5), 309–324. <https://doi.org/10.1038/nri.2017.142>.
- (160) Jain, A.; Lamark, T.; Sjøttem, E.; Bowitz Larsen, K.; Atesoh Awuh, J.; Øvervatn, A.; McMahon, M.; Hayes, J. D.; Johansen, T. P62/SQSTM1 Is a Target Gene for Transcription Factor NRF2 and Creates a Positive Feedback Loop by Inducing Antioxidant Response Element-Driven Gene Transcription. *J. Biol. Chem.* **2010**, *285* (29), 22576–22591. <https://doi.org/10.1074/jbc.M110.118976>.
- (161) Komatsu, M.; Kurokawa, H.; Waguri, S.; Taguchi, K.; Kobayashi, A.; Ichimura, Y.; Sou, Y.-S.; Ueno, I.; Sakamoto, A.; Tong, K. I.; Kim, M.; Nishito, Y.; Iemura, S.; Natsume, T.; Ueno, T.; Kominami, E.; Motohashi, H.; Tanaka, K.; Yamamoto, M. The Selective Autophagy Substrate P62 Activates the Stress Responsive Transcription Factor Nrf2 through Inactivation of Keap1. *Nat. Cell Biol.* **2010**, *12* (3), 213–223. <https://doi.org/10.1038/ncb2021>.
- (162) Jaramillo, M. C.; Zhang, D. D. The Emerging Role of the Nrf2–Keap1 Signaling Pathway in Cancer. *Genes Dev.* **2013**, *27* (20), 2179–2191. <https://doi.org/10.1101/gad.225680.113>.
- (163) Geismann, C.; Arlt, A.; Sebens, S.; Schäfer, H. Cytoprotection “Gone Astray”: Nrf2 and Its Role in Cancer. *Oncotargets Ther.* **2014**, *7*, 1497–1518. <https://doi.org/10.2147/OTT.S36624>.
- (164) Hara, T.; Nakamura, K.; Matsui, M.; Yamamoto, A.; Nakahara, Y.; Suzuki-Migishima, R.; Yokoyama, M.; Mishima, K.; Saito, I.; Okano, H.; Mizushima, N. Suppression of Basal Autophagy in Neural Cells Causes Neurodegenerative Disease in Mice. *Nature* **2006**, *441* (7095), 885–889. <https://doi.org/10.1038/nature04724>.
- (165) Mathew, R.; Kongara, S.; Beaudoin, B.; Karp, C. M.; Bray, K.; Degenhardt, K.; Chen, G.; Jin, S.; White, E. Autophagy Suppresses Tumor Progression by Limiting Chromosomal Instability. *Genes Dev.* **2007**, *21* (11), 1367–1381. <https://doi.org/10.1101/gad.1545107>.
- (166) Karantza-Wadsworth, V.; Patel, S.; Kravchuk, O.; Chen, G.; Mathew, R.; Jin, S.; White, E. Autophagy Mitigates Metabolic Stress and Genome Damage in Mammary Tumorigenesis. *Genes Dev.* **2007**, *21* (13), 1621–1635. <https://doi.org/10.1101/gad.1565707>.
- (167) Mathew, R.; White, E. Why Sick Cells Produce Tumors: The Protective Role of Autophagy. *Autophagy* **2007**, *3* (5), 502–504. <https://doi.org/10.4161/auto.4605>.
- (168) Filomeni, G.; De Zio, D.; Cecconi, F. Oxidative Stress and Autophagy: The Clash between Damage and Metabolic Needs. *Cell Death Differ.* **2015**, *22* (3), 377–388. <https://doi.org/10.1038/cdd.2014.150>.
- (169) Degenhardt, K.; Mathew, R.; Beaudoin, B.; Bray, K.; Anderson, D.; Chen, G.; Mukherjee, C.; Shi, Y.; Gélinas, C.; Fan, Y.; Nelson, D. A.; Jin, S.; White, E. Autophagy Promotes Tumor Cell Survival and Restricts Necrosis, Inflammation, and Tumorigenesis. *Cancer Cell* **2006**, *10* (1), 51–64. <https://doi.org/10.1016/j.ccr.2006.06.001>.
- (170) Komatsu, M.; Waguri, S.; Chiba, T.; Murata, S.; Iwata, J.; Tanida, I.; Ueno, T.; Koike, M.; Uchiyama, Y.; Kominami, E.; Tanaka, K. Loss of Autophagy in the Central Nervous System Causes Neurodegeneration in Mice. *Nature* **2006**, *441* (7095), 880–884. <https://doi.org/10.1038/nature04723>.
- (171) Vander Heiden, M. G.; Cantley, L. C.; Thompson, C. B. Understanding the Warburg Effect: The Metabolic Requirements of Cell Proliferation. *Science* **2009**, *324* (5930), 1029–1033. <https://doi.org/10.1126/science.1160809>.

- (172) Kuma, A.; Mizushima, N. Physiological Role of Autophagy as an Intracellular Recycling System: With an Emphasis on Nutrient Metabolism. *Semin. Cell Dev. Biol.* **2010**, *21* (7), 683–690. <https://doi.org/10.1016/j.semcdb.2010.03.002>.
- (173) Nelson, D. A.; Tan, T.-T.; Rabson, A. B.; Anderson, D.; Degenhardt, K.; White, E. Hypoxia and Defective Apoptosis Drive Genomic Instability and Tumorigenesis. *Genes Dev.* **2004**, *18* (17), 2095–2107. <https://doi.org/10.1101/gad.1204904>.
- (174) Lum, J. J.; Bauer, D. E.; Kong, M.; Harris, M. H.; Li, C.; Lindsten, T.; Thompson, C. B. Growth Factor Regulation of Autophagy and Cell Survival in the Absence of Apoptosis. *Cell* **2005**, *120* (2), 237–248. <https://doi.org/10.1016/j.cell.2004.11.046>.
- (175) Jin, S.; DiPaola, R. S.; Mathew, R.; White, E. Metabolic Catastrophe as a Means to Cancer Cell Death. *J. Cell Sci.* **2007**, *120* (3), 379–383. <https://doi.org/10.1242/jcs.03349>.
- (176) Wang, J.; Wu, G. S. Role of Autophagy in Cisplatin Resistance in Ovarian Cancer Cells. *J. Biol. Chem.* **2014**, *289* (24), 17163–17173. <https://doi.org/10.1074/jbc.M114.558288>.
- (177) Park, J. M.; Huang, S.; Wu, T.-T.; Foster, N. R.; Sinicrope, F. A. Prognostic Impact of Beclin 1, P62/Sequestosome 1 and LC3 Protein Expression in Colon Carcinomas from Patients Receiving 5-Fluorouracil as Adjuvant Chemotherapy. *Cancer Biol. Ther.* **2013**, *14* (2), 100–107. <https://doi.org/10.4161/cbt.22954>.
- (178) Miranda, A.; Hamilton, P. T.; Zhang, A. W.; Pattnaik, S.; Becht, E.; Mezheyeuski, A.; Bruun, J.; Micke, P.; Reynies, A. de; Nelson, B. H. Cancer Stemness, Intratumoral Heterogeneity, and Immune Response across Cancers. *Proc. Natl. Acad. Sci.* **2019**, *116* (18), 9020–9029. <https://doi.org/10.1073/pnas.1818210116>.
- (179) Hu, X.; Ghisolfi, L.; Keates, A. C.; Zhang, J.; Xiang, S.; Lee, D.; Li, C. J. Induction of Cancer Cell Stemness by Chemotherapy. *Cell Cycle Georget. Tex* **2012**, *11* (14), 2691–2698. <https://doi.org/10.4161/cc.21021>.
- (180) García-Prat, L.; Martínez-Vicente, M.; Perdiguero, E.; Ortet, L.; Rodríguez-Ubreva, J.; Rebollo, E.; Ruiz-Bonilla, V.; Gutarra, S.; Ballestar, E.; Serrano, A. L.; Sandri, M.; Muñoz-Cánoves, P. Autophagy Maintains Stemness by Preventing Senescence. *Nature* **2016**, *529* (7584), 37–42. <https://doi.org/10.1038/nature16187>.
- (181) Liang, J.; Shao, S. H.; Xu, Z.-X.; Hennessy, B.; Ding, Z.; Larrea, M.; Kondo, S.; Dumont, D. J.; Gutterman, J. U.; Walker, C. L.; Slingerland, J. M.; Mills, G. B. The Energy Sensing LKB1-AMPK Pathway Regulates P27(Kip1) Phosphorylation Mediating the Decision to Enter Autophagy or Apoptosis. *Nat. Cell Biol.* **2007**, *9* (2), 218–224. <https://doi.org/10.1038/ncb1537>.
- (182) Gupta, A.; Roy, S.; Lazar, A. J. F.; Wang, W.-L.; McAuliffe, J. C.; Reynoso, D.; McMahon, J.; Taguchi, T.; Floris, G.; Debiec-Rychter, M.; Schöffski, P.; Trent, J. A.; Debnath, J.; Rubin, B. P. Autophagy Inhibition and Antimalarials Promote Cell Death in Gastrointestinal Stromal Tumor (GIST). *Proc. Natl. Acad. Sci. U. S. A.* **2010**, *107* (32), 14333–14338. <https://doi.org/10.1073/pnas.1000248107>.
- (183) Lazova, R.; Camp, R. L.; Klump, V.; Siddiqui, S. F.; Amaravadi, R. K.; Pawelek, J. M. Punctate LC3B Expression Is a Common Feature of Solid Tumors and Associated with Proliferation, Metastasis, and Poor Outcome. *Clin. Cancer Res. Off. J. Am. Assoc. Cancer Res.* **2012**, *18* (2), 370–379. <https://doi.org/10.1158/1078-0432.CCR-11-1282>.
- (184) Lazova, R.; Klump, V.; Pawelek, J. Autophagy in Cutaneous Malignant Melanoma. *J. Cutan. Pathol.* **2010**, *37* (2), 256–268. <https://doi.org/10.1111/j.1600-0560.2009.01359.x>.
- (185) Peng, Y.-F.; Shi, Y.-H.; Ding, Z.-B.; Ke, A.-W.; Gu, C.-Y.; Hui, B.; Zhou, J.; Qiu, S.-J.; Dai, Z.; Fan, J. Autophagy Inhibition Suppresses Pulmonary Metastasis of HCC in Mice via Impairing Anoikis Resistance and Colonization of HCC Cells. *Autophagy* **2013**, *9* (12), 2056–2068. <https://doi.org/10.4161/auto.26398>.
- (186) Galavotti, S.; Bartesaghi, S.; Faccenda, D.; Shaked-Rabi, M.; Sanzone, S.; McEvoy, A.; Dinsdale, D.; Condorelli, F.; Brandner, S.; Campanella, M.; Grose, R.; Jones, C.; Salomoni, P. The Autophagy-Associated Factors

- DRAM1 and P62 Regulate Cell Migration and Invasion in Glioblastoma Stem Cells. *Oncogene* **2013**, *32* (6), 699–712. <https://doi.org/10.1038/onc.2012.111>.
- (187) Mowers, E. E.; Sharifi, M. N.; Macleod, K. F. Autophagy in Cancer Metastasis. *Oncogene* **2017**, *36* (12), 1619–1630. <https://doi.org/10.1038/onc.2016.333>.
- (188) Saha, S.; Panigrahi, D. P.; Patil, S.; Bhutia, S. K. Autophagy in Health and Disease: A Comprehensive Review. *Biomed. Pharmacother. Biomedecine Pharmacother.* **2018**, *104*, 485–495. <https://doi.org/10.1016/j.biopha.2018.05.007>.
- (189) Zheng, Y. T.; Shahnazari, S.; Brech, A.; Lamark, T.; Johansen, T.; Brumell, J. H. The Adaptor Protein P62/SQSTM1 Targets Invading Bacteria to the Autophagy Pathway. *J. Immunol. Baltim. Md 1950* **2009**, *183* (9), 5909–5916. <https://doi.org/10.4049/jimmunol.0900441>.
- (190) Sanjuan, M. A.; Dillon, C. P.; Tait, S. W. G.; Moshiah, S.; Dorsey, F.; Connell, S.; Komatsu, M.; Tanaka, K.; Cleveland, J. L.; Withoff, S.; Green, D. R. Toll-like Receptor Signalling in Macrophages Links the Autophagy Pathway to Phagocytosis. *Nature* **2007**, *450* (7173), 1253–1257. <https://doi.org/10.1038/nature06421>.
- (191) Dong, X.; Levine, B. Autophagy and Viruses: Adversaries or Allies? *J. Innate Immun.* **2013**, *5* (5), 480–493. <https://doi.org/10.1159/000346388>.
- (192) Jackson, W. T.; Giddings, T. H.; Taylor, M. P.; Mulinyawe, S.; Rabinovitch, M.; Kopito, R. R.; Kirkegaard, K. Subversion of Cellular Autophagosomal Machinery by RNA Viruses. *PLoS Biol.* **2005**, *3* (5), e156. <https://doi.org/10.1371/journal.pbio.0030156>.
- (193) Su, W.-C.; Chao, T.-C.; Huang, Y.-L.; Weng, S.-C.; Jeng, K.-S.; Lai, M. M. C. Rab5 and Class III Phosphoinositide 3-Kinase Vps34 Are Involved in Hepatitis C Virus NS4B-Induced Autophagy. *J. Virol.* **2011**, *85* (20), 10561–10571. <https://doi.org/10.1128/JVI.00173-11>.
- (194) Wellcome Trust Case Control Consortium. Genome-Wide Association Study of 14,000 Cases of Seven Common Diseases and 3,000 Shared Controls. *Nature* **2007**, *447* (7145), 661–678. <https://doi.org/10.1038/nature05911>.
- (195) Ramos, P. S.; Criswell, L. A.; Moser, K. L.; Comeau, M. E.; Williams, A. H.; Pajewski, N. M.; Chung, S. A.; Graham, R. R.; Zidovetzki, R.; Kelly, J. A.; Kaufman, K. M.; Jacob, C. O.; Vyse, T. J.; Tsao, B. P.; Kimberly, R. P.; Gaffney, P. M.; Alarcón-Riquelme, M. E.; Harley, J. B.; Langefeld, C. D.; International Consortium on the Genetics of Systemic Erythematosus. A Comprehensive Analysis of Shared Loci between Systemic Lupus Erythematosus (SLE) and Sixteen Autoimmune Diseases Reveals Limited Genetic Overlap. *PLoS Genet.* **2011**, *7* (12), e1002406. <https://doi.org/10.1371/journal.pgen.1002406>.
- (196) Deretic, V.; Saitoh, T.; Akira, S. Autophagy in Infection, Inflammation and Immunity. *Nat. Rev. Immunol.* **2013**, *13* (10), 722–737. <https://doi.org/10.1038/nri3532>.
- (197) Paludan, C.; Schmid, D.; Landthaler, M.; Vockerodt, M.; Kube, D.; Tuschl, T.; Münz, C. Endogenous MHC Class II Processing of a Viral Nuclear Antigen after Autophagy. *Science* **2005**, *307* (5709), 593–596. <https://doi.org/10.1126/science.1104904>.
- (198) Jagannath, C.; Lindsey, D. R.; Dhandayuthapani, S.; Xu, Y.; Hunter, R. L.; Eissa, N. T. Autophagy Enhances the Efficacy of BCG Vaccine by Increasing Peptide Presentation in Mouse Dendritic Cells. *Nat. Med.* **2009**, *15* (3), 267–276. <https://doi.org/10.1038/nm.1928>.
- (199) Pua, H. H.; Guo, J.; Komatsu, M.; He, Y.-W. Autophagy Is Essential for Mitochondrial Clearance in Mature T Lymphocytes. *J. Immunol. Baltim. Md 1950* **2009**, *182* (7), 4046–4055. <https://doi.org/10.4049/jimmunol.0801143>.

- (200) Miller, B. C.; Zhao, Z.; Stephenson, L. M.; Cadwell, K.; Pua, H. H.; Lee, H. K.; Mizushima, N. N.; Iwasaki, A.; He, Y.-W.; Swat, W.; Virgin, H. W. The Autophagy Gene ATG5 Plays an Essential Role in B Lymphocyte Development. *Autophagy* **2008**, *4* (3), 309–314. <https://doi.org/10.4161/auto.5474>.
- (201) Rathinam, V. A. K.; Vanaja, S. K.; Fitzgerald, K. A. Regulation of Inflammasome Signaling. *Nat. Immunol.* **2012**, *13* (4), 333–342. <https://doi.org/10.1038/ni.2237>.
- (202) Saitoh, T.; Fujita, N.; Jang, M. H.; Uematsu, S.; Yang, B.-G.; Satoh, T.; Omori, H.; Noda, T.; Yamamoto, N.; Komatsu, M.; Tanaka, K.; Kawai, T.; Tsujimura, T.; Takeuchi, O.; Yoshimori, T.; Akira, S. Loss of the Autophagy Protein Atg16L1 Enhances Endotoxin-Induced IL-1beta Production. *Nature* **2008**, *456* (7219), 264–268. <https://doi.org/10.1038/nature07383>.
- (203) Nakahira, K.; Haspel, J. A.; Rathinam, V. A. K.; Lee, S.-J.; Dolinay, T.; Lam, H. C.; Englert, J. A.; Rabinovitch, M.; Cernadas, M.; Kim, H. P.; Fitzgerald, K. A.; Ryter, S. W.; Choi, A. M. K. Autophagy Proteins Regulate Innate Immune Responses by Inhibiting the Release of Mitochondrial DNA Mediated by the NALP3 Inflammasome. *Nat. Immunol.* **2011**, *12* (3), 222–230. <https://doi.org/10.1038/ni.1980>.
- (204) Tal, M. C.; Sasai, M.; Lee, H. K.; Yordy, B.; Shadel, G. S.; Iwasaki, A. Absence of Autophagy Results in Reactive Oxygen Species-Dependent Amplification of RLR Signaling. *Proc. Natl. Acad. Sci. U. S. A.* **2009**, *106* (8), 2770–2775. <https://doi.org/10.1073/pnas.0807694106>.
- (205) Yang, C.-S.; Rodgers, M.; Min, C.-K.; Lee, J.-S.; Kingeter, L.; Lee, J.-Y.; Jong, A.; Kramnik, I.; Lin, X.; Jung, J. U. The Autophagy Regulator Rubicon Is a Feedback Inhibitor of CARD9-Mediated Host Innate Immunity. *Cell Host Microbe* **2012**, *11* (3), 277–289. <https://doi.org/10.1016/j.chom.2012.01.019>.
- (206) He, C.; Levine, B. The Beclin 1 Interactome. *Curr. Opin. Cell Biol.* **2010**, *22* (2), 140–149. <https://doi.org/10.1016/j.ceb.2010.01.001>.
- (207) Shintani, T.; Klionsky, D. J. Autophagy in Health and Disease: A Double-Edged Sword. *Science* **2004**, *306* (5698), 990–995. <https://doi.org/10.1126/science.1099993>.
- (208) Martinez-Vicente, M.; Cuervo, A. M. Autophagy and Neurodegeneration: When the Cleaning Crew Goes on Strike. *Lancet Neurol.* **2007**, *6* (4), 352–361. [https://doi.org/10.1016/S1474-4422\(07\)70076-5](https://doi.org/10.1016/S1474-4422(07)70076-5).
- (209) Rubinsztein, D. C.; DiFiglia, M.; Heintz, N.; Nixon, R. A.; Qin, Z.-H.; Ravikumar, B.; Stefanis, L.; Tolkovsky, A. Autophagy and Its Possible Roles in Nervous System Diseases, Damage and Repair. *Autophagy* **2005**, *1* (1), 11–22. <https://doi.org/10.4161/auto.1.1.1513>.
- (210) Nixon, R. A. Autophagy, Amyloidogenesis and Alzheimer Disease. *J. Cell Sci.* **2007**, *120* (Pt 23), 4081–4091. <https://doi.org/10.1242/jcs.019265>.
- (211) Lee, J.-H.; Yu, W. H.; Kumar, A.; Lee, S.; Mohan, P. S.; Peterhoff, C. M.; Wolfe, D. M.; Martinez-Vicente, M.; Massey, A. C.; Sovak, G.; Uchiyama, Y.; Westaway, D.; Cuervo, A. M.; Nixon, R. A. Lysosomal Proteolysis and Autophagy Require Presenilin 1 and Are Disrupted by Alzheimer-Related PS1 Mutations. *Cell* **2010**, *141* (7), 1146–1158. <https://doi.org/10.1016/j.cell.2010.05.008>.
- (212) Whyte, L. S.; Lau, A. A.; Hemsley, K. M.; Hopwood, J. J.; Sargeant, T. J. Endo-Lysosomal and Autophagic Dysfunction: A Driving Factor in Alzheimer's Disease? *J. Neurochem.* **2017**, *140* (5), 703–717. <https://doi.org/10.1111/jnc.13935>.
- (213) Spilman, P.; Podlutska, N.; Hart, M. J.; Debnath, J.; Gorostiza, O.; Bredesen, D.; Richardson, A.; Strong, R.; Galvan, V. Inhibition of MTOR by Rapamycin Abolishes Cognitive Deficits and Reduces Amyloid-Beta Levels in a Mouse Model of Alzheimer's Disease. *PLoS One* **2010**, *5* (4), e9979. <https://doi.org/10.1371/journal.pone.0009979>.
- (214) Gelb, D. J.; Oliver, E.; Gilman, S. Diagnostic Criteria for Parkinson Disease. *Arch. Neurol.* **1999**, *56* (1), 33–39. <https://doi.org/10.1001/archneur.56.1.33>.

- (215) Abeliovich, A.; Schmitz, Y.; Fariñas, I.; Choi-Lundberg, D.; Ho, W. H.; Castillo, P. E.; Shinsky, N.; Verdugo, J. M.; Armanini, M.; Ryan, A.; Hynes, M.; Phillips, H.; Sulzer, D.; Rosenthal, A. Mice Lacking Alpha-Synuclein Display Functional Deficits in the Nigrostriatal Dopamine System. *Neuron* **2000**, *25* (1), 239–252. [https://doi.org/10.1016/s0896-6273\(00\)80886-7](https://doi.org/10.1016/s0896-6273(00)80886-7).
- (216) Webb, J. L.; Ravikumar, B.; Atkins, J.; Skepper, J. N.; Rubinsztein, D. C. Alpha-Synuclein Is Degraded by Both Autophagy and the Proteasome. *J. Biol. Chem.* **2003**, *278* (27), 25009–25013. <https://doi.org/10.1074/jbc.M300227200>.
- (217) Choi, K.-C.; Kim, S.-H.; Ha, J.-Y.; Kim, S.-T.; Son, J. H. A Novel MTOR Activating Protein Protects Dopamine Neurons against Oxidative Stress by Repressing Autophagy Related Cell Death. *J. Neurochem.* **2010**, *112* (2), 366–376. <https://doi.org/10.1111/j.1471-4159.2009.06463.x>.
- (218) Gil, J. M.; Rego, A. C. Mechanisms of Neurodegeneration in Huntington’s Disease. *Eur. J. Neurosci.* **2008**, *27* (11), 2803–2820. <https://doi.org/10.1111/j.1460-9568.2008.06310.x>.
- (219) Iwata, A.; Riley, B. E.; Johnston, J. A.; Kopito, R. R. HDAC6 and Microtubules Are Required for Autophagic Degradation of Aggregated Huntingtin. *J. Biol. Chem.* **2005**, *280* (48), 40282–40292. <https://doi.org/10.1074/jbc.M508786200>.
- (220) Ravikumar, B.; Vacher, C.; Berger, Z.; Davies, J. E.; Luo, S.; Oroz, L. G.; Scaravilli, F.; Easton, D. F.; Duden, R.; O’Kane, C. J.; Rubinsztein, D. C. Inhibition of MTOR Induces Autophagy and Reduces Toxicity of Polyglutamine Expansions in Fly and Mouse Models of Huntington Disease. *Nat. Genet.* **2004**, *36* (6), 585–595. <https://doi.org/10.1038/ng1362>.
- (221) Ashkenazi, A.; Bento, C. F.; Ricketts, T.; Vicinanza, M.; Siddiqi, F.; Pavel, M.; Squitieri, F.; Hardenberg, M. C.; Imarisio, S.; Menzies, F. M.; Rubinsztein, D. C. Polyglutamine Tracts Regulate Beclin 1-Dependent Autophagy. *Nature* **2017**, *545* (7652), 108–111. <https://doi.org/10.1038/nature22078>.
- (222) Galluzzi, L.; Bravo-San Pedro, J. M.; Levine, B.; Green, D. R.; Kroemer, G. Pharmacological Modulation of Autophagy: Therapeutic Potential and Persisting Obstacles. *Nat. Rev. Drug Discov.* **2017**, *16* (7), 487–511. <https://doi.org/10.1038/nrd.2017.22>.
- (223) Kim, Y. C.; Guan, K.-L. MTOR: A Pharmacologic Target for Autophagy Regulation. *J. Clin. Invest.* **2015**, *125* (1), 25–32. <https://doi.org/10.1172/JCI73939>.
- (224) Thoreen, C. C.; Kang, S. A.; Chang, J. W.; Liu, Q.; Zhang, J.; Gao, Y.; Reichling, L. J.; Sim, T.; Sabatini, D. M.; Gray, N. S. An ATP-Competitive Mammalian Target of Rapamycin Inhibitor Reveals Rapamycin-Resistant Functions of MTORC1. *J. Biol. Chem.* **2009**, *284* (12), 8023–8032. <https://doi.org/10.1074/jbc.M900301200>.
- (225) Göransson, O.; McBride, A.; Hawley, S. A.; Ross, F. A.; Shpiro, N.; Foretz, M.; Viollet, B.; Hardie, D. G.; Sakamoto, K. Mechanism of Action of A-769662, a Valuable Tool for Activation of AMP-Activated Protein Kinase. *J. Biol. Chem.* **2007**, *282* (45), 32549–32560. <https://doi.org/10.1074/jbc.M706536200>.
- (226) Shoji-Kawata, S.; Sumpter, R.; Leveno, M.; Campbell, G. R.; Zou, Z.; Kinch, L.; Wilkins, A. D.; Sun, Q.; Pallauf, K.; MacDuff, D.; Huerta, C.; Virgin, H. W.; Helms, J. B.; Eerland, R.; Tooze, S. A.; Xavier, R.; Lenschow, D. J.; Yamamoto, A.; King, D.; Lichtarge, O.; Grishin, N. V.; Spector, S. A.; Kaloyanova, D. V.; Levine, B. Identification of a Candidate Therapeutic Autophagy-Inducing Peptide. *Nature* **2013**, *494* (7436), 201–206. <https://doi.org/10.1038/nature11866>.
- (227) Liu, X.; Chhipa, R. R.; Nakano, I.; Dasgupta, B. The AMPK Inhibitor Compound C Is a Potent AMPK-Independent Antiglioma Agent. *Mol. Cancer Ther.* **2014**, *13* (3), 596–605. <https://doi.org/10.1158/1535-7163.MCT-13-0579>.

- (228) Martin, K. R.; Celano, S. L.; Solitro, A. R.; Gunaydin, H.; Scott, M.; O'Hagan, R. C.; Shumway, S. D.; Fuller, P.; MacKeigan, J. P. A Potent and Selective ULK1 Inhibitor Suppresses Autophagy and Sensitizes Cancer Cells to Nutrient Stress. *iScience* **2018**, *8*, 74–84. <https://doi.org/10.1016/j.isci.2018.09.012>.
- (229) Wu, Y.-T.; Tan, H.-L.; Shui, G.; Bauvy, C.; Huang, Q.; Wenk, M. R.; Ong, C.-N.; Codogno, P.; Shen, H.-M. Dual Role of 3-Methyladenine in Modulation of Autophagy via Different Temporal Patterns of Inhibition on Class I and III Phosphoinositide 3-Kinase. *J. Biol. Chem.* **2010**, *285* (14), 10850–10861. <https://doi.org/10.1074/jbc.M109.080796>.
- (230) Blommaert, E. F.; Krause, U.; Schellens, J. P.; Vreeling-Sindelárová, H.; Meijer, A. J. The Phosphatidylinositol 3-Kinase Inhibitors Wortmannin and LY294002 Inhibit Autophagy in Isolated Rat Hepatocytes. *Eur. J. Biochem.* **1997**, *243* (1–2), 240–246. <https://doi.org/10.1111/j.1432-1033.1997.0240a.x>.
- (231) Dowdle, W. E.; Nyfeler, B.; Nagel, J.; Elling, R. A.; Liu, S.; Triantafellow, E.; Menon, S.; Wang, Z.; Honda, A.; Pardee, G.; Cantwell, J.; Luu, C.; Cornella-Taracido, I.; Harrington, E.; Fekkes, P.; Lei, H.; Fang, Q.; Digan, M. E.; Burdick, D.; Powers, A. F.; Helliwell, S. B.; D'Aquin, S.; Bastien, J.; Wang, H.; Wiederschain, D.; Kuerth, J.; Bergman, P.; Schwalb, D.; Thomas, J.; Ugwonali, S.; Harbinski, F.; Tallarico, J.; Wilson, C. J.; Myer, V. E.; Porter, J. A.; Bussiere, D. E.; Finan, P. M.; Labow, M. A.; Mao, X.; Hamann, L. G.; Manning, B. D.; Valdez, R. A.; Nicholson, T.; Schirle, M.; Knapp, M. S.; Keaney, E. P.; Murphy, L. O. Selective VPS34 Inhibitor Blocks Autophagy and Uncovers a Role for NCOA4 in Ferritin Degradation and Iron Homeostasis *in Vivo*. *Nat. Cell Biol.* **2014**, *16* (11), 1069–1079. <https://doi.org/10.1038/ncb3053>.
- (232) Aldrich, L. N.; Kuo, S.-Y.; Castoreno, A. B.; Goel, G.; Kuballa, P.; Rees, M. G.; Seashore-Ludlow, B. A.; Cheah, J. H.; Latorre, I. J.; Schreiber, S. L.; Shamji, A. F.; Xavier, R. J. Discovery of a Small-Molecule Probe for V-ATPase Function. *J. Am. Chem. Soc.* **2015**, *137* (16), 5563–5568. <https://doi.org/10.1021/jacs.5b02150>.
- (233) Tanida, I.; Minematsu-Ikeguchi, N.; Ueno, T.; Kominami, E. Lysosomal Turnover, but Not a Cellular Level, of Endogenous LC3 Is a Marker for Autophagy. *Autophagy* **2005**, *1* (2), 84–91. <https://doi.org/10.4161/auto.1.2.1697>.
- (234) Mauthe, M.; Orhon, I.; Rocchi, C.; Zhou, X.; Luhr, M.; Hijlkema, K.-J.; Coppes, R. P.; Engedal, N.; Mari, M.; Reggiori, F. Chloroquine Inhibits Autophagic Flux by Decreasing Autophagosome-Lysosome Fusion. *Autophagy* **2018**, *14* (8), 1435–1455. <https://doi.org/10.1080/15548627.2018.1474314>.
- (235) Mauvezin, C.; Neufeld, T. P. Bafilomycin A1 Disrupts Autophagic Flux by Inhibiting Both V-ATPase-Dependent Acidification and Ca-P60A/SERCA-Dependent Autophagosome-Lysosome Fusion. *Autophagy* **2015**, *11* (8), 1437–1438. <https://doi.org/10.1080/15548627.2015.1066957>.
- (236) Vats, S.; Manjithaya, R. A Reversible Autophagy Inhibitor Blocks Autophagosome-Lysosome Fusion by Preventing Stx17 Loading onto Autophagosomes. *Mol. Biol. Cell* **2019**, *30* (17), 2283–2295. <https://doi.org/10.1091/mbc.E18-08-0482>.
- (237) Puleston, D. J.; Zhang, H.; Powell, T. J.; Lipina, E.; Sims, S.; Panse, I.; Watson, A. S.; Cerundolo, V.; Townsend, A. R.; Klenerman, P.; Simon, A. K. Autophagy Is a Critical Regulator of Memory CD8+ T Cell Formation. *eLife* **2014**, *3*, e03706. <https://doi.org/10.7554/eLife.03706>.
- (238) Pua, H. H.; Dzhagalov, I.; Chuck, M.; Mizushima, N.; He, Y.-W. A Critical Role for the Autophagy Gene Atg5 in T Cell Survival and Proliferation. *J. Exp. Med.* **2007**, *204* (1), 25–31. <https://doi.org/10.1084/jem.20061303>.
- (239) Cassidy, L. D.; Young, A. R. J.; Young, C. N. J.; Soilleux, E. J.; Fielder, E.; Weigand, B. M.; Lagnado, A.; Brais, R.; Ktistakis, N. T.; Wiggins, K. A.; Pyriou, K.; Clarke, M. C. H.; Jurk, D.; Passos, J. F.; Narita, M. Temporal Inhibition of Autophagy Reveals Segmental Reversal of Ageing with Increased Cancer Risk. *Nat. Commun.* **2020**, *11* (1), 307. <https://doi.org/10.1038/s41467-019-14187-x>.
- (240) Mancias, J. D.; Kimmelman, A. C. Targeting Autophagy Addiction in Cancer. *Oncotarget* **2011**, *2* (12), 1302–1306.

- (241) Bryant, K. L.; Stalneck, C. A.; Zeitouni, D.; Klomp, J. E.; Peng, S.; Tikunov, A. P.; Gunda, V.; Pierobon, M.; Waters, A. M.; George, S. D.; Tomar, G.; Papke, B.; Hobbs, G. A.; Yan, L.; Hayes, T. K.; Diehl, J. N.; Goode, G. D.; Chaika, N. V.; Wang, Y.; Zhang, G.-F.; Witkiewicz, A. K.; Knudsen, E. S.; Petricoin, E. F.; Singh, P. K.; Macdonald, J. M.; Tran, N. L.; Lyssiotis, C. A.; Ying, H.; Kimmelman, A. C.; Cox, A. D.; Der, C. J. Combination of ERK and Autophagy Inhibition as a Treatment Approach for Pancreatic Cancer. *Nat. Med.* **2019**, *25* (4), 628–640. <https://doi.org/10.1038/s41591-019-0368-8>.
- (242) Kinsey, C. G.; Camolotto, S. A.; Boespflug, A. M.; Guillen, K. P.; Foth, M.; Truong, A.; Schuman, S. S.; Shea, J. E.; Seipp, M. T.; Yap, J. T.; Burrell, L. D.; Lum, D. H.; Whisenant, J. R.; Gilcrease, G. W.; Cavalieri, C. C.; Rehbein, K. M.; Cutler, S. L.; Affolter, K. E.; Welm, A. L.; Welm, B. E.; Scaife, C. L.; Snyder, E. L.; McMahon, M. Protective Autophagy Elicited by RAF→MEK→ERK Inhibition Suggests a Treatment Strategy for RAS-Driven Cancers. *Nat. Med.* **2019**, *25* (4), 620–627. <https://doi.org/10.1038/s41591-019-0367-9>.
- (243) Wolpin, B. M.; Rubinson, D. A.; Wang, X.; Chan, J. A.; Cleary, J. M.; Enzinger, P. C.; Fuchs, C. S.; McCleary, N. J.; Meyerhardt, J. A.; Ng, K.; Schrag, D.; Sikora, A. L.; Spicer, B. A.; Killion, L.; Mamon, H.; Kimmelman, A. C. Phase II and Pharmacodynamic Study of Autophagy Inhibition Using Hydroxychloroquine in Patients With Metastatic Pancreatic Adenocarcinoma. *The Oncologist* **2014**, *19* (6), 637–638. <https://doi.org/10.1634/theoncologist.2014-0086>.
- (244) Malhotra, J.; Jabbour, S.; Orlick, M.; Riedlinger, G.; Joshi, S.; Guo, J. Y.; White, E.; Aisner, J. Modulation of Autophagy with Hydroxychloroquine in Patients with Advanced Non-Small Cell Lung Cancer (NSCLC): A Phase Ib Study. *J. Clin. Oncol.* **2018**, *36* (15\_suppl), e21138–e21138. [https://doi.org/10.1200/JCO.2018.36.15\\_suppl.e21138](https://doi.org/10.1200/JCO.2018.36.15_suppl.e21138).
- (245) Eng, C. H.; Wang, Z.; Tkach, D.; Toral-Barza, L.; Ugwonali, S.; Liu, S.; Fitzgerald, S. L.; George, E.; Frias, E.; Cochran, N.; Jesus, R. D.; McAllister, G.; Hoffman, G. R.; Bray, K.; Lemon, L.; Lucas, J.; Fantin, V. R.; Abraham, R. T.; Murphy, L. O.; Nyfeler, B. Macroautophagy Is Dispensable for Growth of KRAS Mutant Tumors and Chloroquine Efficacy. *Proc. Natl. Acad. Sci.* **2016**, *113* (1), 182–187. <https://doi.org/10.1073/pnas.1515617113>.
- (246) Dall'Armi, C.; Devereaux, K. A.; Di Paolo, G. The Role of Lipids in The Control of Autophagy. *Curr. Biol. CB* **2013**, *23* (1), R33–R45. <https://doi.org/10.1016/j.cub.2012.10.041>.
- (247) Zhong, Y.; Wang, Q. J.; Li, X.; Yan, Y.; Backer, J. M.; Chait, B. T.; Heintz, N.; Yue, Z. Distinct Regulation of Autophagic Activity by Atg14L and Rubicon Associated with Beclin 1- Phosphatidylinositol 3-Kinase Complex. *Nat. Cell Biol.* **2009**, *11* (4), 468–476. <https://doi.org/10.1038/ncb1854>.
- (248) Obara, K.; Noda, T.; Niimi, K.; Ohsumi, Y. Transport of Phosphatidylinositol 3-Phosphate into the Vacuole via Autophagic Membranes in *Saccharomyces Cerevisiae*. *Genes Cells Devoted Mol. Cell. Mech.* **2008**, *13* (6), 537–547. <https://doi.org/10.1111/j.1365-2443.2008.01188.x>.
- (249) Nascimbeni, A. C.; Codogno, P.; Morel, E. Phosphatidylinositol-3-Phosphate in the Regulation of Autophagy Membrane Dynamics. *FEBS J.* **2017**, *284* (9), 1267–1278. <https://doi.org/10.1111/febs.13987>.
- (250) Ronan, B.; Flamand, O.; Vescovi, L.; Dureuil, C.; Durand, L.; Fassy, F.; Bachelot, M.-F.; Lambertson, A.; Mathieu, M.; Bertrand, T.; Marquette, J.-P.; El-Ahmad, Y.; Filoche-Romme, B.; Schio, L.; Garcia-Echeverria, C.; Goulaouic, H.; Pasquier, B. A Highly Potent and Selective Vps34 Inhibitor Alters Vesicle Trafficking and Autophagy. *Nat. Chem. Biol.* **2014**, *10* (12), 1013–1019. <https://doi.org/10.1038/nchembio.1681>.
- (251) Honda, A.; Harrington, E.; Cornella-Taracido, I.; Furet, P.; Knapp, M. S.; Glick, M.; Triantafellow, E.; Dowdle, W. E.; Wiedersheim, D.; Maniara, W.; Moore, C.; Finan, P. M.; Hamann, L. G.; Firestone, B.; Murphy, L. O.; Keaney, E. P. Potent, Selective, and Orally Bioavailable Inhibitors of VPS34 Provide Chemical Tools to Modulate Autophagy in Vivo. *ACS Med. Chem. Lett.* **2015**, *7* (1), 72–76. <https://doi.org/10.1021/acsmedchemlett.5b00335>.

- (252) Miller, S.; Tavshanjian, B.; Oleksy, A.; Perisic, O.; Houseman, B. T.; Shokat, K. M.; Williams, R. L. Shaping Development of Autophagy Inhibitors with the Structure of the Lipid Kinase Vps34. *Science* **2010**, 327 (5973), 1638–1642. <https://doi.org/10.1126/science.1184429>.
- (253) Rostislavleva, K.; Soler, N.; Ohashi, Y.; Zhang, L.; Pardon, E.; Burke, J. E.; Masson, G. R.; Johnson, C.; Steyaert, J.; Ktistakis, N. T.; Williams, R. L. Structure and Flexibility of the Endosomal Vps34 Complex Reveals the Basis of Its Function on Membranes. *Science* **2015**, 350 (6257), aac7365–aac7365. <https://doi.org/10.1126/science.aac7365>.
- (254) Baskaran, S.; Carlson, L.-A.; Stjepanovic, G.; Young, L. N.; Kim, D. J.; Grob, P.; Stanley, R. E.; Nogales, E.; Hurley, J. H. Architecture and Dynamics of the Autophagic Phosphatidylinositol 3-Kinase Complex. *eLife* **2014**, 3. <https://doi.org/10.7554/eLife.05115>.
- (255) Yan, Y.; Flinn, R. J.; Wu, H.; Schnur, R. S.; Backer, J. M. HVps15, but Not Ca<sup>2+</sup>/CaM, Is Required for the Activity and Regulation of HVps34 in Mammalian Cells. *Biochem. J.* **2009**, 417 (3), 747–755. <https://doi.org/10.1042/BJ20081865>.
- (256) Liang, C.; Feng, P.; Ku, B.; Dotan, I.; Canaani, D.; Oh, B.-H.; Jung, J. U. Autophagic and Tumour Suppressor Activity of a Novel Beclin1-Binding Protein UVRAG. *Nat. Cell Biol.* **2006**, 8 (7), 688–698. <https://doi.org/10.1038/ncb1426>.
- (257) Noble, C. G.; Dong, J.-M.; Manser, E.; Song, H. Bcl-XL and UVRAG Cause a Monomer-Dimer Switch in Beclin1. *J. Biol. Chem.* **2008**, 283 (38), 26274–26282. <https://doi.org/10.1074/jbc.M804723200>.
- (258) Jaber, N.; Dou, Z.; Chen, J.-S.; Catanzaro, J.; Jiang, Y.-P.; Ballou, L. M.; Selinger, E.; Ouyang, X.; Lin, R. Z.; Zhang, J.; Zong, W.-X. Class III PI3K Vps34 Plays an Essential Role in Autophagy and in Heart and Liver Function. *Proc. Natl. Acad. Sci. U. S. A.* **2012**, 109 (6), 2003–2008. <https://doi.org/10.1073/pnas.1112848109>.
- (259) Kihara, A.; Noda, T.; Ishihara, N.; Ohsumi, Y. Two Distinct Vps34 Phosphatidylinositol 3-Kinase Complexes Function in Autophagy and Carboxypeptidase Y Sorting In *Saccharomyces Cerevisiae*. *J. Cell Biol.* **2001**, 152 (3), 519–530.
- (260) Matsunaga, K.; Morita, E.; Saitoh, T.; Akira, S.; Ktistakis, N. T.; Izumi, T.; Noda, T.; Yoshimori, T. Autophagy Requires Endoplasmic Reticulum Targeting of the PI3-Kinase Complex via Atg14L. *J. Cell Biol.* **2010**, 190 (4), 511–521. <https://doi.org/10.1083/jcb.200911141>.
- (261) Ma, M.; Liu, J.-J.; Li, Y.; Huang, Y.; Ta, N.; Chen, Y.; Fu, H.; Ye, M.-D.; Ding, Y.; Huang, W.; Wang, J.; Dong, M.-Q.; Yu, L.; Wang, H.-W. Cryo-EM Structure and Biochemical Analysis Reveal the Basis of the Functional Difference between Human PI3KC3-C1 and -C2. *Cell Res.* **2017**, 27 (8), 989–1001. <https://doi.org/10.1038/cr.2017.94>.
- (262) Mei, Y.; Su, M.; Sanishvili, R.; Chakravarthy, S.; Colbert, C. L.; Sinha, S. C. Identification of BECN1 and ATG14 Coiled-Coil Interface Residues That Are Important for Starvation-Induced Autophagy. *Biochemistry* **2016**, 55 (30), 4239–4253. <https://doi.org/10.1021/acs.biochem.6b00246>.
- (263) Kim, H. J.; Zhong, Q.; Sheng, Z.-H.; Yoshimori, T.; Liang, C.; Jung, J. U. Beclin-1-Interacting Autophagy Protein Atg14L Targets the SNARE-Associated Protein Snapin to Coordinate Endocytic Trafficking. *J. Cell Sci.* **2012**, 125 (20), 4740–4750. <https://doi.org/10.1242/jcs.100339>.
- (264) Li, X.; He, L.; Che, K. H.; Funderburk, S. F.; Pan, L.; Pan, N.; Zhang, M.; Yue, Z.; Zhao, Y. Imperfect Interface of Beclin1 Coiled-Coil Domain Regulates Homodimer and Heterodimer Formation with Atg14L and UVRAG. *Nat. Commun.* **2012**, 3 (1). <https://doi.org/10.1038/ncomms1648>.
- (265) Wu, S.; He, Y.; Qiu, X.; Yang, W.; Liu, W.; Li, X.; Li, Y.; Shen, H.-M.; Wang, R.; Yue, Z.; Zhao, Y. Targeting the Potent Beclin 1–UVRAG Coiled-Coil Interaction with Designed Peptides Enhances Autophagy and

Endolysosomal Trafficking. *Proc. Natl. Acad. Sci.* **2018**, *115* (25), E5669–E5678.  
<https://doi.org/10.1073/pnas.1721173115>.

(266) Marat, A. L.; Haucke, V. Phosphatidylinositol 3-phosphates—at the Interface between Cell Signalling and Membrane Traffic. *EMBO J.* **2016**, *35* (6), 561–579. <https://doi.org/10.15252/embj.201593564>.

(267) Scarlatti, F.; Maffei, R.; Beau, I.; Codogno, P.; Ghidoni, R. Role of Non-Canonical Beclin 1-Independent Autophagy in Cell Death Induced by Resveratrol in Human Breast Cancer Cells. *Cell Death Differ.* **2008**, *15* (8), 1318–1329. <https://doi.org/10.1038/cdd.2008.51>.

(268) Galluzzi, L.; Green, D. R. Autophagy-Independent Functions of the Autophagy Machinery. *Cell* **2019**, *177* (7), 1682–1699. <https://doi.org/10.1016/j.cell.2019.05.026>.

(269) Hanada, T.; Noda, N. N.; Satomi, Y.; Ichimura, Y.; Fujioka, Y.; Takao, T.; Inagaki, F.; Ohsumi, Y. The Atg12-Atg5 Conjugate Has a Novel E3-like Activity for Protein Lipidation in Autophagy. *J. Biol. Chem.* **2007**, *282* (52), 37298–37302. <https://doi.org/10.1074/jbc.C700195200>.

(270) Romanov, J.; Walczak, M.; Ibiricu, I.; Schüchner, S.; Ogris, E.; Kraft, C.; Martens, S. Mechanism and Functions of Membrane Binding by the Atg5-Atg12/Atg16 Complex during Autophagosome Formation: Role of Atg5-Atg12/Atg16 during Autophagy. *EMBO J.* **2012**, *31* (22), 4304–4317. <https://doi.org/10.1038/emboj.2012.278>.

(271) Chen, D.; Fan, W.; Lu, Y.; Ding, X.; Chen, S.; Zhong, Q. A Mammalian Autophagosome Maturation Mechanism Mediated by TECPR1 and the Atg12-Atg5 Conjugate. *Mol. Cell* **2012**, *45* (5), 629–641. <https://doi.org/10.1016/j.molcel.2011.12.036>.

(272) Kuma, A.; Hatano, M.; Matsui, M.; Yamamoto, A.; Nakaya, H.; Yoshimori, T.; Ohsumi, Y.; Tokuhiya, T.; Mizushima, N. The Role of Autophagy during the Early Neonatal Starvation Period. *Nature* **2004**, *432* (7020), 1032–1036. <https://doi.org/10.1038/nature03029>.

(273) Tekirdag, K. A.; Korkmaz, G.; Ozturk, D. G.; Agami, R.; Gozuacik, D. MIR181A Regulates Starvation- and Rapamycin-Induced Autophagy through Targeting of ATG5. *Autophagy* **2013**, *9* (3), 374–385. <https://doi.org/10.4161/auto.23117>.

(274) Matsushita, M.; Suzuki, N. N.; Obara, K.; Fujioka, Y.; Ohsumi, Y.; Inagaki, F. Structure of Atg5-Atg16, a Complex Essential for Autophagy. *J. Biol. Chem.* **2007**, *282* (9), 6763–6772. <https://doi.org/10.1074/jbc.M609876200>.

(275) Kim, J. H.; Hong, S. B.; Lee, J. K.; Han, S.; Roh, K.-H.; Lee, K.-E.; Kim, Y. K.; Choi, E.-J.; Song, H. K. Insights into Autophagosome Maturation Revealed by the Structures of ATG5 with Its Interacting Partners. *Autophagy* **2015**, *11* (1), 75–87. <https://doi.org/10.4161/15548627.2014.984276>.

(276) Robinson, E.; Leung, E.; Matuszek, A. M.; Krogsaard-Larsen, N.; Furkert, D. P.; Brimble, M. A.; Richardson, A.; Reynisson, J. Virtual Screening for Novel Atg5-Atg16 Complex Inhibitors for Autophagy Modulation. *MedChemComm* **2015**, *6* (1), 239–246. <https://doi.org/10.1039/C4MD00420E>.

(277) Zhao, Z.; Fux, B.; Goodwin, M.; Dunay, I. R.; Strong, D.; Miller, B. C.; Cadwell, K.; Delgado, M. A.; Ponpuak, M.; Green, K. G.; Schmidt, R. E.; Mizushima, N.; Deretic, V.; Sibley, L. D.; Virgin, H. W. Autophagosome-Independent Essential Function for the Autophagy Protein Atg5 in Cellular Immunity to Intracellular Pathogens. *Cell Host Microbe* **2008**, *4* (5), 458–469. <https://doi.org/10.1016/j.chom.2008.10.003>.

(278) Arkin, M. R.; Tang, Y.; Wells, J. A. Small-Molecule Inhibitors of Protein-Protein Interactions: Progressing towards the Reality. *Chem. Biol.* **2014**, *21* (9), 1102–1114. <https://doi.org/10.1016/j.chembiol.2014.09.001>.

(279) Roberts, A. W.; Davids, M. S.; Pagel, J. M.; Kahl, B. S.; Puvvada, S. D.; Gerecitano, J. F.; Kipps, T. J.; Anderson, M. A.; Brown, J. R.; Gressick, L.; Wong, S.; Dunbar, M.; Zhu, M.; Desai, M. B.; Cerri, E.; Heitner Enschede, S.; Humerickhouse, R. A.; Wierda, W. G.; Seymour, J. F. Targeting BCL2 with Venetoclax in Relapsed

- Chronic Lymphocytic Leukemia. *N. Engl. J. Med.* **2016**, *374* (4), 311–322. <https://doi.org/10.1056/NEJMoa1513257>.
- (280) Vu, B.; Wovkulich, P.; Pizzolato, G.; Lovey, A.; Ding, Q.; Jiang, N.; Liu, J.-J.; Zhao, C.; Glenn, K.; Wen, Y.; Tovar, C.; Packman, K.; Vassilev, L.; Graves, B. Discovery of RG7112: A Small-Molecule MDM2 Inhibitor in Clinical Development. *ACS Med. Chem. Lett.* **2013**, *4* (5), 466–469. <https://doi.org/10.1021/ml4000657>.
- (281) Bullock, B. N.; Jochim, A. L.; Arora, P. S. Assessing Helical Protein Interfaces for Inhibitor Design. *J. Am. Chem. Soc.* **2011**, *133* (36), 14220–14223. <https://doi.org/10.1021/ja206074j>.
- (282) Lao, B. B.; Drew, K.; Guarracino, D. A.; Brewer, T. F.; Heindel, D. W.; Bonneau, R.; Arora, P. S. Rational Design of Topographical Helix Mimics as Potent Inhibitors of Protein–Protein Interactions. *J. Am. Chem. Soc.* **2014**, *136* (22), 7877–7888. <https://doi.org/10.1021/ja502310r>.
- (283) Banerjee, S.; Bartesaghi, A.; Merk, A.; Rao, P.; Bulfer, S. L.; Yan, Y.; Green, N.; Mroczkowski, B.; Neitz, R. J.; Wipf, P.; Falconieri, V.; Deshaies, R. J.; Milne, J. L. S.; Huryn, D.; Arkin, M.; Subramaniam, S. 2.3 Å Resolution Cryo-EM Structure of Human P97 and Mechanism of Allosteric Inhibition. *Science* **2016**, *351* (6275), 871–875. <https://doi.org/10.1126/science.aad7974>.
- (284) Kuzmanic, A.; Bowman, G. R.; Juarez-Jimenez, J.; Michel, J.; Gervasio, F. L. Investigating Cryptic Binding Sites by Molecular Dynamics Simulations. *Acc. Chem. Res.* **2020**, *53* (3), 654–661. <https://doi.org/10.1021/acs.accounts.9b00613>.
- (285) Sperandio, O.; Reynès, C. H.; Camproux, A.-C.; Villoutreix, B. O. Rationalizing the Chemical Space of Protein–Protein Interaction Inhibitors. *Drug Discov. Today* **2010**, *15* (5), 220–229. <https://doi.org/10.1016/j.drudis.2009.11.007>.
- (286) Higuero, A. P.; Jubbe, H.; Blundell, T. L. Protein–Protein Interactions as Druggable Targets: Recent Technological Advances. *Curr. Opin. Pharmacol.* **2013**, *13* (5), 791–796. <https://doi.org/10.1016/j.coph.2013.05.009>.
- (287) Ofran, Y.; Rost, B. Protein–Protein Interaction Hotspots Carved into Sequences. *PLOS Comput. Biol.* **2007**, *3* (7), e119. <https://doi.org/10.1371/journal.pcbi.0030119>.
- (288) Magee, T. V. Progress in Discovery of Small-Molecule Modulators of Protein-Protein Interactions via Fragment Screening. *Bioorg. Med. Chem. Lett.* **2015**, *25* (12), 2461–2468. <https://doi.org/10.1016/j.bmcl.2015.04.089>.
- (289) Lamoree, B.; Hubbard, R. E. Current Perspectives in Fragment-Based Lead Discovery (FBLD). *Essays Biochem.* **2017**, *61* (5), 453–464. <https://doi.org/10.1042/EBC20170028>.
- (290) de Vega, M. J. P.; Martín-Martínez, M.; González-Muñiz, R. Modulation of Protein-Protein Interactions by Stabilizing/Mimicking Protein Secondary Structure Elements. *Curr. Top. Med. Chem.* **2007**, *7* (1), 33–62. <https://doi.org/10.2174/156802607779318325>.
- (291) Kritzer, J. A. Stapled Peptides: Magic Bullets in Nature’s Arsenal. *Nat. Chem. Biol.* **2010**, *6* (8), 566–567. <https://doi.org/10.1038/nchembio.407>.
- (292) Peraro, L.; Zou, Z.; Makwana, K. M.; Cummings, A. E.; Ball, H. L.; Yu, H.; Lin, Y.-S.; Levine, B.; Kritzer, J. A. Diversity-Oriented Stapling Yields Intrinsically Cell-Penetrant Inducers of Autophagy. *J. Am. Chem. Soc.* **2017**, *139* (23), 7792–7802. <https://doi.org/10.1021/jacs.7b01698>.
- (293) Moffat, J. G.; Rudolph, J.; Bailey, D. Phenotypic Screening in Cancer Drug Discovery — Past, Present and Future. *Nat. Rev. Drug Discov.* **2014**, *13* (8), 588–602. <https://doi.org/10.1038/nrd4366>.
- (294) Arkin, M. R.; Glicksman, M. A.; Fu, H.; Havel, J. J.; Du, Y. Inhibition of Protein-Protein Interactions: Non-Cellular Assay Formats. In *Assay Guidance Manual*; Sittampalam, G. S., Grossman, A., Brimacombe, K.,

- Arkin, M., Auld, D., Austin, C. P., Baell, J., Bejcek, B., Caaveiro, J. M. M., Chung, T. D. Y., Coussens, N. P., Dahlin, J. L., Devanaryan, V., Foley, T. L., Glicksman, M., Hall, M. D., Haas, J. V., Hoare, S. R. J., Inglese, J., Iversen, P. W., Kahl, S. D., Kales, S. C., Kirshner, S., Lal-Nag, M., Li, Z., McGee, J., McManus, O., Riss, T., Saradjian, P., Trask, O. J., Weidner, J. R., Wildey, M. J., Xia, M., Xu, X., Eds.; Eli Lilly & Company and the National Center for Advancing Translational Sciences: Bethesda (MD), 2004.
- (295) Rossi, A. M.; Taylor, C. W. Analysis of Protein-Ligand Interactions by Fluorescence Polarization. *Nat. Protoc.* **2011**, *6* (3), 365–387. <https://doi.org/10.1038/nprot.2011.305>.
- (296) Azzarito, V.; Prabhakaran, P.; Bartlett, A. I.; Murphy, N. S.; Hardie, M. J.; Kilner, C. A.; Edwards, T. A.; Warriner, S. L.; Wilson, A. J. 2-O-Alkylated Para-Benzamide  $\alpha$ -Helix Mimetics: The Role of Scaffold Curvature. *Org. Biomol. Chem.* **2012**, *10* (32), 6469–6472. <https://doi.org/10.1039/C2OB26262B>.
- (297) Song, Y.; Madahar, V.; Liao, J. Development of FRET Assay into Quantitative and High-Throughput Screening Technology Platforms for Protein-Protein Interactions. *Ann. Biomed. Eng.* **2011**, *39* (4), 1224–1234. <https://doi.org/10.1007/s10439-010-0225-x>.
- (298) Kerppola, T. K. Design and Implementation of Bimolecular Fluorescence Complementation (BiFC) Assays for the Visualization of Protein Interactions in Living Cells. *Nat. Protoc.* **2006**, *1* (3), 1278–1286. <https://doi.org/10.1038/nprot.2006.201>.
- (299) Magliery, T. J.; Wilson, C. G. M.; Pan, W.; Mishler, D.; Ghosh, I.; Hamilton, A. D.; Regan, L. Detecting Protein-Protein Interactions with a Green Fluorescent Protein Fragment Reassembly Trap: Scope and Mechanism. *J. Am. Chem. Soc.* **2005**, *127* (1), 146–157. <https://doi.org/10.1021/ja046699g>.
- (300) Wu, P.; Brand, L. Resonance Energy Transfer: Methods and Applications. *Anal. Biochem.* **1994**, *218* (1), 1–13. <https://doi.org/10.1006/abio.1994.1134>.
- (301) Xie, Q.; Soutto, M.; Xu, X.; Zhang, Y.; Johnson, C. H. Bioluminescence Resonance Energy Transfer (BRET) Imaging in Plant Seedlings and Mammalian Cells. *Methods Mol. Biol. Clifton NJ* **2011**, *680*, 3–28. [https://doi.org/10.1007/978-1-60761-901-7\\_1](https://doi.org/10.1007/978-1-60761-901-7_1).
- (302) Xu, Y.; Piston, D. W.; Johnson, C. H. A Bioluminescence Resonance Energy Transfer (BRET) System: Application to Interacting Circadian Clock Proteins. *Proc. Natl. Acad. Sci. U. S. A.* **1999**, *96* (1), 151–156. <https://doi.org/10.1073/pnas.96.1.151>.
- (303) Arai, R.; Nakagawa, H.; Kitayama, A.; Ueda, H.; Nagamune, T. Detection of Protein-Protein Interaction by Bioluminescence Resonance Energy Transfer from Firefly Luciferase to Red Fluorescent Protein. *J. Biosci. Bioeng.* **2002**, *94* (4), 362–364. [https://doi.org/10.1016/S1389-1723\(02\)80178-5](https://doi.org/10.1016/S1389-1723(02)80178-5).
- (304) Hamdan, F. F.; Percherancier, Y.; Breton, B.; Bouvier, M. Monitoring Protein-Protein Interactions in Living Cells by Bioluminescence Resonance Energy Transfer (BRET). *Curr. Protoc. Neurosci.* **2006**, *Chapter 5*, Unit 5.23. <https://doi.org/10.1002/0471142301.ns0523s34>.
- (305) Machleidt, T.; Woodroffe, C. C.; Schwinn, M. K.; Méndez, J.; Robers, M. B.; Zimmerman, K.; Otto, P.; Daniels, D. L.; Kirkland, T. A.; Wood, K. V. NanoBRET—A Novel BRET Platform for the Analysis of Protein-Protein Interactions. *ACS Chem. Biol.* **2015**, *10* (8), 1797–1804. <https://doi.org/10.1021/acscchembio.5b00143>.
- (306) Blommel, P. G.; Martin, P. A.; Seder, K. D.; Wrobel, R. L.; Fox, B. G. Flexi Vector Cloning. *Methods Mol. Biol. Clifton NJ* **2009**, *498*, 55–73. [https://doi.org/10.1007/978-1-59745-196-3\\_4](https://doi.org/10.1007/978-1-59745-196-3_4).
- (307) Bacart, J.; Corbel, C.; Jockers, R.; Bach, S.; Couturier, C. The BRET Technology and Its Application to Screening Assays. *Biotechnol. J.* **2008**, *3* (3), 311–324. <https://doi.org/10.1002/biot.200700222>.
- (308) Mercier, J.-F.; Salahpour, A.; Angers, S.; Breit, A.; Bouvier, M. Quantitative Assessment of Beta 1- and Beta 2-Adrenergic Receptor Homo- and Heterodimerization by Bioluminescence Resonance Energy Transfer. *J. Biol. Chem.* **2002**, *277* (47), 44925–44931. <https://doi.org/10.1074/jbc.M205767200>.

- (309) Hansson, M. D.; Rzeznicka, K.; Rosenbäck, M.; Hansson, M.; Sirijovski, N. PCR-Mediated Deletion of Plasmid DNA. *Anal. Biochem.* **2008**, *375* (2), 373–375. <https://doi.org/10.1016/j.ab.2007.12.005>.
- (310) Mierzejewska, K.; Siwek, W.; Czapinska, H.; Kaus-Drobek, M.; Radlinska, M.; Skowronek, K.; Bujnicki, J. M.; Dadlez, M.; Bochtler, M. Structural Basis of the Methylation Specificity of R.DpnI. *Nucleic Acids Res.* **2014**, *42* (13), 8745–8754. <https://doi.org/10.1093/nar/gku546>.
- (311) Zhang, J. H.; Chung, T. D.; Oldenburg, K. R. A Simple Statistical Parameter for Use in Evaluation and Validation of High Throughput Screening Assays. *J. Biomol. Screen.* **1999**, *4* (2), 67–73. <https://doi.org/10.1177/108705719900400206>.
- (312) Lilly, E. Assay Guidance Manual. 1338. <https://ascpt.onlinelibrary.wiley.com/doi/full/10.1111/cts.12570>
- (313) Mizushima, N.; Yoshimori, T.; Levine, B. Methods in Mammalian Autophagy Research. *Cell* **2010**, *140* (3), 313–326. <https://doi.org/10.1016/j.cell.2010.01.028>.
- (314) Mizushima, N.; Yoshimori, T. How to Interpret LC3 Immunoblotting. *Autophagy* **2007**, *3* (6), 542–545. <https://doi.org/10.4161/auto.4600>.
- (315) England, C. G.; Luo, H.; Cai, W. HaloTag Technology: A Versatile Platform for Biomedical Applications. *Bioconjug. Chem.* **2015**, *26* (6), 975–986. <https://doi.org/10.1021/acs.bioconjchem.5b00191>.
- (316) Pantoliano, M. W.; Petrella, E. C.; Kwasnoski, J. D.; Lobanov, V. S.; Myslik, J.; Graf, E.; Carver, T.; Asel, E.; Springer, B. A.; Lane, P.; Salemme, F. R. High-Density Miniaturized Thermal Shift Assays as a General Strategy for Drug Discovery. *J. Biomol. Screen.* **2001**, *6* (6), 429–440. <https://doi.org/10.1177/108705710100600609>.
- (317) Huynh, K.; Partch, C. L. Current Protocols in Protein Science. *Curr. Protoc. Protein Sci. Editor. Board John E Coligan Al* **2015**, *79*, 28.9.1–28.9.14. <https://doi.org/10.1002/0471140864.ps2809s79>.
- (318) Martinez Molina, D.; Jafari, R.; Ignatushchenko, M.; Seki, T.; Larsson, E. A.; Dan, C.; Sreekumar, L.; Cao, Y.; Nordlund, P. Monitoring Drug Target Engagement in Cells and Tissues Using the Cellular Thermal Shift Assay. *Science* **2013**, *341* (6141), 84–87. <https://doi.org/10.1126/science.1233606>.
- (319) Jafari, R.; Almqvist, H.; Axelsson, H.; Ignatushchenko, M.; Lundbäck, T.; Nordlund, P.; Molina, D. M. The Cellular Thermal Shift Assay for Evaluating Drug Target Interactions in Cells. *Nat. Protoc.* **2014**, *9* (9), 2100–2122. <https://doi.org/10.1038/nprot.2014.138>.
- (320) Martinez Molina, D.; Nordlund, P. The Cellular Thermal Shift Assay: A Novel Biophysical Assay for In Situ Drug Target Engagement and Mechanistic Biomarker Studies. *Annu. Rev. Pharmacol. Toxicol.* **2016**, *56* (1), 141–161. <https://doi.org/10.1146/annurev-pharmtox-010715-103715>.
- (321) Narvaez, A. J.; Ber, S.; Crooks, A.; Emery, A.; Hardwick, B.; Guarino Almeida, E.; Huggins, D. J.; Perera, D.; Roberts-Thomson, M.; Azzarelli, R.; Hood, F. E.; Prior, I. A.; Walker, D. W.; Boyce, R.; Boyle, R. G.; Barker, S. P.; Torrance, C. J.; McKenzie, G. J.; Venkitaraman, A. R. Modulating Protein-Protein Interactions of the Mitotic Polo-like Kinases to Target Mutant KRAS. *Cell Chem. Biol.* **2017**, *24* (8), 1017–1028.e7. <https://doi.org/10.1016/j.chembiol.2017.07.009>.
- (322) Kawatkar, A.; Schefter, M.; Hermansson, N.-O.; Snijder, A.; Dekker, N.; Brown, D. G.; Lundbäck, T.; Zhang, A. X.; Castaldi, M. P. CETSA beyond Soluble Targets: A Broad Application to Multipass Transmembrane Proteins. *ACS Chem. Biol.* **2019**, *14* (9), 1913–1920. <https://doi.org/10.1021/acscchembio.9b00399>.
- (323) Zaidi, N.; Maurer, A.; Nieke, S.; Kalbacher, H. Cathepsin D: A Cellular Roadmap. *Biochem. Biophys. Res. Commun.* **2008**, *376* (1), 5–9. <https://doi.org/10.1016/j.bbrc.2008.08.099>.
- (324) Frost, L. S.; Dhingra, A.; Reyes-Reveles, J.; Boesze-Battaglia, K. Chapter Three - The Use of DQ-BSA to Monitor the Turnover of Autophagy-Associated Cargo. In *Methods in Enzymology*; Galluzzi, L., Bravo-San Pedro,

J. M., Kroemer, G., Eds.; Molecular Characterization of Autophagic Responses, Part A; Academic Press, 2017; Vol. 587, pp 43–54. <https://doi.org/10.1016/bs.mie.2016.09.052>.

- (325) Ikononov, O. C.; Sbrissa, D.; Shisheva, A. Mammalian Cell Morphology and Endocytic Membrane Homeostasis Require Enzymatically Active Phosphoinositide 5-Kinase PIKfyve. *J. Biol. Chem.* **2001**, *276* (28), 26141–26147. <https://doi.org/10.1074/jbc.M101722200>.
- (326) Kimple, A. J.; Yasgar, A.; Hughes, M.; Jadhav, A.; Willard, F. S.; Muller, R. E.; Austin, C. P.; Inglese, J.; Ibeanu, G. C.; Siderovski, D. P.; Simeonov, A. A High-Throughput Fluorescence Polarization Assay for Inhibitors of the GoLoco Motif/G-Alpha Interaction. *Comb. Chem. High Throughput Screen.* **2008**, *11* (5), 396–409.
- (327) Hall, M. D.; Yasgar, A.; Peryea, T.; Braisted, J. C.; Jadhav, A.; Simeonov, A.; Coussens, N. P. Fluorescence Polarization Assays in High-Throughput Screening and Drug Discovery: A Review. *Methods Appl. Fluoresc.* **2016**, *4* (2), 022001. <https://doi.org/10.1088/2050-6120/4/2/022001>.
- (328) Lea, W. A.; Simeonov, A. Fluorescence Polarization Assays in Small Molecule Screening. *Expert Opin. Drug Discov.* **2011**, *6* (1), 17–32. <https://doi.org/10.1517/17460441.2011.537322>.
- (329) Fan, W.; Nassiri, A.; Zhong, Q. Autophagosome Targeting and Membrane Curvature Sensing by Barkor/Atg14(L). *Proc. Natl. Acad. Sci.* **2011**, *108* (19), 7769–7774. <https://doi.org/10.1073/pnas.1016472108>.
- (330) Lu, J.; He, L.; Behrends, C.; Araki, M.; Araki, K.; Jun Wang, Q.; Catanzaro, J. M.; Friedman, S. L.; Zong, W.-X.; Fiel, M. I.; Li, M.; Yue, Z. NRBF2 Regulates Autophagy and Prevents Liver Injury by Modulating Atg14L-Linked Phosphatidylinositol-3 Kinase III Activity. *Nat. Commun.* **2014**, *5* (1), 1–15. <https://doi.org/10.1038/ncomms4920>.
- (331) Matsunaga, K.; Saitoh, T.; Tabata, K.; Omori, H.; Satoh, T.; Kurotori, N.; Maejima, I.; Shirahama-Noda, K.; Ichimura, T.; Isobe, T.; Akira, S.; Noda, T.; Yoshimori, T. Two Beclin 1-Binding Proteins, Atg14L and Rubicon, Reciprocally Regulate Autophagy at Different Stages. *Nat. Cell Biol.* **2009**, *11* (4), 385–396. <https://doi.org/10.1038/ncb1846>.
- (332) Malo, N.; Hanley, J. A.; Cerquozzi, S.; Pelletier, J.; Nadon, R. Statistical Practice in High-Throughput Screening Data Analysis. *Nat. Biotechnol.* **2006**, *24* (2), 167–175. <https://doi.org/10.1038/nbt1186>.
- (333) Liu, J.; Xia, H.; Kim, M.; Xu, L.; Li, Y.; Zhang, L.; Cai, Y.; Norberg, H. V.; Zhang, T.; Furuya, T.; Jin, M.; Zhu, Z.; Wang, H.; Yu, J.; Li, Y.; Hao, Y.; Choi, A.; Ke, H.; Ma, D.; Yuan, J. Beclin1 Controls the Levels of P53 by Regulating the Deubiquitination Activity of USP10 and USP13. *Cell* **2011**, *147* (1), 223–234. <https://doi.org/10.1016/j.cell.2011.08.037>.
- (334) Tan, X.; Thapa, N.; Liao, Y.; Choi, S.; Anderson, R. A. PtdIns(4,5)P<sub>2</sub> Signaling Regulates ATG14 and Autophagy. *Proc. Natl. Acad. Sci.* **2016**, *113* (39), 10896–10901. <https://doi.org/10.1073/pnas.1523145113>.
- (335) He, R.; Peng, J.; Yuan, P.; Xu, F.; Wei, W. Divergent Roles of BECN1 in LC3 Lipidation and Autophagosomal Function. *Autophagy* **2015**, *11* (5), 740–747. <https://doi.org/10.1080/15548627.2015.1034404>.
- (336) Kageyama, S.; Omori, H.; Saitoh, T.; Sone, T.; Guan, J.-L.; Akira, S.; Imamoto, F.; Noda, T.; Yoshimori, T. The LC3 Recruitment Mechanism Is Separate from Atg9L1-Dependent Membrane Formation in the Autophagic Response against Salmonella. *Mol. Biol. Cell* **2011**, *22* (13), 2290–2300. <https://doi.org/10.1091/mbc.e10-11-0893>.
- (337) Runwal, G.; Stamatakou, E.; Siddiqi, F. H.; Puri, C.; Zhu, Y.; Rubinsztein, D. C. LC3-Positive Structures Are Prominent in Autophagy-Deficient Cells. *Sci. Rep.* **2019**, *9* (1), 10147. <https://doi.org/10.1038/s41598-019-46657-z>.
- (338) Rai, S.; Arasteh, M.; Jefferson, M.; Pearson, T.; Wang, Y.; Zhang, W.; Bicsak, B.; Divekar, D.; Powell, P. P.; Naumann, R.; Beraza, N.; Carding, S. R.; Florey, O.; Mayer, U.; Wileman, T. The ATG5-Binding and Coiled Coil Domains of ATG16L1 Maintain Autophagy and Tissue Homeostasis in Mice Independently of the WD Domain

Required for LC3-Associated Phagocytosis. *Autophagy* **2019**, *15* (4), 599–612.  
<https://doi.org/10.1080/15548627.2018.1534507>.

## VITA

NAME: Ivan Pavlinov

EDUCATION: B.S., Biochemistry and Chemical Biology, Wayne State University, Detroit, MI, 2015  
Ph.D., Chemistry, University of Illinois at Chicago, Chicago, IL, 2020

HONORS: Wiley Award in Advanced Organic Chemistry, 2015  
Moriarty Fellowship, 2020

TEACHING: Department of Chemistry, University of Illinois at Chicago  
Experience:  
Survey of Organic and Biochemistry      Fall 2017, Spring 2018, Summer 2020  
General Chemistry II                              Summer 2018, Spring 2020  
Biochemistry I                                      Spring 2017, Fall 2018, Spring & Fall 2020  
Summery Enrichment Chemistry Workshop   Summer 2019  
Organic Chemistry Lab                            Summer 2017  
General Chemistry I                                Spring & Fall 2016  
Chemistry 101                                        Fall 2015

PRESENTATIONS: Pavlinov, I.; Gao, Q.; Aldrich, L. N. Discovering Small Molecule Inhibitors of Early Autophagy. Presented at MIKI, Chicago, 2018.

PUBLICATIONS: Hippman, R. S.; Pavlinov, I.; Gao, Q.; Mavlyanova, M. K.; Gerlach E. M.; Aldrich L. N. Multiple chemical features impact biological performance diversity of a highly active flavonoid natural product-inspired library. *ChemBioChem* **2020**, ASAP.  
Pavlinov, I.; Salkovski, M.; Aldrich, L. N. Beclin1-ATG14L protein-protein interaction inhibitor selectively inhibits autophagy through disruption of VPS34 Complex I. *J. Am. Chem. Soc.* **2020**, *142* (18), 8174-8182.  
Gerlach, E. M.; Korkmaz, A. M.; Pavlinov, I.; Gao, Q.; Aldrich, L. N. Systematic diversity-oriented synthesis of reduced flavones from  $\gamma$ -pyrones to probe biological performance diversity. *ACS Chem. Biol.* **2019**, *14* (7), 1536-1545.  
Pavlinov, I.; Gerlach, E. M.; Aldrich, L. N. Next generation diversity-oriented synthesis: a paradigm shift from chemical diversity to biological diversity. *Org. Biomol. Chem.* **2019**, *17*, 1608-1623.  
Helgren, T. R.; Xu, L. L.; Sotelo, D.; Mehta, Y. R.; Korkmaz, M. A.; Pavlinov, I.; Aldrich, L. N. Microwave-Assisted, Asymmetric Synthesis of 3-Amino-2, 3-Dihydrobenzofuran Flavonoid Derivatives from Chalcones. *Chem. Eur. J.* **2018**, *24* (18), 4509-4514.

## APPENDIX

Permission for the reproduction of ACS articles:

PERMISSION/LICENSE IS GRANTED FOR YOUR ORDER AT NO CHARGE

This type of permission/license, instead of the standard Terms & Conditions, is sent to you because no fee is being charged for your order. Please note the following:

- Permission is granted for your request in both print and electronic formats, and translations.
- If figures and/or tables were requested, they may be adapted or used in part.
- Please print this page for your records and send a copy of it to your publisher/graduate school.
- Appropriate credit for the requested material should be given as follows: "Reprinted (adapted) with permission from (COMPLETE REFERENCE CITATION). Copyright (YEAR) American Chemical Society." Insert appropriate information in place of the capitalized words.
- One-time permission is granted only for the use specified in your request. No additional uses are granted (such as derivative works or other editions). For any other uses, please submit a new request.

Permission for the reproduction of Wiley article:

Dear Ivan Pavlinov,

John Wiley & Sons - Books has approved your recent request. Before you can use this content, you must accept the license fee and terms set by the publisher.

Use this link to accept (or decline) the publisher's fee and terms for this order.

Request Summary:

Submit date: 16-Jul-2020

Request ID: 600019085

Publication: Chembiochem

Title: Multiple chemical features impact biological performance diversity of a highly active natural product-inspired library.

Type of Use: Republish in other published product

Permission to reuse material adapted for [Figure 2](#):

Permission is not required to use original figures or tables for noncommercial and educational use (i.e., in a review article, in a book that is not for sale) if the article published under the exclusive PNAS License to Publish. Please include a full journal reference and, for articles published in volumes 90–105 (1993–2008), include "Copyright (copyright year) National Academy of Sciences" as a copyright note. Commercial reuse of figures and tables (i.e., in promotional materials, in a textbook for sale) requires permission from PNAS.

Permission to reuse material adapted for [Figure 3](#):

Dear Ivan Pavlinov,

Thank you for placing your order through Copyright Clearance Center's RightsLink® service.

Order Summary

Licensee: Ivan Pavlinov  
Order Date: Jun 24, 2020  
Order Number: 4855591259612  
Publication: Angewandte Chemie International Edition  
Title: Biology-Oriented Synthesis of a Withanolide-Inspired Compound Collection Reveals Novel Modulators of Hedgehog Signaling  
Type of Use: Dissertation/Thesis  
Order Total: 0.00 USD

Dear Ivan Pavlinov,

Thank you for placing your order through Copyright Clearance Center's RightsLink® service.

Order Summary

Licensee: Ivan Pavlinov  
Order Date: Jun 24, 2020  
Order Number: 4855600051466  
Publication: Nature Chemistry  
Title: A ring-distortion strategy to construct stereochemically complex and structurally diverse compounds from natural products  
Type of Use: Thesis/Dissertation  
Order Total: 0.00 USD

Dear Ivan Pavlinov,

Thank you for placing your order through Copyright Clearance Center's RightsLink® service.

Order Summary

Licensee: Ivan Pavlinov  
Order Date: Jun 24, 2020  
Order Number: 4855600206016  
Publication: Nature Chemistry  
Title: A strategy for the diversity-oriented synthesis of macrocyclic scaffolds using multidimensional coupling  
Type of Use: Thesis/Dissertation  
Order Total: 0.00 USD

Permission for reuse of material in [Figure 7](#):

Reference 109: This is an open access article distributed under the terms of the Creative Commons CC BY license, which permits unrestricted use, distribution, and reproduction in any medium, provided the original work is properly cited.

You are not required to obtain permission to reuse this article.

Reference 111: Permission is granted at no cost for use of content in a Master's Thesis and/or Doctoral Dissertation, subject to the following limitations. You may use a single excerpt or up to 3 figures tables. If you use more than those limits, or intend to distribute or sell your Master's Thesis/Doctoral Dissertation to the general public through print or website publication, please return to the previous page and select 'Republish in a Book/Journal' or 'Post on intranet/password-protected website' to complete your request.

Permission for reuse of material in [Figure 10](#):

Reference 117: Permission is granted at no cost for use of content in a Master's Thesis and/or Doctoral Dissertation, subject to the following limitations. You may use a single excerpt or up to 3 figures tables. If you use more than those limits, or intend to distribute or sell your Master's Thesis/Doctoral Dissertation to the general public through print or website publication, please return to the previous page and select 'Republish in a Book/Journal' or 'Post on intranet/password-protected website' to complete your request.

Permission for reuse of material in [Figure 26](#):

Dear Ivan Pavlinov,

Thank you for placing your order through Copyright Clearance Center's RightsLink® service.

Order Summary

Licensee: Ivan Pavlinov  
Order Date: Jun 24, 2020  
Order Number: 4855611357653  
Publication: Nature Reviews Drug Discovery  
Title: Pharmacological modulation of autophagy: therapeutic potential and persisting obstacles  
Type of Use: Thesis/Dissertation  
Order Total: 0.00 USD

Permissions for reuse of materials in [Figure 27](#).

Dear Ivan Pavlinov,

Thank you for placing your order through Copyright Clearance Center's RightsLink® service.

Order Summary

Licensee: Ivan Pavlinov  
Order Date: Jun 24, 2020  
Order Number: 4855681338694  
Publication: Science  
Title: Structure and flexibility of the endosomal Vps34 complex reveals the basis of its function on membranes  
Type of Use: Thesis / Dissertation  
Order Total: 0.00 USD

Dear Ivan Pavlinov,

Thank you for placing your order through Copyright Clearance Center's RightsLink® service.

Order Summary

Licensee: Ivan Pavlinov  
Order Date: Jun 24, 2020  
Order Number: 4855690233797  
Publication: Cell Research

Title: Cryo-EM structure and biochemical analysis reveal the basis of the functional difference between human PI3KC3-C1 and -C2

Type of Use: Thesis/Dissertation

Order Total: 0.00 USD

Reference 262: PERMISSION/LICENSE IS GRANTED FOR YOUR ORDER AT NO CHARGE

This type of permission/license, instead of the standard Terms & Conditions, is sent to you because no fee is being charged for your order. Please note the following:

- Permission is granted for your request in both print and electronic formats, and translations.
- If figures and/or tables were requested, they may be adapted or used in part.
- Please print this page for your records and send a copy of it to your publisher/graduate school.
- Appropriate credit for the requested material should be given as follows: "Reprinted (adapted) with permission from (COMPLETE REFERENCE CITATION). Copyright (YEAR) American Chemical Society." Insert appropriate information in place of the capitalized words.
- One-time permission is granted only for the use specified in your request. No additional uses are granted (such as derivative works or other editions). For any other uses, please submit a new request.

If credit is given to another source for the material you requested, permission must be obtained from that source.

Permission to reuse material in [Figure 29](#):

Dear Ivan Pavlinov,

Thank you for placing your order through Copyright Clearance Center's RightsLink® service.

#### Order Summary

Licensee: Ivan Pavlinov

Order Date: Jun 24, 2020

Order Number: 4855690643862

Publication: Nature Structural & Molecular Biology

Title: Structure of the human ATG12~ATG5 conjugate required for LC3 lipidation in autophagy

Type of Use: Thesis/Dissertation

Order Total: 0.00 USD

Permission to reuse material in Figure 30:

Reference 281: PERMISSION/LICENSE IS GRANTED FOR YOUR ORDER AT NO CHARGE

This type of permission/license, instead of the standard Terms & Conditions, is sent to you because no fee is being charged for your order. Please note the following:

- Permission is granted for your request in both print and electronic formats, and translations.
- If figures and/or tables were requested, they may be adapted or used in part.
- Please print this page for your records and send a copy of it to your publisher/graduate school.
- Appropriate credit for the requested material should be given as follows: "Reprinted (adapted) with permission from (COMPLETE REFERENCE CITATION). Copyright (YEAR) American Chemical Society." Insert appropriate information in place of the capitalized words.
- One-time permission is granted only for the use specified in your request. No additional uses are granted (such as derivative works or other editions). For any other uses, please submit a new request.

If credit is given to another source for the material you requested, permission must be obtained from that source.

Permission to reuse material in Figure 31:

Reference 305: PERMISSION/LICENSE IS GRANTED FOR YOUR ORDER AT NO CHARGE

This type of permission/license, instead of the standard Terms & Conditions, is sent to you because no fee is being charged for your order. Please note the following:

- Permission is granted for your request in both print and electronic formats, and translations.
- If figures and/or tables were requested, they may be adapted or used in part.
- Please print this page for your records and send a copy of it to your publisher/graduate school.
- Appropriate credit for the requested material should be given as follows: "Reprinted (adapted) with permission from (COMPLETE REFERENCE CITATION). Copyright (YEAR) American Chemical Society." Insert appropriate information in place of the capitalized words.
- One-time permission is granted only for the use specified in your request. No additional uses are granted (such as derivative works or other editions). For any other uses, please submit a new request.

If credit is given to another source for the material you requested, permission must be obtained from that source.

Permission to reuse material for [Figure 33](#):

Reference 312: All Assay Guidance Manual content, except where otherwise noted, is licensed under a Creative Commons Attribution-NonCommercial-ShareAlike 3.0 Unported license (CC BY-NC-SA 3.0), which permits copying, distribution, transmission, and adaptation of the work, provided the original work is properly cited and not used for commercial purposes. Any altered, transformed, or adapted form of the work may only be distributed under the same or similar license to this one.

Permission to reuse material from [Figure 34](#):

Reference 311: Permission is granted at no cost for use of content in a Master's Thesis and/or Doctoral Dissertation, subject to the following limitations. You may use a single excerpt or up to 3 figures tables. If you use more than those limits, or intend to distribute or sell your Master's Thesis/Doctoral Dissertation to the general public through print or website publication, please return to the previous page and select 'Republish in a Book/Journal' or 'Post on intranet/password-protected website' to complete your request.

Permission to reuse material from [Figure 37](#):

Reference 322: PERMISSION/LICENSE IS GRANTED FOR YOUR ORDER AT NO CHARGE

This type of permission/license, instead of the standard Terms & Conditions, is sent to you because no fee is being charged for your order. Please note the following:

- Permission is granted for your request in both print and electronic formats, and translations.
- If figures and/or tables were requested, they may be adapted or used in part.
- Please print this page for your records and send a copy of it to your publisher/graduate school.
- Appropriate credit for the requested material should be given as follows: "Reprinted (adapted) with permission from (COMPLETE REFERENCE CITATION). Copyright (YEAR) American Chemical Society." Insert appropriate information in place of the capitalized words.
- One-time permission is granted only for the use specified in your request. No additional uses are granted (such as derivative works or other editions). For any other uses, please submit a new request.

If credit is given to another source for the material you requested, permission must be obtained from that source.

Permission to reuse material for [Figure 38](#):

Thank you for your order!

Dear Ivan Pavlinov,

Thank you for placing your order through Copyright Clearance Center's RightsLink® service.

Order Summary

Licensee: Ivan Pavlinov  
Order Date: Jun 24, 2020  
Order Number: 4855700930326  
Publication: Elsevier Books  
Title: Methods in Enzymology  
Type of Use: reuse in a thesis/dissertation  
Order Total: 0.00 USD